

**Multicomponent 3D-printing for core - shell
capsule composites and supramolecular
polymers**

Dissertation

zur Erlangung des
Doktorgrades der Naturwissenschaften (Dr. rer. nat.)

der

Naturwissenschaftlichen Fakultät II
Chemie, Physik und Mathematik

der Martin-Luther-Universität
Halle-Wittenberg

vorgelegt

von Herrn Harald Rupp
geb. am 22.07.1990 in Homburg/Saar

Gutachter

1. Prof. Dr. Wolfgang H. Binder
2. Prof. Dr. Brigitte Voit

Verteidigt am: 04.05.2021

Danksagung

Ich danke Herrn Prof. Dr. W. H. Binder für das interessante Thema meiner Promotion über neue Applikationen mit Hilfe des 3D-Drucks und für die stets freundliche Unterstützung bei der Anfertigung dieser Arbeit.

Ich bedanke mich bei allen aktuellen und ehemaligen Kollegen für ihre Unterstützung und das nette Arbeitsklima. Frau Julia Großert und Frau Susanne Tanner danke ich für die Messungen zahlreicher Analysen meiner Proben. Des Weiteren stellten sie Chemikalien und Glasgeräte bereit, die zur Durchführung aller Experimente benötigt wurden. Bei Frau Anke Hassi bedanke ich mich für das Verständnis und die Unterstützung bei allen organisatorischen Angelegenheiten.

Bei allen Mitarbeitern der analytischen Abteilung des Instituts für Organische Chemie bedanke ich mich für die Anfertigung der NMR-Spektren.

Frau Dr. Diana Döhler danke ich für die fortwährende offene Diskussionsbereitschaft für alle theoretischen und praktischen Probleme und Herausforderungen, die während der Promotionszeit anfielen.

Herrn Frank Syrowatka und Frau Dr. Annette Meister für die Messung von SEM- und entsprechend TEM-Proben in anderen Arbeitsgruppen. Auch danke ich M. Sc. Toni Buttler für die Messungen von XRD-Daten und die Nutzung von Brennöfen zu Analysen und Wartungszwecken.

Meinen direkten Laborkollegen, sowie allen weiteren Kollegen, danke ich für die stets angenehme und lustige Arbeitsatmosphäre, wenn der Laboralltag mal etwas trist war. Sie haben mich stets inspiriert und geistige Anregungen gegeben. Hier möchte ich auch Herrn Dr. Sebastian Funtan für die gelungene Teamarbeit während des gesamten Studiums danken.

Abschließend gilt mein ganz besonderer Dank meiner Familie, sowie meinen Freunden, die mich fortwährend in der Promotionszeit unterstützt haben. Sie haben mein Jammern und Klagen jahrelang ertragen und mich immer wieder aufgerichtet. Ihr könnt euch nicht vorstellen, wie wichtig dieser Rückhalt war.

Abstract

This project adapted encapsulation methods for a 3D-printing process, new encapsulation additive manufacturing with a dual printing head system. There are methods developed to form capsules with biocompatible materials based on emulsion-/solvent evaporation method and 3D-printing technologies. For the capsule shell material different, well known biodegradable polyesters are tested. The hydrophobic core filling is based on different model components of the terpenes. The synthesized capsules will be analyzed regarding size, distribution, ratio and composition. The critical manufacturing process is the simultaneous build up of capsule shell and liquid core filling in a layer by layer approach for micrometer sized capsules (100 – 800 μm). After several printing cycles and finished printing process, a macro-scaled specimen is manufactured including several capsule-like structures. As a proof of concept “click”-reaction systems, based on liquid trivalent resin monomers, are manufactured. PCL composites with nano- and micro-fillers are combined with reactive liquids. The 3D-printed core-shell capsule composite can be used for post-printing reactions and damage sensing when combined with a fluorogenic dye.

With a similar approach, stress-sensing materials, based on high- and low molecular weight mechanophores (latent copper(I)bis(N-heterocyclic carbenes)) are manufactured. Post-printing, the mechanophores can be activated by compression to trigger a fluorogenic dye inside a bulk polymeric material. Focus is placed on the printability and post-printing activity of the latent mechanophores using “click”-reaction.

Another concept for 3D-printing multi-material composites is based on hydrogen-bonded supramolecular polymers, known to increase mechanical strength. The printability is relies on reversible thermal- and shear-induced dissociation of the supramolecular interactions, which generates stable and self-supported structures after 3D-printing. Thus, linear and three-arm star poly(isobutylene)s PIB-B2 , PIB-B3, and linear poly(ethylene glycol)s PEG-B2 were prepared and probed by melt-rheology to adjust the viscosity for the proper printing window. The supramolecular PIB polymers showed a rubber like behavior and were able to form self-supported 3D-printed objects at room temperature and below. To further strengthen the PIB-B2, nanocomposites with silica nanoparticles (12 nm, 5-15 wt%) were analyzed and led to an improvement of the shape stability.

Kurzdarstellung

Diese Arbeit beschäftigt sich mit der Umsetzung von Enkapsulierungsmethoden in 3D-Druckprozesse, wobei ein 3D-Drucker mit zwei verschiedenen Köpfen verwendet wird. Für die Enkapsulierung sind verschiedene Methoden zum Einsatz gekommen, wie z.B. Emulsion-/Evaporationsverfahren und 3D-Drucktechniken, die mit biokompatiblen Polymeren funktionieren. Für die Kapselhülle wurden verschiedene biologisch abbaubare Polyester getestet. Die hydrophoben, flüssigen Füllungen basieren fürs Erste auf Modelverbindungen aus der Klasse der Terpene. Die synthetisierten Kapseln wurden auf ihre Größe, Verteilung, Anteile und Zusammensetzung analysiert. Der wichtigste Punkt der Arbeit ist das Drucken von der Kapselhülle, gleichzeitig kombiniert mit dem Füllen der Kapseln mit Flüssigkeiten, in einem Schicht-für-Schicht Ansatz für mikrometer-große Kapseln (100 – 800 μm). Nach mehrfacher Wiederholung dieser Prozesse entsteht ein makroskopischer Probenkörper mit vielen Kapsel-ähnlichen Strukturen im Inneren. Das entwickelte System wurde auf ein „Click“-Reaktion basierendes System angewendet, das auf flüssige trivalente Monomere basiert. Dafür wurden PCL-Komposite mit Nano- und Mikro-Partikeln mit den reaktiven Flüssigkeiten kombiniert. Das entstehende Kompositmaterial wurde für post-printing Reaktionen verwendet und wurde zur Stressdetektion verwendet, wenn es mit einem Fluoreszenzfarbstoff kombiniert wurde.

Mit dem gleichen Druckverfahren wurden auch stress-fühlende Materialien erprobt, die auf Mechanophore (labile Kupfer(I)bis(N-heterozyklische Carbene) mit kleinem und hohem Molekulargewicht basieren. Nach dem Drucken, können die Mechanophore mit Kompression aktiviert werden, um eine Fluoreszenzreaktion auszulösen. Hauptsächlich wurde sich auf die Druckbarkeit und Aktivität der Mechanophore konzentriert, bei Verwendung der „Click“-Reaktion.

In einem weiteren Teil der Arbeit zum 3D-Drucken von Multimaterial-Kompositen basiert auf supramolekulare Polymere mit Wasserstoffbrückenbindungen, die ihre mechanischen Eigenschaften verbessern. Die Druckbarkeit wird auf die temperatur- und scherabhängigen Eigenschaften der supramolekularen Wechselwirkungen zurückgeführt, die auch für die Formstabilität nach dem 3D-Drucken verantwortlich sind. Dafür wurden lineare und dreiarmlige Poly(isobutylene) PIB-B2, PIB-B3 und lineare Polyethylenglycole PEG-B2 synthetisiert und mittels Schmelzrheologie auf ihre Druckbarkeit untersucht. Die supramolekularen PIB-polymere zeigten Gummiartiges Verhalten bei Raumtemperatur oder niedrigeren Temperaturen. Um die Formstabilität dieser Materialien weiter zu verbessern wurden sie mit Silica-Nanopartikel (12 nm, 5-15 wt%) angereichert.

Parts of this thesis have been published in:

Rupp, H., Binder, W. H., 3D Printing of Core–Shell Capsule Composites for Post-Reactive and Damage Sensing Applications, *Adv. Mater. Technol.* **2020**, 2000509.

<https://doi.org/10.1002/admt.202000509> (CC BY-NC 4.0)

Rupp, H., Binder, W. H., Multicomponent Stress-Sensing Composites Fabricated by 3D-Printing Methodologies, *Macromol. Rapid Commun.* **2020**, 2000450.

<https://doi.org/10.1002/marc.202000450> (CC BY-NC 4.0)

Rupp, H., Döhler, D., Hilgeroth, P., Mahmood, N., Beiner, M., Binder, W. H., 3D Printing of Supramolecular Polymers: Impact of Nanoparticles and Phase Separation on Printability, *Macromol. Rapid Commun.* **2019**, 40, 1900467.

<https://doi.org/10.1002/marc.201900467> (CC BY-NC-ND 4.0)

For open access articles, an Open Access Agreement with a Creative Commons license was signed, the author retains copyright and the public is allowed to reuse the content. Results, discussions and experimental data were adapted, modified and partly reused in this thesis.

Table of Contents

1.0 Introduction	18
1.1 Additive manufacturing - 3D-printing	18
1.1.1 Fused Deposition Modeling (FDM)	18
1.1.1.1 <i>Melt rheology of polymers</i>	19
1.1.1.2 <i>Extrusion of neat polymers</i>	21
1.1.1.3 <i>Extrusion of composites</i>	22
1.1.2 Stereolithography (SLA)	23
1.1.3 Selective Laser Sintering (SLS)	24
1.1.4 Binder Jetting (BJ)	25
1.1.5 Material Jetting (MJ)	26
1.2 Multicomponent 3D-printing	28
1.2.1 3D-printing of Core/Shell structures	28
1.2.1.1 <i>Assembled structures after manufacturing</i>	28
1.2.1.2 <i>Structures fabricated in one printing cycle</i>	30
1.2.2 3D-printing of supramolecular polymers	32
1.2.2.1 <i>Hydrogen-bonding polymers</i>	33
1.2.2.2 <i>Rheology of supramolecular polymers</i>	36
1.2.3 3D-printing of mechanophore polymers	37
1.3 Traditional nano-encapsulation techniques	39
1.3.1 Emulsification solvent evaporation method	39
1.3.2 Emulsion polymerization	40
1.3.3 Interfacial polymerization	42

1.3.4 Solvent displacement and interfacial deposition	42
1.3.5 Emulsification/solvent diffusion	43
2.0 Aims	45
2.1 Concept	47
3.0 Results and discussion	49
3.1 3D-printer evaluation	49
3.1.1 Polymer extruder	49
3.1.1.1 Melt rheology	50
3.1.1.2 Melt rheology of PCL	51
3.1.1.3 Melt rheology of polyethers	51
3.1.1.4 Melt rheology of polyesters	52
3.1.2 Rheology for the liquid inkjet print head	54
3.2 3D-printing of core-shell capsule composites	56
3.2.1 Encapsulation of hydrophobic model liquids	58
3.2.1.1 Contact angle measurements PCL – hydrophobic liquid	59
3.2.1.2 Setup for the 3D-printing process	60
3.2.1.3 Capsule specimen analysis	61
3.2.1.4 Degradation of PCL during 3D-printing	63
3.2.2 Reactive capsule composites	64
3.2.2.1 Preparation of the composites	64
3.2.2.2 Synthesis of the monomers	65
3.2.2.3 Synthesis of the catalyst: TRGO	66

3.2.2.4	<i>3D-printing of reactive capsule composites</i>	67
3.2.2.5	<i>Thermal stability of the composites</i>	67
3.2.2.6	<i>Post-printing reactivity (DSC)</i>	68
3.2.2.7	<i>Post-printing reactivity (Fluorescence)</i>	70
3.2.2.8	<i>Conclusion</i>	71
3.3	3D-printing of labile copper(I)-(NHC)-mechanophores	72
3.3.1	Mechanophore-based capsule composites	72
3.3.1.1	<i>Synthesis of the mechanophores</i>	73
3.3.2	3D-printing of mechanophores composites	77
3.3.2.1	<i>Stability of mechanophores after printing</i>	79
3.3.2.2	<i>Activity of mechanophores after printing</i>	80
3.3.2.3	<i>Conclusion</i>	81
3.4	3D-printing of supramolecular polymers and their composites	83
3.4.1	Synthesis for the supramolecular polymers	84
3.4.2	Analysis for the supramolecular polymers	85
3.4.3	3D-printing window for supramolecular polymers	89
3.4.4	Melt rheology of the barbiturate-based PIBs	90
3.4.5	Melt rheology of the barbiturate-based PEGs	91
3.4.6	FDM of the barbiturate polymers	92
3.4.7	SAXS of the barbiturate-based polymers	93
3.4.8	Conclusion on FDM of supramolecular polymers	94
3.4.9	Synthesis of carbon fillers for supramolecular polymer composites	95

3.4.10 Melt rheology of the carbon-based fillers in PIB-B2	96
3.4.11 Correlation between the relaxation time and the form stability	96
3.4.12 Melt rheology of the ureidopyrimidinone-based PIB	98
3.4.13 FDM of the ureidopyrimidinone-based PIB	98
3.4.14 Melt rheology of the carbon-based fillers in PIB-U2	99
3.4.15 Correlation between the relaxation time and the form stability	100
3.4.16 Melt rheology of the tetronic based supramolecular polymers	101
3.4.17 Thermal stability of the supramolecular polymers	103
3.5 Emulsion / solvent evaporation encapsulation	104
3.5.1 Scanning electron microscopy (SEM)	105
3.5.2 Transmission electron microscopy (TEM)	107
3.5.3 Influence of different parameters on the nanocapsules	108
3.5.4 Encapsulation efficiency	110
3.5.5 Fluorescence of capsule suspensions	112
4.0 Experimental Part	118
4.1 Chemicals and Materials	118
4.2 Instrumentation	118
4.3 Syntheses	122
4.3.1 Monomers for “Click”-reaction resins	122
4.3.1.1 <i>Synthesis of 1,1,1-Trimethylolpropane tri(3-azido-2-hydroxypropanyl)ether (1)</i>	122

4.3.1.2 Acetylation of 1,1,1-Trimethylolpropane tri(3-Azido-2-hydroxy-propanyl)ether (2)	123
4.3.1.3 Synthesis of 1,1,1-Trimethylolpropane tripropargylether (3)	124
4.3.1.4 Synthesis of Bisphenol A/E propargylether (4/5)	124
4.3.2 Syntheses of supramolecular polymers	125
4.3.2.1 Synthesis of telechelic bimesylated PEG (400, 1500, 8000) (6)	125
4.3.2.2 Synthesis of telechelic biazido PEG (400, 1500, 8000) (7)	126
4.3.2.3 Synthesis of tetravalent telechelic azido Tetronic 3600 (8)	126
4.3.2.4 Synthesis of bivalent telechelic azido PIB (9)	127
4.3.2.5 Synthesis of diethyl 2-hexynyl-2-ethylmalonate (10)	128
4.3.2.6 Synthesis of 2-hexynyl-2-ethyl barbiturate (11)	129
4.3.2.7 Synthesis of UPy isocyanate (12)	130
4.3.2.8 Synthesis of alkyne thymine (13)	130
4.3.2.9 Synthesis of bivalent PEG-barbiturate via click reaction (14)	131
4.3.2.10 Synthesis of tetravalent Tetronic-barbiturate via click reaction (15)	131
4.3.2.11 Synthesis of bivalent PIB-8000-barbiturate via click reaction (16)	132
4.3.2.12 Synthesis of bivalent PIB-8000-UPy (17)	132
4.3.2.13 Synthesis of tetravalent Tetronic-UPy (18)	133
4.3.3 Syntheses of other “Click”-reaction compounds	133
4.3.3.1 Synthesis of α -propargyl- ϵ -caprolactone (19)	133
4.3.3.2 Synthesis of poly(ϵ -caprolactone)-co-(α -propargyl- ϵ -caprolactone) (20)	134

4.3.3.3 <i>Synthesis of 5-Azido-fluorescein (21)</i>	134
4.3.3.4 <i>“Click”-reaction of 5-azido-fluorescein (22)</i>	135
4.3.4 <i>Syntheses of the mechanophores</i>	135
4.3.4.1 <i>Synthesis of bromo-poly(ϵ-caprolactone) (23)</i>	135
4.3.4.2 <i>Synthesis of 1-methylimidazole-poly(ϵ-caprolactone) (24)</i>	136
4.3.4.3 <i>Synthesis of PCL-mechanophore (25)</i>	136
4.3.4.4 <i>Synthesis of 1-methylimidazole-undecanol (C11) (26)</i>	137
4.3.4.5 <i>Synthesis of C11-mechanophore (27)</i>	137
4.3.4.6 <i>Synthesis of NCO-mechanophore (28)</i>	138
4.3.4.7 <i>Synthesis of PCL-urethane-mechanophore (29)</i>	138
4.3.5 <i>Syntheses of carbon materials</i>	138
4.3.5.1 <i>Synthesis graphene oxide (GO) (30)</i>	138
4.3.5.2 <i>Synthesis of graphene oxide + Cu²⁺ (GO-Cu²⁺) (31)</i>	139
4.3.5.3 <i>Synthesis of thermally reduced graphene oxide - Cu/Cu₂O nanoparticles (TRGO) (32)</i>	139
4.3.5.4 <i>Synthesis of chemically reduced graphene oxide (CRGO) (33)</i>	140
4.3.5.5 <i>Synthesis of nanocapsules</i>	140
5.0 Summary	141
6.0 Appendix	143
6.1 <i>Chemical reaction between trivalent azide and trivalent alkyne.</i>	143
6.2 <i>Chemical reaction between alkyne_PCL with trivalent azide.</i>	143
6.3 <i>Chemical reaction between BEPE and trivalent azide.</i>	144

6.4 Nanocapsules of trivalent azide in PVF polymer shells.	144
6.5 PCL analysis <i>via</i> GPC and DSC before and after 3D-printing.	145
6.6 DSC analysis of PCL composites before and after 3D-printing.	146
6.7 Calibration of 3-Azido-7-hydroxycoumarin in THF.	147
6.8 Analysis of carbon based materials.	148
6.9 TEM analysis of TRGO based material.	149
6.10 TEM analysis of CRGO based material.	149
6.11 FAAS analysis of copper content.	149
6.12 Rheology measurements for 3D-printing.	150
6.13 Frequency sweep measurements of supramolecular polymers and their composites.	153
6.14 Temperature-dependent FT-IR for supramolecular polymers.	156
6.15 Rheology data for printable supramolecular polymers.	157
6.16 Rheology analysis for mechanophore 3D-printing.	160
6.17 Control reaction between PCL and Cu ₂ O in 1,4-dioxane.	161
6.18 Fluorescence calibration (solid state reflection mode).	162
6.19 Absorption and fluorescence of 5-azido-fluorescein and the “clicked” product	162
6.20 NMR spectra of the tetronic polymers.	163
6.21 NMR spectra of the intermediates.	165
7.0 References	177
8.0 Curriculum Vitae	191
9.0 Eigenständigkeitserklärung	194

Abbreviations

3DP	3D-printing
ABS	Acrylonitrile butadiene styrene
ACN	Acetonitrile
AM	Additive manufacturing
ATRP	Atom transfer radical polymerization
B	Barbiturate
BAPE	Bisphenol A dipropargyl ether
BEPE	Bisphenol E dipropargyl ether
BJ	Binder jetting
CAD	Computer-aided design
CHCl ₃	Chloroform
CLIP	Continuous Liquid Interface Production
CMC	Critical micelle concentration
CN-PPV	Cyano-Polyphenylene vinylene
CRGO	Chemically reduced graphene oxide
CuAAC	Copper(I)-catalyzed azide-alkyne cycloaddition
CuI	Copper(I) iodide
Cu ₂ O	Copper(I) oxide
DBTDL	Dibutyltin dilaurate
DCM	Dichloromethane
DIPEA	N,N-Diisopropylethylamine
DLG-50-3A	Poly(D,L-lactide-co-glycolide) 50:50 -COOH
DLG-75-5A	Poly(D,L-lactide-co-glycolide) 75:25 -COOH
DLG-50-7E	Poly(D,L-lactide-co-glycolide) 50:50 -ester
DLG-50-6P	Poly(D,L-lactide-co-glycolide) 50:50 -PEG
DLG-50-7P	Poly(D,L-lactide-co-glycolide) 50:50 -PEG

DLP	Digital light processing
4-DMAP	4-Dimethylaminopyridine
DMF	Dimethylformamide
DMSO	Dimethyl sulfoxide
DP	Degree of polymerization
Et ₂ O	Diethyl ether
EtOH	Ethanol
FDM	Fused deposition modeling
G'	Storage modulus
G''	Loss modulus
GO	Graphene oxide
H ₂ O	Water
H ₂ O ₂	Hydrogen peroxide
H ₂ SO ₄	Sulfuric acid
H ₃ PO ₄	Phosphoric acid
HCl	Hydrochloric acid
HDI	Hexamethylene diisocyanate
HEC	Hydroxyethyl cellulose
HMI	Human machine interface
HPC	Hydroxypropyl cellulose
HPMC	Hydroxypropyl methylcellulose
ISO	a file format
K ₂ CO ₃	Potassium carbonate
KMnO ₄	Potassium permanganate
LCCP	Living carbocationic polymerization
LDA	Lithium diisopropylamide
MCT	Middle-chain triglyceride

MeOH	Methanol
MJ	Material jetting
MMA	Methyl methacrylate
NaN ₃	Sodium azide
NaNO ₂	Sodium nitrite
NaOH	Sodium hydroxide
PBCA	Poly(butyl cyanoacrylate)
PC	Polycarbonates
PCL	Polycaprolactone
PCPDTBT	Poly[2,1,3-benzothiadiazole-4,7-diyl[4,4-bis(2-ethylhexyl)-4H-cyclopenta[2,1-b:3,4-b']dithiophene-2,6-diyl]]
PDI	Polydispersity
PECA	Poly(ethyl cyanoacrylate)
PEEK	Polyether ether ketone
PEO / PEG	Polyethylene glycol
PF8BT	Poly(9,90-dioctylfluorene-co-benzothiadiazole)
PHCA	Poly(hexyl cyanoacrylate)
PIB	Poly(isobutylene)
PLA	Poly(lactide (amorphous))
PLGA	Poly(lactic-co-glycolic acid)
PLLA	Poly-L-lactide
PMCA	Poly(methyl cyanoacrylate)
PMMA	Poly(methyl methacrylate)
PP	Polypropylene
PTHF	Poly(tetrahydrofuran)
PVA	Poly(vinyl alcohol)
RAFT	Reversible addition-fragmentation chain transfer
SDS	Sodium dodecyl sulfate

Sn(Oct) ₂	Tin(II) 2-ethylhexanoate
SLA	Stereolithography
SLS	Selective laser sintering
STL	a file format
SNP	Silica nanoparticles
T	Thymine
TBAB	Tetra-n-butylammonium bromide
TBAF	Tetra-n-butylammonium fluoride
THF	Tetrahydrofuran
TMP	1,1,1-Trimethylolpropane
TMSA	Trimethylsilyl azide
TPGS	D- α -tocopheryl polyethylene glycol succinate
TPU	Thermoplastic polyurethane
TRGO	Thermally reduced graphene oxide
U + UPy	Ureido-pyrimidinone

Instruments

DLS	Dynamic light scattering
DSC	Differential scanning calorimetry
EDX	Energy dispersive X-ray spectroscopy
ESI	Electrospray Ionization
GPC	Gel permeation chromatography
FT-IR	Fourier-transform infrared spectroscopy
MALDI	Matrix-assisted laser desorption / ionization
MS	Mass spectrometry

NMR	Nuclear Magnetic Resonance
SAXS	Small-angle X-ray scattering
SEM	Scanning electron microscope
TEM	Transmission electron microscopy
TGA	Thermogravimetric analysis
TLC	Thin-layer chromatography
ToF	Time-of-flight
UV/Vis	ultraviolet-visible
XRD	X-ray diffraction

1.0 Introduction

1.1 Additive manufacturing - 3D-printing

3D-printing is a manufacturing technique to fabricate complex structures and a large pool of different designs and geometries. Commonly the process consists of creating a three-dimensional model by computer-aided design (CAD) software resulting in a STL file format; transfer it to the 3D-printer and the printer manufacturing the object in a layer-by-layer approach (Figure 1). An STL file stores information about 3D models. This format describes the surface geometry of a three-dimensional object. Different techniques like stereolithography (SLA)¹, fused deposition modeling (FDM)², powder bed fusion³ and material jetting⁴ are well known techniques for additive manufacturing. In the beginning 3D-printer were used for design and prototyping in small batches offering fast and cheap manufacturing. The advantages of the high developed technique are high precision, fast speed, material saving, personalized design and production on demand. In the future the advantages of 3D-printing will be defined new by ongoing research activities, which eliminate limitations of the technology and help to understand fundamental processes.⁵

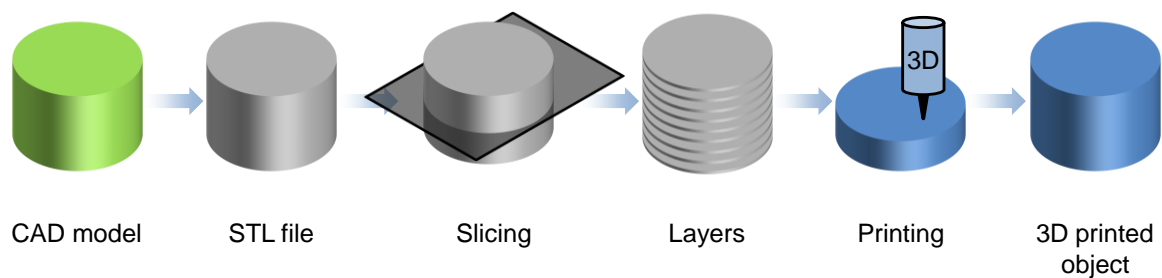


Figure 1: General steps for any 3D-printing technology starting with a digital model. The file is converted in an official additive manufacturing file format (STL) and sliced into several layers of some micrometers. The 3D-printing setup will print in a layer-by-layer process to obtain a 3D object.

1.1.1 Fused Deposition Modeling (FDM)

FDM is one of the most common used printing technologies in industry and prototyping. FDM was developed by Stratasys Inc. in the 1990s.⁶ In this process, the polymer filament is heated inside the printing head to reach a viscous melt state. The molten material is deposited through a metal nozzle onto the printing platform following the pathway for the created structure. The hot filaments fuse together between each layer and solidify during cooling (Figure 2).⁷ The thermal and mechanical properties of the used polymer determine a lot printing parameters and the resulting object properties. Furthermore, printing parameters like layer thickness, orientation, filling percentage; all influence the final mechanical properties of the specimen.⁸ The inter-layer connection being the weakest part of the structure leads to mechanical failures. In modern applications, the FDM process needs to deliver highly durable, stiff, strong materials while being fast during manufacturing, safe, cheap and have a high reproduction quality. To meet these

expectations, the FDM process parameters have to be evaluated for each application. Optimizing each single parameter is a complex process due to the large amount conflicts and properties affecting each other. The orientation of polymer strands and general orientation of the object on the printing platform influence the anisotropic behavior of the material. The printing nozzle determines the polymer strand and layer thickness depending on the material and composite mixtures. The factor having the most influence on the surface roughness is the layer thickness.⁹⁻¹² The amount of grid filling inside the 3D object as well as the angles between each layers add to the mechanical stability. A denser grid leads to a more rigid, strong interior, while an emptier interior requires less manufacturing time. The parts normally have lower mechanical properties than the parts made by conventional manufacturing process such as injection molding.¹³ For improving general quality and mechanical strength for FDM processed parts, it is necessary to understand the correlations between material properties and process parameters. Environmental factors (temperature, humidity) are also affecting FDM materials (ABS, PC, nylon, PVA), as they may have an effect on dimensional accuracy and surface roughness. Some researchers did develop and analyzed biocompatible polymers like polylactic acid (PLA)^{14, 15} and polycaprolactone (PCL)^{16, 17} in FDM for biomaterial applications in the production of scaffolds. Since the polyesters are non-toxic *in vitro* and *in vivo*, they are used in tissue engineering.^{2, 18, 19}

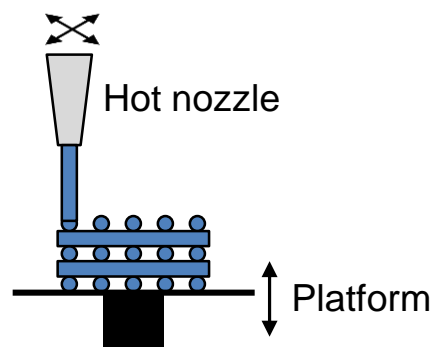


Figure 2: FDM printing process.

1.1.1.1 Melt rheology of polymers

Rheology is an important tool to analyze new materials for any polymer fabrication technique. The characterization of properties in the melt state can be correlated to the manufacturing process to be able to predict the hot melt extrusion. FDM uses heat to obtain a semi-molten state for a thermoplastic polymer, which is then pushed through a nozzle. Therefore high temperature rheology and the shearing effect are of interest. If the viscosity window of the used printing setup is known new materials can be tested to fit inside the viscosity range. Having the knowledge about the printing properties beforehand will save “trial and error” time, prevents nozzle blockage or polymer dripping. With commercial polymers and known printing temperatures a well established printing window can be determined.²⁰⁻²²

With rheology the melt flow and shear thinning behavior is determined, especially for non-Newtonian fluids. Long polymer chains often show shear thinning behavior for large shear forces.²³ They have properties of viscous liquids and elastic solids depending on the deformation, temperature and time; a so called viscoelastic material.²⁴ For the rheological properties there are two types of flow for non-Newtonian liquids. There are simple shear flow (easy to determine) and extensional flow (pressure driven flow) taking place in extrusion and injection molding.²² The viscosity property is the most important to characterize the flow in relation to applied shear force. Ideal Newtonian fluids show a constant viscosity for any shear rate. Since polymer materials are non-Newtonian fluids and show shear thinning behavior based on entangled chains getting disentangled and orientated along the force. A typically shear viscosity curve has different regions depending on the shear rate starting with the low shear rates a plateau with Newtonian behavior is formed where the polymer chains are still entangled. With increasing shear rate the polymer chains get orientated and disentangled resulting in a reduction of viscosity. When most of the polymer chains are disentangled a secondary Newtonian plateau is formed. The second plateau is difficult to measure experimentally for polymer melts (Figure 3).^{22, 25} Other typical fluids like ideal Newtonian liquids, dilatants, supramolecular polymers²⁶⁻²⁸ and hydrogels²⁹⁻³¹ are shown as well.

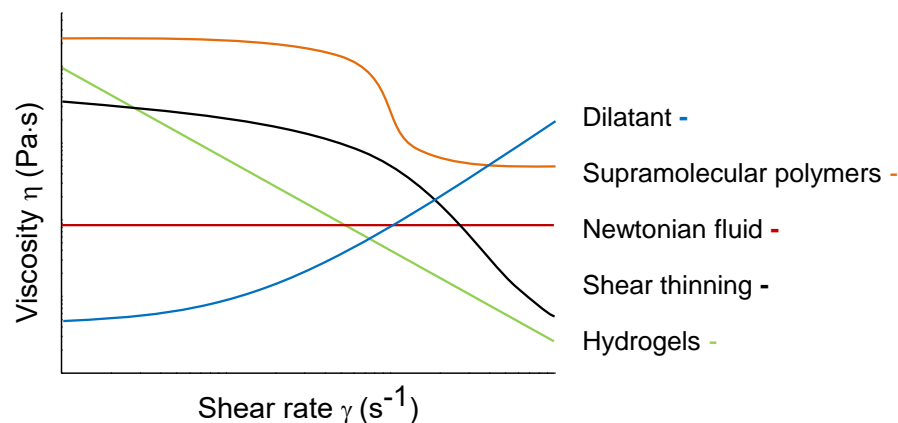


Figure 3: General behavior of different fluid systems (newtonian, dilatant, shear thinning) and polymer materials (supramolecular polymers, hydrogels).

The viscosity of the polymer melt is strongly affected by temperature.^{32, 33} The long polymer chains have different possibilities to move around (rotation, different conformations, side groups) and inhibit their movement (entanglements, loops) due to their surroundings. All these effects and in general closed packing of chains in the polymer melt effect the movement of single chains. The most important parameters for the extrusion process in FDM are on the side of the printer: the temperature and the extruder screw speed.³⁴ If the viscosity of the polymer melts increases the torque of the extruder is strongly affected to higher values. To counter the increase in viscosity an increase in temperature can be performed, but always in reference to decomposition temperatures.^{22, 34} For shear thinning polymers, an increase of rotation speed helps to

decrease the viscosity, too.³⁵ When the polymer material has a too low viscosity, it will not hold its shape after extrusion. For an optimal extrusion of an unknown polymer material the knowledge of the relation between the three parameters temperature, viscosity and shear rate have to be analyzed.³⁶ The rheological behavior can be related to the polymer behavior inside the extrusion nozzle, where the polymer notice low shear force inside the extruder and in the polymer strand behind the nozzle. Inside the printing nozzle the polymer chains are under shear force and orientated into the extrusion direction (Figure 4).²²

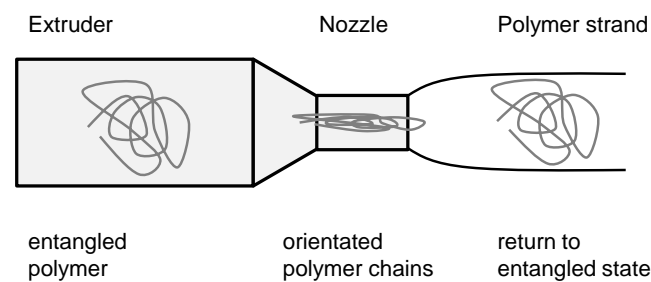


Figure 4: Behavior of long polymer chains under shear stress in an extrusion nozzle.

1.1.1.2 Extrusion of neat polymers

The success for a good FDM printing result depends on two major factors like the choice of material and the settings of the FDM printer during manufacturing. In general amorphous polymers are suitable for the FDM process. The polymer chains of the melt and solid state are all random orientated. Without crystallization, the solidifying process from the melt occurs relative fast. A good solidification speed is required for a good printing result while adding thin layers on top of each. For semi-crystalline polymers the degree of crystallinity can vary from 15 to 80 % depending on molecular weight, chemical structure and cooling rate.³⁷ If they are located at the lower end of crystallinity, they are suitable for FDM because of the large amount of amorphous state like in polyamides and PEEK.³⁸⁻⁴² If the crystallinity is higher, the polymers may not be suited for FDM due to high amount of shrinkage (delamination from the printing platform) or low cooling speed.⁴³ The second critical factor of course is the printing machine and its process parameters being discussed earlier. The used temperature during melting and extrusion plays an important role as it determines the viscosity of the polymer melt. By setting a high temperature for printing, the melt can get to liquid resulting in a dropping liquid. There will be single big drops formed and no uniform long molten polymer strand. On the other hand, if the temperature is too low the connection between the layers will not be sufficient or at worst the polymer will not move through the printing nozzle at all. The right temperature settings for printing result in a good extrusion and a good bonding between the polymer strands of each layer. Combined with the extrusion temperature is the cooling and solidification process, which should cause small stress on

the printed parts. Stress can cause delamination between the layers or warping of the sample starting from the edges. The shrinkage of the edges is very strong, it leads to a curved base layer and the printed part could completely detach from the platform.

1.1.1.3 Extrusion of composites

Next to printing neat polymers in FDM research has been done in the field of composite material printing by use of fillers and fibers. The shortcomings of FDM printed parts can be reduced and new high-end materials can be manufactured. Most of the time, filaments are produced by mixing the materials in the melt and extrude them. In early years, conventional FDM polymers like ABS were combined with different fillers like graphene, fibers, inorganic particles and metals (all in nm and μm size).⁴⁴⁻⁴⁶ The amount of fillers normally is in the low percentage range of 0.2 – 10 % (nano-sized) and 10 – 40 % (micro-sized). The addition of fillers changed mechanical, thermal and electrical properties in the intended way, but at the same time lowered the process ability for FDM in some cases. The solid particles reduce the general movement of the polymer chains in the melt and in the solid state, processing gets more difficult due to higher viscosity and more brittle material. Dul et al.⁴⁷ researched the properties of 2- 8 % graphene content strengthened ABS. The graphene composites showed increased elastic modulus and dynamic modulus, while decreasing the tensile strength and elongation length at the break point. The best printing results were achieved by the 4 % graphene ABS composite. SEM images prove the good distribution of graphene sheets in the material.⁴⁷ Other polymer composites were also processed with FDM e.g. PLA^{14, 48}, PP⁴³, PCL^{16, 49, 50} and polyamides.^{41, 51}

In summary, the key for successful FDM printing of any thermoplastic polymer / composite is the compatibility and suitability of the material with the existing FDM printer. No major changes should be involved to the hardware, tools and software for a fast adaption. Nevertheless, a lot of research still has to be done to overcome the challenges in printing high quality results with new developed materials.⁵²

Table 1: Overview about critical features of FDM.

Advantages	<ul style="list-style-type: none"> • Cheap and accessible • Beginner friendly • Dual-setup (multi-material) • Wide range of polymers
Disadvantages	<ul style="list-style-type: none"> • Resolution depends on the machine (layers visible) • Limited complexity • Warping and anisotropy
Layer thickness	<ul style="list-style-type: none"> • 0.1 – 0.8 mm

1.1.2 Stereolithography (SLA)

The oldest 3D-printing technology being developed in 1986 is based on UV-light curable resins.¹ Thin layers of resin are cured with UV-light initiating a radical formation of a photo-initiator and then a chain reaction of acrylic or epoxy monomers occur.⁵³⁻⁵⁵ Layer by layer of thin harden resin will slowly form the finished object. The non-reacted resin solution is removed and can be reused in some cases. The finished printed parts sometimes need post-printing treatment to further cure the resin with heat or UV-light. In early SLA printers, laser scanning stereolithography was used to print a 3D object by scanning a focused laser beam over the resin surface to cure it.^{56, 57} The second generation stereolithography is called projection stereolithography and prints each layer simultaneously with a single light exposure by using projecting mask patterns onto the resin surface.⁵⁸⁻⁶⁰ The first two methods are not a continuous manufacturing processes. The formation of one printed layer require three steps: 1. expose the resin to UV light, 2. move the cured part to separate it from the surface and 3. repositioning of the object.

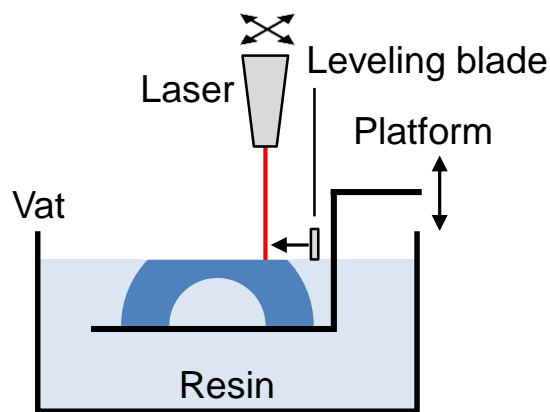


Figure 5: The SLA printing technique.

CLIP method (Continuous Liquid Interface Production)⁶¹ eliminated the last two steps of printing with SLA by creating a persistent liquid interface (dead zone) with an oxygen-permeable window below the UV-light projection plane. The oxygen-containing dead zone (between the window and the polymerizing part) inhibits the resin curing reaction, which allows the part to be continuously exposed to UV-light while elevating. By using the CLIP technique, the parts can be drawn out of the resin continuously.^{61, 62} The most modern SLA technique is based on volumetrically SLA, similar to holographic lithography, forming directly cured 3D volumes of resin. A volumetric stereolithography system was developed in which the printing structure was manufactured by three orthogonal light beams projecting into a photosensitive resin. By controlling each beam, volumetric 3D geometries inside the resin were cured in a single exposure.^{63, 64}

Table 2: The important points about SLA.

Advantages	<ul style="list-style-type: none">• Complex geometry• Accuracy and resolution• Smooth surface• High degree of automation
Disadvantages	<ul style="list-style-type: none">• Expensive machines• Weak mechanical properties• Limited to photo-polymerization• Long printing time
Layer thickness	<ul style="list-style-type: none">• 0.05 – 0.15 mm

1.1.3 Selective Laser Sintering (SLS)

Selective laser sintering processes powdered materials being fused together with a high energy laser. This process can handle different materials from plastic over metal to ceramics.⁶⁵ For polymers, generally polyamides and TPU materials are used.⁶⁶ A powder bed of thermoplastic polymer is threatened with a laser to melt the particles together. The bed is moved down one layer thickness. New powder is spread over the surface by the use of a roller mechanism. The excess powder material around the part will support the printed structure.

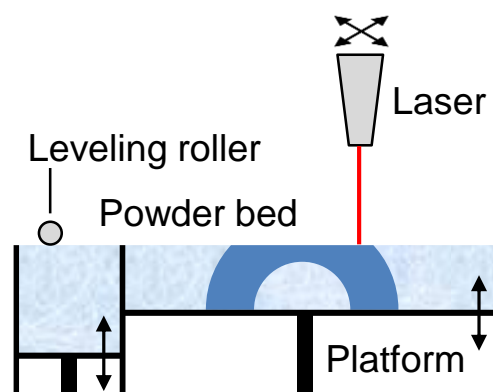


Figure 6: The SLS printing process is illustrated.

In SLS powders with sizes of 10 μm to 300 μm are used while containing flow ability agents like silica. Polymer materials in use are polyamide, PP, PC.^{66, 67} Research in the biological field concentrates on other polymers e.g. PVA, PCL, PLLA, PLGA.^{68, 69} Advantages of SLS are its fast and solvent-free printing process, no support structures are required, very complex designs, high resolution and easy work up. On the other hand

have the manufactured part a rough grainy surface and are porous inside. Also the harsh conditions of laser energy and polymer melting have hindered this technique in the pharmaceutical field due to drug degradation.^{70, 71}

Table 3: A short overview over SLS.

Advantages	<ul style="list-style-type: none"> • Accuracy and high detail • Good amount of materials • No need for support structure, powder reusable • Good mechanic properties
Disadvantages	<ul style="list-style-type: none"> • Rough surface • High energy laser • Expensive machines
Layer thickness	<ul style="list-style-type: none"> • 0.06 – 0.15 mm

1.1.4 Binder Jetting (BJ)

This technology is similar to SLS, but handling different materials like polymers, metals and ceramics.⁷² With the right choice of binder liquid any powdered material can be 3D-printed, since it only prints the binder. Each layer of the fabricated part starts with a fresh layer of powder using a roller mechanism. The binder is then deposited on the powder in the designed pattern. The particles are glued together forming a solid 2D pattern. After each layer the complete platform is lowered around some micrometers to open space for a new layer.⁷³

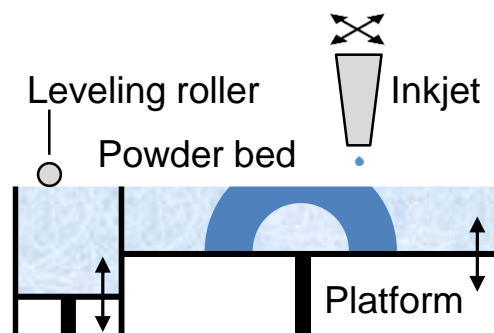


Figure 7: The BJ printing is showcased.

The typical layer heights for polymers are 100 μm , for metals 50 μm and for ceramics 200 - 400 μm .⁷⁴ Post-printing processes have to be done due to fragile properties of the manufactured parts like powder removal, solvent evaporation and sintering for metal

parts. Its unique feature is the printing at room temperature since it does not require energy to fuse the material together like the other additive manufacturing processes.⁷⁵ Patirupanusara et al.⁷⁶ report on the development of polymethyl methacrylate-based mixture, suitable for binder jetting 3D-printing. They found, that the successful fabrication of PMMA powder required a minimum of 10 % of binder content. While using binder content higher than 40 % a distortion of the shape occurred. The increase in binder content (20 to 60 %) affected the density (600 to 750 kg·m⁻³) and porosity (57 to 42 %) of the manufactured specimen. The mechanical strength and modulus also increased with higher binder content.⁷⁶

Table 4: Overview about critical features of BJ.

Advantages	<ul style="list-style-type: none"> • Room temperature • A lot of different materials, full color printing • No need for support structure, powder reusable • Fast, simple, cheap
Disadvantages	<ul style="list-style-type: none"> • Poor mechanical properties • Complex post-printing treatment
Layer thickness	<ul style="list-style-type: none"> • 0.05 – 0.4 mm

1.1.5 Material Jetting (MJ)

Material jetting 3D printing can be compared to common inkjet printer (2D) for printing documents, books and pictures. Liquid photopolymer droplets are jetted onto the printing platform and cured with UV-light.⁴ The chemical principles are the same like with SLA, but the printing process is completely different, as SLA uses a filled resin vat, the MJ printer sprays tiny droplets.⁷⁷

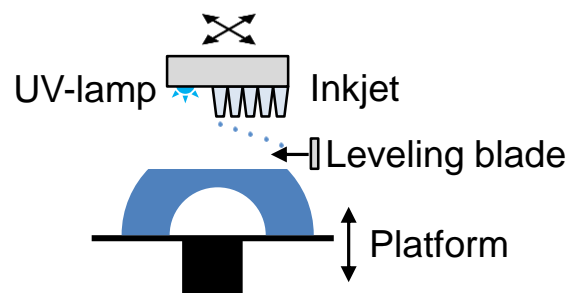


Figure 8: The MJ printing process.

The two main parts for MJ are the inkjet print heads and the UV-light source, both moving synchronic in the same axis. The printing starts with depositing resin droplets in the required locations, followed by curing with UV-light, moving the platform down and repeating everything. Common materials used are waxy polymers and acrylic or methacrylate resins.⁷⁴ The finished printed parts sometimes need post-printing treatment to further cure the resin with heat or UV-light.

Table 5: The important points about MJ.

Advantages	<ul style="list-style-type: none"> • Building speed • Accuracy and resolution • Smooth surface • Full color and multi-material
Disadvantages	<ul style="list-style-type: none"> • Very expensive • Weak mechanical properties • Limited to photo-polymerization
Layer thickness	<ul style="list-style-type: none"> • 0.016 - 0.032 mm

1.2 Multicomponent 3D-printing

1.2.1 3D-printing of Core/Shell structures

Multicomponent 3D-printing is realized by combining different techniques (e.g. FDM, drop-on-demand, material jetting) or by creating multicomponent printing inks / composites. While premixed materials in this field are used for quite some time including composites of polymer and heterogeneous fillers (carbon, ceramics, silica or fibers), the use of multi-head printing setups to create multicomponent materials has only recently started.⁷⁸ Therefore, printing heads which include mixing tools inside them are developed, two printing heads of the same additive manufacturing technique can be used or at the top end of technology several different techniques and dispensing methods are combined in one 3D-printer setup. The 3D-printing industry is placed in a position of being an effective process to replace or complement traditional manufacturing processes, particularly when its advantages (e.g. on-demand production, individual customization, high design complexity) can be fully utilized.⁷⁹ As a branch, next to the industrial areas, the technologies got attention in pharmaceutical and medical fields to manufacture customized devices, prostheses or tissue scaffolds.⁸⁰⁻⁸³

A huge advantage of the capsule manufacturing with FDM is based on the avoidance of organic solvents, which is critical for pharmaceutically or medical applications. On the other hand, the liquid fillings are limited by the high extrusion temperatures of the differently used polymers. They also reduce the micro bacterial contamination during the printing process. The printing temperatures can also impact the physical stability of printed samples due to shrinking or warping of the polymeric parts during cooling. On the other hand, thermal degradation of the liquid filling could take place. In this regard, a well chosen selection of polymer materials and compatible liquid fillings is required, taking the different processing conditions into account.⁸⁴ The parameters used during 3D-printing influence not only the physical properties of the starting polymer, but also are varied by loading pressure, feed rate, temperature, deposition rate, strand thickness, filling percentage and counts of shell layers, influencing the quality and resolution of the final product. The resolution of the finished item is most of the time the biggest issue with FDM, being improved by smaller nozzles and reduced layer height.^{22, 85-88} The big challenge of FDM is still based on the scalability (quantity) and with it the related process time, which can be slower compared to established traditional large-scale production.

1.2.1.1 Assembled structures after manufacturing

In general, these systems rely on 3D-printing to fabricate different shaped hollow shells which are assembled after the manufacturing. The capsular systems can vary from simple configurations (two fitting capsule halves) to complex internal geometries (capsules nested inside each other). Melocchi et al. are the first to do research on FDM produced capsule shells.^{87, 89, 90} The polymeric capsule shell is manufactured in several

parts being filled and connected after FDM.⁹¹ The release of filled capsule devices is controlled by the shell material and different designs (e.g. shell thickness, dissolution efficiency). Large quantities of polymeric materials were tested, giving a good overview about compositions and useable printing conditions. Capsule structures (in a disk-shape) were processed with a shell thickness of several hundred microns made of different filaments like PEO, HPC, HPMC, PVA and more.⁸⁹ In result, proving the successful manufacturing of enclosed spaces and shell structures by using FDM technology to obtain matrices, which incorporate active compounds. Charoenying et al.⁹² used a system based on two matching capsule halves based on the idea of Melocchi et al.⁸⁷. The cap and body parts were manufactured by FDM with PVA filament and were thermally cross linked afterwards. The cross linking of the PVA shell changed from dissolution behavior in aqueous mediums to different states of insolubility. With increasing curing time and temperature the printed capsules got more and more insoluble connected with a reduction in water uptake capability. The drug release studies based on non-cross linked and cross linked devices resulted in a lag phase and then slow steady release, while cross linked samples didn't show typical release profiles, only a small diffusion through the PVA shell could be observed. When small holes were formed during the release study and the diffusion rate increased.

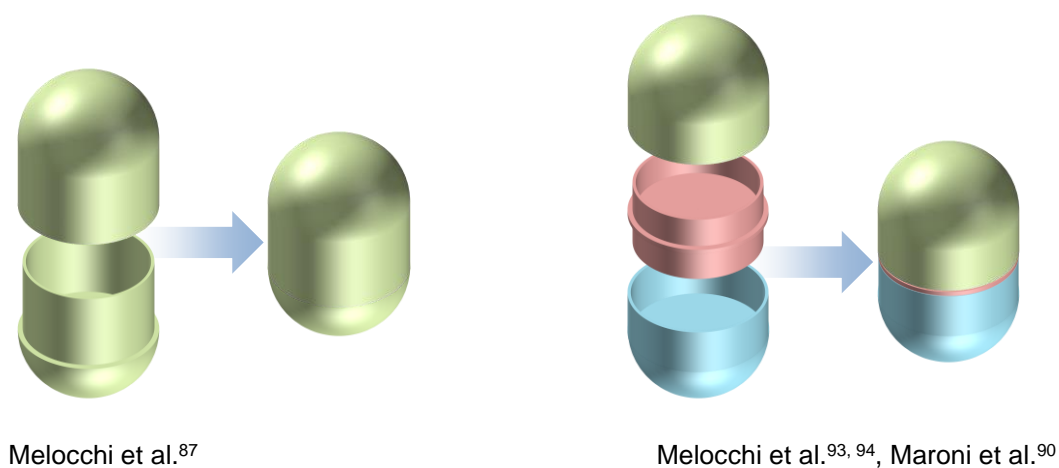


Figure 9: Hollow systems printed by FDM to manufacture capsule shells.

Improving the idea of simple, printable hollow systems to more complex systems (e.g. capsules nested inside each other) got some attention in recent years. Huanbutta and Sangnim⁹⁵ created capsule halves with PVA and ABS filaments providing different solubility properties in aqueous medium. The printed shapes were varied from spherical, cylindrical to conical designs, only the cylindrical one was worth for further optimization. Similar systems based on PLA filaments were manufactured by Shin et al and Fu et al.^{96, 97}

Next to printing empty or half-full capsule devices drug- or liquid-filled systems are more difficult to manufacture. Maroni et al. printed three modular part (two capsule halves and a joint) while differ the shell thickness as well as the material composition.⁹⁰ Shell thicknesses of 600 and 1200 μm were printed and three different joints were designed as CAD files to join same and different capsule halves. The finished parts could be combined and filled with various drugs, doses and formulations. The composition and shell thickness determined the release profile, so by combining two different shell thicknesses, a two-bursed release was realized. Capsule devices with two separated chambers, which can be filled with different components were developed by Genina et al.⁹⁸ They used commercial available PLA and PVA filaments to manufacture a cylindrical PLA container (non-soluble) with PVA caps on both ends. The system was minimized to fit $2 \times 5 \mu\text{L}$ of liquid, separated by a PLA wall. The release of the drug system was determined by the dissolution speed of the PVA caps. More capsules with a similar design were manufactured by Matijašić et al.⁹⁹ Two separate capsule voids can include incompatible reactive ingredients or realizing a dual release profile.

1.2.1.2 Structures fabricated in one printing cycle

The next evolution step of creating filled capsule structures with FDM is the combination of shell printing and filling the void in a single printing cycle. The approach can be realized by using dual- or multi-head printing systems with different dispensing systems. With a dual FDM-setup Kempin et al. printed solid-filled core-shell capsules.¹⁰⁰ Starting with an approach of printing a hollow capsule shell in one step, filling in a preprinted core and finishing the top layers with FDM. In this way the capsule enclosure was done during the printing cycle, not two printed halves were connected. The core material consisted of drug loaded PCL or PEG to have a low processing temperature (for drug stability). The printed layers on top of filled voids generally showed weak mechanic performance and maybe could be poorly connected to the layers below. The printing of liquid filled cores with polymeric shells is much more difficult. Smith et al. aimed for high quality capsules with liquid filling.^{101, 102} By modifying a simple 3D-printer setup was used to manufacture PLA/PVA based capsule filled with a water-based drug solution. In three steps the filled capsules were prepared: fabrication of an open capsule shell with 400 μm strands, liquid filling of the void and finally printing the closing top layer. The optimized process would feature similar shell thickness at every location, good connection between lower and upper FDM-printed parts and perfect enclosure of the filled liquid. The design and printing parameters were steadily modified and adjusted to finally obtain a shape of a tablet with rounded edges. The aqueous-filled PVA capsules showed swelling of the PVA layers, including detachment of several layers. The used aqueous formulations (HEC-based gels with 15 wt% of metformin hydrochloride) were located at the highest manageable viscosity for controlled and continuous filling, as well as reduced water evaporation due to the high printing temperature above 200 °C for the PVA filament.

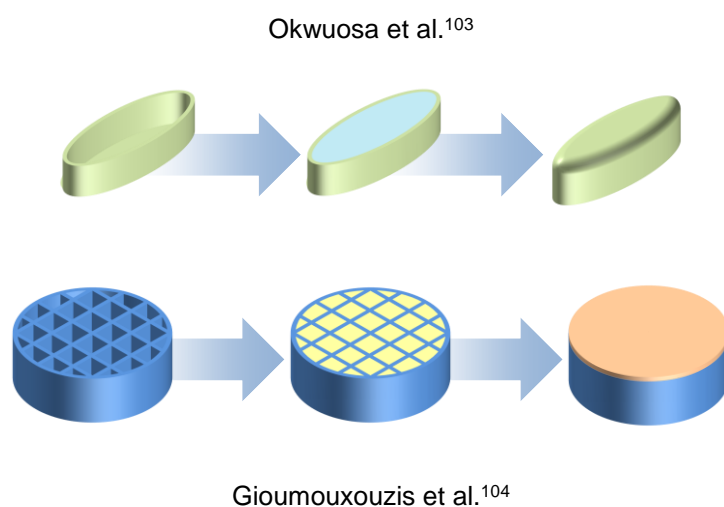


Figure 10: Filled capsule systems manufactured in one printing cycle.

Goyanes et al. researched the topic of filled tablets by FDM printing in recent years,¹⁰⁵⁻¹⁰⁸ starting with the influence of the printed geometry on drug release profiles. Drug-enriched PVA-filament (5 wt% paracetamol) was printed at 180 °C into shapes of a cube, pyramid, cylinder, sphere and torus. The dissolution profiles of the different geometries led to no dependence on the surface area, but more on the ratio of surface area to volume in regard of geometrical shape. Samples with similar masses didn't showed large differences. Furthermore, large capsule-shaped structures were printed by FDM with PVA-filament containing either one drug¹⁰⁵ or two different fillings.¹⁰⁷ Okwuosa et al. developed hollow systems by FDM being combined with an automatic liquid dispenser.¹⁰³ Both printing heads were synchronized to work simultaneously together. The main challenges in this project were the tightness between the polymer layers and the direct filling of small voids with liquid. Their minimum shell thickness of the capsules was around 1.6 mm enabling 3D-printing without leaking of liquid even for storage conditions. For the filled voids, a cubic shape was used for easier calculation of the volumes (80 – 320 μL). Different printing concepts were tested like alternating printing between FDM and inkjet-dispensing for each new deposited layer and the better option with sequentially printing of an open void system, filling with liquid and then enclosing the shell. Zhao and colleagues printed a special geometry with PVA-filaments creating a sphere (12 mm) with a tetrahedron void inside. The developed shape showed an interesting release profile with low release till 300 minutes and a burst release in the next 150 minutes. Linares and coworkers¹⁰⁹ manufactured dosage tablets with two printing techniques (FDM and injection volume filling) creating customized scaffolds which are filled at room temperature with liquid. By combining these two printing techniques in the same 3D-printer, the addition of liquids (inkjet) can be done while processing the polymer with FDM in one printing cycle. Traditionally, the production of filled tables / capsules is a multi-step manufacturing process, now could be reduced in energy, time and space with 3D-printing. The FDM head used PLA (220 °C)

with strand thickness of around 0.35 mm. As base area two layers of completely filled circle were printed. The next layers were printed as a mesh (1.2 mm distance between strands). The still empty voids were filled by use of the inkjet print head injecting 200 μL of hydro-alcoholic solution at 4 spots. The open, porous inner structure allowed for equal liquid distribution. Finally, three layers of polymer with FDM were printed on top and filled with Eudragit FS30D dispersion (working as a release delaying polymer sealing). Gioumouxouzis et al. printed a similar device.^{104, 110} A slightly different approach with hydrogel as matrix material was developed by Gupta et al.¹¹¹ creating core / shell capsules for programmable release with gradients inside the hydrogel. The capsules were based on an aqueous core and PLGA polymer shell being filled as a suspension inside the hydrogel during 3D-printing. The new 3D-printing method resulted in monodisperse core / shell capsules, good patterning arrays, possible gradient distribution and composite printing. A different approach with FDM of PCL and the incorporation of nanocapsules was published by Beck et al.¹¹² The printed specimens were soaked in drug-loaded nanocapsules (138 nm) to form printed tablets loaded with them. The addition of the nanocapsules was performed after the FDM process while soaking the printed tablets into a suspension. The use of nanocapsules, directly mixed into the polymer / filament, is not reported for FDM printing, as well as for multi head printers using a second printing head with injection function. Creating small voids during 3D-printing processes and filling them with aqueous solutions can be strongly influenced by their size. Surfaces with micro holes were printed in different sizes and their wetting properties with water were tested. Simulation and experiments showed a change in contact angle of water (65° for flat surface up to 113° for microstructures). The interaction between the surface, the microstructure and the resulted air pockets between water droplets and voids influence the use of liquids during a multi-material printing.¹¹³ Sanders et al. reported a capsule based self-healing composite fabricated by stereolithography printing. An UV-vis reactive resin was mixed with microcapsules containing a mixture of PMMA-anisole (5:95 wt%), printed with layer height of 200 μm , and tested for their solvent based self-healing properties.¹¹⁴

Creating small voids during FDM printing (micrometer range) and filling them in the same printing cycle with hydrophobic or hydrophilic liquids present a big challenge. The interaction between material surface and liquid, printing micrometer structures with FDM, printing temperature interaction with the liquid as well as simultaneous printing of both components need to be analyzed and optimized.

1.2.2 3D-printing of supramolecular polymers

Supramolecular polymers feature improved material characteristics by dynamic interactions like enhanced material strength, toughness, self-assembly and stimuli-responsiveness.¹¹⁵⁻¹¹⁹ The mechanical and thermal properties of these self-assembled materials are strongly influenced by the nature and amount of the non-covalent bonds and their interactions (hydrogen bonding, π - π stacking, metal complexation, ionic

interactions).¹²⁰ The chemistry and structural design of a supramolecular moiety influences the assembly architecture, strength of interaction and their behavior.^{26, 121-124} The change in material characteristic is chemically programmed by the different supramolecular moieties. The field of non-covalent interactions is dominated by materials based on hydrogen bonding. In the following chapter focus will be placed on hydrogen bonding polymers and their interaction with themselves or other molecules. Additive manufacturing of supramolecular materials rely on different techniques like material extrusion, vat polymerization inkjet printing and bioprinting.¹²⁵⁻¹²⁷ The individual printing techniques require different polymer properties and supramolecular interactions, while offering their own advantages and disadvantages. The polymer and supramolecular design has to be individually designed and adapted.¹²⁸ Traditional, the extrusion of thermoplastics require the melting of the polymer. Supramolecular polymers are ideal candidates for direct extrusion due to their temperature and shear force dependent supramolecular interactions.

1.2.2.1 Hydrogen-bonding polymers

In nature, hydrogen bonds play a very important role contributing to the formation of different peptide structures (α -helix, β -sheet), ligand-receptor binding or enzymatic catalysis.^{129, 130} The peptide hydrogen bondings are based on the interaction between amides, urethanes or ureas due to the presence of a proton donor (NH, general: XH or D) and a proton acceptor (C=O, general Y or A).^{116, 131} The resulting strength of hydrogen bonding complexes is not determined by one single interaction, but more by the number of hydrogen bonds and their architecture. In a study, the association strength K_s of different tripe hydrogen bonds including different donor and acceptor side arrangements (Figure 11a). The simplest case (AAA \leftrightarrow DDD) showed highest association constant getting weaker while exchanging one position (AAD \leftrightarrow DDA) and in the last case (DAD \leftrightarrow ADA) the lowest association constant.¹³²⁻¹³⁴ The effect is explained by secondary electrostatic interactions between the moieties. The interactions of diagonally linked sides show strong attraction if they are of different kind (A \leftrightarrow D) and if they are of the same kind they repel each other (A \leftrightarrow A, D \leftrightarrow D). The secondary attraction and repel interactions deliver a tool for tuning supramolecular materials with only slight change in chemical structure. The change in number of hydrogen bonds in the moiety also allows for influence the association strength ranging from two hydrogen bonds per site (adenine / thymine) up to six hydrogen bonds (barbituric acid / Hamilton wedge, Figure 11).^{116, 132, 135-138} The next level of interaction is archived by the architecture of the hydrogen bonding moieties by developing self-complementary and complementary groups. In self-complementary systems the interaction occurs between one species interacting with itself. Complementary systems are based on two different groups interacting *via* hydrogen bonds offering more tunability.^{116, 123, 136, 139, 140}

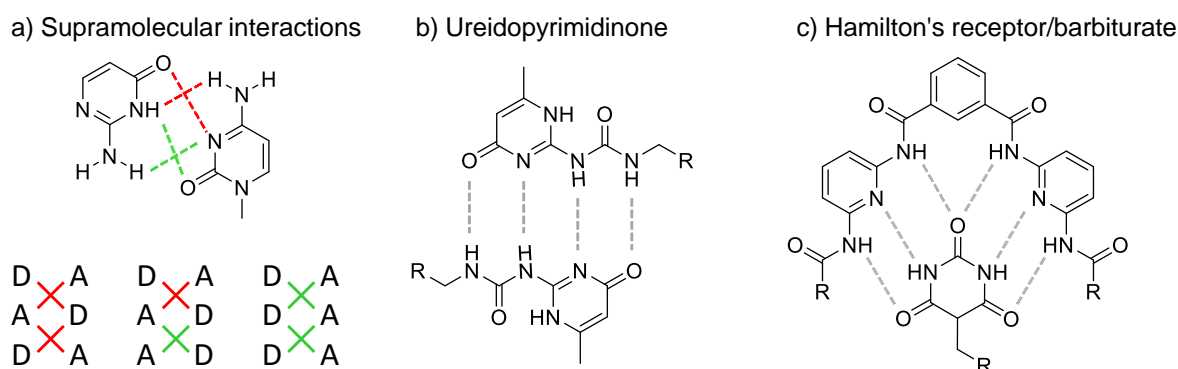


Figure 11: When tripe hydrogen bonds including different donor and acceptor side arrangements, there are different association strength (a), the ureidopyrimidinone group with an AADD bonding scheme (b), a very strong hydrogen-based interaction between Hamilton's receptor and barbiturate group (c).

The strong influences of hydrogen bonding groups can be easily observed in polyisobutylene (PIB) based systems with thymine (T), barbiturate (B) or ureidopyrimidinone (U) telechelic endgroups.^{26, 117, 118, 137, 138, 141-143} The barbiturate hydrogen-bonded PIBs, known to form nano-sized micellar clusters, arranged into a dense supramolecular network of interconnected aggregates mediating increased mechanical strength.¹⁴⁴ This network formation is driven by segregation of the attached hydrogen-bonding moieties from the non-polar PIB-chains, in turn connecting the polymer chains into a transient network. The achieved thermo-mechanical behavior can be tuned¹⁴⁴ with the terminal relaxation dominated by the opening and closing of the hydrogen bonds. In contrast to a covalent network, the dynamic character of the attached supramolecular bonds enables macroscopic flow of the polymer on a longer timescale, allowing solvent-free 3D-printing.^{26, 145} Furthermore, the reassembly of the network structure, driven by dynamic exchanges within the nano-sized micellar clusters, additionally features multiple self-healing properties at room temperature and below.^{26, 117, 144, 146, 147} Telechelic supramolecular polymers are easy to synthesize supramolecular materials to change their properties based on the assembly of the endgroups (Figure 12). The molecular weights M_w are mostly in the lower range of 1000 to 10000 Da.^{28, 117, 146, 148} The relative low molecular weights result in a still good concentration of supramolecular endgroups compared to the polymer backbone as well as better viscosity properties and no chain entanglements.¹⁴⁹⁻¹⁵¹ Controlled polymerization techniques are required to obtain telechelic functionalized polymer backbones being further modified to supramolecular groups. In general, ring-opening, step-growth polymerizations, controlled radical polymerizations (ATRP)¹⁵², reversible-addition-fragmentation chain-transfer polymerization (RAFT)¹⁵³, ring-opening metathesis polymerization (ROMP)¹⁵⁴ and living polymerization techniques (LCCP)¹⁵⁵ are used. After polymer synthesis, the supramolecular endgroups are attached by different coupling reactions like isocyanate-alcohol, esterification and "click"-reactions.^{28, 141, 146, 156} While using rather non-polar polymer backbones, the phase separation between the polar endgroups and the polymer is enhanced as well as the assembly of the supramolecular groups is supported. The telechelic supramolecular polymers are in

general based on low glass transition temperature T_g polymers featuring good mobility and dynamics for the assembled nanostructures to enable the exchange of groups inside the material. Other polymers with high T_g or crystalline parts mostly don't show such drastic changes except the general increase in stiffness.^{157, 158}

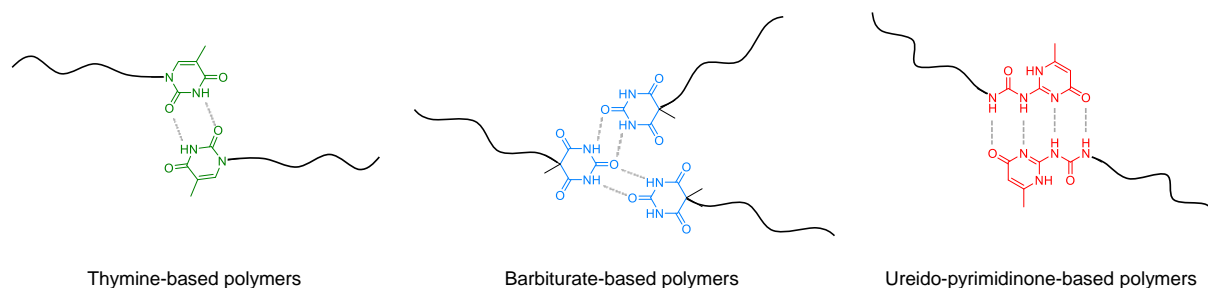


Figure 12: Telechelic polymers based on different hydrogen-bonding moieties, ordered by their overall bonding strength related to the amount of hydrogen bonds per molecule.

Additive manufacturing and processing of supramolecular polymers have the advantage to support the fabricated structures and shapes. In the field of tissue scaffold engineering supramolecular polymers offer the possibility of self-healing materials recovering from applied stress.¹²⁹ The supramolecular materials are processed by electro spinning to build up fiber constructs. The fibers are spun in a diameter range of nanometers to micrometers and can be fabricated into fiber mats. The electro spinning of supramolecular polymers highly depends on their interaction strength. The electro spinning properties are strongly influenced by the strength of supramolecular interactions vary the viscosity to obtain droplets or fibers.¹⁵⁹ This approach has been utilized with telechelic PCL-U2 polymer. The PCL-U2 material could be processed with different techniques like solvent casting of films, compression molding, melt spinning, electro spinning for meshes and of course FDM for tissue scaffolds. The grids were printed with strand thickness down to around 220 μm of diameter. Due to the dynamic properties of supramolecular polymers manufacturing was possible below 80 $^{\circ}\text{C}$.^{160, 161} A similar approach was performed with inkjet based 3D-printing. A supramolecular polymer system, which can be ejected through the small needle (shear force), forms a self-supporting structure after deposition.¹⁶² Already small amounts of supramolecular polymers or end group concentration change the Young's modulus and tensile strength for PMMA-polymers using FDM printing. Different ratio of PMMA to PMMA-*co*-UPyMA influenced the rheological and resulting printing properties and parameters.¹⁶³ Long et al.¹⁴⁰ FDM printed polyureas with UPy groups inside the polymer backbone. The supramolecular interaction increased mechanics due to hydrogen bonding based cross linking and phase separation of the functional groups, leading to improved adhesion between printed layers of different angles (0° and 90°).¹⁴⁰ Polymers with supramolecular interactions drastically improve their mechanical properties compared to non-modified analogs.¹⁶⁴ Invernizzi et al.¹⁶⁵ developed a self-healing and shape memory material based on PCL and UPy being co-cross linked, while both contain methacrylate units. A solution of both monomers and a photo initiator were used in a

DLP printer.^{165, 166} Other supramolecular interactions based in ionic interactions or metal complexation were also used in FDM printing and further printing technologies. Wilts et al.¹⁶⁷ reported on stereolithography of ionic monomers based on acrylates, acrylamides and vinyls to manufacture water soluble parts. The new polymer offers the possibility for a high resolution support material.

1.2.2.2 Rheology of supramolecular polymers

The melt rheology of supramolecular polymers is far more complex than the rheology of the neat polymer materials. The modified polymers undergo multiple relaxation processes during different shear rates and temperature ranges. Supramolecular polymers with a plateau in the storage modulus G' at low frequencies are interpreted as a rubbery plateau, where multiple associations of the supramolecular moieties take place forming a dynamic network being based on hydrogen-bonds. For example UPy groups have shown aggregates, beyond two groups, in telechelic poly(ethylenebutylene)¹⁶⁸ and the material formed long fibers. It was proposed to stacking of the UPy groups, which is supported by hydrogen bonding of urethane / urea groups next to the UPy moieties.^{141, 158}

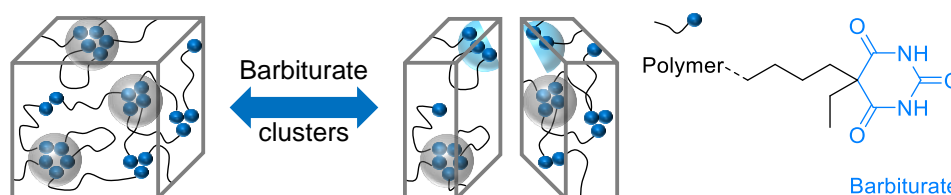


Figure 13: Cluster formation of the barbiturate aggregates in bivalent telechelic PIB-barbiturate forming a dynamic network.

Polymers containing telechelic barbiturate groups form hydrogen bonds in multiple directions base on the angled direction of the bonds. This results in a thermo-reversible, hydrogen-bonded polymers, known to form nano-sized micellar clusters, arranged into a dense supramolecular network of interconnected aggregates (Figure 13).¹³⁸ In contrast to a covalent network, the dynamic character of the attached supramolecular bonds enables macroscopic flow of the polymer on a longer timescale depending on temperature. In rheology the dynamic character was observed with frequency studies. Bivalent telechelic PIB-barbiturate shows very different behavior at high frequencies, rubber like, than compared to low frequencies, flow behavior is observed. The difference in time scale and related to that the lifetime of the aggregates. At high frequencies, the lifetime of an aggregate is much longer than the applied frequency and for low frequencies the change between the aggregates can be monitored.¹¹⁷ Due to the low molecular weight of individual PIB-chains (below the M_c for PIB) the plateau in the modulus is explained by a dynamic network. As a result, by combining rheology with

published SAXS data the aggregates at the chain ends have to be connected by bridging PIB-chains.¹⁴⁴

For 3D-printing with FDM, the influence of temperature on the system is also of interest. As expected is the temperature dependence of the relaxation time of neat PIB considerably weaker than that of the telechelic PIB-barbiturate. The temperature dependence of the terminal relaxation time is controlled by the functional groups, not by chain dynamics.¹⁴⁴

1.2.3 3D-printing of mechanophore polymers

Mechano-responsive polymers constitute an important class of materials, able to sense and visualize stress *via* easily recordable responses.¹⁶⁹ Conventionally appropriate reporter molecules or components are embedded into polymers where stress-response should be detected.¹⁷⁰ Various chemical stress-quantification-tools have been demonstrated by so called mechanophores including stress-induced chemiluminescence¹⁷¹⁻¹⁷³, the release of small molecules¹⁷⁴⁻¹⁷⁷ and direct mechanochromic indicators¹⁷⁸⁻¹⁸⁶. Alternatively, the induction of catalytic reactions based on the decoupling metal-ligand complexes by mechanical stimuli is used.¹⁸⁷⁻¹⁹³ The most commonly used mechanochromic polymers are based on spiropyranes^{184, 186}, able to generate a merocyanine chromophores upon mechanical activation depending on their substitution pattern. Especially, the NO₂-functionalized dyes manifest in an intense purple color (Figure 14). Finally, allowing to quantify the exerted stress within the material.^{178, 194-198} Therefore, in view of the multicomponent nature of such polymeric materials the use of 3D-printing methodologies is attractive, allowing to place components for the direct stress-detection as well as additional reporter molecules required for the quantification of stress into the same material.^{199, 200} Peterson et al.²⁰⁰ combined FDM with mechanochromic PCL to print complex structures with specific spots of the stress-responsive material using a dual FDM print head. In these studies the mechano-chemical isomerization of a NO₂-spiropyran to the merocyanine structure was used as well.^{199, 200}

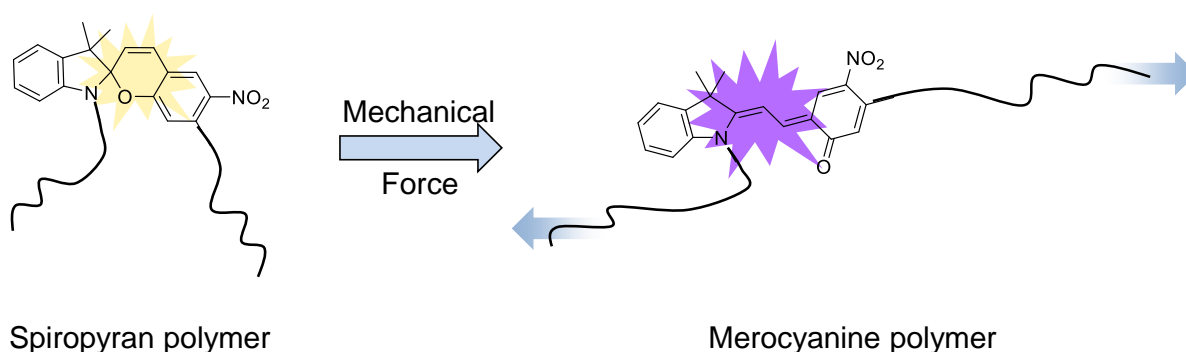


Figure 14: Mechanochromic reaction of a spiropyran polymer due to mechanical force, resulting in stretching of the polymer chain and cleavage of the C-O bond. The new formed merocyanine polymer shows a deep violet color.

An efficient methodology for stress-detection uses mechanophores directly activated by metal/ligand cleavage, coupled to a subsequent catalytic reaction of the then freed metal-coordination-site.^{191, 193, 201, 202} The catalysts used to this endeavor in our group are based on copper(I) bis(N-heterocyclic carbene) mechano-catalysts, connected to a fluorogenic CuAAC-click-reaction of 3-azido-7-hydroxycoumarin with phenylacetylene. Both components are non-fluorescent before mechano-chemical activation, but react to a highly fluorescent dye to visualize applied stress induced onto the polymer backbone *via* sonication force, grinding or tensile / compression forces.²⁰³⁻²⁰⁵ As in FDM printing, stress-responsive materials have been manufactured in resin based vat polymerization. Boydston et al.¹⁷⁵ developed a flex-activated mechanophore system printed by digital light polymerization. The included oxanorbornadiene functions undergo reverse Diels-Alder reaction during mechanical stress releasing the small molecule (benzyl furfuryl ether). The released amount correlated to the amount of applied stress.^{175, 176, 206}

Using mechano-active materials in FDM printing and activating them after the manufacturing process is a quite new research field. The activation and stability of the mechanophores during the printing conditions in FDM presents an interesting challenge. The shear force interactions between extrusion and mechanophore activation need to be studied.

1.3 Traditional nano-encapsulation techniques

For the encapsulation of hydrophobic liquids with biodegradable polymers different methods have been developed to synthesize micro- and nano-sized core-shell capsules. Different techniques like solvent evaporation²⁰⁷⁻²¹⁰, interfacial polymerization²¹¹⁻²¹³ or *in-situ* polymerization were used in the past.²¹⁴⁻²¹⁶ The encapsulation of drugs into nano-sized carriers (1 – 1000 nm) for drug delivery offer major advantages over micro-sized capsules. Nanoparticles have a higher intracellular uptake compared to microparticles. Furthermore, the therapeutic goal can only be achieved by nano-sized carriers and not with micro-sized drug delivery systems.^{217, 218} Some applications rely on poor water solubility of the injected nanocapsules and active drug targeting. The capsule shell prevents the direct contact of the active components with the environment, being protected from degradation reactions and external influences. An economic factor for capsule based drug systems clearly is the long time stability and the good storage possibilities. The composition of the nanocapsules play an important role for encapsulation efficiency, drug release and *in-vivo* interactions. The polymer properties (hydrophobicity, bio degradation, solubility and surface charge) have to be adjusted for individual drug loads.^{217, 219} The improved drug delivery of nanocapsules provides numerous challenges and opportunities for research and future development.

1.3.1 Emulsification solvent evaporation method

The preparations of nanocapsules start with an organic solution containing its components and being the internal phase during the emulsification in water. The emulsion / solvent evaporation method includes two critical steps: the emulsification of a polymer-drug solution into water and the solvent evaporation to precipitate the polymer. An organic solution of a polymer and the active component is dispersed into micro- and nano-droplets by stirring and respectively by sonication, homogenizer or colloid mills.^{207, 220}

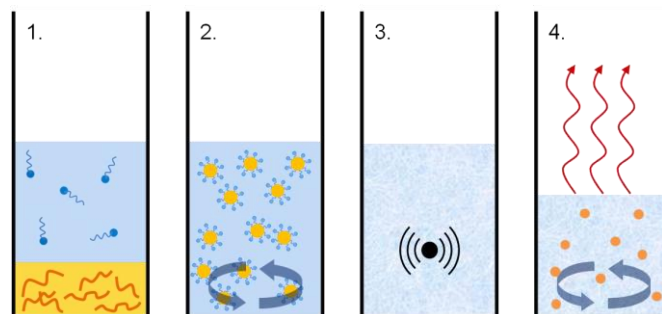


Figure 15: Two-phase mixture of organic solvent and water (1.), forming an oil-in-water emulsion (2.), ultrasonication of the emulsion (3.) and solvent evaporation to form nanocapsules (4.).

The homogenization step is the critical part for the synthesis of nano-sized particles. During evaporation of the solvent while stirring, increase of temperature or reduced pressure, the polymer precipitate in nano-sized spheres. The diffusion of the organic solvent into the aqueous phase is very slow and when the critical solubility point for the polymer is reached, phase separation take place at the interface.²⁰⁷ Most of the time chlorinated solvents like chloroform or dichloromethane are used due to their water immiscibility, good solvation and low boiling points. By changing the process parameters during emulsification and evaporation (concentration, ratio, stirring rate, viscosities, surfactants) the average size and size distribution can vary. The method is generally applied to hydrophobic drugs, since water soluble drugs are poorly included inside the polymer due to diffusion into the aqueous phase during preparation. Typically used polymers are PLLA, PLGA, PCL, ethylcellulose and PVF.²⁰⁷⁻²¹⁰

Table 6: Encapsulation of drugs with emulsion / solvent evaporation technique.

Polymer	Drug load	Solvent	Emulsifier	Size (nm)	Reference
PLA	Testosterone	-	SDS	~ 450	208
PLA	Roxithromycin	CHCl ₃	PVA	~ 200 / 300	209
PCL	-	DCM	PVA	~ 300	209
PLA / PCL	-	CHCl ₃ / EA	SDS, Poloxamer	~ 300	210
PLA	-	DCM	Albumin	~ 100-400	221
PLGA	Cyclosporin A	DCM	PVA	~ 300	222
PLGA	IBP 5823	DCM	Albumin	-	223
PLLA	Hexadecane	CHCl ₃	SDS	~ 300	207
	Cyclohexane			~ 250	
PVF	Hexadecane	CHCl ₃	SDS	~ 250	207
	Lauryl methacrylate			~ 260	
PLGA	Haloperidol	DCM	PVA	~ 800	224
PEO- <i>co</i> -PLGA	Paclitaxel	DCM	PVA	~ 150	225
PLGA	Tetanus toxoid	EA	-	~ 200	226

1.3.2 Emulsion polymerization

The formation of polymers directly in the emulsion state offers a controlled and fast encapsulation method. A large pool of different polymerization techniques are used like radical, anionic, cationic, enzymatic polymerization, but also polyaddition and polycondensation.^{227, 228} In the emulsion dispersed and stabilized droplets are formed in the continuous phase. The droplets are homogenized with high pressure or

ultrasonication (droplet size 50 – 500 nm).²²⁹ The capsule shell is formed during the polymerization process due to phase separation of the polymer between the oil-water interface. The resulting size is determined by the surfactant concentration and costabilizer counteracting the Laplace pressure.

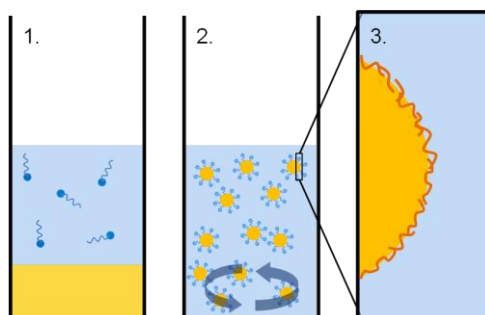


Figure 16: Two-phase mixture of monomer solution and water (1.), forming an oil-in-water emulsion (2.), polymerization at the oil-water interface (3.).

First experiments were based on PMMA capsules by radical polymerization. Till the year 1986 only pure monomer MMA was used for the encapsulation, when the cross linking polymerization with comonomers (ethylene glycol dimethacrylate) was introduced.²³⁰ In general, the encapsulation of hydrophobic liquids with PMMA were done by Alkan et al. with *n*-octacosane, heptadecane, docosane and *n*-hexadecane.²³¹⁻²³⁴ The preparation of PMMA capsules is very easy and was used successfully to encapsulate drugs.

Table 7: Encapsulations by emulsion polymerization.

Polymer	Drug load	Solvent	Emulsifier	Size (nm)	Reference
PMMA	Influenza antigen	H ₂ O		~ 130	214
PMMA	Doxorubicin	H ₂ O		~ 300	215
PMCA	Vinblastine	H ₂ O		~ 200 / 300	216
PECA	Insulin	H ₂ O		~500	235
PBCA	Progesterone	H ₂ O		~ 250	236
PBCA	Ampicillin	H ₂ O		~ 50	237
PHCA	Vincamine	H ₂ O		~ 200	238

Poly(methyl cyanoacrylate) = PMCA, Poly(ethyl cyanoacrylate) = PECA, Poly(butyl cyanoacrylate) = PBCA, Poly(hexyl cyanoacrylate) = PHCA.

1.3.3 Interfacial polymerization

Liquid core / shell capsules were synthesized by interracial polymerization of small droplets containing the monomer and the drug. In general, alkylcyanoacrylates are used as monomers, due to their ability to polymerize in contact with water. The direct polymerization on the surface of the droplets led to high encapsulation efficiencies and good drug release restraint.^{211, 239-241} Other polymer systems like polypyrrole, polyaniline, polyureas were developed as well.^{242, 243}

Table 8: Encapsulation of drug *via* interfacial polymerization.

Polymer	Drug load	Solvent	Emulsifier	Size (nm)	Reference
PECA	Insulin	CHCl ₃	Polysorbate 80	~ 150	211
PBCA	Indomethacin	EtOH	Pluronic F 68	~ 220	212
	Darodipine	EtOH	Pluronic F 68	~ 150	213
	Insulin	EtOH	Poloxamer 188	~ 200	244
	Octreotide	EtOH	Poloxamer 188	~ 260	245

1.3.4 Solvent displacement and interfacial deposition

Both methods are similar and rely on solvent replacement. Solvent displacement is based on the precipitation of preformed polymers by diffusion of the organic solvent (acetone, ethanol) into the aqueous phase creating nanospheres, nanocapsules, liposomes and nanoemulsions.²⁴⁶⁻²⁴⁸ By manual dropping or injection the polymeric solution into the aqueous phase the polymer is deposited on the interface of oil-water. Mono-dispersed nanoparticles can be prepared by controlled conditions, as well as high encapsulation efficiency for hydrophobic oils into nanocapsules.²⁴⁹ This encapsulation system is limited to some drug / polymer / solvent systems based on the solubility of drug and efficient entrapment.^{230, 249} Mixtures of DCM / acetone can be used to improve the system and drug encapsulation, unfortunately the particle size increased.²⁵⁰ The formation of the nanoparticles show similarities to the “diffusion and standing” process of spontaneous emulsification.²⁵¹

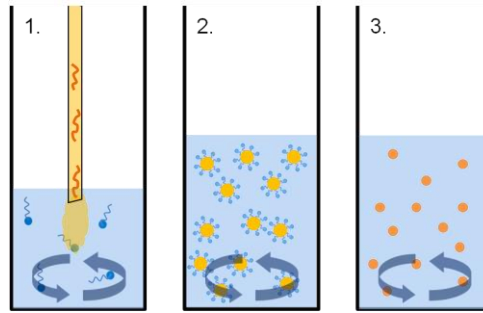


Figure 17: The organic solvent is dropped controlled into water (1.), forming small droplets (2.), nanocapsule formation due to solvent displacement (3.).

Interfacial deposition is a further developed method that creates nanocapsules by polymer precipitation around the liquid oily core. The oil component is miscible with the polar organic solvent, but immiscible with the water phase. The polymer is forming a shell-like wall around the drug-oil mixture.^{246, 252}

Table 9: Solvent displacement and interfacial deposition encapsulation.

Polymer	Drug load	Solvent	Emulsifier	Size (nm)	Reference
PLGA	Vancomycin	Acetone	Pluronic F-68	~ 190	253
	Phenobarbital			~ 160	
	Indomethacin			~ 170	
	Cyclosporin			~ 170	
	Ketoprofen			~ 170	
PLGA	Doxorubicin	Acetone	Pluronic F-68	~ 270	254
PLA	Doxorubicin	Acetone	Pluronic F-68	~ 270	254
PLA	Taxol	Acetone	Pluronic F-68	~ 260	246
	Dexamethasone			~ 300	
	Vitamin K			~ 270	
PLA	Indomethacin	Acetone	Poloxamer	~ 230	246, 252

1.3.5 Emulsification/solvent diffusion

In a partly water soluble solvent, the encapsulating polymer is dissolved and the aqueous phase is saturated with the solvent to ensure thermodynamic equilibrium between both phases. The organic phase is emulsified by stirring, homogenization or ultrasonication in the water phase containing stabilizers. By diluting with an excess of water, the diffusion of the organic solvent into the aqueous phase is promoted. In the end, the organic solvent is removed by evaporation under reduced pressure or filtration.^{249, 255}

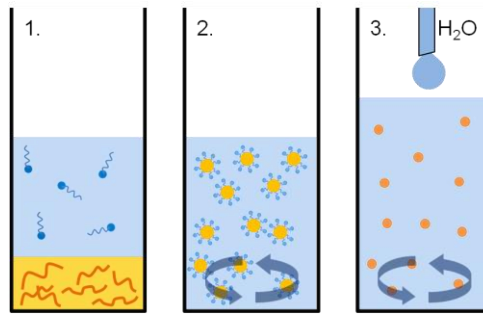


Figure 18: Two-phase mixture of partly water-soluble solvent and water (1.), forming an oil-in-water emulsion (2.), diluting the emulsion with water to diffuse the solvent (3.).

Commonly used polymers are biodegradable polyesters, e.g. PCL, PLA and PLGA. The core of the nanocapsules contains the oil and active substances. The most often used solvent is ethyl acetate. Other solvents like propylene carbonate, benzyl alcohol and DCM can also be used.²¹⁷ Regarding the external phase, the used solvent is an aqueous PVA-solution. Other stabilizing agents such as poloxamer and ionic emulsifiers have been chosen.

Table 10: Emulsification/solvent diffusion.

Polymer	Drug load	Solvent	Emulsifier	Size	Reference
PLGA	p-THPP	Benzyl alcohol	PVA	~ 120	256
PLA	DNA	CHCl ₃ ^{a)}	PVA	~ 130	257
PLGA	Rifampicin	DCM / acetone	TPGS	~ 250	258

a) The emulsion was diluted with EtOH

2.0 Aims

Biocompatible particles *via* encapsulation methods: Emulsion-/evaporation method and 3D-printing.

3D-printing of new materials and composites represent a challenge in term of functionality, printing parameters, stability, thermal behavior and simultaneous printing of several manufacturing techniques. This project will adapt encapsulation methods for a 3D-printing process, new encapsulation additive manufacturing with a dual printing head system and finally compare both methods (traditional encapsulation and 3D-printed encapsulation).

Aim is to develop methods to fabricate capsules of biocompatible materials based on emulsion-/solvent evaporation method. For the capsule shell material different, well known biodegradable polyesters will be tested. The hydrophobic core filling should be based on different model components of the terpenes. The encapsulation mechanism is based on the evaporation of a water-immiscible organic solvent. During the concentration increase and occurring phase separation, the polymer will precipitate at the water-oil interface (shell) and include the liquid oil inside (core). The synthesized capsules will be analyzed regarding size, distribution, ratio and composition.

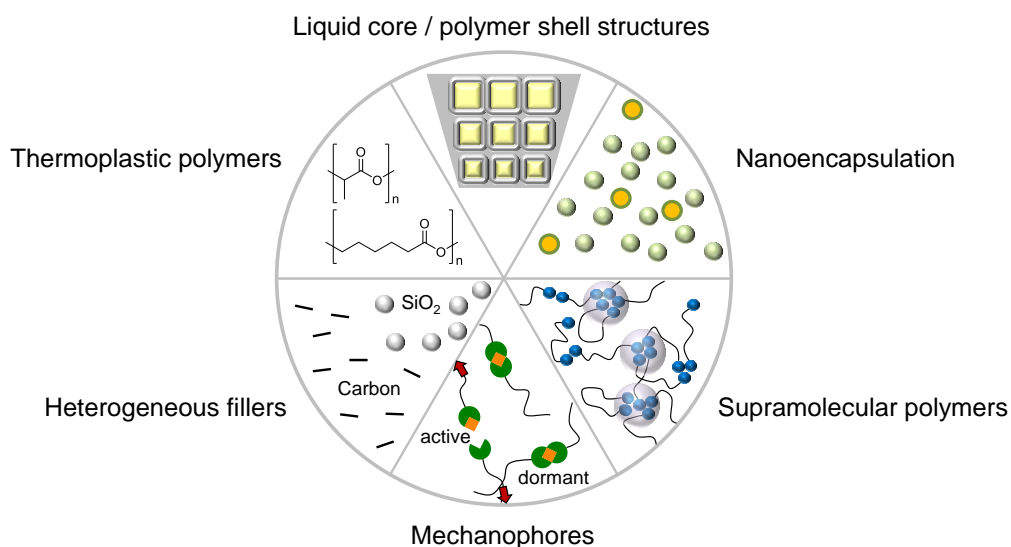


Figure 19: Multi-material 3D-printing based on different printing technologies (FDM and inkjet dispensing) resulting in different composites and functional materials. By printing different polyesters combined with liquid fillings or nanocapsules core-shell structures were implemented during the manufacturing process. Supramolecular polymers, mechanophores and heterogeneous fillers were synthesized and tested for FDM.

A second part of the project develops a 3D-print method for encapsulation of liquids and combining it with traditional encapsulation methods (recommended as a composite material). The goal for the 3D-printing method is to develop a gentle and

environmentally friendly encapsulation process. The critical manufacturing process should be the simultaneous build up of capsule shell and liquid core filling in a layer by layer approach for micrometer sized capsules (100 – 800 μm). After several printing cycles and the finished printing process, a macro-scaled specimen should be manufactured including several capsule-like structures.

3D-printing of functionalized, low glass transition temperature, amorphous polymers with supramolecular moieties is realized. Hydrogen-bonding polymers, known to form nano-sized micellar clusters arrange itself into a dense supramolecular network. The printability is based on reversible thermal- and shear-induced dissociation of the network.

With successful development, the new technologies can be used in medicine, artificial fertilizers, functional composites, self-healing materials or stress-sensing applications. The choice of polymer will influence the printing parameters and the release properties of the resulting core-shell composite. New high-end and post-printing functional materials like mechanophores, where a reaction of the liquid filling occurs, can be manufactured in different shapes, thicknesses and sizes.

2.1 Concept

3D-printing of multi-component materials as a new method over traditional methods is reported, by developing small core-shell capsule composites fabricated by an one-step 3D-printing process resulting in drug-filled and reactive composites. Using a two print head system (FDM extruder and a liquid inkjet print head), micro-sized capsules are manufactured (100 – 800 μm). Thermoplastic polymer poly(ϵ -caprolactone) (PCL) is chosen as matrix / shell material due to its optimal interaction with embedded hydrophobic liquids. Firstly, the core-shell capsules are printed with model liquids and pure PCL to optimize the printing parameters and to ensure fully enclosed capsules inside the polymer. As a proof of concept “click”-reaction systems, used in self-healing and stress-detection applications, are manufactured. PCL composites with nano- and micro-fillers are combined with reactive liquids. The 3D-printed core-shell capsule composite can be used for post-printing reactions and damage sensing when combined with a fluorogenic dye. (for more details: see Figure 28)

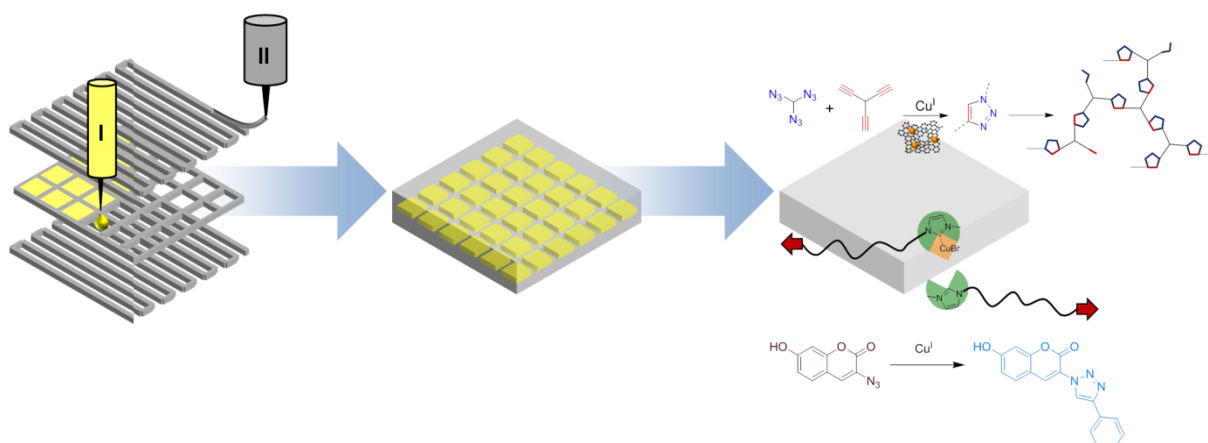


Figure 20: Manufacturing of core-shell composites *via* FDM and inkjet printing generating drug-filled specimen and post-printing reactive materials based on the “CuAAC-Click” reaction. The reactions are triggered by applied force and led to resin curing reaction and stress sensing applications.

The preparation and characterization of mechano-responsive, 3D-printed composites is researched using the same dual-printing setup. The stress-sensing materials are based on high- and low molecular weight mechanophores, including poly(ϵ -caprolactone)- and alkyl-based latent copper(I)bis(N-heterocyclic carbenes), which can be activated by compression to trigger a fluorogenic, Cu(I)-catalyzed azide/alkyne “click”-reaction inside a bulk polymeric material. Focus is placed on the printability and post-printing activity of the latent mechanophores and the fluorogenic “click”-components. (for more details: see Figure 37)

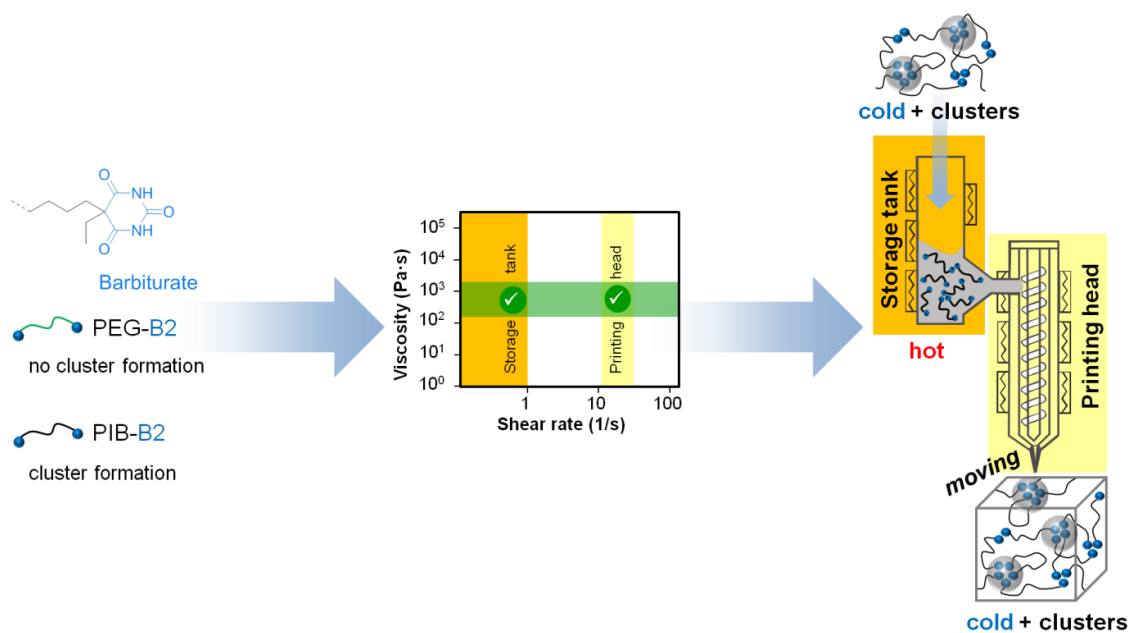


Figure 21: 3D printing of supramolecular polymers based on linear PEG, linear PIB and three-arm star PIB with barbiturate (B) end groups. The desired rheological properties for thermal-extrusion based 3D printing, like viscosity and shear rate, and the resulting printing windows are shown in the diagram.

A second concept is based on hydrogen-bonded supramolecular polymers, known to form nano-sized micellar clusters, arranged into a dense supramolecular network mediating increased mechanical strength. The printability is based on reversible thermal- and shear-induced dissociation of the supramolecular polymer network, which generates stable and self-supported structures after printing, checked with rheology and X-ray scattering. Thus, linear and three-arm star poly(isobutylene)s PIB-B2, PIB-B3, and linear poly(ethylene glycol)s PEG-B2 were prepared and probed by melt-rheology to adjust the viscosity for the proper printing window. The supramolecular PIB polymers showed a rubber like behavior and were able to form self-supported 3D-printed objects at room temperature and below. To further strengthen the PIB-B2, nanocomposites with silica nanoparticles (12 nm, 5-15 wt%) were analyzed and led to an improvement of shape stability. With a blend of linear polymer PIB-B2 and three-arm star polymer PIB-B3 (ratio $\sim 3/1$ mol) even higher structural stability is reached, able to build free-standing structures. (for more details: see Figure 46)

3.0 Results and discussion

3.1 3D-printer evaluation

For 3D-printing the complex geometrical shape was programmed with the help of the CAD-program *BioCAD*TM. Each polymer strand was drawn with the CAD-program (Figure 22). With the possibility to preview the designed shapes and structures errors and programming mistakes could be detected and fixed (Figure 22). The CAD-file was saved, transformed to an ISO-file and sent to the 3D-printer. In the human machine interface (HMI) software most of the printing parameters were controlled like printing head selection, nozzle length measurement, temperatures, screw speeds and pressures inside the printing heads. Depending on the complexity of the design structures one or two printing heads were used simultaneously (Figure 23).

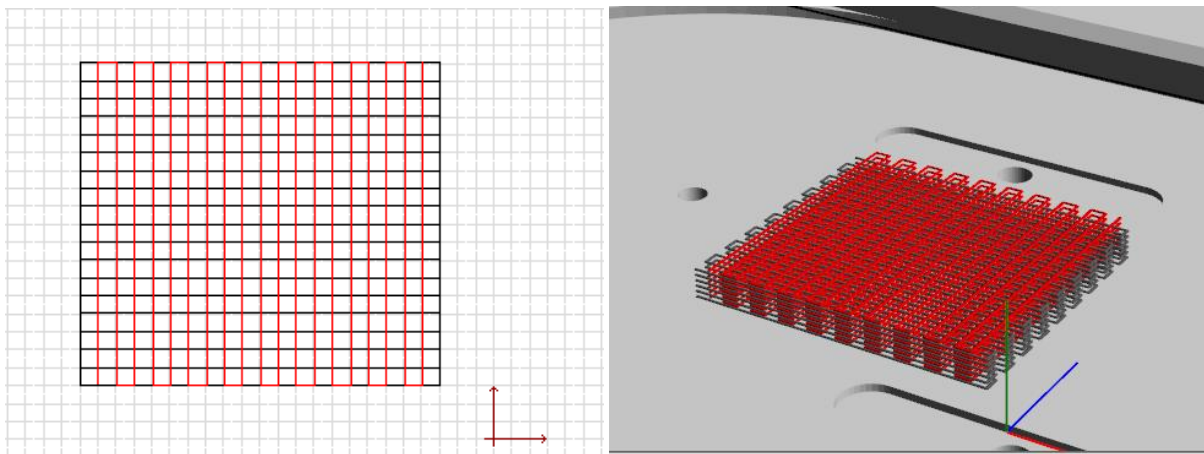


Figure 22. With the help of CAD-program *BioCAD*TM different shapes and grids were designed and programmed for different materials (l.). After a successful creation, a preview could be generated (r.).

3.1.1 Polymer extruder

The printer regenHU 3DDiscovery, equipped with a heatable polymer extrusion printing head with a metal nozzle, was used for printing of different polymers. The printing window for the used 3D-printer is set by the nozzle geometry, printing speed and temperature settings. A polymer extrusion printing head of a regenHU 3D-Discovery printer was equipped with a 0.20 or 0.33 mm inner diameter nozzle, impeding a viscosity range of 200 to 2000 Pa·s, which was researched using several polymers (see Table 11). The printing window was estimated by temperature-dependent rheology investigations. The viscosity of the printable polymers had to suffice both parts of the polymer extrusion head consisting of the heatable storage tank and a heatable screw extruder for a fixed $\Delta\theta = 10\text{ }^{\circ}\text{C}$ between both of them. Due to the construction of the 3D-printer the shear rates of the storage tank ($< 0.1\text{ s}^{-1}$) and the printing head (0.20 or 0.33 mm inner diameter nozzle, shear rate 14 - 26 s^{-1}) are different, thus determining an area of printability.



Figure 23. The human machine interface (HMI) for the *regenHU 3D-Discovery*, where most of the printing parameters could be changed (l.). The installed printing head of the 3D-printer are liquid inkjet head (drop-on-demand) and a polymer extruder with storage tank and screw extrusion unit (r.).

3.1.1.1 Melt rheology

Most of the polymer samples for rheology were used as delivered and PVA, PEG, PTHF were dried in vacuum at 60 - 80 °C for one day. The rheology experiments were executed on an Anton Paar MCR-101 DSO rheometer using parallel plate-plate geometry with a diameter of 8 mm. The temperature was controlled with a thermoelectric cooler/heater in a chamber filled with dry air (10 – 180 °C). For each measured temperature the sample were preheated for 30 minutes reaching their equilibrium state. For 3D-printing the mandatory measurement of viscosity versus shear rate was performed. With combination of rheology data and 3D-printing / extrusion results a printing window could be determined (200 to 2000 Pa·s). For the planned applications in capsule-3D-printing and supramolecular-based polymer 3D-printing, at first poly(ϵ -caprolactone) (PCL, $M_n = 14$ kDa, 45 kDa, 80 kDa) as well as polyethylene glycol (PEG, $M_w = 1500, 8000$ Da) and poly(tetrahydrofuran) (PTHF, $M_w = 3000$ Da) were tested. A combined analysis between measured rheology data and extrusion respectively 3D-printing results led to the resulting printing windows shown in the rheology graphs (Figure 24, Figure 25).

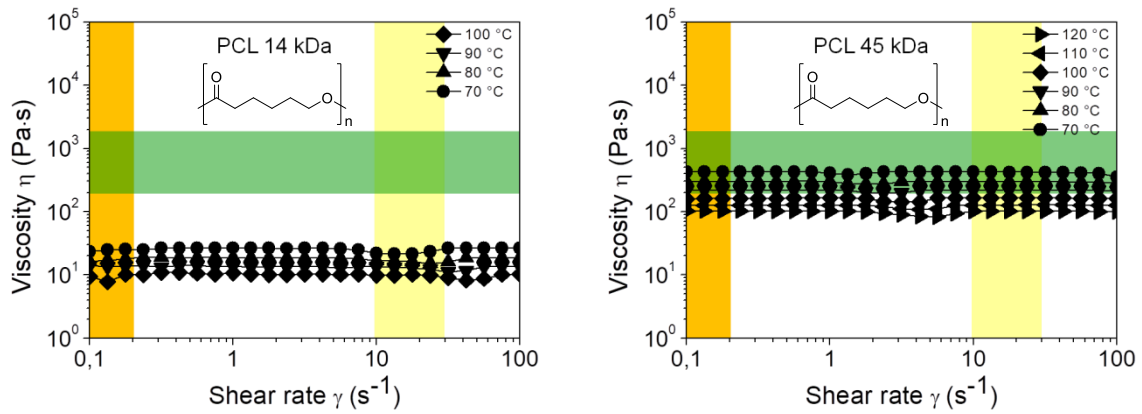


Figure 24. Rheology measurements of viscosity-shear rate-temperature dependence for PCL (14 kDa, l) and PCL (45 kDa, r.).

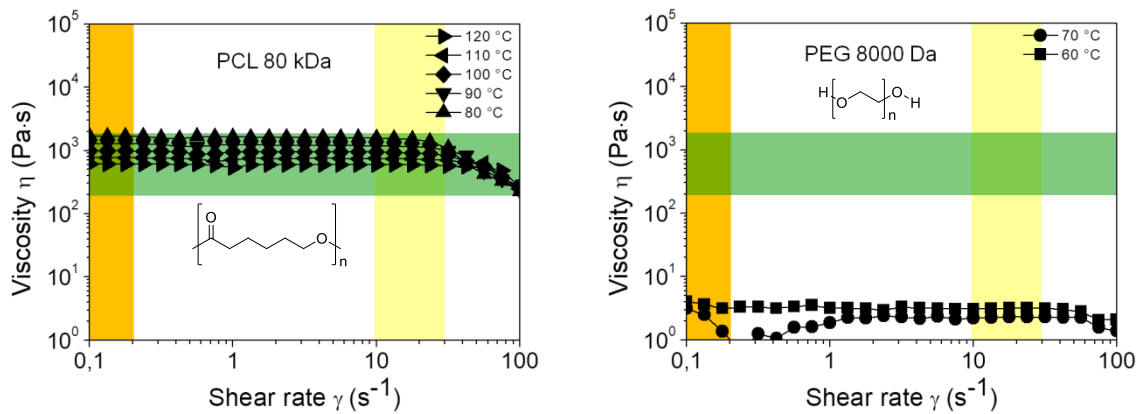


Figure 25. Rheology measurements of viscosity-shear rate-temperature dependence for PCL (80 kDa, l) and PEG (8000 Da, r.).

3.1.1.2 Melt rheology of PCLs

Polymers with relative low melting points, but still being above room temperature, were chosen to create liquid filled, 3D-printed objects. The use of high melting polymers was avoided for better compatibility with liquids (reduce evaporation) and other sensible filling materials. The PCL polymers with different molecular weights showed very different results for the 3D-printing application. The low molecular weight PCL (14 kDa) was not suitable for extrusion due to its low viscosity in the melt. The viscosity decreased from 10 Pa·s to 30 Pa·s while changing the temperature from 70 °C to 100 °C (Figure 24). During extrusion, the polymer was dripping in droplets out of the nozzle and no uniform polymer strand could be obtained. The melted polymer was too liquid for the printing with the polymer extruder. With increasing molecular weight the printability is improved significant. The PCL (45 kDa) showed a viscosity range of 425 Pa·s to 100 Pa·s while changing the temperature from 70 °C to 120 °C leading to a very good extrusion and easy to handle printing properties (Figure 24). A very uniform polymer strand could be extruded at 80 °C, which solidified in a good time range of 5 –

10 seconds. Using higher temperatures than 90 °C led to a very soft polymer strand resulting in saggy polymer strands in printed samples. Further increase in molecular weight to PCL (80 kDa) shifted the printable viscosity range to higher temperatures. In a temperature range of 80 °C to 120 °C dropped the viscosity from 1600 Pa·s to 600 Pa·s (Figure 25). The printing at higher temperatures for PCL were not preferred due to the concept of filling it with liquids during printing.


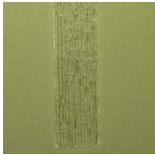
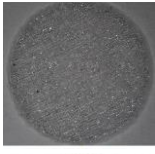
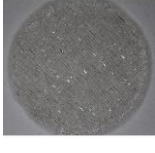
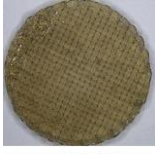

3.1.1.3 Melt rheology of polyethers

The other tested polymers with low melting points PEG (1500, 8000 Da) and PTHF (3000 Da) unfortunately showed very low viscosities in the melt below 10 Pa·s (Figure 25, Appendix 6.12). These melted polymers were dripping out of the printing needle while being extruded. Also concerning was that the solidification / crystallization after deposition were very slow at room temperature (taking more than one minute). These polar polymers with low melting point could not be used within melt extrusion 3D-printing. Other biodegradable polymers with high melting points were printed to confirm the 3D-printing window for the heatable polymer extrusion printing head.

3.1.1.4 Melt rheology of polyesters

Already well known 3D-printing polymers like PLA or PVA were tested as well. Since both of them melt at high temperatures, rheology measurements could not be performed (temperature limit $\vartheta_{\max} = 180\text{ °C}$) and the printing temperatures were estimated directly during the printing process. The PLA polymer was printable at nearly 200 °C with good extrusion and printing results. The printing of PVA (31 kDa) on the other hand was more difficult due to the absorbed water. The first printing attempts failed due to bubble formation of evaporated water inside the extrusion head. After drying the PVA and use of nitrogen as protection atmosphere inside the printing head a uniform extrusion at around 190 °C was possible. Five more amorphous biopolymers based on PLGA-copolymers ($T_g = 35 - 50\text{ °C}$) were also evaluated for 3D-printing. The polymer DLG-50-3A showed a viscosity range of 70 – 700 Pa·s in a temperature range of 150 – 120 °C. DLG-75-5A had a viscosity range of 60 – 400 Pa·s in a temperature range of 170 – 140 °C. The rheology of the biopolymer DLG-50-7E resulted in a viscosity range of 150 – 850 Pa·s in a temperature range of 180 – 150 °C. DLG-50-6P displayed a viscosity range of 200 – 650 Pa·s in a temperature range of 170 – 140 °C. The polymer DLG-50-7P presents a viscosity range of 250 – 700 Pa·s in a temperature range of 180 – 150 °C. All the PLGA-copolymers were extruding in a uniform polymer strand. Unfortunately, polymer DLG-50-7E was too brittle after extrusion that the printed object broken while trying to recover them off the printing platform. The printing results for the other four polymers are shown in Table 11.

Table 11. Polymer extrusion and 3D-printing results for biocompatible polymers. The printing temperatures were determined by rheology measurements and extrusion testing with the *regenHU 3DDiscovery*. For good 3D-printing results, as in the pictures, fine adjustments in the temperature ranges were made.

Entry	Polymer	Molecular weight [kDa]	Printing Temperature [°C]	Viscosity [Pa·s]	Picture
1	PCL	14	-	10 - 30	<i>liquid</i>
2	PCL	45	75 – 85	250 - 400	
3	PCL	80	110 – 120	580 - 750	-
4	PLA	>100	195 – 200	-	
5	PVA	31	~ 190	-	<i>brittle</i>
6	DLG-50-3A	17	120 – 130	280 - 690	
7	DLG-75-5A	27	130 – 140	350 - 510	
8	DLG-50-7E	41	150 – 160	420 - 830	<i>brittle</i>
9	DLG-50-6P	32	140 – 150	400 - 660	
10	DLG-50-7P	46	150 – 160	440 - 690	
11	PEG	1.5	-	< 1	<i>liquid</i>

12	PEG	8	-	2 - 3	<i>liquid</i>
13	PTHF	3	-	1 - 4	<i>liquid</i>

3.1.2 Rheology for the liquid inkjet print head

The second printing head based on inkjet technology is optimized for low viscosity materials (10^{-3} – 1 Pa·s). The used jetting nozzle with a drop-on-demand function can eject single droplets. The rheology experiments were executed on an Anton Paar MCR-101 DSO rheometer using cone-plate geometry with a diameter of 1.25 cm. The temperature was controlled with a thermoelectric cooler/heater in a chamber filled with dry air (20 – 100 °C). For each measured temperature the sample were preheated for 15 minutes to reach their equilibrium state. The viscosity (at a constant shear rate: 50 s^{-1}) were measured in the temperature range of 20 – 100 °C confirming the viscosity range of the inkjet print head (Figure 26).

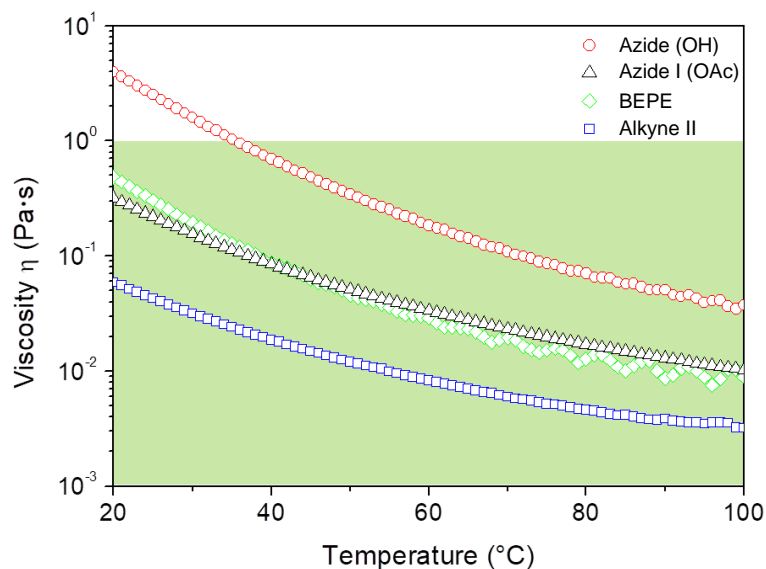


Figure 26: Viscosity-temperature measurements for the oils of trivalent azides, trivalent alkyne and BEPE.

All oils, except trivalent azide (OH), can be used in the inkjet print head depending on the viscosity values at room temperature (Table 12). The trivalent azide (OH) had a high viscosity of 3.86 Pa·s, which was not suitable for the print head leading to uncontrolled formation of small droplets. The oil collected itself to big drops at the bottom of the print head. The trivalent azide I (OAc) as well as BEPE showed similar viscosities of around 0.4 Pa·s and could be used. Regardless of their fitting viscosity, they produced quite large, single droplets. The synthesized trivalent alkyne II showed the lowest viscosity of them of around 0.06 Pa·s jetting very small singular droplets. Commercial available linalool and limonene with very low viscosities were easily dispensable in a drop-on-demand manner.

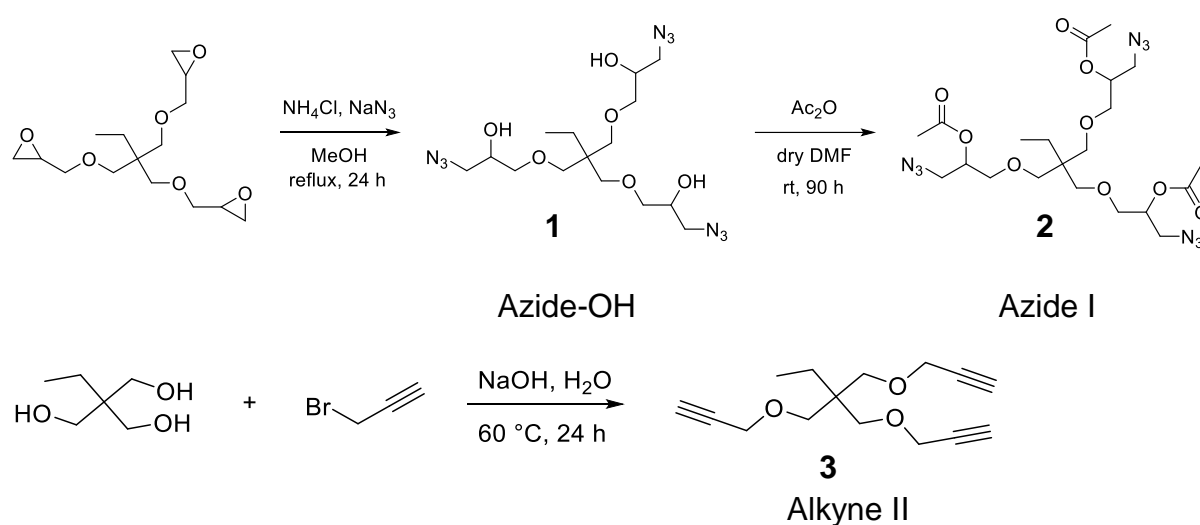


Figure 27: Synthesis of and the synthesis of trivalent azide (named azide I) *via* two steps trivalent alkyne (named alkyne II).^{259, 260}

Table 12: Viscosities of different oils including self-synthesized trivalent azides, trivalent alkynes and BEPE.

Oil	Viscosity at 20 °C
	(Pa·s)
Azide (OH)	3.86
Azide I (OAc)	0.32
Alkyne II	0.06
BEPE	0.461
Linalool	0.006 ²⁶¹
Limonene	$9 \cdot 10^{-4}$ ²⁶¹

3.2 3D-printing of core-shell capsule composites

Modified FDM printers offer more possibilities in material design when combined with additional printing heads of a different nature.²⁶²⁻²⁶⁴ While using a second printing head (a liquid dispensing unit), the dual-head printer is able to create capsule-like structures. A dual setup 3D-printer could generate big liquid core - shell capsules by interrupting the printing of the shell, subsequently filling the void with liquid and then finishing the printing process with closing the capsule.²⁶⁵ Early research of creating liquid-filled capsules *via* FDM-methods relied on the printing of two capsule halves, subsequently filled with liquid after printing and at last the connection of both parts.^{87, 90, 93, 266} In this field general large liquid-filled capsules (core sizes 4 – 7 mm) were 3D-printed using FDM for the capsule shell, simultaneous dispensing a drug solution by a second printing head into the capsule.¹⁰³ Further approaches on 3D-printed capsules (mm sized) have been published^{88, 101, 107, 267, 268}, but printing of μm -sized capsule systems is far less known using FDM printing, as processing of very small structures with FDM are difficult.²⁶⁹ Successful methods were published based on hydrogels selectively filled with inkjet printing²⁷⁰⁻²⁷³, presenting a method to 3D-print core - shell capsules within hydrogel matrices. These 3D-printing-based methods included capsules suspensions (200 μm), precise patterning of capsule arrays and the ability to control the core volumes, compositions, and shell thicknesses.¹¹¹ Recently, solid dosage tablets containing drug-loaded nanocapsules were prepared by FDM using PCL filament. After printing of the tablets, they were placed into a nanocapsules suspension to attach the nanocapsules onto the surface of the printed structures.¹¹²

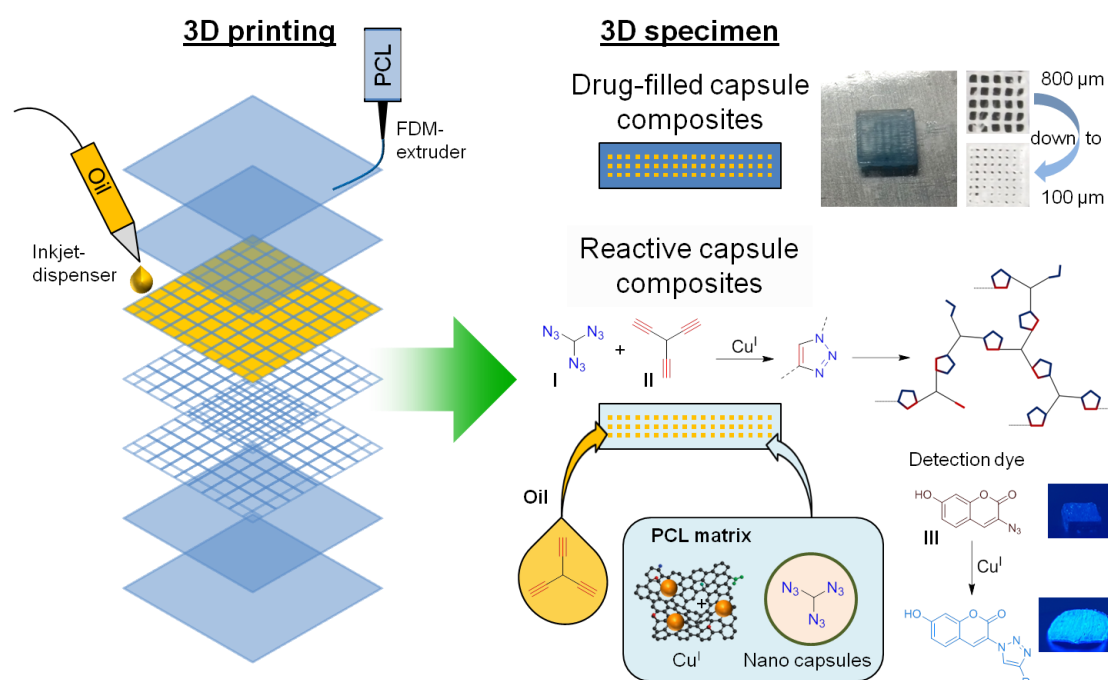


Figure 28. In the FDM process, the base layer was manufactured first and the polymer grid was deposited on top. Microcapsule-voids were filled with oil by a second printing head and finally closed by the top layer processed with FDM again. The process was adapted to reactive system of component I and II, being able to react in a Cu^I -catalyzed “Click”-reaction after 3D-printing.

By combining different 3D-printing techniques and composite printing, a novel method to 3D-print micro-sized capsules into a thermoplastic polymer matrix was developed. Composite materials based on mixing a biodegradable polymer (PCL) with nanocapsules and micro scaled fillers were printed, while creating micro-sized capsules during printing and filling them with hydrophobic liquids (Figure 28). The void spaces generated during the FDM-process were filled with liquids using a separate liquid dispenser which was part of the 3D-printing system (Figure 23). The combination of two printing heads resulted in the creation of a capsule-based reactive material superior to previous conventional mold casting methods.²⁷⁴⁻²⁷⁷ The challenge here was the embedding of two reactive components into a thermoplastic polymer with 3D-printing, but still being separated from each other. The reaction between both components after printing, triggered by external force, led to cross linking chemistry. One of the major obstacles was the embedding of the nanocapsules (component 1), a catalyst, as well as the second reaction component into the same thermoplastic matrix during FDM-printing. In contrast to conventional encapsulation methods, such as in-situ polymerization²⁷⁸, interfacial polymerization²⁷⁹, sol-gel methods²⁸⁰ or solvent-evaporation emulsion,^{207, 281} the here used 3D-printing created capsules directly by dispensing the liquid within voids of the solid matrix during the FDM-printing process. Therefore new advantages as well as disadvantages will be mentioned. The conventional methods are based on easy synthesis, low temperatures and very well known techniques. They often use on chlorinated solvents and result in randomly distributed capsule sizes and not always controllable distribution inside a matrix material. Their sizes can range from large micrometer to small nanometer sized capsules. The 3D-printing technique allows to manufacture the finished matrix-based specimen in one go while creating different shapes and controlling the capsule locations. On top, no organic solvents are used. The disadvantages of the 3D-printed capsules are very thick capsule walls, high extrusion temperatures and the large sizes of micrometer up to millimeter.

With fused deposition modeling (FDM) an area (5 x 5 mm), completely filled with polymer composite, was manufactured. The next layer was placed as a grid structure to form micrometer sized voids with a width of ~ 100 – 800 μm . Due to the relative low melting temperature and partial elasticity of PCL, both strand directions of the grid could be printed in one level (Figure 30c,d). The grid being completely in the same level fully enclosed capsule shells were produced. The still open gaps were filled with a liquid component in a drop-on-demand manner, enclosing them with a top layer by the FDM-process (Figure 28). The base structure was designed in a CAD program creating a fully closed base and top layer with tightly connected polymer strands. The capsule structure was programmed as an oil-filled grid system, placed between the base and the top layers. In the FDM process, the base layer was first manufactured and the polymer grid was deposited on top. The still open voids / microcapsules were then filled with oil by a second printing head and finally closed by the top layer processed with FDM. These combined 3D-printing techniques created the opportunity to manufacture drug-filled capsule systems as well as reactive capsule composites in one 3D-printing cycle. As a

final proof of principle the reactive capsule composites were filled with two different liquids for a fluorogenic CuAAC-“click” reaction.

3.2.1 Encapsulation of hydrophobic model liquids

The printing of non-reactive liquids, such as farnesol, linalool, limonene and a reactive trivalent alkyne (**I**) into structures of pure polycaprolactone (PCL) were tested. The core-shell capsule composite was generated with the help of the *regenHU BioCAD™* software with three different layer styles. Three different molecular weights (14 kDa, 45 kDa and 80 kDa) were tested for their temperature depended viscosity to ensure the printability with the regenHU 3DDiscovery (Figure 29a). The viscosity range of the polymer extruder was situated in the range of 200 – 2000 Pa·s.¹⁴⁵ Combined with a melting point of around 60 °C for PCL, this allows the use of 45 kDa molecular weight at a printing temperature of 80 - 90 °C, whereas both, the 80 kDa PCL and the low molecular weight PCL (14 kDa) required either too high printing temperatures (above 100 °C), or were showing too low a viscosity for stable printing. Thermal stability of all printed compounds was sufficient at around 80 °C (Figure 29b), (details in Table 13). Therefore all model-liquids could be used in this 3D-printing process in a temperature range of 40 – 100 °C, as the contact with the freshly extruded, hot PCL did not lead to evaporation or decomposition of the embedded liquids.

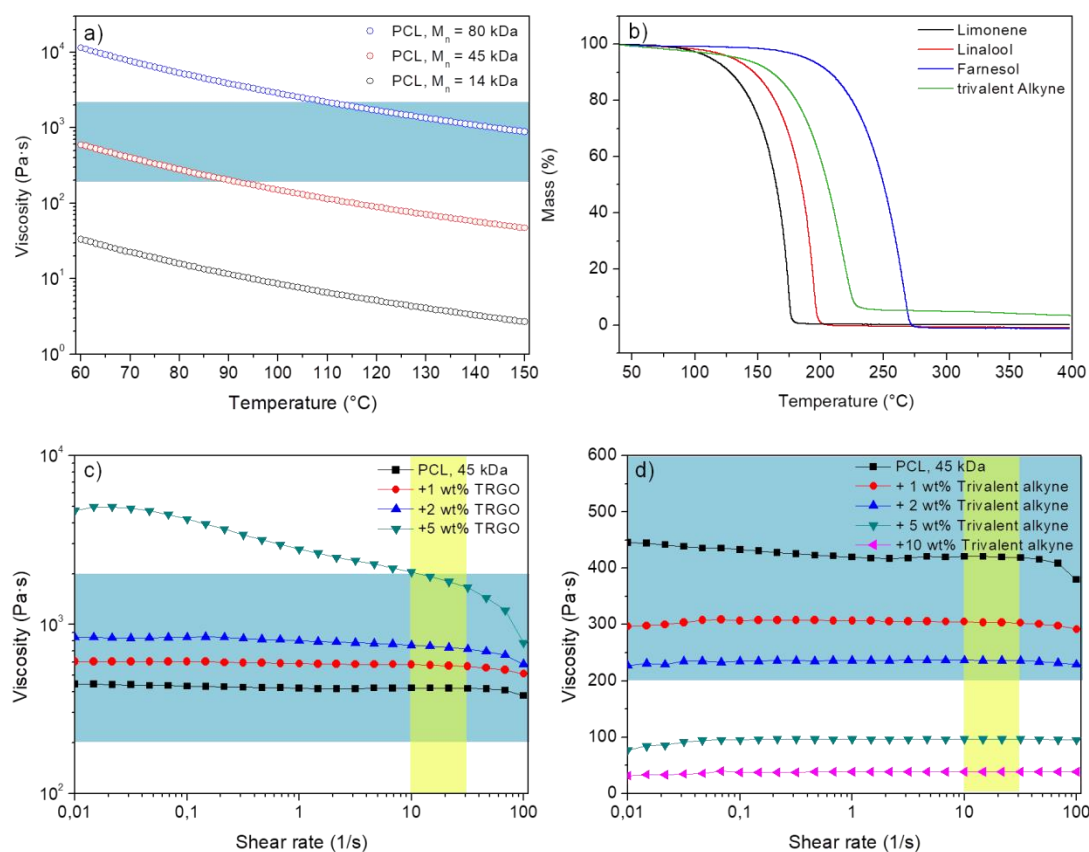


Figure 29: Viscosity-temperature rheology measurements for polycaprolactone (PCL) with different molecular weights ($M_n = 14\text{k}, 45\text{k}, 80\text{k Da}$). The printing range of the 3D-printer is marked in blue (a). Thermal decomposition measurements of the used hydrophobic oils under nitrogen atmosphere with a heating rate of $10\text{ }^\circ\text{C}\cdot\text{min}^{-1}$ (b). Melt-rheology of PCL composites at $80\text{ }^\circ\text{C}$ with TRGO (c) and trivalent alkyne (d) to ensure printability with regenHU 3D-Discovery printer ($\eta = 200 - 2000\text{ Pa}\cdot\text{s}$, $\gamma = 10 - 30\text{ s}^{-1}$).

Table 13. Thermal stability and analysis of Limonene, Linalool, Farnesol and trivalent alkyne.

Liquid	$\nu_{\text{Onset}}\text{ (}^\circ\text{C)}$	$\nu_{\text{End}}\text{ (}^\circ\text{C)}$	Mass loss $400\text{ }^\circ\text{C}$ (%)
Limonene	102	177	99.9
Linalool	116	197	99.9
Farnesol	178	270	99.9
Alkyne II	109	225	97.2

3.2.1.1 Contact angle measurements PCL – hydrophobic liquid

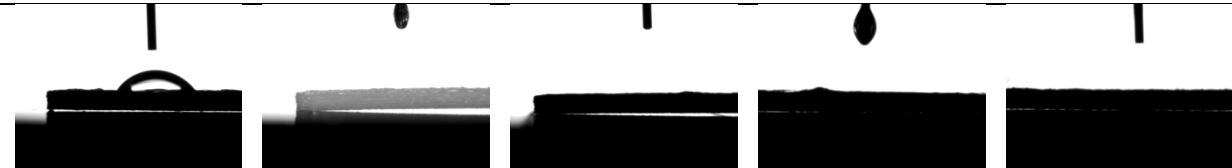
The interaction between the hot PCL surface directly after FDM-deposition and the hydrophobic liquid drops plays an important role in the 3D-printing process. The liquids are deposited as small droplets (nL) into the created gaps between the PCL strands and on top of the base-PCL layer. Therefore wetting between the dispensed liquid and the

PCL-polymer is essential for proper filling of the voids with the liquids. After the 3D-printing of PCL (5 x 30 x 0.9 mm) the contact angle of the dispensed liquids (limonoene, linalool, farnesol and the alkyne I) were determined as $\gamma = \sim 0^\circ$. Since the surface of the 3D-printed samples was relative rough, this result was optimal for the processing of core-shell capsule composites with 3D-printing, as the liquid oil would fill up all the small irregularities and created voids. In contrast, when dispensing pure water, a droplet on top of the PCL formed, an air filled gap is left due to the largely different surface tension.^{113, 282}

The interaction between PCL surface and hydrophobic liquid drops analyzed with the help of contact angle measurements. Therefore, blocks of PCL (5 x 30 x 0.9 mm) were 3D-printed. The surface of FDM-based specimen still had a relative rough surface and parts of the individually polymer strands were still visible. On top of the PCL specimen three single drops of liquid (each 5.0 μ L) were placed. With the help of a camera pictures were taken and the contact angles were determined.

Table 14: Contact angle measurements of 3D-printed PCL with water and hydrophobic liquids.

Water [°]	Linalool [°]	Limonene [°]	Farnesol [°]	Alkyne II [°]
56.0	~ 0	~ 0	~ 0	~ 0
56.9	~ 0	~ 0	~ 0	~ 0
53.8	~ 0	~ 0	~ 0	~ 0
Ø 55.6	~ 0	~ 0	~ 0	~ 0



3.2.1.2 Setup for the 3D-printing process

For simultaneous printing of two different materials with large difference in viscosity the multi-head 3D-printer regenHU 3DDiscovery was used. The printer was equipped with a heatable polymer printing head that consisted of a storage tank and a screw extruder as well as a drop-on-demand inkjet printing head for liquids. The 3D-printer was reported in a previous publication,¹⁴⁵ requiring a viscosity range of the extruded polymers of 200 – 2000 Pa·s. The inkjet head could be used with liquids in the range of 1 – 10 mPa·s. The preheated PCL in the storage tank (90 °C) was moved with high air pressure of $p = 0.20$ MPa into the screw extruder and then extruded through a steel nozzle, printing the objects on top of double-sided adhesive tape. The hydrophobic liquids were then dispensed *via* a 3 mL syringe, attached onto the drop-on-demand

printing head, applying an air pressure of 0.01 – 0.04 MPa. After printing of core-shell capsule composites, the sample surfaces were rinsed with ethanol to remove excess liquid and adhesive residues. The process is shown in Figure 30, displaying the cleaned PCL-grids.

3.2.1.3 Capsule specimen analysis

A critical point in this work was to obtain completely closed capsules, which contain the hydrophobic oil or a dye for visualization. Tightness of the 3D-printed composite was proven by light microscopy and *via* diffusion tests of fluorescein filled capsules (Figure 3a, b). As shown in Figure 30c it was possible to 3D-print completely closed layers with capsule sizes down to 100 microns, starting from 800 microns. The single polymer strands were well connected and the turn over points at the end of the specimen were also filled with PCL. Gaps in the range of micrometer or millimeter were not visible. With good development of the design and optimal printing conditions a core-shell capsule matrix could therefore be realized.

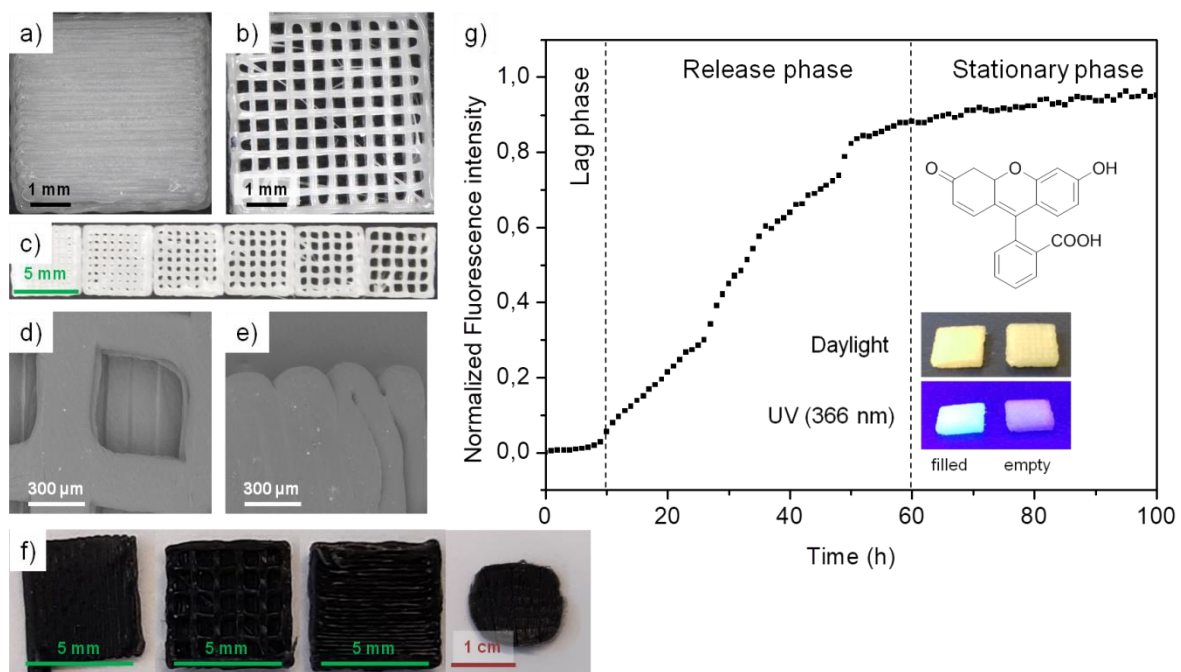


Figure 30. Microscopic image of the printed top layer (5 mm x 5 mm) to ensure visible enclosure of the core-shell capsule system (a), the inner grid structure forming the capsule system (b) and different grid sizes with gaps from 100 μm to 800 μm (c). SEM-images (d,e) and pictures (f) of different layers (the composite 10). Diffusion test of printed core-shell capsule systems with fluorescein saturated farnesol solution as capsule filling. The release of the solution in ethanol was analyzed by fluorescence measurements (g).

To further prove the encapsulation of liquids inside the core-shell capsule matrix diffusion tests were done (see Figure 30f). A saturated solution of fluorescein in farnesol

was prepared and used in the above described printing process. The so prepared specimen was placed in a quartz cell filled with 3 mL ethanol, checking efflux of fluorescein with fluorescence measurements at 519 nm for up to 100 hours. The filled capsules started to continuously leach after ten hours into ethanol, observing a linear increase of fluorescence intensity, stopping after ~50 hours. Based on the lag phase of ~ten hours and the subsequent slow release, we conclude the formation of very well enclosed capsules.

An advantage for the use of our 3D-printing technology is the ability to create capsule based specimens with the opportunity to steplessly change the size of the capsules (see Figure 30c). The grid arrays defining the capsule size in the final material could be tuned in all three dimensional directions to gain capsule sizes from 100 – 800 μm . The reprintability of the core-shell capsule composites were analyzed with weight measurements being around 43 mg with a standard deviation below 1 mg. The capsule sizes were determined by the image analysis software ImageJ^{283, 284}, able to measure distances, areas and other graphical data of Figure 30.

Table 15: Reprintability of core-shell capsule composites were analyzed by weight measurements of reprinted samples.

Liquid	Capsule size [μm]	Mass [mg]	Average [mg]	Standard deviation <i>n</i>
Farnesol	~300	44.8	44.2	0.9
		44.9		
		43.0		
Farnesol	~550	41.8	42.0	0.1
		42.0		
		42.1		
Farnesol	~800	40.6	40.2	0.3
		39.8		
		40.2		
Alkyne II	~300	45.7	45.5	0.2
		45.3		
		45.5		
Alkyne II	~550	43.1	42.6	0.5
		41.9		
		42.9		
Alkyne II	~800	40.0	40.1	0.1
		40.2		
		40.0		

3.2.1.4 Degradation of PCL during 3D-printing

Another important is to test whether the printing conditions lead to degradation of the PCL-polymer. It is well known that polymers can be depredated, when pushed through a screw extruder at higher temperatures.²⁸⁵ In the case of polycaprolactone this effect should be minor due to its low melting point of around $T_M = 60\text{ }^\circ\text{C}$. Nevertheless a degradation of the PCL took place due to the harsh conditions during printing like shear force of the screw, high air pressure in the printing head and contact with moisture after extrusion. The degradation was noticeable with the help of GPC measurements. The PCL showed a molecular weight of $M_n = 47\text{ kDa}$ and a PDI of 1.7 before printing. After printing the specimen with the different hydrophobic liquids the chains of the PCL degraded a little bit to $M_n = 34\text{ kDa}$ with a PDI of 2.0. The reduction in chain length and increase in PDI could affect properties like Young's modulus or crystallinity, but don't interfere with the applied encapsulation technique.

Table 16: Polycaprolactone analysis before and after printing with GPC and DSC methods.

Polymer	M_n [Da]	M_w [Da]	PDI	ϑ_{Peak} [$^\circ\text{C}$]	ΔH_m [$\text{J}\cdot\text{g}^{-1}$]
PCL, before	47000	80000	1.7	61.9	90.7
Limonene	34000	55000	2.0	62.2	96.5
Linalool	33000	54000	2.0	60.4	92.2
Farnesol	34000	56000	2.0	60.2	90.3
TA	32000	52000	2.0	60.1	82.0

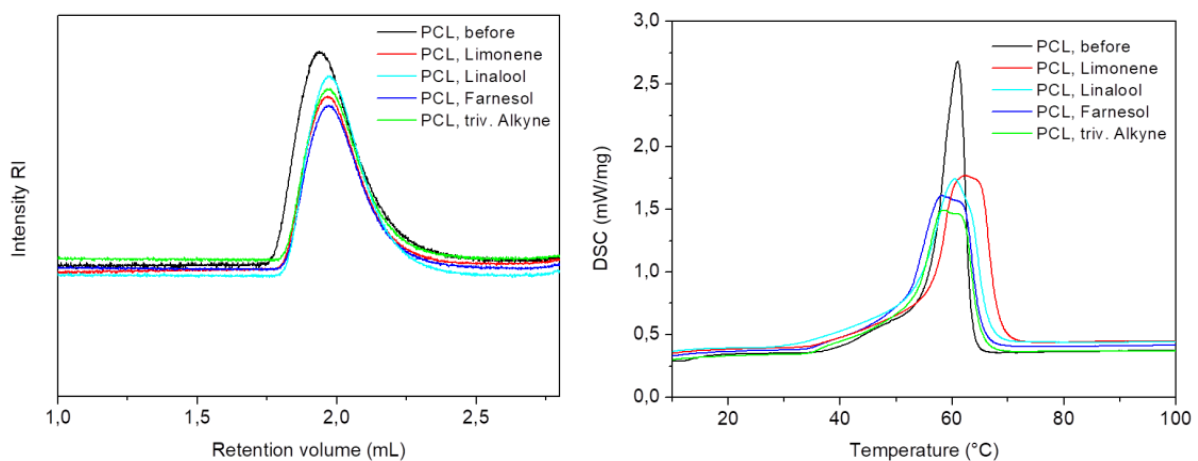


Figure 31: GPC measurement of PCL before printing and the printed capsule systems (l.) and DSC measurement of the same polymers (r.).

3.2.2 Reactive capsule composites

The 3D-printing approach was adapted to a capsule based self-healing composite, consisting of a heterogeneous Cu(I)-catalyst, a trivalent azide I and a trivalent alkyne II²⁷⁴⁻²⁷⁶. The desired composites are based on PCL as base-polymer, containing 10 – 15 wt% azide(I)-nanocapsules and a corresponding amount of TRGO²⁷⁴, able to catalyze a chemical reaction triggered by an external stimulus (azides and alkynes, reactive *via* the “CuAAC-click”-reaction). Two different trivalent monomers, one bearing azide groups (I), the other bearing alkyne groups (II), are separated by encapsulation methods and can react after activation *via* a metal-catalyzed Huisgen-1,3-dipolar cycloaddition under a formation of 1,4-triazole cross linked resin (Appendix 6.1).^{205, 286-288} Aim was the transformation of mold based fabrication techniques into a 3D-printed based approach. Since the final composite consisted of the PCL matrix, a graphene-based TRGO catalyst (containing catalytic Cu^IO₂-nanoparticles), the azide(I)-filled nanocapsules (200 nm) and a trivalent, reactive alkyne II, the changes in melt-viscosity of the PCL at 80 °C upon addition of the catalyst in amounts of 1 – 5 wt% TRGO were probed (Figure 29c). In the range of shear rates applied during printing, the viscosity of the composite increases from 440 to 4800 Pa·s. Considerable shear-thinning behavior was observed, in line with known effects from graphene-sheets in molten polymers, where the carbon layers arrange parallel to the extrusion direction of the filament.²⁸⁹ Admixing the liquid trivalent alkyne II with PCL at 80 °C (Figure 29d) lead to a decrease of the viscosity from 440 to 32 Pa·s. There was no significant shear rate dependency due to the solvent like behavior of trivalent alkyne in the PCL. Based on the printing range of the 3D-printer¹⁴⁵, PCL with up to 5 % TRGO content and a trivalent alkyne II content of up to 2 % was identified as printable.

3.2.2.1 Preparation of the composites

The prepared *composites 10, 10C and 15* containing PCL mixed with TRGO and PVF-azide nanocapsules, were placed into the FDM printing head at a temperature of 85 - 90 °C. The use of poly(vinyl formal), PVF ($T_g = 105$ °C) as shell material is crucial to maintain a stable capsule shell at the FDM temperature. At the printing needle (330 μm) the composites were extruded at 75 - 80 °C. The second reaction component, the trivalent alkyne II, was placed into the second liquid inkjet print head.

The synthesis of the PVF-azide nanocapsules and further nanoencapsulations will be discussed in chapter 3.5 Emulsion / solvent evaporation encapsulation.

Table 17. The core-shell capsule composite components are listed here. The composites include poly(ϵ -caprolactone), PVF-azide(I)-nanocapsules and heterogeneous Cu(I)-catalyst TRGO mixed. The alkyne component II was added with the liquid printing head in a drop-on-demand process (d.o.d). The composites were based on 500 x 500 x 400 micrometer capsule size created by FDM.

Sample	PCL	Capsules	Azide I content in capsules	TRGO	Alkyne II
<i>Composite 10</i>	2 g	0.2 g	0.090 g	3 mg	2.5 μ L
<i>Composite 10C</i>	2 g	0.2 g	0.090 g + 2.34 mg Coumarin	3 mg	2.5 μ L
<i>Composite 15</i>	2 g	0.3 g	0.135 g	4.5 mg	2.5 μ L

3.2.2.2 Synthesis of the monomers

The azide-alkyne “Click”-reaction is a Huisgen 1,3-dipolar cycloaddition forming a 1,2,3-triazole ring. The thermal reaction at higher temperatures often results in mixtures of two regioisomers. The Cu^I-catalyzed version of the reaction follows a different mechanism resulting only in the 1,4-regioisomer. On the other hand, results the Ru^{II}-catalyzed reaction only in the 1,5-regioisomer. For the post-printing reactive system the CuAAC-reaction was chosen and trivalent variants of azide and alkyne were synthesized. The trivalent azide was synthesized in a two step reaction plan and the synthesis of trivalent alkyne was produced in a one pot reaction (Figure 27).^{259, 260}

In addition to the dual capsule system containing liquid trivalent azide I and trivalent alkyne II, a system based on PCL having alkyne groups in the backbone have been synthesized²⁹⁰ (Figure 32). An approach for a less complex / heterogeneous system with only azide I capsules embedded into the PCL matrix containing mixed in poly(α -propargyl- ϵ -caprolactone)₁₀-co-(ϵ -caprolactone)₉₀ (called alkyne-PCL).

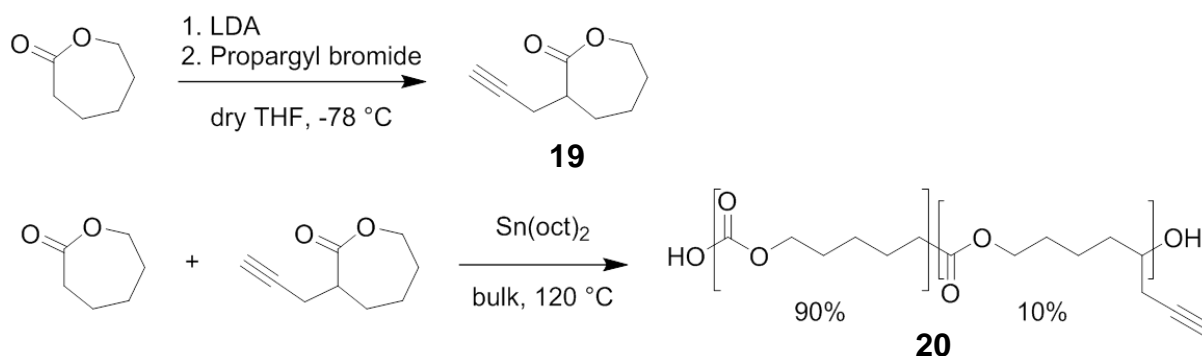


Figure 32. Synthesis of alkyne-PCL starting with the modification of ϵ -caprolactone to α -propargyl- ϵ -caprolactone was performed in bulk with $\text{Sn}(\text{oct})_2$ as catalyst.²⁹⁰

DSC measurements of a mixture containing alkyne-PCL and trivalent azide I with and without TRGO unfortunately showed to very high “click”-reaction temperatures of $106\text{ }^\circ\text{C}$ up to $187\text{ }^\circ\text{C}$, not suitable for the above developed application (Appendix 6.2). Compared to the temperatures of both trivalent compounds I,II the reaction temperatures were at least $30\text{ }^\circ\text{C}$ higher and therefore not suitable for reactions below the melting point of PCL. Since both “click”-reaction partners should be able to flow to mix with each other, but the alkyne-PCL was trapped inside the matrix material.

Further alkynes were synthesized based on bisphenol structures²⁹¹ to form similar reactive resins with the trivalent azide. First, the bisphenol E dipropargyl ether (BEPE) was synthesized (Figure 33) because it is a viscous oil at room temperature, maybe suitable for the inkjet print head. The second produced compound was the bisphenol A dipropargyl ether (BAPE), which unfortunately turned out to be a solid material at room temperature (Figure 33). As a result it could not be used in the inkjet printing head (only for liquids). Nevertheless, both bivalent monomers form resins in DSC measurements (Appendix 6.3).

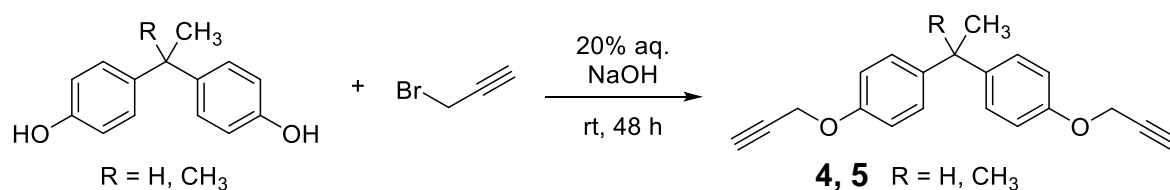


Figure 33: Synthesis of bisphenol E dipropargyl ether (BEPE) and bisphenol A dipropargyl ether (BAPE).²⁹¹

3.2.2.3 Synthesis of the catalyst: TRGO

For the catalyst for the “Click”-reaction in the prepared composites a heterogeneous and thermally stable $\text{Cu}(\text{I})$ -catalyst was chosen. The catalyst has to endure the harsh printing conditions of higher temperature and compressed air. The carbon based TRGO catalyst fulfilled the conditions and on the other hand improved the mechanical strength of the

materials.^{274, 276} In a multistep synthesis starting from graphite (< 20 μm flakes) graphene oxide was synthesized by the improved method of Marciano.²⁹² In a next step was the graphene oxide enriched with Cu(II)-ions and thermally reduced under nitrogen atmosphere at 700 °C.^{274, 276} Analytical details can be found in the appendix.

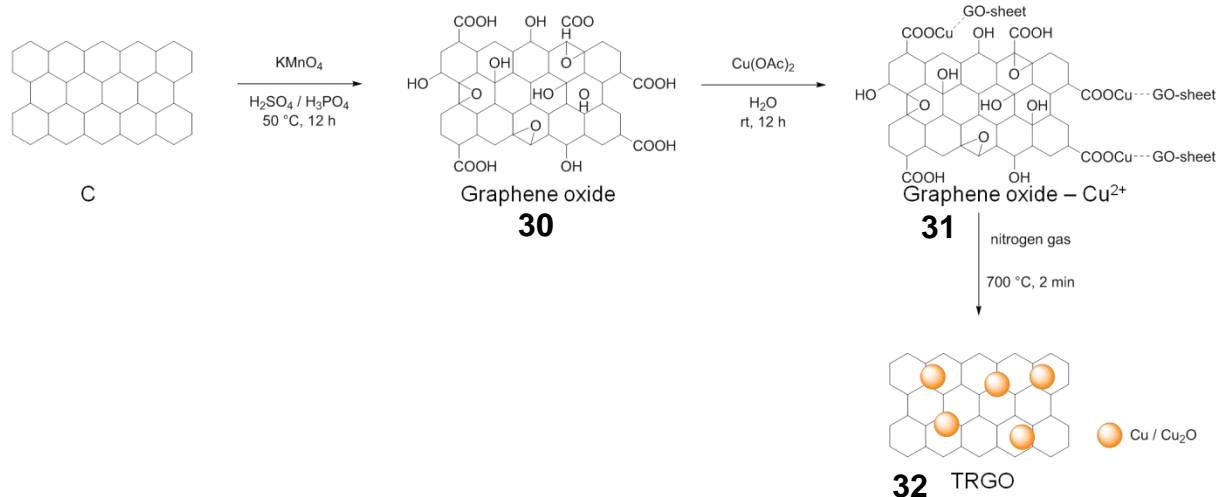


Figure 34. Synthesis of TRGO-catalyst *via* graphite (C), graphene oxide (GO), copper-(II)-enriched GO and TRGO containing Cu / Cu₂O nanoparticles.^{274, 276, 292}

3.2.2.4 3D-printing of reactive capsule composites

A composite structure with a square base of 5 x 5 mm and a grid with gaps of around 500 μm were designed in the BioCAD program. Firstly the two layers of a completely filled base area were printed. Subsequently 2 - 3 layers of the grid structure, forming the 3D-printed capsules, were printed on top. In between, the 2nd printing head with the liquid drop on demand function dispensed the trivalent alkyne II into the created gaps, filling them up with a volume of 6 nL to 380 nL per capsule void. As a final closing layer two completely filled composite layers were printed again on top. In Figure 30e-f each step was stopped separately to obtain images and SEM images. A good closure of the 3D-printed capsules could be achieved, also showing uniform extrusion in the SEM-pictures and the formation of rectangular capsules, filled with the trivalent alkyne.

3.2.2.5 Thermal stability of the composites

The thermal stability of the composite, the azide I and the catalyst were analyzed with thermogravimetric analysis (see Figure 35) under nitrogen and a heating rate of $10\text{ }^\circ\text{C}\cdot\text{min}^{-1}$. The reactive trivalent azide I was stable up to $200\text{ }^\circ\text{C}$ and decomposed in a temperature range of $200 - 400\text{ }^\circ\text{C}$ leading to a composite mixture stable in the temperature range of FDM printing ($75 - 90\text{ }^\circ\text{C}$). In the range of $250 - 400\text{ }^\circ\text{C}$ a small mass loss of 7.4 % or 9.7 % occurred, which could be related to the decomposition of the

azide filling. The matrix polymer PCL and the capsule shell material PVF decomposed at temperatures of 400 – 450 °C, indicating that no thermal induced decomposition reactions took place during printing of the composites.

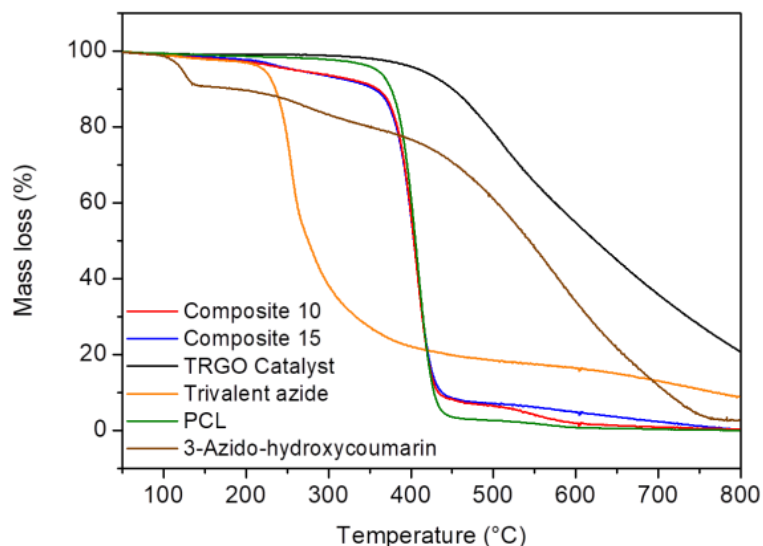


Figure 35. Thermal decomposition measurement of the composite mixtures (10, 15 wt%), TRGO catalyst, PCL and the trivalent azide under nitrogen atmosphere with a heating rate of 10 °C·min⁻¹.

3.2.2.6 Post-printing reactivity (DSC)

The residual reactivity of the embedded components were tested, both able to react *via* “click”-reactions, catalyzed by the TRGO-catalyst *via* the embedded Cu(I)O-nanoparticles. Reaction tests for the self-healing application were accomplished by calorimetry *via* DSC to check for the presence of chemical reactivity of the embedded healing components and the TRGO catalyst after printing (Table 18, Appendix 6.1). We tested the reactivity of all components directly after printing (Table 3, entry 3 and 6 and second-run DSC entry 4 and 7) and after heating to a temperature of 40 °C for 3 days, where “click”-reaction has already taken place, but PCL remains structurally stable (entry 5 and 8).

The ruptured nano- and microcapsules after pressing released their liquid fillings (I, II), which then mix and react in a Cu^I-catalyzed “click”-reaction. One sample of each composite was analyzed directly after printing *via* DSC (Figure 36). In the composites (entry entry 3 and 6 and second-run DSC entry 4 and 7), the trivalent monomers reached conversions of 7 % (*composite 10*) and 22 % (*composite 15*), concluding that the two “click”-components I and II were still active after the printing process. The purely thermal, non-catalyzed reaction showed an overall conversion of around 47 % (entry 1), the reaction with the heterogeneous TRGO catalyst lead to a conversion of 33 % (entry 2). As expected, the second DSC run for all samples (entry 4 and entry 7) did not show a

“click”-reaction after the melting of PCL as both reaction components I and II have then already reacted. After treating the printed samples of the same composites at 40 °C for three days (after capsule rupturing)²⁷⁴⁻²⁷⁶ (entry 5 and entry 8, Figure 36) indicating that under these conditions the “click”-reaction has already taken place. The DSC measurements and reaction heat analysis proved our concept of reactive component encapsulation with a multi-material 3D-printing, still being active after printing and able to react partially below the melting point of PCL.

Table 18. DSC analysis of the reactive “click”-mixture after printing and compression as well as the samples after self-healing test for three days at 40 °C. n.r. = no reaction.

Entry	Reaction	T_{Onset} (°C)	T_{Peak} (°C)	ΔH_{R} (J·mol⁻¹)	Conv. (%)
1	Thermal click reaction of pure I and II	86.5	140.8	-124.10	47
2	Click reaction of pure I and II with TRGO	58.1	72.1	-86.78	33
3	Composite 10 directly after printing	79.8	104.4	-0.82	7
4	Composite 10 (2 nd run)	n.r.	n.r.	0	No reaction
5	Composite 10 (40 °C, 3 days)	n.r.	n.r.	0	No reaction
6	Composite 15, directly after printing	84.7	103.1	-3.91	22
7	Composite 15 (2 nd run)	n.r.	n.r.	0	No reaction
8	Composite 15 (40 °C, 3 days)	n.r.	n.r.	0	No reaction

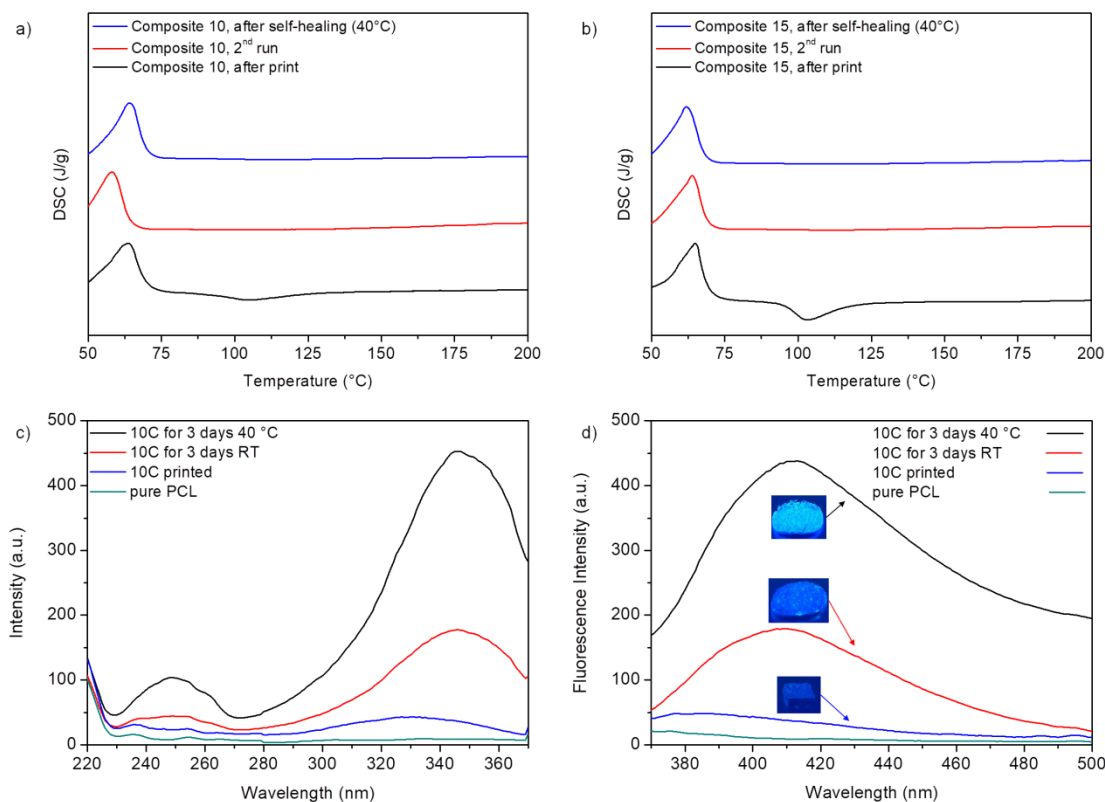


Figure 36. DSC analysis of the “click-based” reaction between trivalent alkyne and trivalent azide. The freshly printed and ruptured composites (-) show a reaction peak after the melting of point of PCL (a, composite 10 and b, composite 15). In the second run of these samples (-) no reaction is observed. When the samples are threatened at 40 °C for three days (-) there is also no reaction peak concluding the reaction already occurred. Fluorescence excitation (c) and emission measurements (d) of solid composite 10C samples are shown for different stages of the “click” reaction as well as images of the composite 10C in UV light (366 nm).

3.2.2.7 Post-printing reactivity (Fluorescence)

The reactivity of the core-shell capsule composites can be quantified further with the inclusion of a “click”-reaction sensitive fluorescence dye for stress- or damage detection. The used fluorogenic dye shows a strongly increased intensity after the “click” reaction.²⁹³⁻²⁹⁵ PVF-azide(I)-filled nanocapsules were modified with 1.5 wt% of 3-azido-hydroxycoumarin III leading to yield *composite 10C*. After calibration and evaluation of the dye content inside the capsules, *composite 10C* was printed adding the fluorogenic dye III in the same way as *composites 10, 15*. Similar reaction tests were performed and the increase of fluorescence intensity was measured. A significant change in fluorescence intensity could be measured by solid state fluorescence measurements in the reflection mode and visualized by a UV-lamp at 366 nm (Figure 36c-d). Pure PCL and the freshly printed *composite 10C* were showing very weak fluorescence at 410 nm. Increased fluorescence intensity as compared to the virgin *composite 10C* was observed. Therefore, the “click”-reaction between the trivalent alkyne, dispensed by the second

printing head, and the 3-azido-hydroxycoumarin can be used for damage detection as well as reaction control. This proves the concept of successful core-shell capsule printing. The possibility to perform a “click” reaction at temperature around 40 °C opens the field for self-healing capsule based composites without destroying the created and printed structures.

3.2.2.8 Conclusion

A novel 3D printing process is reported, where a dual-dispensing system allows printing liquid-filled capsules into a solid, thermoplastic matrix. The approach enables to generate functional composite materials based on multi-compartment structures, with a biodegradable polymer (PCL) filled with premixed nanocapsules and micro scaled liquid-filled capsules. Voids generated during the printing process are filled with various hydrophobic liquids, ranging from simple farnesol, limonene, to trivalent alkyne, useful for a subsequent capsule based, self-healing material. Capsules with sizes down to 100 micron and up to 800 microns can be printed reliably. It was demonstrated that the two reactive components can be efficiently separated *via* closed capsules, directly embedded into the PCL-polymer. Thermal stability of the printing process allows retaining sufficient reactivity for a subsequent “click”-reaction, underscoring the possibility to embed two separate, highly reactive components into one and the same thermoplastic material. This approach was used for a proof-of-concept self-healing material based on capsules and a triggered “click” reaction and visualized by a fluorogenic dye. With the here developed methodology, a large variety of multicomponent materials can now be addressed, allowing to choose the components, their embedding into multicomponent materials and the final morphology in a highly flexible manner. Based on this method, 3D-printing of multicomponent materials is possible as an advanced method over the conventional mold casting methods.

3.3 3D-printing of labile copper(I)-(NHC)-mechanophores

Mechano-responsive polymers constitute an important class of materials, able to sense and visualize stress *via* easily recordable responses.¹⁶⁹ Conventionally appropriate reporter molecules or components are embedded into polymers where stress-response should be detected.¹⁷⁰ Various chemical stress-quantification-tools have been demonstrated by including stress-induced chemiluminescence, so called mechanophores¹⁷¹⁻¹⁷³, the release of small molecules¹⁷⁴⁻¹⁷⁷ and direct mechanochromic indicators¹⁷⁸⁻¹⁸⁶. Alternatively, the induction of catalytic reactions based on the decoupling metal–ligand complexes by mechanical stimuli is used.^{187-193, 201} The most commonly used mechanochromic polymers are based on spiropyranes^{184, 186}, able to generate a merocyanine chromophores upon mechanical activation depending on their substitution pattern, especially the NO₂-functionalized dyes manifest in an intense purple color. Finally allowing to quantify the exerted stress within the material.^{178, 194-198} Therefore, in view of the multicomponent-nature of such polymeric materials the use of 3D-printing methodologies is attractive and allows to place components for the direct stress-detection as well as additional reporter molecules required for the quantification of stress into the same material.^{199, 200}

An efficient methodology for stress-detection uses mechanophores directly activated by metal/ligand cleavage and coupled to a subsequent catalytic reaction of the then freed metal-coordination-site.^{191, 193, 201, 202} The used catalysts to do this endeavor in our group are based on copper(I) bis(*N*-heterocyclic carbene) mechano-catalysts, connected to a fluorogenic CuAAC-click-reaction of 3-azido-7-hydroxycoumarin with phenylacetylene. Both components are non-fluorescent before mechano-chemical activation, but react to a highly fluorescent dye to visualize applied stress induced onto the polymer backbone *via* sonication force, grinding or tensile / compression forces.²⁰³⁻²⁰⁵

3.3.1 Mechanophore-based capsule composites

A novel 3D-print method to manufacture a stress-responsive polymer, based on micro-sized capsules, embedded into a thermoplastic polymer matrix is reported. The approach aims to generate functional composite materials based on mixing a polymer (PCL) with different Cu-based-mechanophores (1a, 1b, 1c) and 3-azido-7-hydroxycoumarin to create micro-sized capsules during 3D-printing, filled with phenylacetylene (Figure 37) as the second reactive component for the fluorogenic “click”-reaction. The 3D-printing method aimed to directly dispense the liquid into a solid matrix during the FDM-printing process, thus largely suppress a primordial thermal activation of the “click” reaction during 3D-printing.²⁹⁶

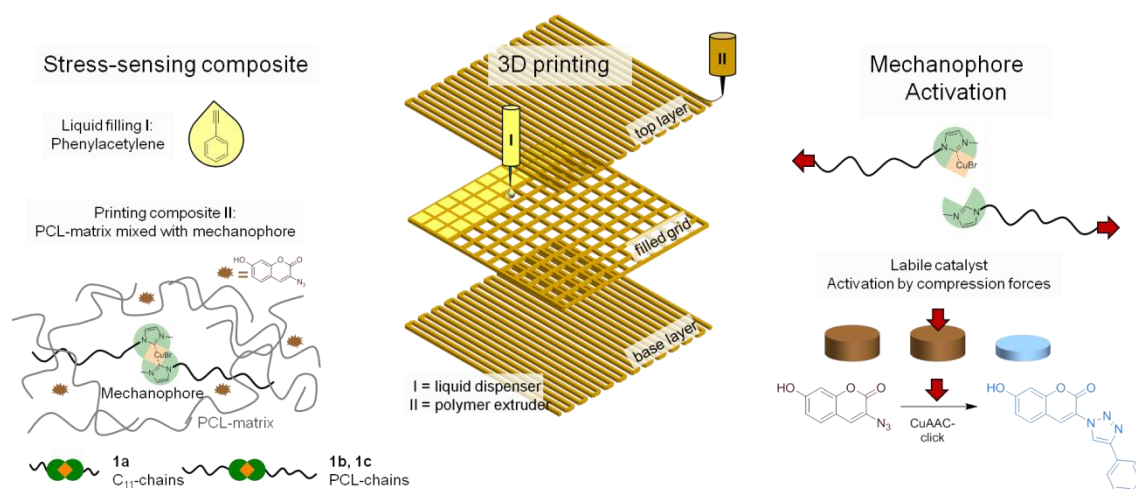


Figure 37: Concept for the 3D-printing of multicomponent-polymers containing the copper(I)-bis(NHC)-mechanophores based on C₁₁-chains (**1a**) and poly(ϵ -caprolactone) (**1b**, **1c**), successfully embedded into 3D-printable PCL together with a fluorogenic dye. The second reaction component (phenylacetylene) (liquid filling I) was added as a liquid into 3D-printed voids by direct dispensing. 3D-printed specimens were tested with compression cycles for their catalytic activity of the “CuAAC-click” reaction.

3.3.1.1 Synthesis of the mechanophores

The first step in the chemical design constituted the synthesis of a suitable mechanophore, able to be 3D-printed under preservation of its stress-reporting function. To this endeavor *copper*(I)-bis(NHC)-mechanophores **1a**, **1b**, **1c** (Figure 38), where either a C₁₁-chain (**1a**), a PCL-chain (**1b**) or an urethane (**1c**) are attached to the bis-N-heterocyclic-carbene (NHC)-Cu(I)-complexes as the active, mechano-responsive elements were prepared. Synthesis was accomplished by quaternization reaction of telechelic bromo-functionalized C₁₁- and short PCL-chains ($M_w = 1800$ Da) to yield the 1-methylimidazolium bromide functionalized chains, followed by conversion of the 1-methylimidazole-chains to the respective *copper*(I)-bis(NHC)-mechanophores with Cu₂O-powder (5 μ m). To check for possible side-reactions during the Cu₂O-treatment, hydroxy-functionalized PCL-OH was treated with the same reaction conditions detecting no side-reactions (e.g. oxidation or degradation) between pure PCL and Cu₂O *via* ¹H-NMR measurements (Appendix 6.17). The bromo-functionalized PCL (Figure 39a) showed the expected signals for the CH₂-Br-functionality at 3.39 ppm (t, J = 6.9 Hz, 2H). After quaternization reaction, new signals for the 1-methylimidazolium bromide function appeared. The NHC-proton signal was detected at 10.76 ppm (s, 1H) besides the aromatic bonds at 7.25 ppm (s, 1H) and 7.21 ppm (s, 1H), also for the CH₂-group 4.34 – 4.28 (m, 2H), the methyl group at 4.12 (s, 3H) (Figure 39b).

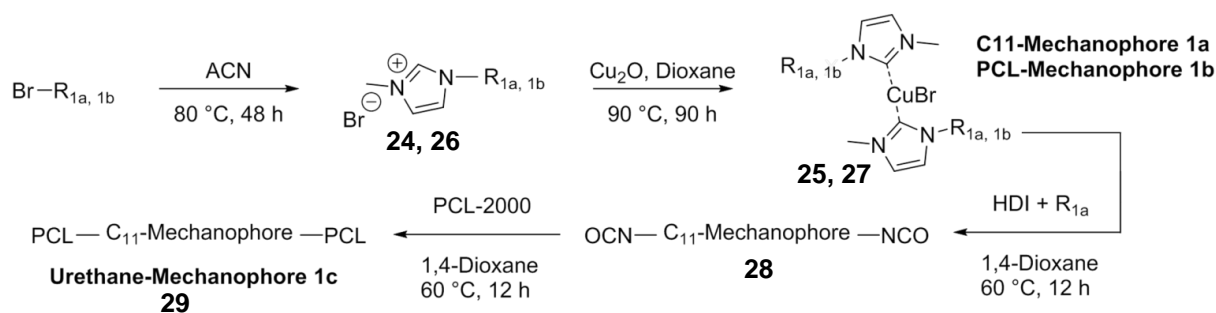
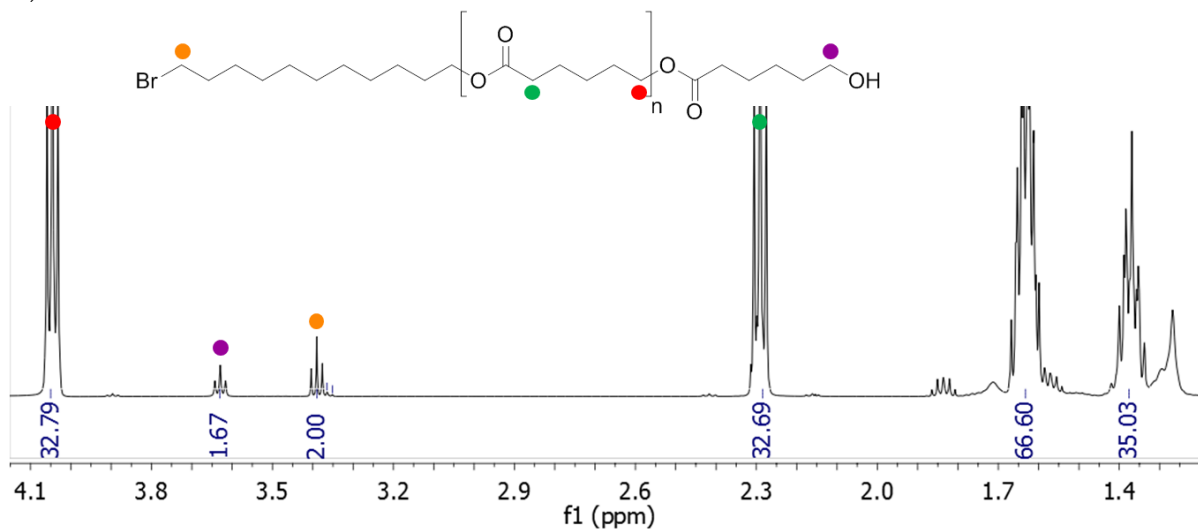


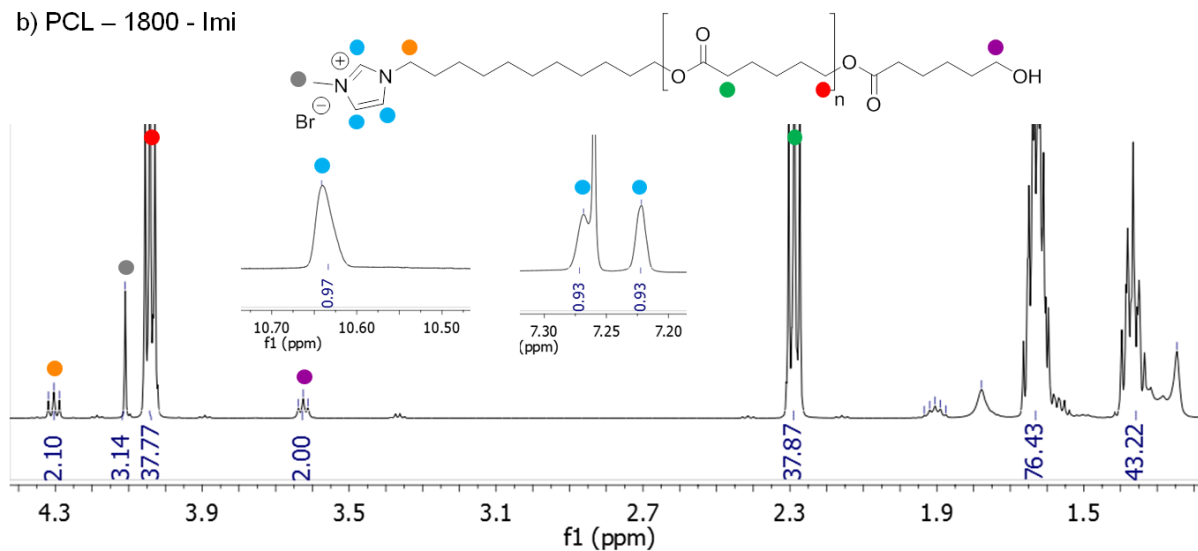
Figure 38: Reaction schema for the synthesis of different copper(I)-bis(NHC)-mechanophores **1a** (C11), **1b** (PCL-M) and **1c** (Urethane-M).

The last reaction step, the conversion to the *copper*(I)-bis(NHC)-mechanophore resulted in the PCL polymer containing the desired product 6.14 (dd, $J = 7.0, 2.8$ Hz, 4H), 3.66 – 3.54 (m, 8H) and 3.23 (s, 6H)(Figure 39c). The polymer was generated in an acceptable yield for the final mechanophore **1b** of 32%. The conversion to the 1-methylimidazolium bromide functionalized chains were supported by MALDI-ToF-MS measurements, showing all details for the reactions as proven by MALDI-TOF (Figure 40), indicating the desired MS-spectra and isotopic patterns for all intermediates. Proof for the formation of the mechanophore **1b** could be obtained by SEC, resulting in a doubling of the molecular weight in the bis-Cu(I)-NHC-complex in comparison to the starting-polymers as checked *via* GPC-measurements in THF (Figure 41). Using the calibration for polystyrene-standards ($300\text{ g}\cdot\text{mol}^{-1}$ to $170,000\text{ g}\cdot\text{mol}^{-1}$) the following shifts were measured in GPC: PCL-Br ($M_n = 3800$, $M_w = 5100$, $\text{PDI} = 1.3$) vs. PCL-M **1b** ($M_n = 7600$, $M_w = 11000$, $\text{PDI} = 1.4$). Mechanophore **1c**, based on a chain extension *via* hexamethylene diisocyanate (HDI) was prepared according to previously reported methodologies¹⁹² by reaction of the C11-mechanophore **1a** with hexamethylene diisocyanate (HDI, molar ration **1a**/HDI = 1:30).

a) PCL – 1800 - Br



b) PCL – 1800 - Imi



c) PCL - Mechanophore

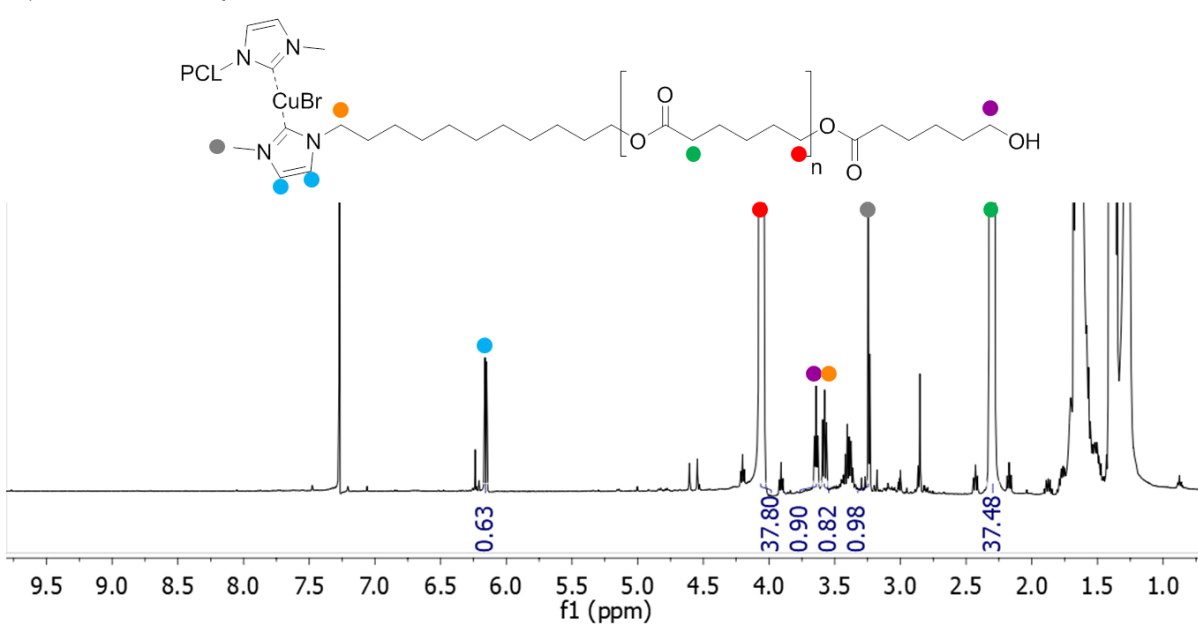


Figure 39: $^1\text{H-NMR}$ analyses of the different modification steps for the PCL-mechanophore 1b. Synthesis via PCL-Br (a), PCL-Imi (b) and the PCL-copper(I)-bis(NHC)-mechanophore (c).

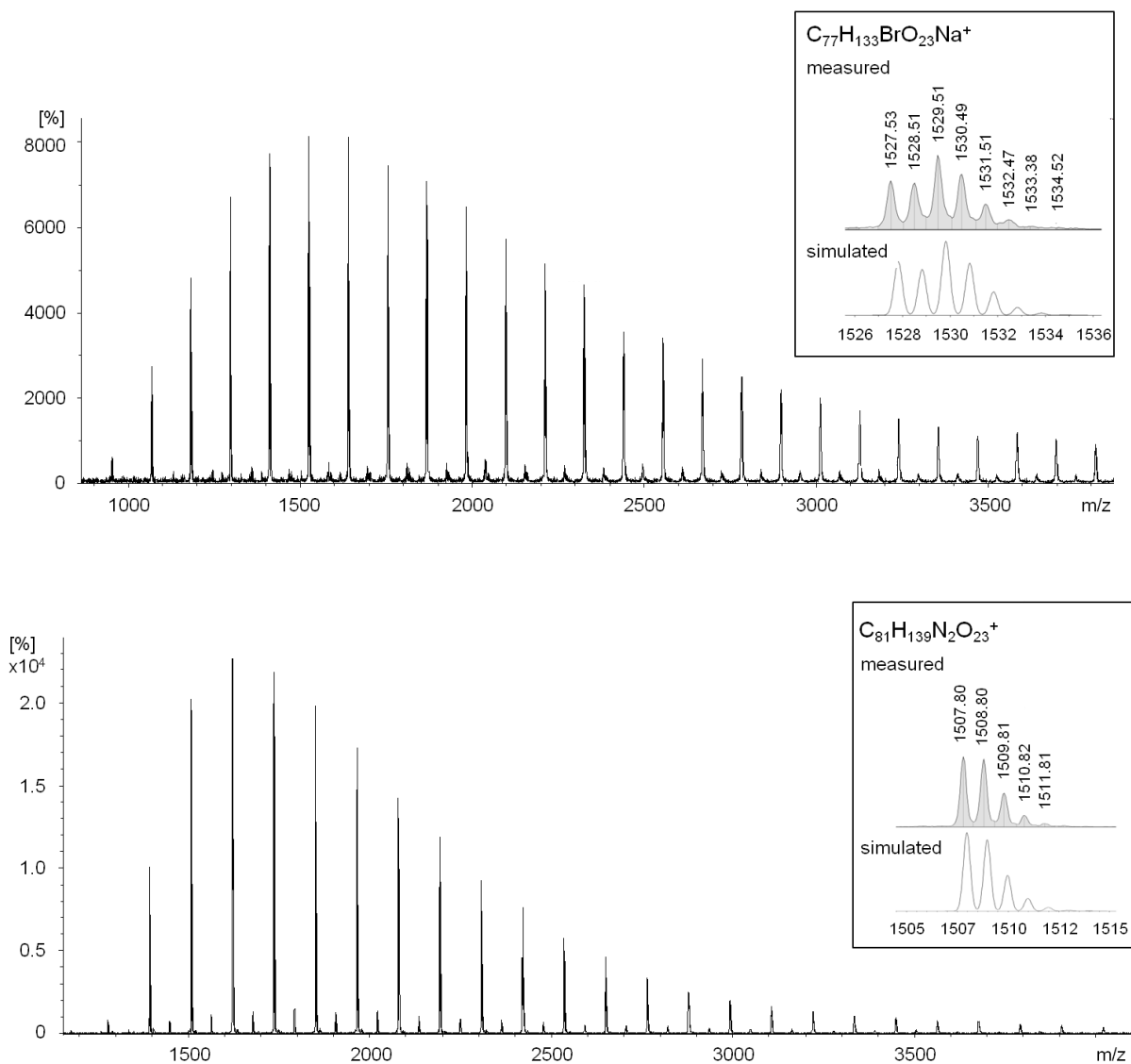


Figure 40: MALDI-ToF-MS) measurements of initially Bromo-poly(ϵ -caprolactone) and the second reaction step 1-Methylimidazole-poly(ϵ -caprolactone) are shown.

The bromide functionalized PCL (DP = 11) showed as $[C_{77}H_{133}BrO_{23}]Na^+$. The measured isotopic pattern did correspond well with the simulated one well. After quarternization, the molecular weights shifted and PCL (DP = 11) changed to $[C_{81}H_{139}N_2O_{23}]^+$, which flew without a metal ion. A new isotopic pattern was obtained and fitted well with the simulated.

3.3.2 3D-printing of mechanophores composites

3D-printing was accomplished using PCL as the base matrix (PCL ($M_w = 45$ kDa)), embedding the required components directly during the printing process. The printer, a *regenHU 3D Discovery*, equipped with a heatable polymer extrusion printing head with a metal nozzle, was used for printing of the polymer composites. Firstly, the printed composites were based on PCL as matrix-polymer containing 1 wt% coumarin-azide ($5 \cdot 10^{-5}$ mmol \cdot mg $^{-1}$ matrix) with a corresponding amount of the mechanophore **1a**, **1b**, or **1c** ($5 \cdot 10^{-6}$ mmol \cdot mg $^{-1}$ matrix). The catalytic activity will be discussed in chapter 3.3.2.2 Activity of mechanophores after printing.

Table 19: The different materials of mold-casted and 3D-printed (3D) composites including different mechanophore catalysts 1a, 1b, 1c are listed (calculated for 99% purity), as well as the final catalytic activity of each mixture.

Entry	Sample ^{a)}	Mechanophore (mg/g _{Matrix})	Coumarin dye (mg/g _{Matrix})	Phenyl acetylene (μ L)	Catalytic activity Δ^b (%)
I	No catalyst	-	10	2.5	0.34
II	C11-M	2	10	2.5	0.62
III	PCL-M	12	10	2.5	0.98
IV	Urethane-M	13	10	2.5	1.67
V	No (3D)	-	10	2.5	0.47
VI	C11-M (3D)	2	10	2.5	0.51

a) The samples entry I-IV were prepared by mold-casting method (SI), samples V-VI were manufactured by 3D-printing.

b) For the solid state measurements the sample was fixed between two glass slides and the reflected fluorescence was detected. For each sample the measurements were done for both sides. After calibration, the fluorescence intensity was calculated to the “click”-reaction yield.

A 3D-printed structure with a square-shaped base of 5 x 5 mm and a grid with gaps of around 300 μ m were designed in a BioCAD™ program. First, two layers of the 100% filled base area were printed using FDM for the PCL composite. Subsequently, two layers of the grid structure, forming the 3D-printed capsules, were printed on top. In between, the second printing head dispensed phenylacetylene into the created gaps by drop-on-demand jetting and completely filling the voids. The top closing layers consisted of two completely filled composite layers was printed again by FDM (results in Figure 43a,b). The temperature of the printing nozzle was adjusted to 70 – 80 °C according to the rheology data, with the temperature of the tank of the printing head set 10 °C higher than the temperature of the printing nozzle.

The composites were printed on a standard glass slide equipped with a masking tape for mechanical adhesion. Based on the rheology data of our previous publication¹⁴⁵ and the known 3D-printing window of the here used 3D printer ($\eta = 200 - 2000 \text{ Pa}\cdot\text{s}$, $\gamma = 10 - 30 \text{ s}^{-1}$, $\vartheta = 30 - 240 \text{ }^\circ\text{C}$), PCL polymers with an intermediate molecular weight can be printed. Since the influence of the mechanophores **1a**, **1b**, **1c** (catalytic amounts, amounts see Table 1) and the fluorogenic dye (1 wt%) on the rheological properties of the matrix was negligible compared to the pure PCL matrix (Appendix 6.16). PCL (45 kDa) showed a viscosity range of 700 Pa·s to 360 Pa·s while changing the temperature from 70 °C to 90 °C leading to an excellent extrusion and easy to handle printing properties. A very uniform polymer strand could be extruded at 80 °C, which solidified in a reasonable time range of 5 - 10 seconds. Subsequently the drop-on-demand liquid printing head was set to one drop per grid hole at room temperature. The 3 mL cartridge was filled with phenylacetylene and pressed with air of 0.01 – 0.04 MPa to move the liquid through the inkjet nozzle and deposit 2,5 μL phenylacetylene into the void (Figure 43a,b).

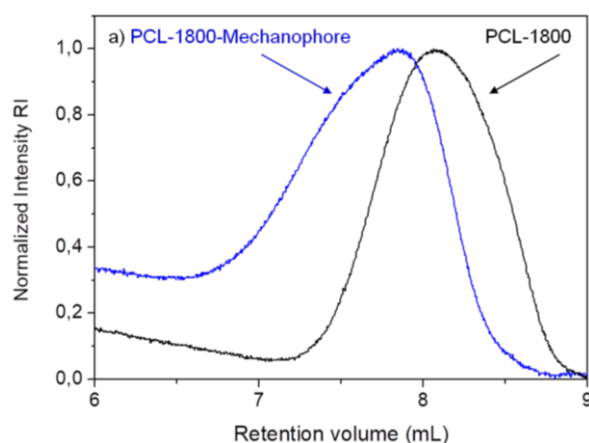


Figure 41: GPC data of the initial PCL-Br polymer and the final PCL-mechanophore 1b with a percentage content of 32 %.

3.3.2.1 Stability of mechanophores after printing

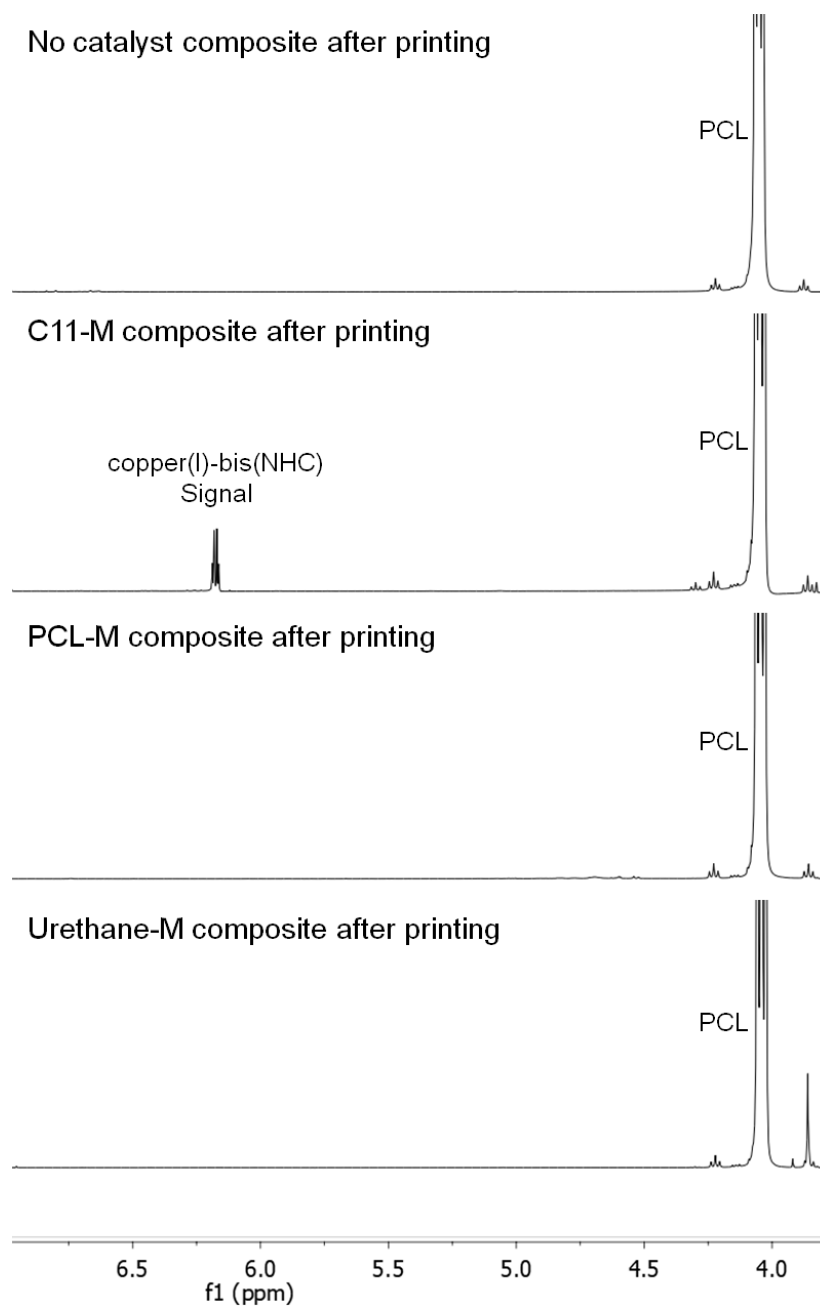


Figure 42: $^1\text{H-NMR}$ s of the composites No catalyst, C₁₁-mechanophore, PCL-mechanophore and urethane-mechanophore after threatening them with the printing conditions of 85 °C in air.

The printing composites were analyzed *via* $^1\text{H-NMR}$ after heating and extrusion checking for the presence of the copper(I)-bis(NHC) signal (6.15 ppm, dd, 4H) after the extrusion-process of the 3D-printing. Only the mechanophore with C₁₁-chains (**1a**) outlasted the printing conditions. Both, PCL-mechanophore (**1b**) and urethane-mechanophore (**1c**),

did not survive the extrusion, because no signal for the copper(I)-bis(NHC)-moieties could be detected (Figure 42). The printed composites were printed with the following conditions: printing head at ~ 85 °C, extrusion nozzle at ~ 75 °C and 0.2 MPa of air pressure.

3.3.2.2 Activity of mechanophores after printing

Then both, the mold-prepared and the 3D-printed samples (for preparation see SI) were analyzed for their mechanophore activity by a combination of compression cycles and subsequent correlated solid state fluorescence measurements, indicative for the fluorogenic “click”-reaction.

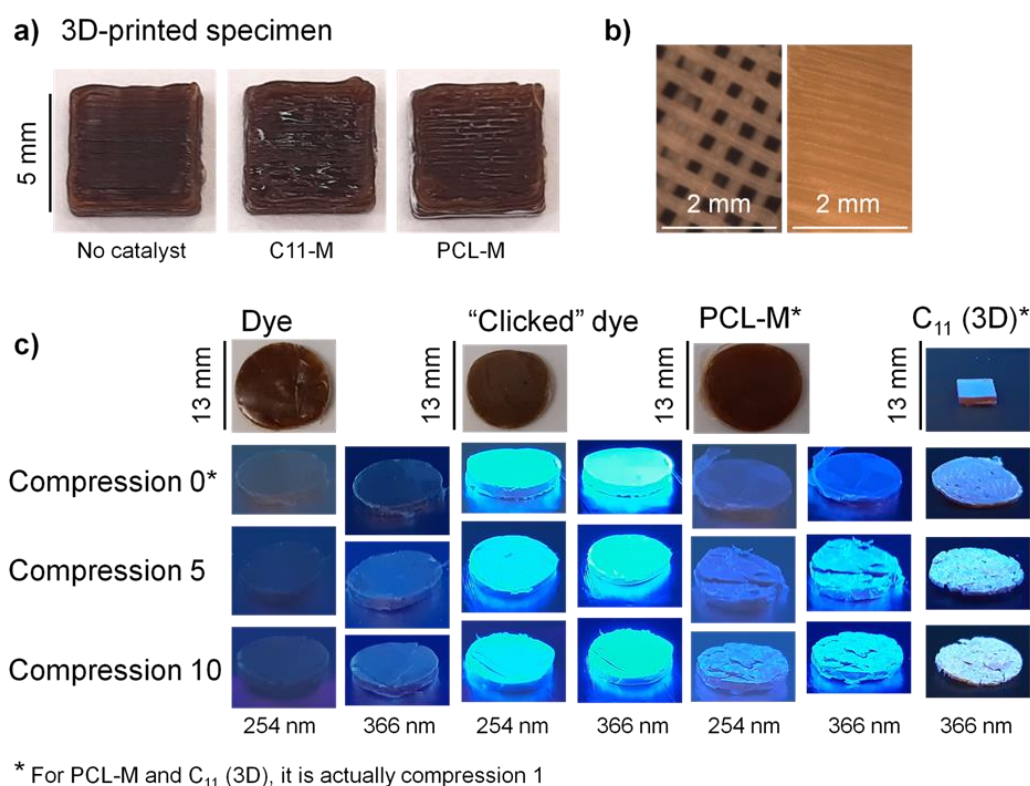


Figure 43: Pictures of the 3D-printed specimen with different composites prepared by using a dual-head 3D-printer (a). Microscopic images of a emptied inner grid structure and the top closing layer (b). Photos of mold-casted samples after compression cycles under normal light and UV-light (254 + 366 nm) showing the increase in fluorescence activity after compression force was applied (c). The samples refer to pure dye samples of the calibration curve determination (dye and “clicked” dye), as well as PCL-M (Table 1, Entry III) and C11-M (3D) (Table 1, Entry VI).

With solid state fluorescence reflection measurements as well as images under UV-light the change in fluorescence intensities were measured / visualized (Figure 43, Figure 44). For calibration of the system see appendix 6.18. The sample with no mechanophoric catalyst showed only minor activation of the fluorogenic dye of ~ 0.3 % for the molded sample (Entry I) and ~ 0.5 % for the 3D-printed sample (Entry V), presumably by

thermal activation during the printing process. The C₁₁-mechanophore (**1a**) samples showed catalytic activities of ~0.6 % (mold, entry II) and ~0.5 % respectively (3D-printed, entry VI). The higher fluorescence intensity for the C₁₁ (3D) sample was due to the thermal “click-reaction” occurring during the final FDM process, where hot printed composite gets in direct contact with phenylacetylene. For the PCL-based mechanophores only the molded samples could be measured. The samples showed activities of ~1.0 % (PCL-M, entry III) and ~1.7 % (urethane-M, entry IV). The 3D-printing of the labile copper(I)-bis(NHC)-bond could be achieved still retaining at least parts of its active form keeping the copper(I)-bis(NHC)-bonds intact, whereas the larger mechanophores based on the PCL-mechanophore **1b** and the urethane-mechanophore **1c** did not withstand the printing conditions. Presumably, their easier activation during extrusion in view of their increased chain length is responsible for this observation.

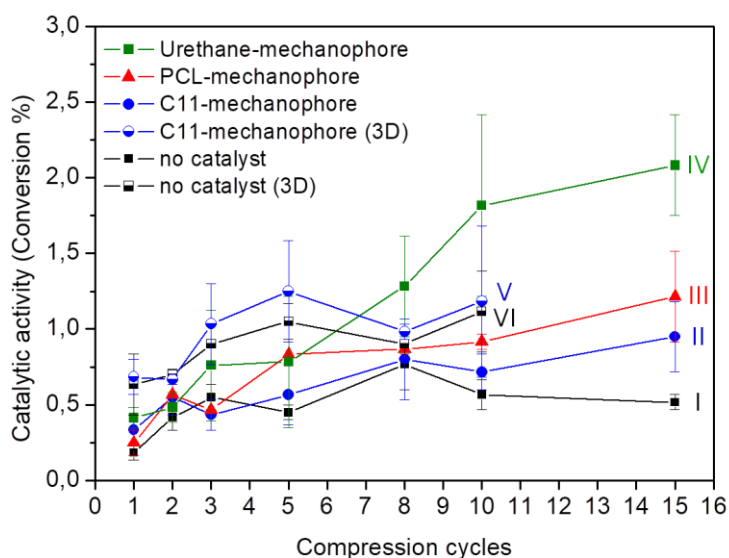


Figure 44: Catalytic activity of different mechanophore composites (no catalyst, C₁₁-mechanophore (**1a**), PCL-mechanophore (**1b**), urethane-mechanophore (**1c**)) using compression cycles to activate the copper(I)-bis(NHC)-mechanophores.

The use of 5-azido-fluorescein, as was originally planned to show a color change in the visible light, did not show large shifts in absorption spectra in MeOH or fluorescence spectra in MeOH after successful “click”-reaction (Appendix 6.19). For the absorption are the main signals at the same intensity ($\lambda = 474 \text{ nm}, 494 \text{ nm}$). Only local maxima differ at lower wavelength. 5-azido-fluorescein showed one at 364 nm and the “clicked” product shifted it to 326 nm. The shape of the fluorescence emission spectra stays the same during the “click”-reaction and the maxima only shift about 3 nm (from 518 nm to 521 nm). The reaction with phenylacetylene increased the aromatic system of the dye (Figure 45), but has no significant effect on the absorption or fluorescence was detected. In regard to these results, the standard dye for observing “click”-reactions (3-azido-7-hydroxycoumarin) was used.

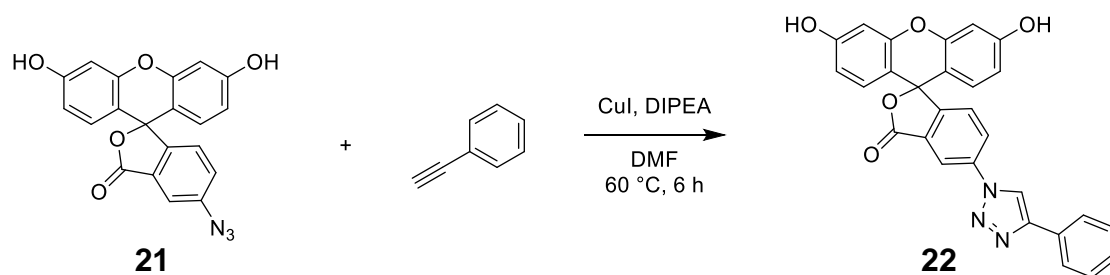


Figure 45: "Click"-reaction of 5-azido-fluorescein with phenylacetylene to increase the size of the aromatic system.

3.3.2.3 Conclusion

In conclusion, the 3D-printing of copper(I)-bis(NHC)-mechanophores was investigated using a multicomponent-printed-system, generating polymer-composites with stress-detecting properties. As demonstrated here the printing-results and final activities of the three different mechanophores strongly depended on the chain length under the 3D-printing conditions of 80 °C. Whereas short chain mechanophores with side chains of C₁₁ (**1a**) can easily be mixed with the printable PCL polymer and subsequently be extruded retaining their mechanophoric activity. The higher molecular weight mechanophores (**1b**, $M_{w, PCL-M} = 1800$ Da, and **1c**, $M_{w, Urethane-M} = 2000$ Da) could not be 3D-printed, although both showed catalytic activity (1.0 – 1.7 %) in compression force cycles when produced by a mold casting method, comparable to previous results.¹⁹³ Thus, the reported methodology can be advantageous for the fabrication of multilayer-polymers, where the stress-reporting toll is placed in a specific part of the polymeric-specimen. Only at some locations stress-detection is required, while keeping all other parts of the polymer structurally native. We think that this methodology can be advantageous when integrated into production-techniques where 3D-printing technology is already established.

3.4 3D-printing of supramolecular polymers and their composites

The concept is based on thermo reversible, hydrogen-bonded polymers, known to form nano-sized micellar clusters, arranged into a dense supramolecular network of interconnected aggregates. This network formation is driven by segregation of the attached hydrogen-bonding moieties from the non-polar poly(isobutylene) (PIB)-chains, in turn connecting the polymer chains into a transient network. The so achieved thermo-mechanical behavior can be tuned with the terminal relaxation dominated by the opening and closing of the hydrogen bonds (Figure 46). In contrast to a covalent network, the dynamic character of the attached supramolecular bonds enables macroscopic flow of the polymer on a longer timescale. Furthermore, the reassembly of the network structure, driven by dynamic exchanges within the nano-sized micellar clusters, additionally features multiple self-healing properties at room temperature and below.

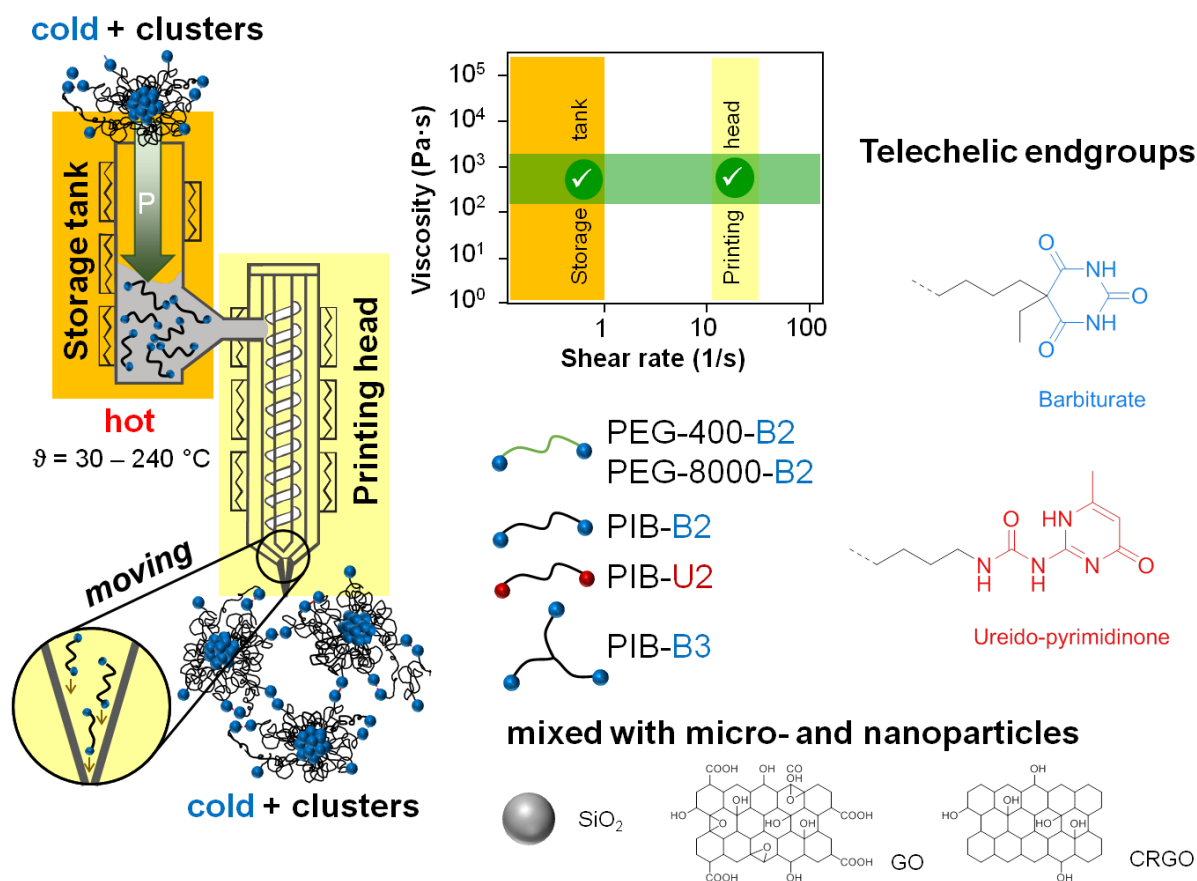


Figure 46. 3D-printing concept for supramolecular polymers based on PIB and PEG polymers, which were not printable without endgroup modification to barbiturate (B, Barbi) or ureidopyrimidinone (U, UPy).

Supramolecular polymers attached with barbiturate-moieties (B or Barbi, displaying multiple hydrogen-bonds) enable 3D-printing based on filament-extrusion, which can form reversible crosslinks *via* their two hydrogen donor-acceptor-donor (ADA)-faces. On the other hand, stronger ureidopyrimidinone-moieties (U or UPy, with four linear hydrogen-bonds) were used in 3D-printing, while forming a different hydrogen-bonding geometry with two donor-donor-acceptor-acceptor (DDAA)-faces. PIB, a hydrophobic polymer, was selected due to the strong phase segregation of the attached polar hydrogen-bonding moieties from the non-polar polymer backbone. PEG with its more hydrophilic polymer backbone was investigated for comparison, expected to display reduced segregation and consequently no cluster formation.

3.4.1 Synthesis for the supramolecular polymers

Linear PIB- and PEG-polymers bearing barbiturate moieties were prepared starting from commercially available linear polymers (Figure 47), while three-arm star PIB was synthesized *via* living carbocationic polymerization. Modifications of the linear PEG- and PIB-polymers were accomplished *via* the corresponding bivalent or three-arm star functionalized azido-telechelic polymers using “CuAAC-click”-reactions to completely functionalize the respective chain ends, generating the final PIB-B2 ($M_n = 8\,500\text{ g}\cdot\text{mol}^{-1}$), PIB-B3 ($M_n = 16\,000\text{ g}\cdot\text{mol}^{-1}$) and PEG-B2 ($M_n = 900\text{ g}\cdot\text{mol}^{-1}$, $8\,500\text{ g}\cdot\text{mol}^{-1}$) polymers. The ureidopyrimidinone-moieties were linked as an isocyanate derivate with the hydroxyl-telechelic polymers leading to PIB-U2 ($M_n = 8\,500\text{ g}\cdot\text{mol}^{-1}$).

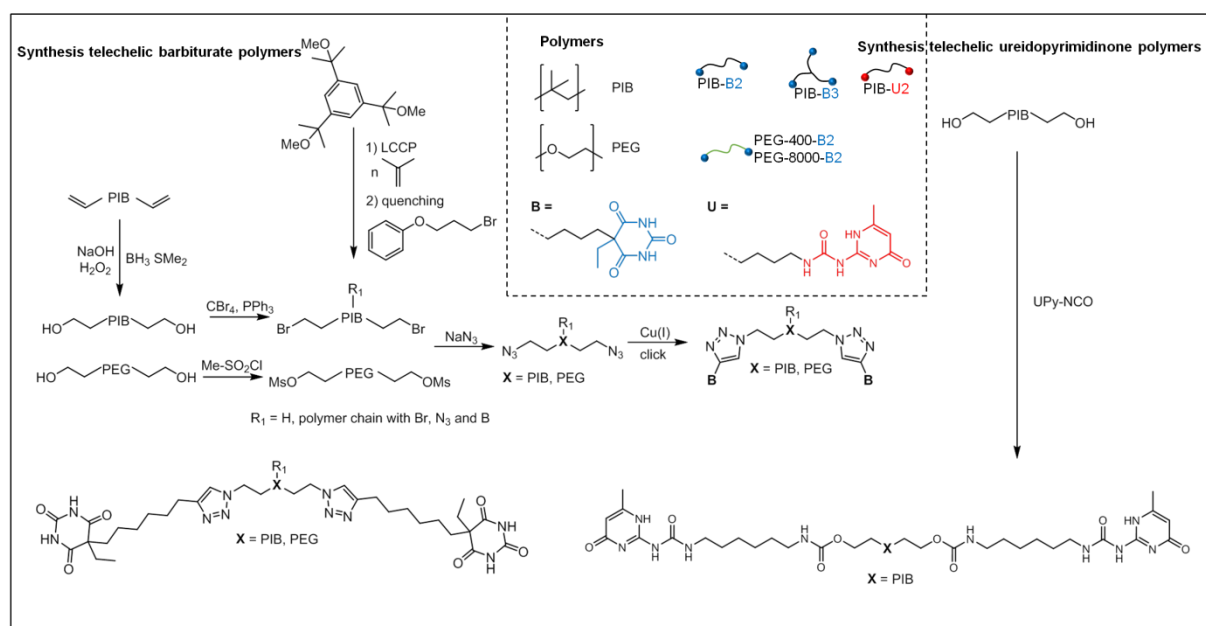


Figure 47. Synthesis scheme for telechelic functionalized polymers based on PIB- and PEG-backbones. In multistep reactions allyl- respectively hydroxy-functionalized polymers got modified to an azide group and reacted in a “click”-reaction to the barbiturates. The ureidopyrimidinone PIB was synthesized by reaction of hydroxyl-PIB with UPy-isocyanate.

3.4.2 Analysis for the supramolecular polymers

The $^1\text{H-NMR}$ s of the final supramolecular polymers were analyzed and discussed. The complex and repetitive structures of the bivalent and trivalent polymers were simplified by only showing one side / one arm of the polymer in complete detail. Successful conversion to bivalent and trivalent PIB-barbiturates and PEG-barbiturates were confirmed by $^1\text{H-NMR}$. Figure 48 shows the $^1\text{H-NMR}$ of PEG-400-B2 with the corresponding signals for bivalent modified PEG. The signal for the barbiturate moieties at 11.5 ppm is related to the NH -groups. The new formed triazole ring and its related hydrogen are located at 7.8 ppm. The protons for the polymer PEG chain are located at 4.4 ppm, 3.8 ppm, and 3.6 ppm. The rest of the alkyl-chain can be assigned as well. A similar picture can be seen for PEG-8000-B2 in Figure 49 with another molecular weight and integration value for the polymer chain.

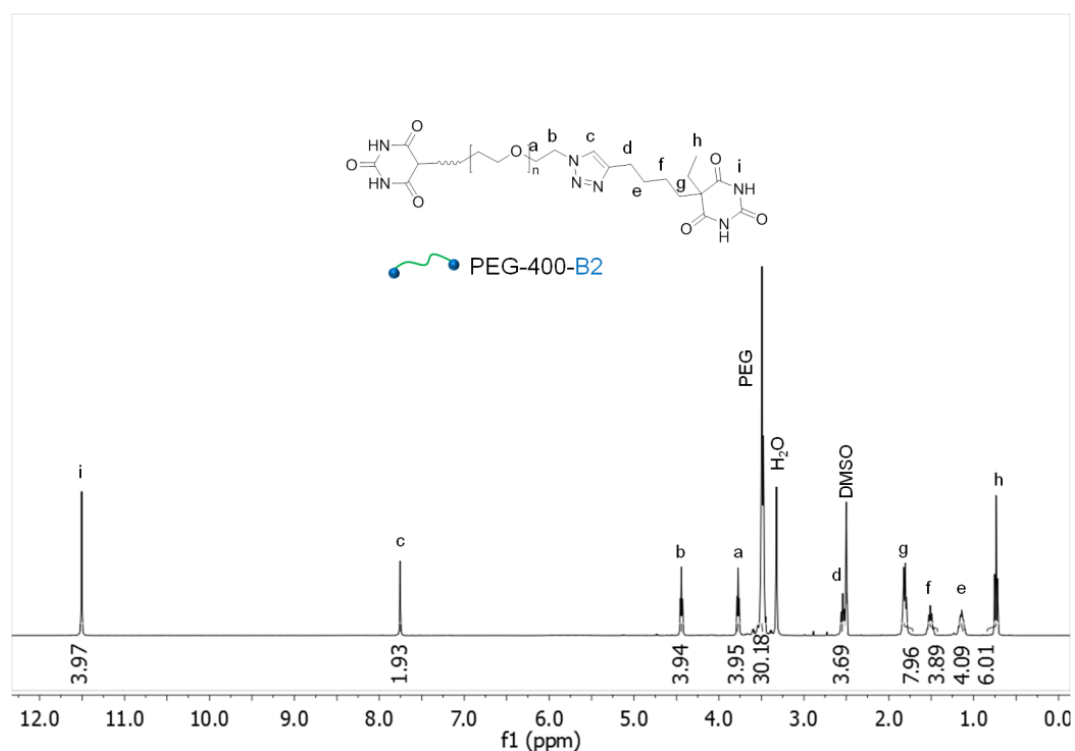


Figure 48: $^1\text{H-NMR}$ spectrum of PEG-400-B2.

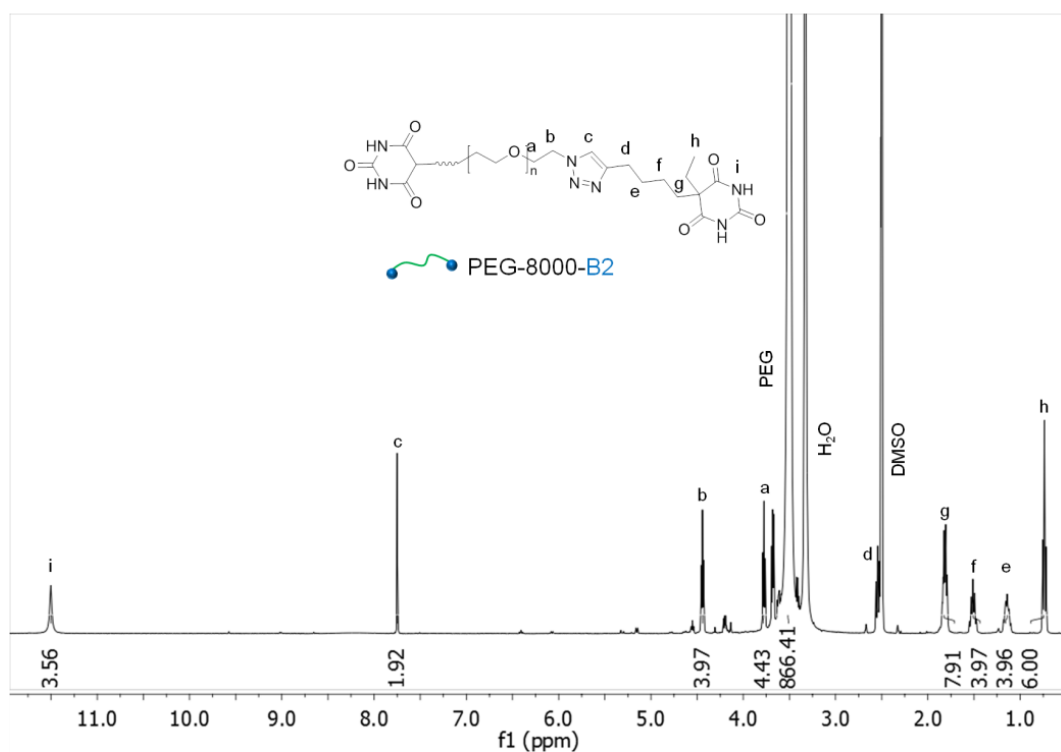


Figure 49: ¹H-NMR spectrum of PEG-8000-B2.

The trivalent PIB-B3 was previously synthesized in the working group of Prof. Wolfgang Binder and was used as obtained. The following ¹H-NMR spectra Figure 50 shows the complete functionalization with barbiturate end groups. The signal for the barbiturate moieties at 8.3 ppm is related to the *NH*-groups. The new formed triazole ring and its related hydrogen are located at 7.3 ppm. The protons the initiator benzene ring (7.1 ppm) as well as the quenching benzene ring (6.8 ppm). The rest of the protons related between barbiturate and PIB-chain can be assigned and fit with their integration value.

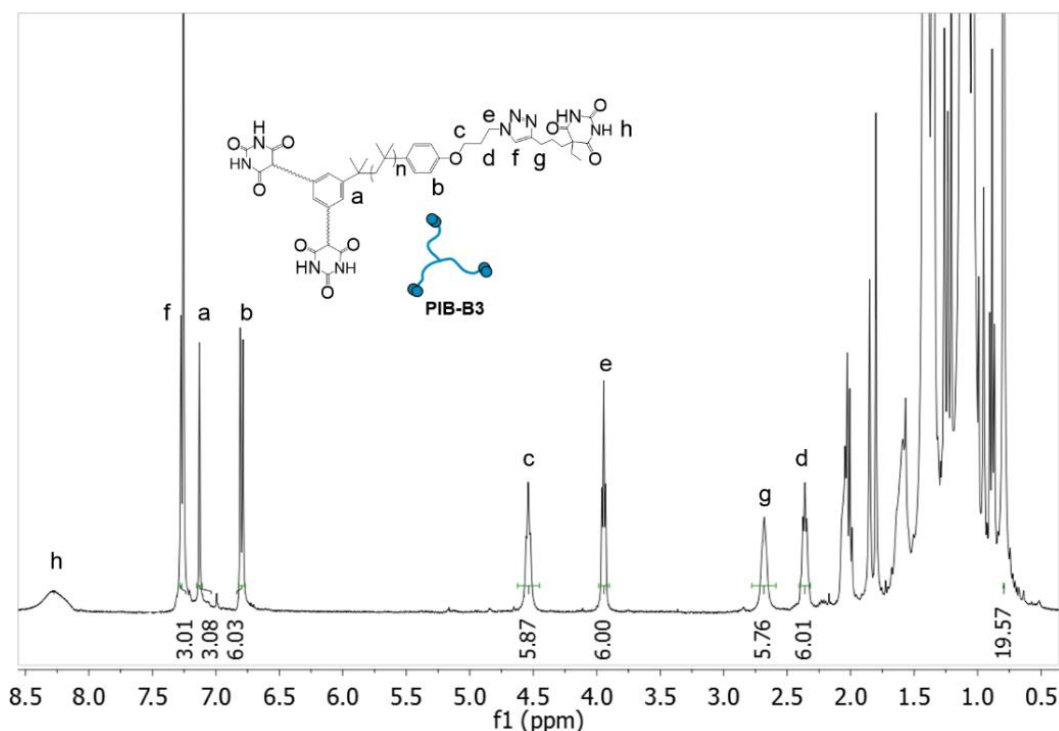


Figure 50: $^1\text{H-NMR}$ spectrum of three-arm star PIB-B3, previously synthesized in the working group of Prof. Wolfgang Binder.

In Figure 51, the $^1\text{H-NMR}$ of linear PIB-B2 is illustrated. The signal for the barbiturate moieties at 8.2 ppm is related to the NH -groups. The new formed triazole ring and its related hydrogen are located at 7.2 ppm. The connecting CH_2 -group of the polymer chain and the triazole ring is located at 4.3 ppm, while the CH_2 -group on the other side of the triazole ring is placed at 2.7 ppm. Both signals represent a triplet coupling. The rest of the protons related between barbiturate and PIB-chain can be assigned and fit with their integration value. The resulting integrals for the PIB signals at 1.4 ppm and 1.1 ppm lead to a overall molecular weight of $9600 \text{ g}\cdot\text{mol}^{-1}$.

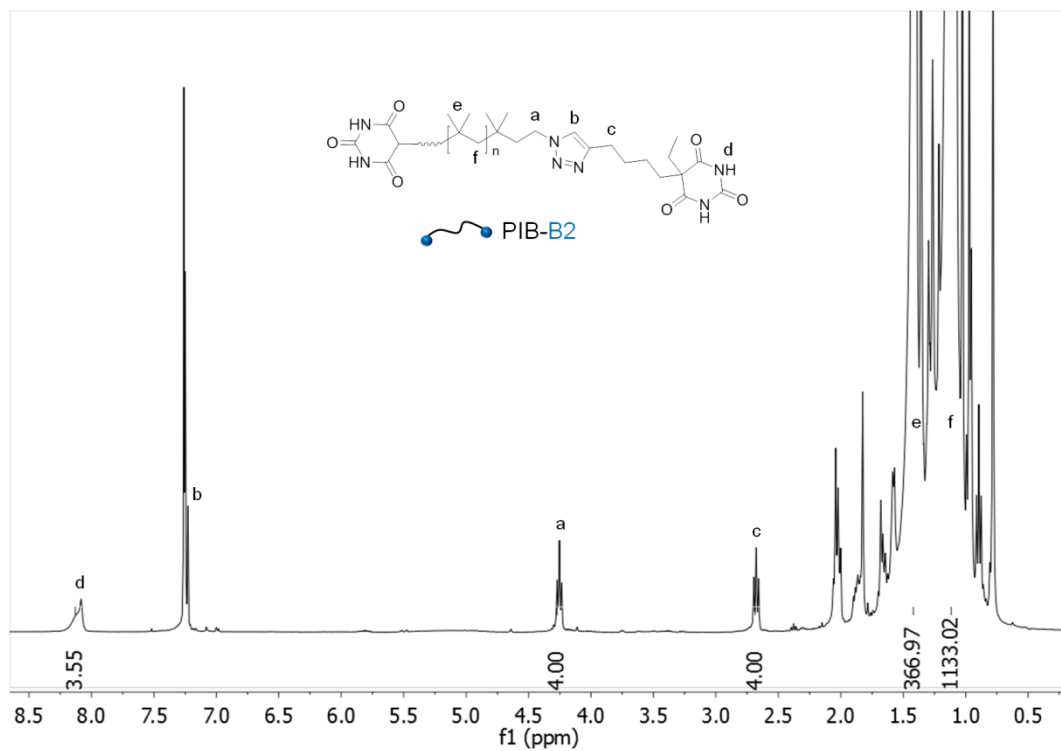


Figure 51: ¹H-NMR spectrum of linear PIB-B2.

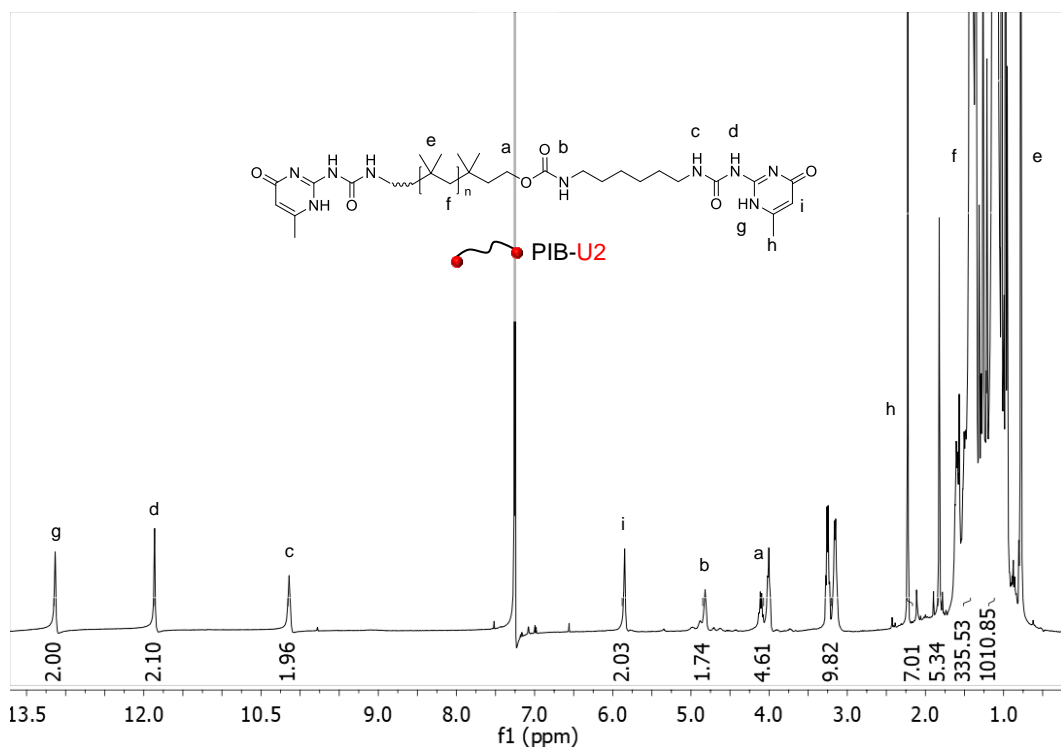


Figure 52: ¹H-NMR spectrum of linear PIB-U2.

The $^1\text{H-NMR}$ of linear PIB-U2 is shown in Figure 52. The new introduced UPy signals are located at 13.1 ppm, 11.9 ppm, 10.1 ppm, 5.8 ppm, 4.8 ppm, 3.2 ppm, 3.1 ppm, 2.2 ppm and 1.8 ppm. The signals can be assigned and the integrals are matching well. The resulting integrals for the PIB signals at 1.4 ppm and 1.1 ppm lead to a molecular weight of $8600 \text{ g}\cdot\text{mol}^{-1}$.

3.4.3 3D-printing window for supramolecular polymers

After confirming the chemical structures of the different supramolecular polymers with $^1\text{H-NMR}$, IR (Appendix 6.14), they were tested for their 3D-printability with the following mentioned 3D-printer. The printing window for the used 3D-printer is set by the nozzle geometry, printing speed and temperature settings. A polymer extrusion printing head of a regenHU 3D-Discovery printer was equipped with a 0.20 or 0.33 mm inner diameter nozzle, impeding a viscosity range of 200 to 2000 Pa·s. The printing window was estimated by temperature-dependent rheology investigations. The viscosity of the printable supramolecular polymers had to suffice both parts of the polymer extrusion head consisting of the heatable storage tank and a heatable screw extruder for a fixed $\Delta\theta = 10 \text{ }^\circ\text{C}$. Due to the construction of the 3D-printer the shear rates of the storage tank ($< 0.1 \text{ s}^{-1}$) and the printing head (0.20 or 0.33 mm inner diameter nozzle, shear rate 14 – 26 s^{-1}) are different, thus determining an area of printability. For rheology measurements the polymer samples were filtered through a Teflon GPC-filter (0.2 μm) and dried in vacuum at 60 - 80 $^\circ\text{C}$ for three days. The rheology experiments were executed on an Anton Paar MCR-101 DSO rheometer using parallel plate-plate geometry with a diameter of 8 mm. The temperature was controlled with a thermoelectric cooler/heater in a chamber filled with dry air. For each measured temperature the sample were preheated for 30 minutes reaching their equilibrium state. For 3D-printing the mandatory measurements of viscosity versus shear rate at different temperatures were performed. Confirmation of the printing window (cross-section of the green and yellow / orange areas) was initially probed with bivalent PEG-400-barbiturate (PEG-400-B2, Figure 53) and bivalent PIB barbiturate (PIB-B2). Subsequently, more complex polymer structures with different molecular architecture (such as three-arm star polymers) were probed, where the expected rheological profile is supposed to be different due to the more round shaped structure. Furthermore, different volume fractions of nano- or microparticles were added, in order to modify the rheological profile during printing and also to address the structural stabilities after printing.

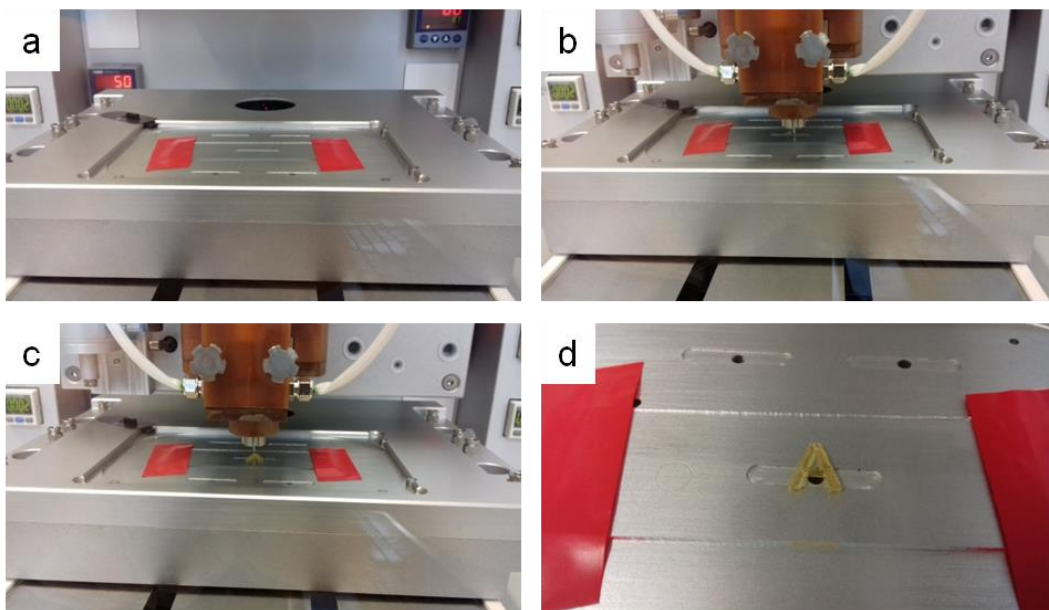


Figure 53. In general, the printing process started with heating up the polymer in the storage tank and modification of printing platform with a microscope glass slide (a). The designed shape was printed in a layer by layer approach in a fused-deposition-modeling method to obtain a three dimensional object (b, c). Model compound PEG_400_Barbi was printed in an A shape with six layers (d).

3.4.4 Melt rheology of the barbiturate-based PIBs

Taking into account the conditions at the printing head (temperature $\vartheta = 30 - 240\text{ }^{\circ}\text{C}$, shear rate $\gamma = 10 - 30\text{ s}^{-1}$, viscosity $\eta = 200 - 2000\text{ Pa}\cdot\text{s}$ and printing speed $v = 1 - 10\text{ mm}\cdot\text{s}^{-1}$) initial melt-rheology measurements were accomplished to evaluate the 3D-printability of the polymers. Most of the polymers and the composites showed viscosities at shear rates located within the printing window. Especially the supramolecular PIB based polymers, which are structurally composed of nano-sized micellar clusters, display excellent printability at the required printing conditions. The viscosity of PIB-B2 dropped from 4500 to 220 Pa·s in the temperature range of 70 to 100 °C, leading to its printability at temperatures around 80 °C with a viscosity of 1800 Pa·s. Low and middle shear rates ($0.1 - 10\text{ s}^{-1}$) did not change the viscosity, but at high shear rates (above 10 s^{-1}) a viscosity drop was observed for temperatures below 90 °C, indicating the reversible rupture of the hydrogen bonds (Figure 54), in line with temperature-dependent IR-measurements of PIB-B2 (Appendix 6.14).

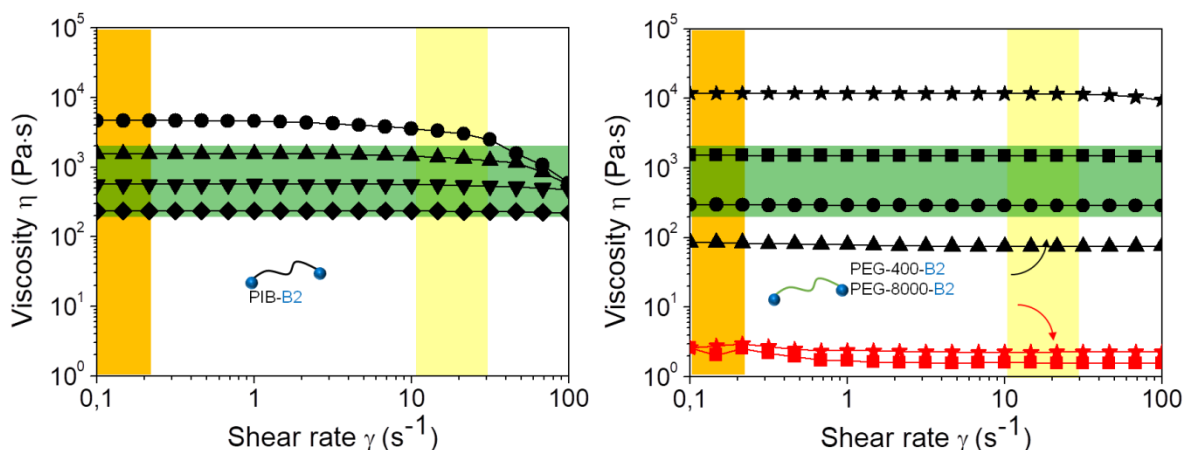


Figure 54. Rheology measurements of PIB-B2 (l.) and PEG-400-B2 (r., black) and PEG-8000-B2 (r., red) showing viscosity versus shear rate at different temperatures.

Based on the consideration that nano-sized particles can change the flow abilities of (supramolecular) polymers, the addition of SNP (5-15 wt%) increased the viscosity of the prepared PIB-B2-SNP composites as well as their form stability after 3D-printing significantly. The shear thinning behavior of these composites is more pronounced for higher shear rates. Secondly, the influence of the polymer architecture on printability was studied. As the three-arm star-polymer, PIB-B3 ($M_n = 16\,000\text{ g}\cdot\text{mol}^{-1}$) could not be printed at temperatures between 30 °C and 180 °C (Figure 55), a polymer blend containing linear PIB-B2 and three-arm star PIB-B3 was prepared in a molar ratio of ~ 3 to 1. Interestingly, this new PIB-B-blend showed rheological properties comparable to PIB-B2 at higher temperatures, indicating excellent printability at a temperature of 120 °C (Figure 55).

3.4.5 Melt rheology of the barbiturate-based PEGs

PEG-400-B2 displayed a viscosity range of around $10^4 - 10^2\text{ Pa}\cdot\text{s}$ within the temperature range from 50 to 80 °C, in which the printing window would be located. However, a shear rate dependence was not observed within the monitored frequency range at all temperatures indicating a liquid like behavior due to the polar nature of the polymer chain and the barbiturate endgroup (Figure 54). Thus, slow spreading after printing at 60 °C was observed and the printed objects lost their original printed shape after one day at room temperature. This result is consistent with the absence of phase segregation and consequently the absence of a dynamic supramolecular network composed of interconnected nano-sized micellar clusters. With increasing molecular weight (PEG-8000-B2) no further improvement of printability was observed, as the polymer was too liquid in the melt with a viscosity of around 2 Pa·s being far below the printable viscosity range.

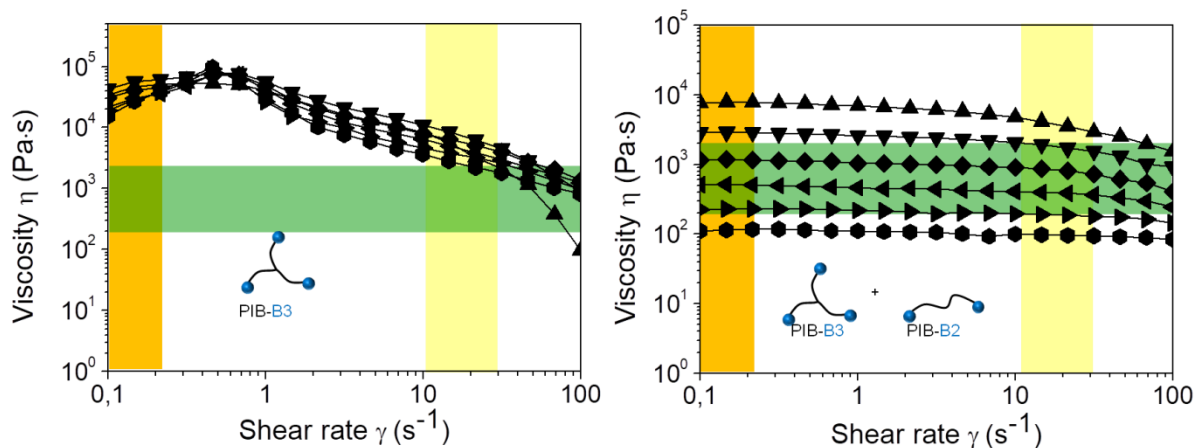


Figure 55. Rheology measurements of PIB-B3 (l.) and PEG-B-blend (r.) showing viscosity versus shear rate at different temperatures.

3.4.6 FDM of the barbiturate polymers

PIB-B2 was printed at 80 °C (Figure 56) and the freshly printed grid of pure PIB-B2 was analyzed *via* SEM and conventional microscopy, proving a polymer strand diameter of around 180 μm and grid gaps of ~300 μm. Compared to the extrusion of filaments described in literature²⁹⁷ (0.2 – 1 mm) improved resolution was achieved. Thus, even better results than with inkjet based printing²⁹⁸ (0.5 – 1 mm) were obtained, since the filigree is lost within drop-based printing methods due to increasing droplet radii while adding more layers of ink. After printing, the structural stability was checked by observation of printed structures at room temperature and it was stopped at a complete shape loss. In line with expectations, the micellar aggregates mediated a certain structural stability after printing and PIB-B2 lost its desired shape after 24 hours at room temperature. At lower temperatures, the structures were more stable and self-supporting due to the slow-down of the dynamics within the reversible supramolecular network structure (Figure 58).

Thus, the printed structures of PIB-B2 showed a large improvement in their shape stability below 5 °C. It should be mentioned that compared to an unmodified PIB polymer with the similar molecular weight of 8 000 g·mol⁻¹, the self-supporting strength was significantly improved by attaching the hydrogen-bonding groups onto the polymers. Whereas unmodified PIB shows a liquid behavior, PIB-B2 possesses gel-like properties indicated by a crossover of G' and G'' and a rubbery plateau. A further method to improve the final strength of the hydrogen bonding-network was the use of silica nanoparticles, which strongly interacted with the barbiturate moieties and less with the hydrophobic PIB-chains. Similar to PIB-B2, the according composites showed a rubbery plateau, while the increase in network strength was clearly indicated. Thus, with increasing SNP content (5 - 15 wt%) the dynamics of the hydrogen-bonding groups was reduced, leading to longer shape stability compared to pure PIB-B2. With increasing SNP

content the viscosity shifted to higher values for fixed temperatures leading to increased temperatures for the printing window.



Figure 56: Supramolecular PIB-B2 was printed in an MLU shape with six layers.

Since PIB-B2 and PIB-B3 contain the same hydrogen-bonding moieties (barbiturates) and PIB-chains, a homogeneous blend (PIB-B-blend) was formed. The PIB-B-blend was printed at 120 °C showing a printing viscosity of $\eta = 200 \text{ Pa}\cdot\text{s}$ and after extrusion with a slower printing speed of $1 \text{ mm}\cdot\text{s}^{-1}$ the rubbery material relaxed to stick on the layers printed beneath. When using a printing needle with a slightly larger diameter (0.33 mm) a "Z"-shape and a grid was printed. The "Z"-PIB-B-blend was set up to a free-standing structure and was checked for its self-supporting strength at room temperature being in proper shape even after ten days (Figure 58). Thus, the strength of the supramolecular network of PIB-B2 was drastically improved by the addition of a specific amount of PIB-B3, presumably due to the presence of more cross-linking points between different clusters as indicated by the observed rheological behavior and the extrusion at higher temperatures.

3.4.7 SAXS of the barbiturate-based polymers

Based on observations in small angle X-ray scattering patterns a polymer network, non-covalently cross-linked by the barbiturate moieties, was observed for pure PIB-B2 as well as for the PIB-B-blend. A practically identical periodicity of about 8.85 nm was found for both samples and the observed structure remains unchanged after printing. The estimated coherence length is about 55 nm. The detected periodicity was compatible with an average distance between neighbored barbiturate moieties considering coiled poly(isobutylene) chains. In line with this interpretation the situation in all these samples is characterized by the existence of barbiturate clusters, which are quite regularly arranged within the poly(isobutylene) matrix. Note that there were seemingly higher order peaks in the SAXS pattern of PIB-B2 samples and the PIB-B-blend at scattering vectors around 1.3 nm^{-1} (Figure 57).

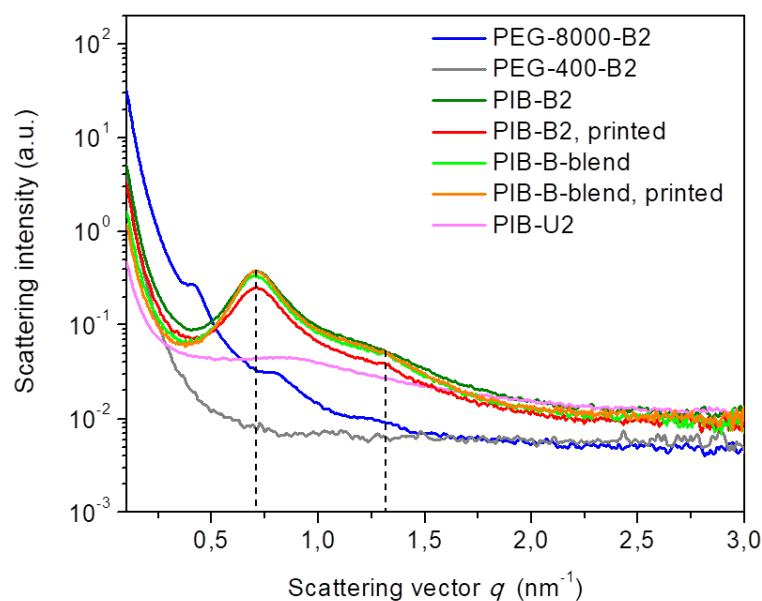


Figure 57: SAXS measurements of the barbiturate polymers and the PIB-B-blend. All PIB-barbiturates show a peak at 0.71 nm^{-1} and about 1.3 nm^{-1} indicating the formation of aggregates.

3.4.8 Conclusion on FDM of supramolecular polymers

Printing of amorphous polymers with low glass transition temperatures was achieved by attaching hydrogen-bonding groups to the end of the polymer chain. Thus, for the first time self-supporting, supramolecular PIB-based polymers were successfully printed and compared to more polar based PEG supramolecular polymers, which did not show a phase separation between polymer chain and the barbiturate moieties. The polar PEGs did not show a good printing behavior and no shape stability compared to the supramolecular PIBs, clearly due to the missing supramolecular cluster (network) formation, and their hygroscopic nature. These supramolecular PIB polymers with linear and star architecture showed a rubber like behavior and were able to form self-supported 3D-printed objects at room temperature, reaching printing resolutions and polymer strand diameters down to $200 - 300 \text{ }\mu\text{m}$, depending on the elasticity of the supramolecular polymers and the according diameter of the needle attached to the printing head. The observed phase segregated structure (micellar aggregates) enabled the tune-ability the printability, with the blends and composites allowing to address both, a proper printability window and self-supporting strength.

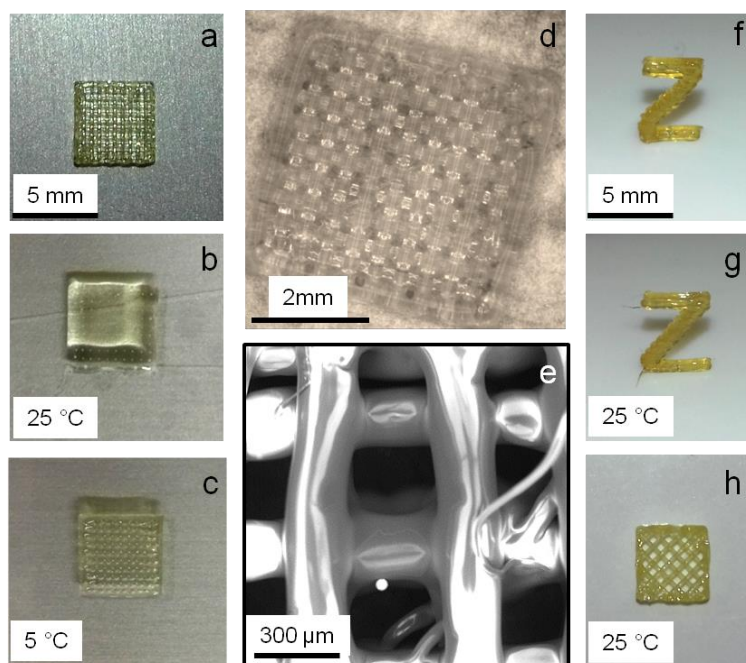


Figure 58: Showcase of 3D printed PIB-B2 in different shapes like a grid (5 mm x 5 mm) and a "Z". The freshly printed grid (a) showed uniform strands and gaps. After 24 hours at room temperature, the grid started to spread (b), but the grid showed good stability stored below 5 °C (c). The microscope image (d) and SEM picture (e) verify the homogeneous strand extrusion. The PIB-B-blend printed "Z" was put up to stand free (f) and after days at room temperature, the Z was still in shape (g). Silica strengthened PIB-B2-SNP10% showed improved shape stability (h).

3.4.9 Synthesis of carbon fillers for supramolecular polymer composites

Since PIB-B2 composites with silica nanoparticles showed positive results for the form stability after FDM, other filler materials based on carbon were tested as well (Figure 59). Therefore, graphene oxide was synthesized from graphite (< 20 μm flakes) and it was chemically reduced in a next step. The main difference between these two materials is the kind and amount of functional groups on the graphene layers.²⁹⁹

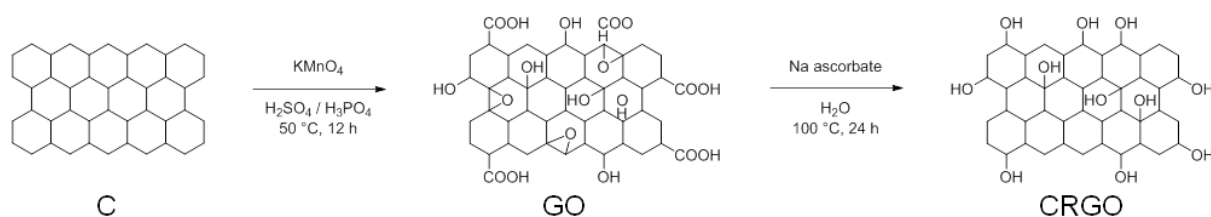


Figure 59. Synthesis of graphene oxide (GO) and chemical reduced GO (CRGO) as filler for supramolecular polymers starting with graphite (20 μm).^{275, 292}

3.4.10 Melt rheology of the carbon-based fillers in PIB-B2

Further rheology measurements based on PIB-B2 composites with different fillers (GO, CRGO) were performed (Table 20). The fillers containing polar groups (hydroxyl, epoxy and carbon acid) were tested to improve the form stability dynamics. The carbon-flakes enriched PIB-B2 composites showed similar behavior in the measurements of viscosity versus shear rate at different temperatures compared to silica composites. With increasing GO content, the viscosities were shifted to higher values as well as a more pronounced shear rate dependence was developed. The viscosity range of PIB-B2 was around 4500 to 220 Pa·s in the temperature range of 70 to 100 °C. PIB-B2-GO5 showed slightly reduced viscosities of 3600 to 200 Pa·s in the same temperature range. When increasing the GO weight% to 10 %, PIB-B2-GO10 changed viscosity to 5700 - 400 Pa·s, while maintaining the same temperature range. By using even more GO, PIB-B2-GO15 resulted in viscosities of around 13000 to 1300 Pa·s. On the other hand showed CRGO a slightly different behavior. PIB-B2-CRGO5 showed slightly reduced viscosities of 4000 to 260 Pa·s in the same temperature range. If 10 wt% CRGO were mixed into PIB-B2, the viscosity changed to 6400 - 600 Pa·s. The PIB-B2-CRGO15 composite was difficult to measure on the rheometer since the sample was pushed out a little bit. The viscosity resulted in low values of 2400 - 640 Pa·s.

Table 20: Carbon-based composites of PIB-B2 for rheology analysis.

Sample	PIB-B2 [mg]	GO / CRGO [mg]	Mass fraction %
PIB-B2-GO5	39.6	2.01	4.83
PIB-B2-GO10	37.8	3.72	8.96
PIB-B2-GO15	32.4	4.96	13.28
PIB-B2-CRGO5	40.2	2.10	4.96
PIB-B2-CRGO10	35.2	3.56	9.19
PIB-B2-CRGO15	33.3	4.99	13.03

3.4.11 Correlation between the relaxation time and the form stability

Based on frequency sweep measurements (Appendix 6.13) and observed structure stability, a correlation between relaxation time of the hydrogen-bonds and form stability was developed (Figure 60, Table 21). Since non-modified PIB showed liquid behavior without a crossover point in the frequency sweep measurement, the relaxation time was set to zero. The relaxation times for PIB-B2 and its composites were calculated based on the values for the reversed crossover points.^{117, 118, 300} The influence of the supramolecular barbiturate endgroups strongly changed the properties of material, now having a relaxation time of 24 seconds and a form stability of one day. By adding trivalent star PIB-B3 to the PIB-B2 the crosslinking density of the barbiturate clusters

increased and so the relaxation time further improved to 91 seconds as well as the form stability to 10+ days. When using silica nanoparticles, the relaxation time end up in the range of 40 – 56 seconds with form stabilities of 2 – 5 days. In the following only composites based on GO and CRGO were analyzed with the frequency sweep and stability conclusions were based on previous results. The addition of GO-flakes (20 μm) increased the performance of the material in huge steps. The relaxation times increased from 32 to 111 seconds with form-stability of 1, 7 and 14 days (for increasing GO content). The use of CRGO flakes (20 μm) did not significant improved the form stability of the composite compared to pure PIB-B2. The relaxation times were calculated to 21 – 35 seconds (Figure 60, Table 21).

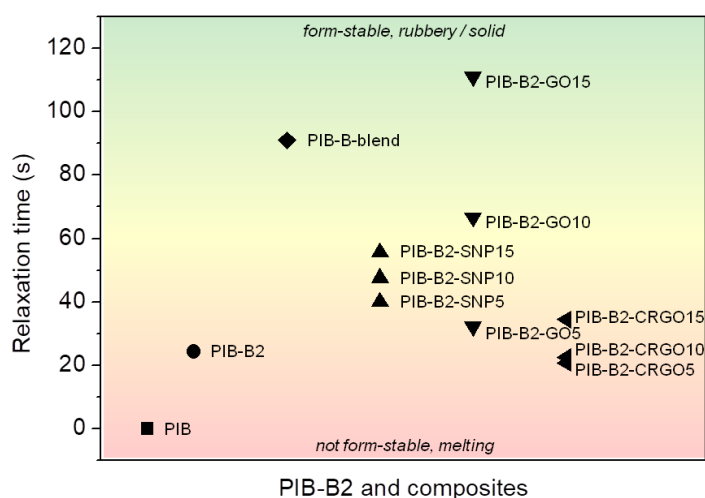


Figure 60. Relaxation time of barbiturate endgroups in PIB-B2 and its composites.

Table 21. Frequency sweep for barbiturate-based PIB polymers and composites at 20 °C.

Sample	Crossover [$\text{rad}\cdot\text{s}^{-1}$]	Relaxation time [s]
PIB	-	-
PIB-B2	0.041	24.4
PIB-B-blend	0.011	90.9
PIB-B2-SNP5	0.025	40.0
PIB-B2-SNP10	0.021	47.6
PIB-B2-SNP15	0.018	55.6
PIB-B2-GO5	0.031	32.3
PIB-B2-GO10	0.015	66.7
PIB-B2-GO15	0.009	111.1
PIB-B2-CRGO5	0.048	20.8
PIB-B2-CRGO10	0.044	22.7
PIB-B2-CRGO15	0.029	34.5

3.4.12 Melt rheology of the ureidopyrimidinone-based PIB

The 3D-printability of the polymer and its composites were analyzed by melt rheology. The obtained knowledge of previous measured polymers, most of them showed viscosities at shear rates located within the printing window. The viscosity of PIB-U2 dropped from 3800 to 400 Pa·s in the temperature range of 80 to 110 °C leading to its printability at temperatures around 100 °C with a viscosity of 800 Pa·s (Figure 61). At low and middle shear rates (0.1 - 10 s⁻¹) no change in viscosity was observed but at high shear rates (above 10 s⁻¹) a viscosity drop was seen for temperatures below 110 °C indicating the reversible rupture of the hydrogen bonds, in line with temperature-dependent IR-measurements of PIB-U2 (Appendix 6.14). Based on the consideration that nano-sized particles can change the flow abilities of (supramolecular) polymers, the addition of SNP (5-15 wt%) increased the viscosity of the prepared PIB-U2-SNP composites as well as their form stability after 3D-printing significantly. The shear thinning behavior of these composites is more pronounced for higher shear rates. With increasing SNP content, the viscosity shifted to higher values for fixed temperatures leading to increased temperatures for the printing window.

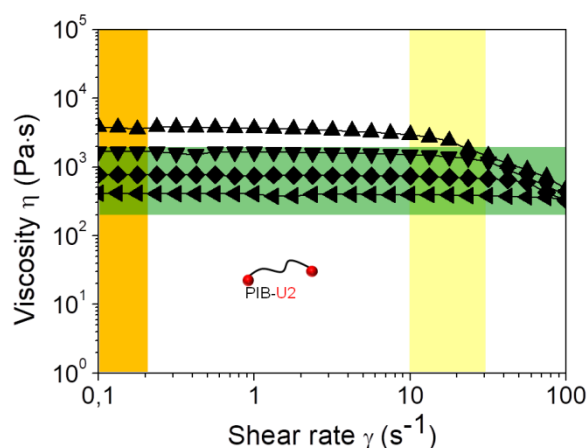


Figure 61. Rheology measurements of PIB-U2 showing viscosity versus shear rate at different temperatures.

3.4.13 FDM of the ureidopyrimidinone-based PIB

PIB-U2 was printed at 100 °C (Figure 62). After printing, the structural stability was checked by observation of printed structures at room temperature and was stopped at a complete shape loss. In line with expectations the micellar aggregates mediated a certain structural stability after printing and PIB-U2 lost its desired shape after 48 hours at room temperature. At lower temperatures, the structures were more stable and self-supporting due to the slow-down of the dynamics within the reversible supramolecular network structure. It should be mentioned, compared to an unmodified PIB polymer with the similar molecular weight of 8 000 g·mol⁻¹, the self-supporting strength was significantly improved by attaching the hydrogen-bonding groups to the polymers.

Whereas unmodified PIB showed a liquid behavior, PIB-U2 possessed gel-like properties, indicated by a crossover of G' and G'' and a rubbery plateau. A further method to improve the final strength of the hydrogen bonding was the use of silica nanoparticles, which strongly interacted with the ureidopyrimidinone moieties and lesser with the hydrophobic PIB-chains. Similar to PIB-U2, the composites showed a rubbery plateau, while the increase in network strength was clearly visible. Thus, with increasing SNP content (5-15 wt%) the dynamics of the hydrogen-bonding groups was reduced, leading to longer shape stability compared to pure PIB-U2.



Figure 62. Supramolecular PIB-U2 was printed in an MLU shape with six layers.

3.4.14 Melt rheology of the carbon-based fillers in PIB-U2

Further rheology measurements based on PIB-U2 composites with different fillers (GO, CRGO) were performed (Table 22). The fillers containing polar groups (hydroxyl, epoxy and carbon acid) were tested to improve the form stability dynamics. The carbon-flakes enriched PIB-U2 composites showed similar behavior of viscosity versus shear rate at different temperatures compared to silica composites. With increasing GO content the viscosities were shifted to higher values as well as a more pronounced shear rate dependence was developed. The viscosity range of PIB-U2 decreased from 3800 to 400 Pa·s in the temperature range of 80 to 110 °C. PIB-U2-GO5 showed increased viscosities of 7000 to 850 Pa·s in the same temperature range. When increased the GO weight% to 10 %, PIB-U2-GO10 changed viscosity to 7500 - 1200 Pa·s, while maintaining the same temperature range. With even more GO was used, PIB-U2-GO15 resulted in viscosities of around 20000 to 2600 Pa·s. On the other hand showed CRGO a slightly different behavior. PIB-U2-CRGO5 raised the viscosities of 7300 to 800 Pa·s in the same temperature range. If 10 wt% CRGO were mixed into PIB-U2, the viscosity has changed to 4200 - 1500 Pa·s. The PIB-B2-CRGO15 composite was very difficult to measure on the rheometer setup because the sample was pushed out. The viscosity resulted in to wrong values of 12400 - 10 Pa·s.

Table 22: Carbon-based composites of PIB-U2 for rheology analysis.

Sample	PIB-U2 [mg]	GO / CRGO [mg]	Mass fraction
PIB-U2-GO5	41.7	2.07	4.73
PIB-U2-GO10	39.9	4.06	9.24
PIB-U2-GO15	27.5	4.17	13.17
PIB-U2-CRGO5	40.1	2.05	4.86
PIB-U2-CRGO10	35.2	3.54	9.14
PIB-U2-CRGO15	31.7	4.80	13.15

3.4.15 Correlation between the relaxation time and the form stability

A correlation between relaxation time of the hydrogen-bonds and form stability was developed (Figure 63, Table 23, Appendix 6.13). Since non-modified PIB showed liquid behavior without a crossover point in the frequency sweep measurement and the relaxation time was set to zero. The relaxation times for PIB-U2 and its composites were calculated based on the values for the reversed crossover points. The influence of the supramolecular ureidopyrimidinone endgroups strongly changed the properties of material, now having a relaxation time of 35 seconds. By using silica nanoparticles, the relaxation time ended up out of range with > 115 seconds with form stabilities of weeks. The following composites based on GO and CRGO were only analyzed with the frequency sweep and stability conclusions were based on previous results. The addition of GO-flakes (20 μm) increased the performance of the material in huge steps. The relaxation times increased to 50 – 111 seconds with form-stability of 5, 10 and 14 days (for increasing GO content). The use of CRGO flakes (20 μm) also did significant improved the form stability of the composite compared to pure PIB-U2. The relaxation times calculated to 67 – 111 seconds for the PIB-U2-CRGO5 respectively PIB-U2-CRGO10. The measuring of PIB-U2-CRGO15 was not possible since the composite was pressed out of the measuring system during frequency sweep analysis.

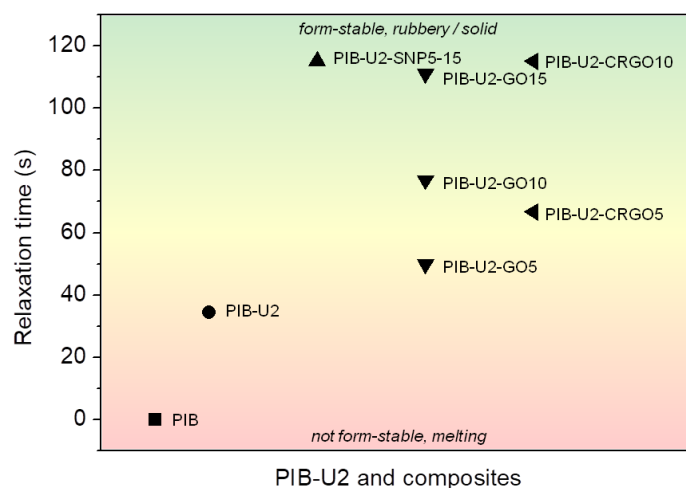


Figure 63. Relaxation time of ureidopyrimidinone endgroups in PIB-U2 and its composites.

Table 23. Frequency sweep for ureidopyrimidinone based PIB polymers and-composites at 20 °C.

Sample	Crossover [$\text{rad}\cdot\text{s}^{-1}$]	Relaxation time [s]
PIB	-	-
PIB-U2	0.029	34.5
PIB-U2-SNP5	< 0.009	> 111.1
PIB-U2-SNP10	< 0.009	> 111.1
PIB-U2-SNP15	<< 0.009	>> 111.1
PIB-U2-GO5	0.020	50.0
PIB-U2-GO10	0.013	76.9
PIB-U2-GO15	0.009	111.1
PIB-U2-CRGO5	0.015	66.7
PIB-U2-CRGO10	< 0.009	> 111.1
PIB-U2-CRGO15	n.d.	n.d

3.4.16 Melt rheology of the tetronic based supramolecular polymers

Another approach was to use commercial available tetronic-3600 as polymer backbone. 4-arm star shaped tetronic polymer (ethylenediamine tetrakis(propoxylate-block-ethoxylate) tetrol) bearing either barbiturate- or ureidopyrimidinone endgroups were tested for their 3D-printability (Figure 64).. Modifications were accomplished *via* functionalized azido-telechelic polymers. Finally using “CuAAC-click”-reactions to completely functionalize the respective chain ends, generating the final Tetronic-B4. The ureidopyrimidinone-moieties were linked as an isocyanate derivate with the hydroxyl-telechelic polymers. The complex $^1\text{H-NMRs}$ of the tetronic polymers can be found in the appendix 6.19.

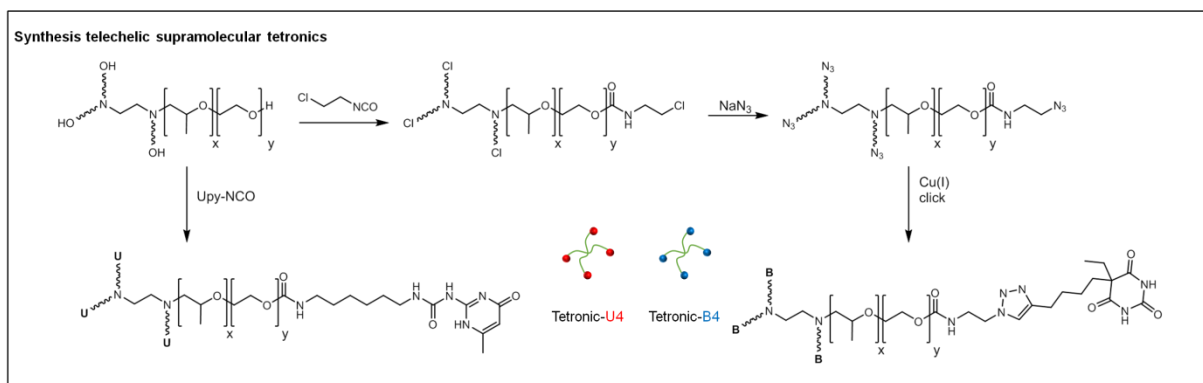


Figure 64. Synthesis scheme for telechelic functionalized polymers based on tetronic-backbone. In multistep reactions hydroxy-functionalized polymers got modified to an azide group and reacted in a “click”-reaction to the barbiturates.

The 3D-printability of the polymers was analyzed by melt rheology and the earlier obtained knowledge (Figure 65). The viscosity of tetronic-B4 dropped from 7800 to 7 Pa·s in the temperature range of 30 to 100 °C leading to its printability at temperatures around 45 °C with a viscosity of 900 Pa·s. At all measured shear rates (0.1 - 100 s⁻¹) no change in viscosity was observed, indicating the same weak supramolecular bonds like PEG-400-B2. The use of ureidopyrimidinone endgroups changed the rheology properties significant. All the viscosities were shear rate dependent leading to viscosity drops while applying higher shear forces. With the printing conditions of the polymer extrusion head being fixed $\Delta\theta = 10$ °C between tank and nozzle tetronic-U4 was not extrudable in a uniform, stable polymer strand. Either the polymer was too viscous to reach the printing nozzle (60 – 70 °C) or too liquid for the extrusion (>80 °C). Both polymers did not result in good printability, as it is too liquid at the shear rate window.

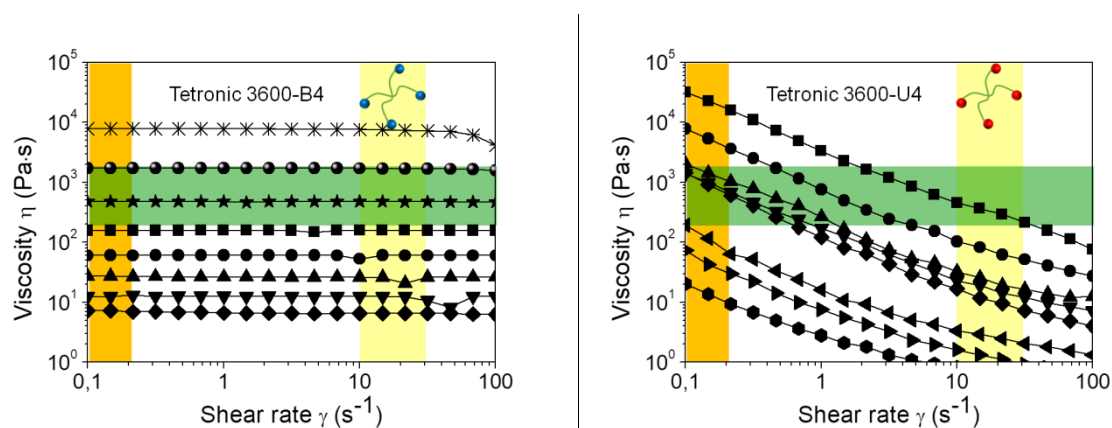


Figure 65. Rheology measurements of Tetronic-B4 (l.) and Tetronic-U4 (r.) showing viscosity versus shear rate at different temperatures.

3.4.17 Thermal stability of the supramolecular polymers

The thermal stability of the pure supramolecular polymers was analyzed under nitrogen atmosphere (40 mL/min) with a heating rate of 10 °C·min⁻¹. All polymers showed no thermal decomposition in the range of the printing temperatures from 45 °C to 100 °C. They showed thermal decomposition between 150 °C and 450 °C (Figure 66). The barbiturate telechelic polymers have a better thermal stability (250+ °C) compared to the ureidopyrimidinone telechelic polymers (150+ °C). Nevertheless all polymers are stable to be printed at the set temperature in the printing head.

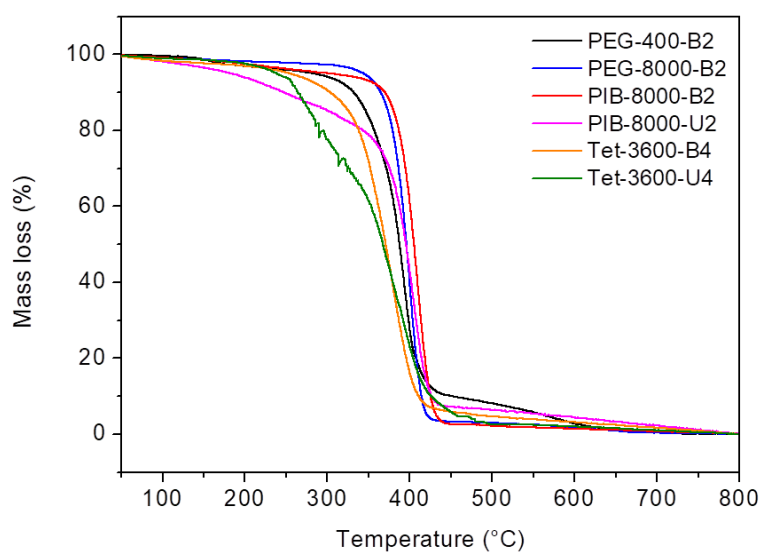


Figure 66: Thermal stability of the supramolecular polymers PEG-400-B2, PEG-8000-B2, PIB-8000-B2, PIB-8000-U2, Tet-3600-B4 and Tet-3600-U4.

3.5 Emulsion / solvent evaporation encapsulation

For the encapsulation of hydrophobic liquids with biodegradable polymers different methods have been developed to synthesize micro- and nano-sized core-shell capsules. Different techniques like solvent evaporation, coacervation, interfacial polymerization or *in-situ* polymerization were used in the past. The solvent evaporation technique was used in this work due to its simply and cheap processing as well as scalability for capsule size and overall amount of material masses (Table 24).

Table 24. Core-shell encapsulation of various polymers and hydrophobic liquids synthesized in this work.

Capsule Shell	Core	Surfactant	R_h (nm)	Wt% core	Encapsulation Efficiency	Freeze dry
<i>Polymer</i>	<i>Oil</i>			50 %	100 %	
PLLA	Triazide	SDS	100 ± 12	46 %	92 %	Powder
PLLA	Trialkyne	SDS	131 ± 16	48 %	96 %	Sticky
PLLA	BEPE	SDS	114 ± 10	49 %	98%	Sticky
PLLA	Farnesol	SDS	101 ± 10	39 %	78 %	Powder
PLLA	Limonene	SDS	92 ± 13	-	-	Powder
PLLA	Linalool	SDS	104 ± 11	21 %	42 %	Powder
PVF	Trialkyne	SDS				Sticky
PVF	Triazide	SDS	104 ± 15	45 %	90 %	Powder
PVF	Triazide + Coumarin	SDS	108 ± 14	46 %	90 % + 78 %	Powder
PCL	Farnesol	SDS	106 ± 12	49 %	98 %	Sticky
PCL	Limonene	SDS	117 ± 10	-	-	Sticky
PCL	Linalool	SDS	103 ± 12	2 %	4 %	Sticky
PCL	Hexadecane	SDS	115 ± 11	49 %	98 %	Sticky
PLLA	MCT	SDS	84 ± 11	35 %	70 %	Powder
PCL	MCT	SDS	109 ± 17	50 %	100 %	Sticky
PLLA	MCT	PVA	150 ± 15	n.d.	n.d.	Cake
PCL	MCT	PVA	165 ± 20	n.d.	n.d.	Cake

2 min sonication with 90% amplitude.

In general encapsulation by solvent evaporation was used to synthesize core-shell capsules with either solid or liquid core filling. Depending on the used polymers and liquid fillings different states of capsules were created. Depending on polymeric properties like degree of crystallinity or amorphous properties as well as molecular weight, the encapsulation of liquids formed non-, meta- or stable nanocapsules. Poly(L-lactide) nanocapsules generated most of the time stable and powder-like material after freeze drying. Exceptions for this trend were the used alkyne compounds leading to a sticky polymer film after freeze-dry. These meta-stable nanocapsules were formed during the solvent evaporation encapsulation process in an aqueous medium. After the synthesis and in aqueous medium the capsules were stable, proven by later by DLS and TEM. The nanocapsules did not survive a normal drying or the more gently freeze drying method. The removing of the aqueous phase led to a sticky polymer film with a fibrous polymer structures. With poly(ϵ -caprolactone) the same problem occurred for all samples. PCL nanocapsules were only meta-stable in aqueous solution after synthesis. Conventional drying and freeze drying resulted in polymer films without core shell capsules. The very low glass transition temperature of PCL ($T_g = -60$ °C) probably resulted in a relative weak and still "flowing" capsule shell, which did not resist the harsh conditions of drying. The amorphous polymer polyvinyl formal showed similar encapsulation behavior like PLLA.

The meta-stable capsules were stabilized by the use of a polyvinyl alcohol aqueous solution acting as surfactant solution for the emulsion and as a protecting foam after freeze drying. The PVA polymers attached themselves to formed nanocapsules in aqueous solution and separated individual nanocapsules from each other. This technique was used for the PLLA-Triglyceride nanocapsules as well for some PCL nanocapsules.

3.5.1 Scanning electron microscopy (SEM)

Freeze-dried samples of the core-shell capsules were analyzed with an electron microscope to obtain a detailed view of the shape, surface and size. In general, the textures of the samples already let assume that there are capsules or not. For the three fine powdered, fluffy PLLA samples (Farnesol, Limonene, Linalool) a spherical capsule shell shape could be obtained (Figure 67). The PLLA capsules showed a low size distribution with rare exceptions of larger capsules (> 500 nm) confirming the results of DLS measurements. The crystallinity of PLLA and the high glass transition temperature (55 °C) support the formation of stable, hard shells. The capsule sizes for DLS and SEM measurements were in the same size region with a value shift for the DLS measurements of around 50 nm (Figure 68). The increased diameters in liquid media were related to swelling of the PLLA shell as well as attached surfactants to the surface. The freeze-dried samples shrank in diameter size due to drying of the shell material and probably partly lose of liquid core material for the liquids with lower boiling points. The PLLA-Farnesol capsules showed very similar sizes with a maxima difference of ~30 nm, while

both distributions were quite symmetric. The PLLA-Limonene and PLLA-Linalool capsules were a little bit more shifted with a maxima difference of around ~ 70 nm. The partially lose of the liquid filling, evaluated by NMR, and the already discussed factors were the factor for the larger difference. Both distributions were quite symmetric led to the conclusion of a good encapsulation technique with a small size distribution.

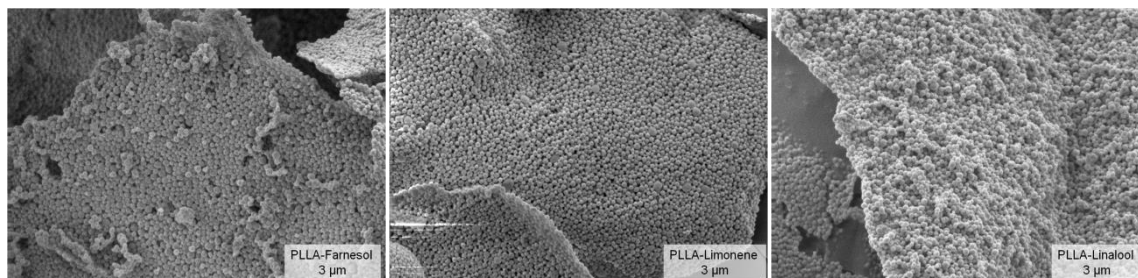


Figure 67. SEM images of PLLA capsules with different liquid filling (farnesol, limonene, linalool), after freeze-drying. In all images sphere-shaped capsules with a size around 100 nm (radii) were observed.

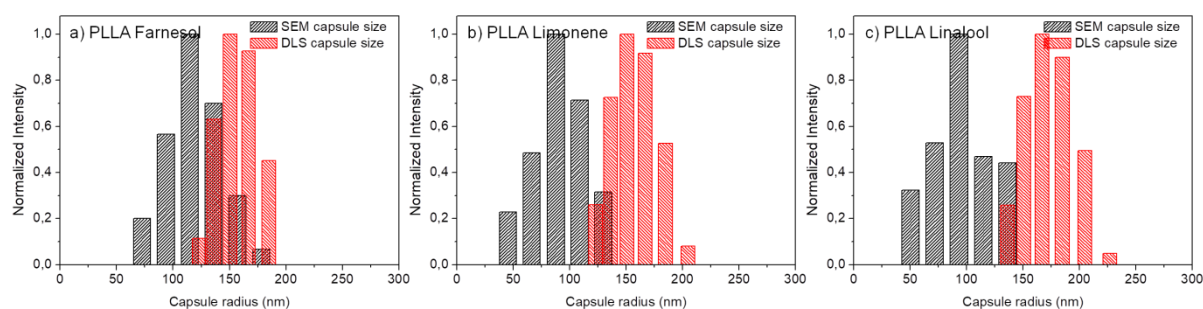


Figure 68. Size comparison (radii) of core shell PLLA capsules between SEM- and DLS-measurements. The sizes are in the same range with slightly bigger sizes in DLS-solution.

On the other hand the PCL samples resulted in different sticky, fibrous layers after freeze-drying. The results were confirmed by SEM measurements showing large structures of different shapes (Figure 69). Small nanocapsules, like in the case of PLLA, were not visible leading to the conclusion that they did not survived the freeze-dry process. PCL has a similar crystallinity as PLLA, but a much lower glass transition temperature (-60 °C), while water freezes at 0 °C. The formation of water crystals probably destroyed the shell of the nanocapsules during freezing. The ruptured PCL-material agglomerated to large fibrous layers after freeze-drying.

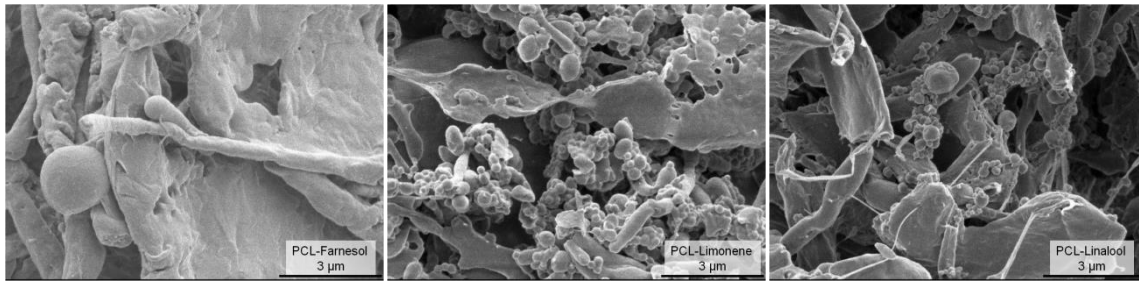


Figure 69. SEM images of PCL capsules with different liquid filling (farnesol, limonene, linalool), after freeze-drying. Unfortunately, no sphere-shaped nanocapsules could be obtained in a dry state.

The reactive compounds (trivalent alkyne and trivalent azide) were tried to get encapsulated into PLLA and PVF (Figure 70). The experiments with the trivalent alkyne led to similar results like the synthesis of PCL capsules. After freeze-drying, sticky, fibrous polymer layers were formed. In the SEM images no capsule structures were visible. The encapsulation of the trivalent azide showed better results and after freeze-drying it was a fluffy, slightly sticky powder. In the electron microscope images non-spherical capsules were visible. Nevertheless, they could be seen as individual capsules and could be easily mixed into composite materials.

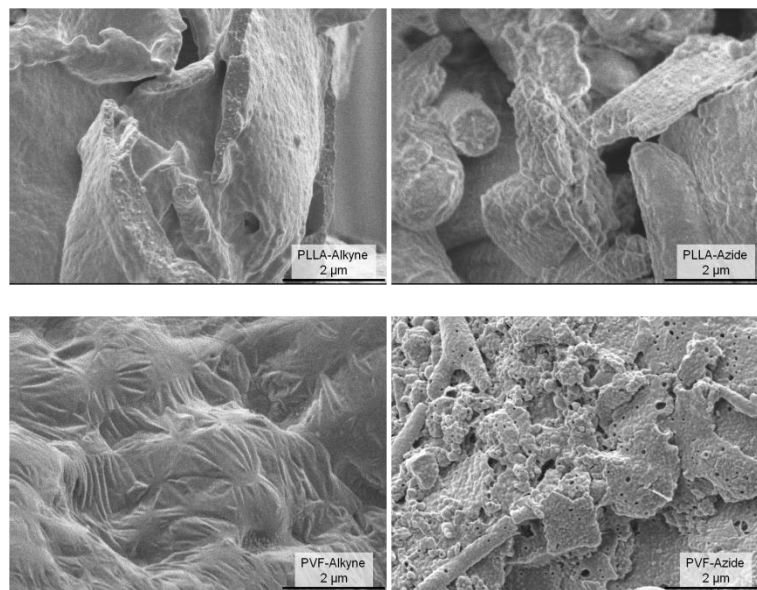


Figure 70. SEM images of PLLA / PVF capsules with different reactive, liquid filling (triazide, trialkyne), after freeze-drying. The encapsulation of alkyne did not lead to any kind of nanocapsules. On the other hand the azide containing capsules were strongly agglomerated after freeze-drying.

3.5.2 Transmission electron microscopy (TEM)

Diluted solutions of the finished nanocapsule suspension were measured in TEM. In the case of PLLA capsules (farnesol, limonene, linalool) dark capsules were found. The capsules core-shell structure was not visible may due to the relative large ratio of shell material (shell / core 1:1)(Figure 71).

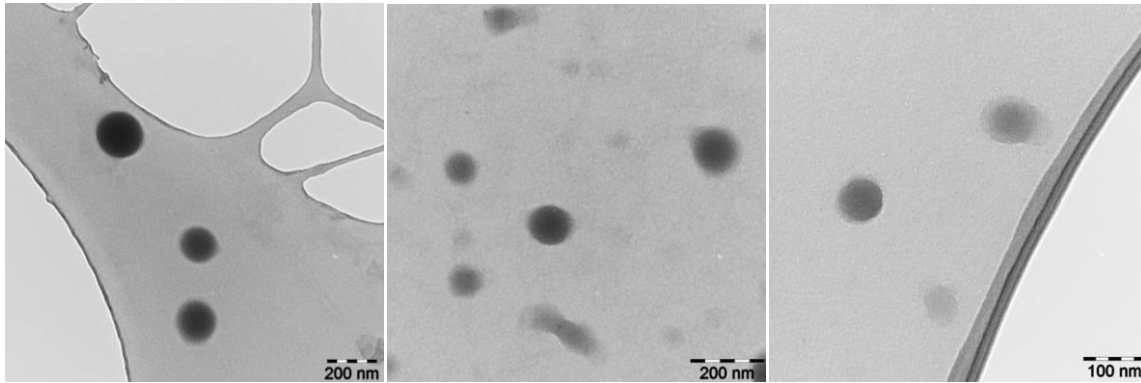


Figure 71. TEM images of PLLA capsules with different liquid filling (farnesol, limonene, linalool) of a diluted solution, after synthesis. In all images sphere-shaped capsules with a size lower than 100 nm were observed.

The weak shell of PCL nanocapsules led to larger capsules being much lighter in TEM pictures than PLLA capsules. The phenomenon could be explained due to flattening of the capsules on top of the TEM-grid. The measured radii were to large radii compared to DLS results (Figure 72).

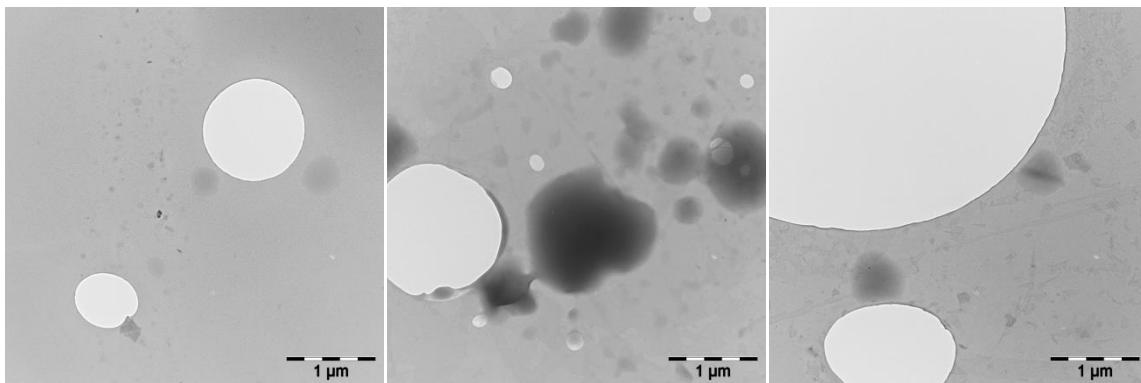


Figure 72. TEM images of PCL capsules with different liquid filling (farnesol, limonene, linalool) of a diluted solution, after synthesis. In all images relative large, flatten shapes with a size 200-500 nm were observed, leading to a weak capsule shell.

3.5.3 Influence of different parameters on the nanocapsules

With a model system of PCL and *n*-hexadecane the influence of some important system parameters were analyzed in an aqueous solution directly after synthesis. In the standard system the following parameters were used:

100 mg oil, 100 mg polymer, 2 mL DCM, 10 mL aqueous surfactant, 2 min sonication time with 30 pulse and 15 pause, 90 % amplitude

The variation in sonication duration showed a strong influence in term of average capsule size and broadness of capsule size distribution. With increasing sonication time from 30 to 120 second the capsule size reduced from 150 ± 40 nm down to 110 ± 20 nm. The increase in sonication time had an influence on the nano-scaled emulsion (Figure 73a) because the formed oil droplets get smaller and more uniform in size with elapsing time. Due to stabilization with surfactants the small droplets were not agglomerated and formed nanocapsules after evaporation of DCM. The influence of the SDS solution concentration with constant volume showed no relevant change in capsule size of around 115 ± 30 nm for all concentration between $0.1 \text{ mg}\cdot\text{mL}^{-1}$ and $1 \text{ mg}\cdot\text{mL}^{-1}$ (Figure 73b). All used SDS concentrations were below the CMC of SDS (8.2 mM, $2.36 \text{ mg}\cdot\text{mL}^{-1}$). The experiments for scaling up the encapsulation process in volume resulted in similar and slightly smaller capsules due to an increase of sonication time for compensations of a larger volume while using the same sonication device (Figure 73c). With increasing oil content, while keeping the amount of capsule mass (200 mg) and the total volume constant, the capsule size increased as well. The lowest volume ratio of 0.2 led to 110 ± 20 nm sized nanocapsules and the largest volume ratio 0.7 resulted in 140 ± 40 nm (Figure 73d). The variation of the amplitude had a small effect on capsule size and size distribution, but a slight increase in capsule size with higher amplitude can be observed (Figure 73e). A big influence on the capsule size had the used amount of capsule material in the DCM phase. At low concentrations smaller capsules are formed. With more material the sizes increased and reached a plateau while adding more material (Figure 73f).

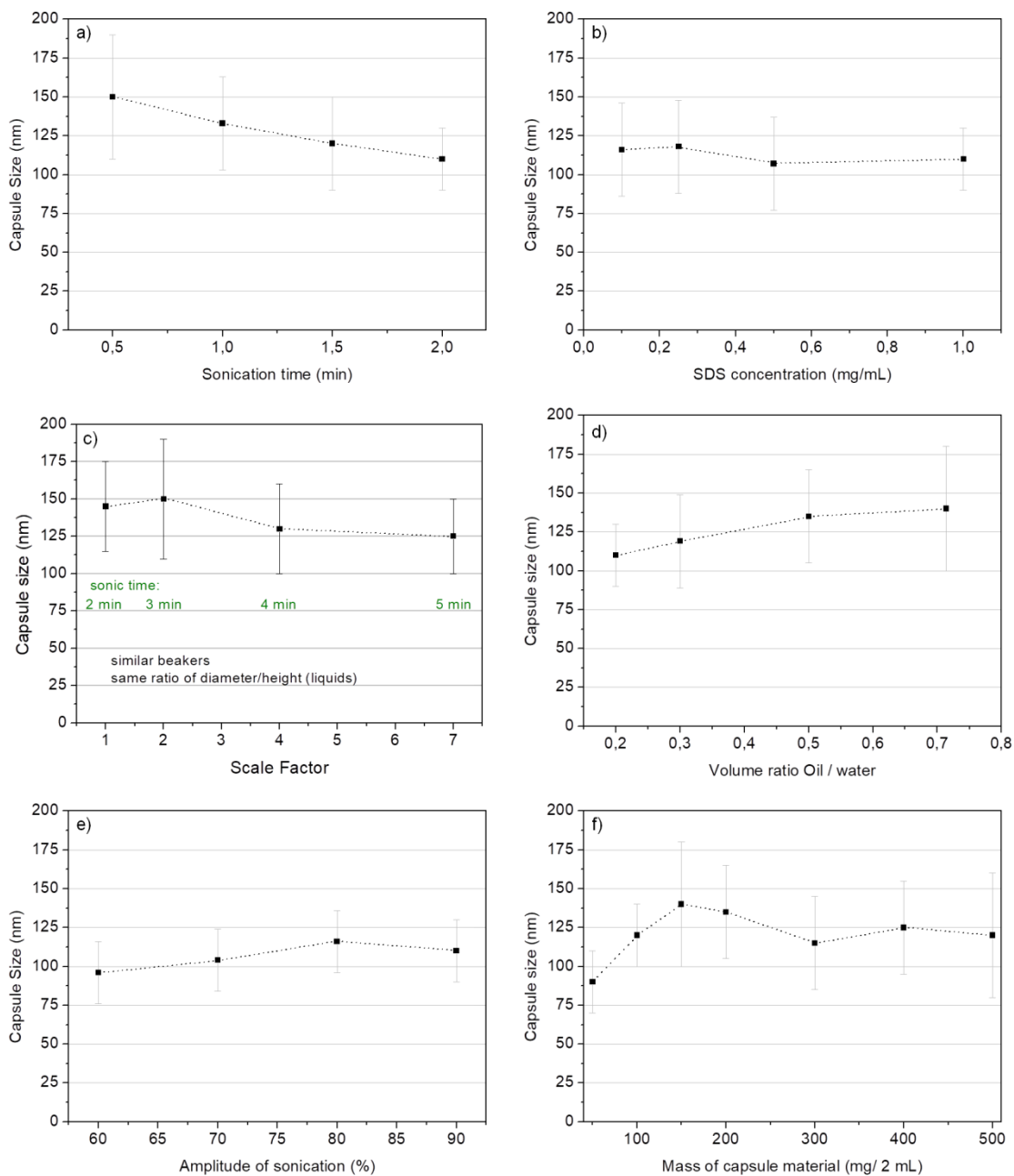


Figure 73. Influence of system parameters on the nanocapsule size and distribution: a) Variation of sonication time, b) surfactant concentration, c) up-scaling the encapsulation, d) volume ratio between oil / water, e) sonication amplitude and f) capsule material concentration.

3.5.4 Encapsulation efficiency

The encapsulation efficiency for the synthesized capsules describes the ratio of core to shell as well as the encapsulation yield of the liquid core. In theory, ideal synthesized capsules contained of 50 % core ad 50 % shell material. After freeze-drying the core-shell capsules were dissolved in CDCl_3 . The concentration was set of around $43 \text{ mg}\cdot\text{mL}^{-1}$ and the standard toluene ($10 \text{ }\mu\text{L}$, $12.4 \text{ mg}\cdot\text{mL}^{-1}$) was added. The ratio between the

integral values of toluene and the resulting integral values of the liquid filling were used to calculate the core and shell ratio (Table 25, Figure 74). The integral values were normalized to get a molar ratio between toluene and liquid filling. The molar ratio was transferred into mass fraction between both components. Due to the known mass values of added materials, the real masses could be determined and in hence the core shell ratio, too. The example capsules of PLLA_Triazide (35.08 mg) had a ratio of 46 % core liquid (16.14 mg, triazide) and 54 % shell material (18.94 mg, PLLA). The encapsulation efficiency of triazide in PLLA capsules was 92 % of the initially used amount. Reasons for low core content respectively low encapsulation efficiency in other core shell combinations could be the relative low boiling of some liquid components (farnesol 284 °C, limonene 176 °C, linalool 198 °C) connected with a partially evaporating during synthesis or the freeze-dry process.

Table 25. Encapsulation efficiency calculation based on the example PLLA_Triazide.

Compound	Hydrogen atoms	Integral value	Normalized value (mol)	Molar mass	Mass	Mass fraction	Real Mass
Toluene	3	3	1	92.14	92.14	0.35	8.7
Triazide	3	0.92	0.31	557.56	170.99	0.65	16.14
Capsules	-	-	-	-	-	-	35.08

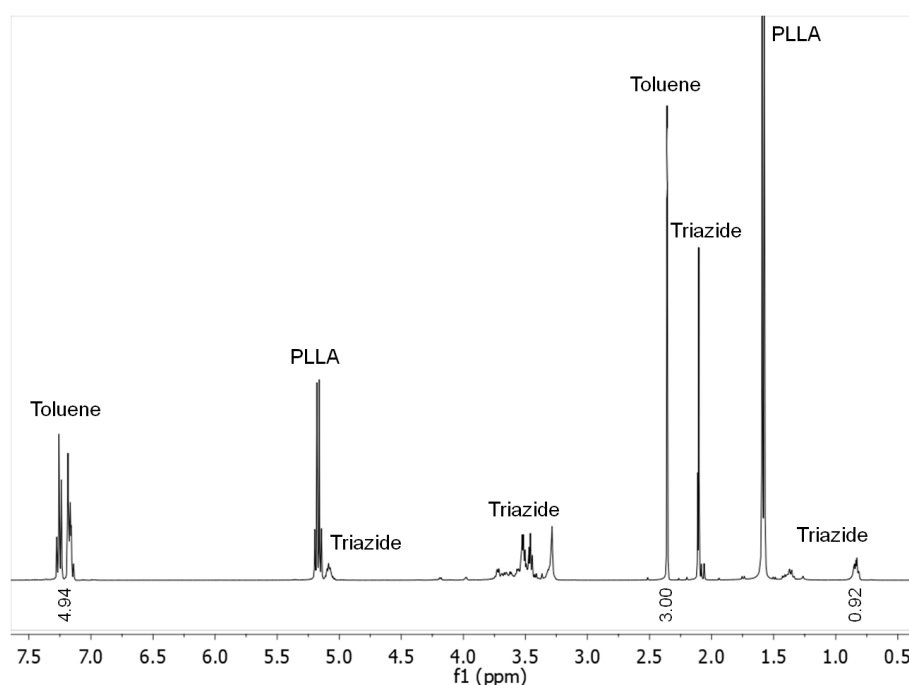


Figure 74. 1H-NMR of core shell capsules (PLLA_Triazide) with toluene as a calculation standard.

The same method has been used for the most synthesized nanocapsules. In literature commonly encapsulation efficiencies of 10 – 90 % were reported.^{207, 217} Depending on various factors encapsulation efficiencies up to ~98 % for well shaped core-shell nanocapsules were reached. The here synthesized nanocapsules were in the same size range and size distribution, regardless the used polymers or oils.

3.5.5 Fluorescence of capsule suspensions

For detection application fluorescence active, hydrophobic polymer dyes were encapsulated together with medium-chain triglycerides (MCT), (Table 26). For the solvent-evaporation encapsulation PLLA (40k Da, 100 mg), Triglycerides (100 mg) and fluorescence dyes (15, 30, 50, 60, 150, 300 µg) were mixed. The samples with 50 µg dyes were freeze-dried together with the PVA-solution. Samples made in SDS-solution could not be freeze-dried because the capsules seemed to be soft and needed a supporting structure after freeze-drying.^{207, 281}

Table 26. DLS results for core-shell encapsulation of MCT together with fluorescence polymers (PF8BT, CN-PPV, PCPDTBT).

Capsules	Dye	Surfactant	Sonication	R_h (nm)	D_h (nm)
PLLA MCT	PF8BT	PVA	5 min	143 ± 21	
PLLA MCT	CN-PPV			155 ± 24	ca. 300
PLLA MCT	PCPDTBT			150 ± 27	
PLLA MCT	PF8BT	SDS	5 min	84 ± 12	
PLLA MCT	CN-PPV			76 ± 11	ca. 160
PLLA MCT	PCPDTBT			80 ± 14	

Nanocapsules synthesized with PVA-solution had a diameter of ca. 300 nm and synthesized with SDS-solution, a diameter of ca. 160 nm. All capsules showed a symmetric particle size distribution in DLS measurements. When freeze-drying the capsules with PVA-solution, the produced cake consists of the PLLA capsules distributed in a PVA matrix. The PVA coated all capsules and separated them from each other, consequently there is less agglomeration taking place. Due to the water solubility of PVA the capsules could be re-dispersed in water again.

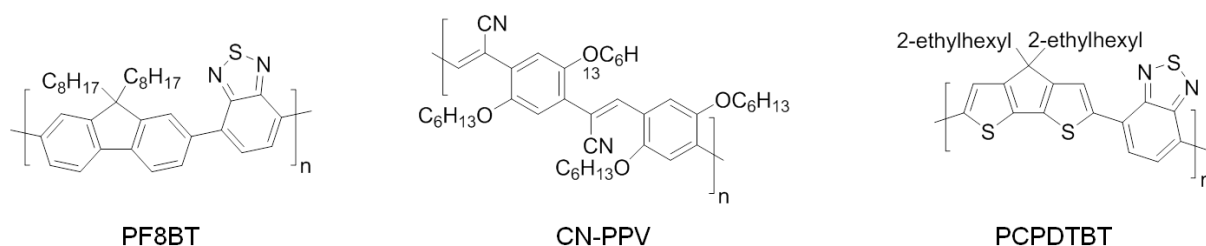


Figure 75. Fluorescence active polymers for the encapsulation together with MCT into PLLA.

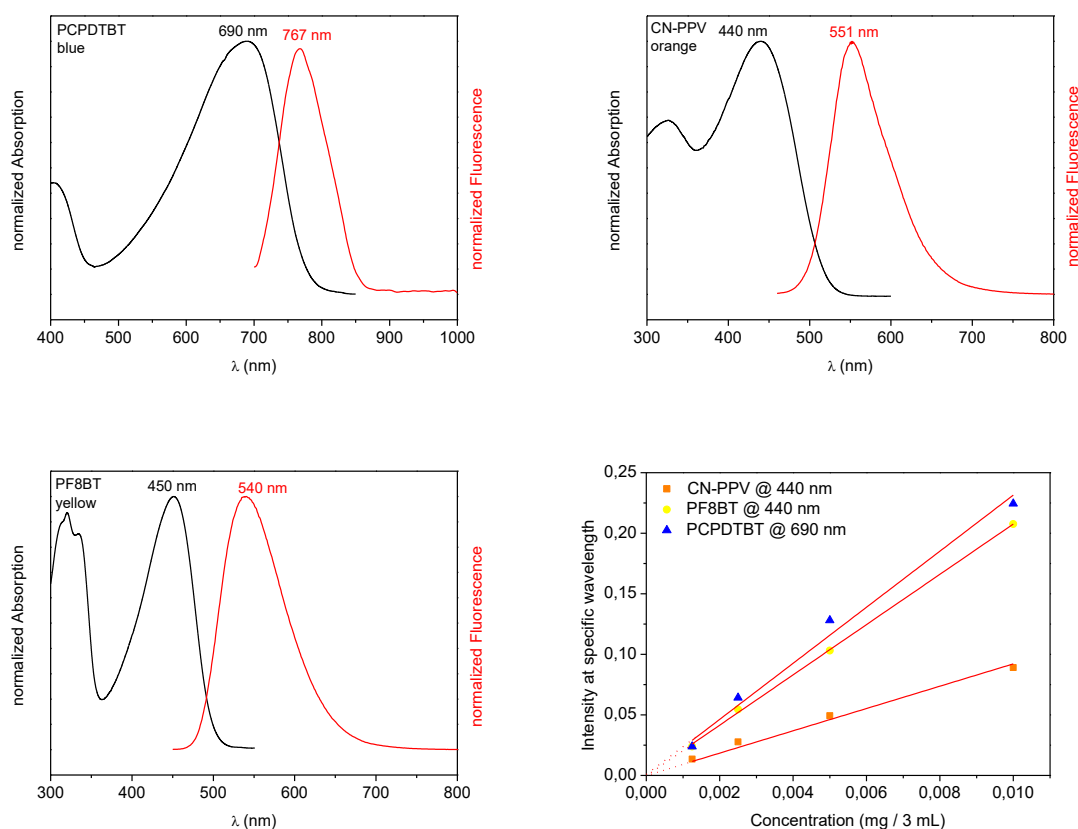


Figure 76. Absorption- and fluorescence measurements in CHCl_3 for the pure fluorescence polymers (PCPDTBT, CN-PPV, PF8BT), as well as a calibration curve (at maxima absorption) for dye content determination.

The absorption and fluorescence spectra of the polymer dyes PF8BT³⁰¹, CN-PPV³⁰² and PCPDTBT³⁰³ were measured in 3 mL CHCl_3 (Figure 75, Figure 76). The yellow PF8BT is showing two absorption maxima at 230 nm and 450 nm and a fluorescence maximum at 540 nm. CN-PPV, which was orange in color, was absorbing at 440 nm and emitted fluorescence at 551 nm. The NIR-fluorescence dye PCPDTBT was absorbing light at 690 nm and showed a fluorescence emission at 767 nm. These polymer dyes were normally used in organic solar cells as a polymer acceptor.³⁰⁴ In this study these dyes were encapsulated into biological compatible nanocapsules for visualizing application in

an aqueous dispersed medium. Normally, indocyanine green (ICG) was used in aqueous medium³⁰⁵⁻³⁰⁷. The calibration curves for all three polymers were measured in CHCl₃ as well. Based on the linear fits three dye content equations could be determined (Figure 76).

$$\text{Amount dye (mg)} = \frac{I_{max}}{K}$$

I_{max} ... Absorption intensity at maximum wavelength

K ... Calibration constant, determined with the linear fit

$$K_{PF8BT} = 20.763$$

$$| K_{CN-PPV} = 9.213$$

$$| K_{PCPDTBT} = 23.152$$

In this case specific amounts (ca. 35 mg) of freeze-dried PVA coated capsules were grinded in a mortar. The residues were extracted with CHCl₃ (3x1 mL) and the absorption was measured in CHCl₃. With the calibration equations the extracted amount of dye was calculated for the nanocapsules with 50 µg of dye content. The dye encapsulation efficiencies were around 95 – 99 %. Nearly the whole amount of added hydrophobic, fluorescence polymer was encapsulated as part of the nanocapsules. Detailed conclusions of the exact location inside the nanocapsules could not be made. Because several attempts with confocal laser scanning microscopy did not lead to a clear picture of the nanocapsules. Based on the nature of the polymer dyes they could be dissolved in the MCT-core or they could be part of the PLLA shell (Table 27).

Table 27. Encapsulated dye content determination by absorption calibration curves.

Dye	Mass (mg)	Measured amount dye (µg)	Theo. amount dye (µg)	Encapsulation dye (%)
PF8BT	36.40	~ 6.0	6.1	~ 98.4
CN-PPV	37.07	~ 6.0	6.2	~ 96.8
PCPDTBT	25.33	~ 4.0	4.2	~ 95.2
Theoretically	300.00	50.0	50.0	100.0

Table 28: Concentration series of fluorescence active capsules.

Amount Dye (µg)	Wt%	PLLA (mg)	MCT (mg)	PVA (mg)	Water (mL)
300	0.1	100	100	100	10
150	0.05	100	100	100	10
60	0.02	100	100	100	10
30	0.01	100	100	100	10
15	0.005	100	100	100	10

The synthesized nanocapsules suspensions were refilled with water to 10 mL and the fluorescence was measured directly. Despite the cloudiness some good fluorescence spectra could be measured (Table 28, Figure 77). The yellow dye PF8BT ($\lambda_{\text{ex}} = 450 \text{ nm}$) showed a fluorescence maximum from 538 nm to 545 nm and was in good agreement with the measured maximum of the pure dye in CHCl_3 at 540 nm. With increasing amount of PF8BT the fluorescence intensity was increasing as well, from 350 to 1000 counts (Figure 78). The orange dye CN-PPV ($\lambda_{\text{ex}} = 440 \text{ nm}$) emitted fluorescence in the area between 548 nm and 584 nm. The pure dye solution in CHCl_3 showed a maximum of the fluorescence at 551 nm. With increasing amount of orange marker the fluorescence increased up to 0.02 wt%. Further increase of dye led to a decrease of fluorescence intensity (Figure 79). Finally, the blue dye PCPDTBT ($\lambda_{\text{ex}} = 690 \text{ nm}$) was showing a very weak fluorescence in the range from 754 nm to 761 nm. When using more than 0.01 wt% of blue dye a decrease of fluorescence intensity was clearly visible (Figure 80). PCPDTBT was known for its self-quenching properties due to polymer chain agglomeration in literature.³⁰⁸



Figure 77. PLLA_MCT capsules with increasing amount of PF8BT (yellow), CN-PPV (orange) and PCPDTBT (blue).

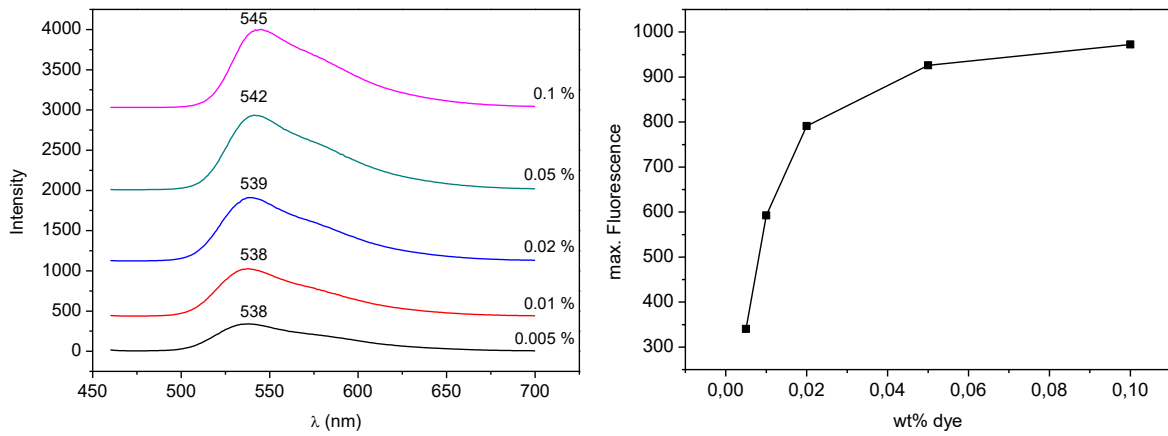


Figure 78. Fluorescence measurements for PLLA_MCT_PF8BT capsules (0.005 – 0.1 wt% dye).

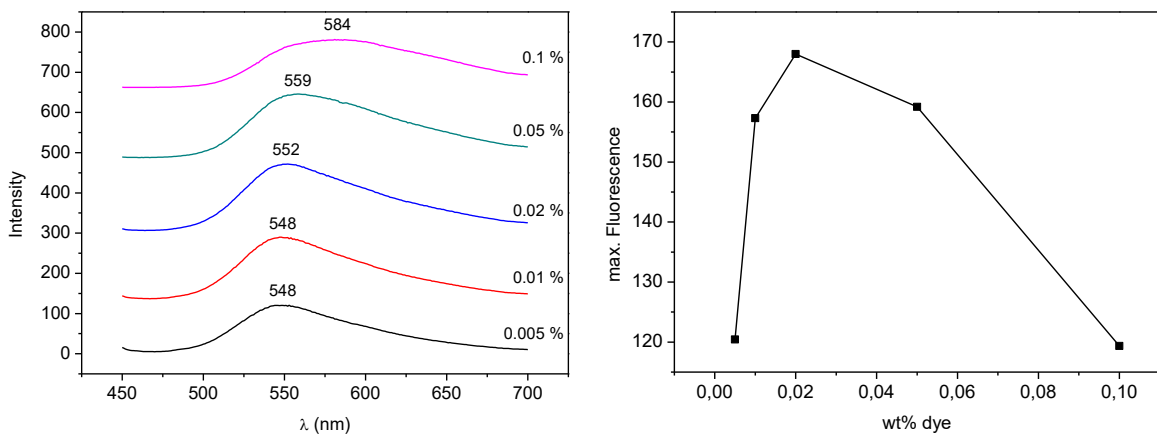


Figure 79. Fluorescence measurements for PLLA_MCT_CN-PPV capsules (0.005 – 0.1 wt% dye).

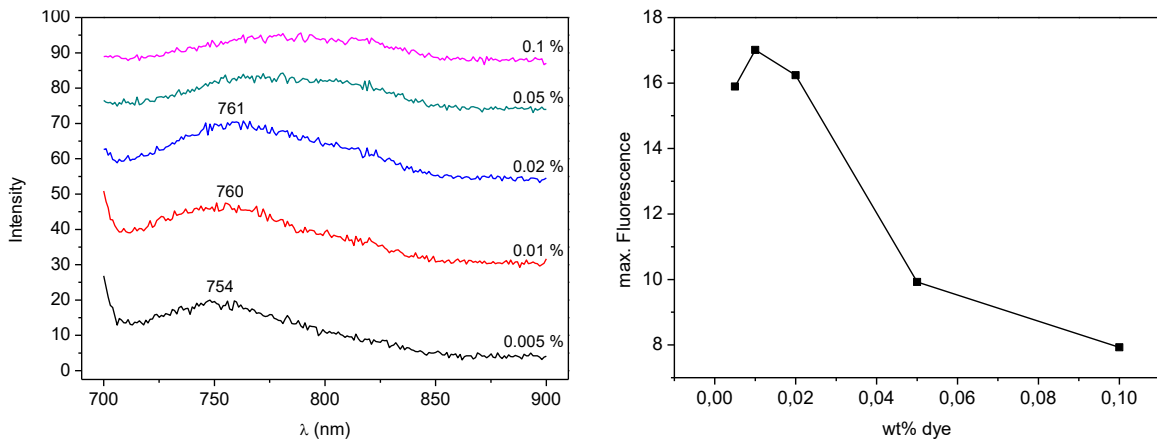


Figure 80. Fluorescence measurements for PLLA_MCT_PCPDTBT capsules (0.005 – 0.1 wt% dye).

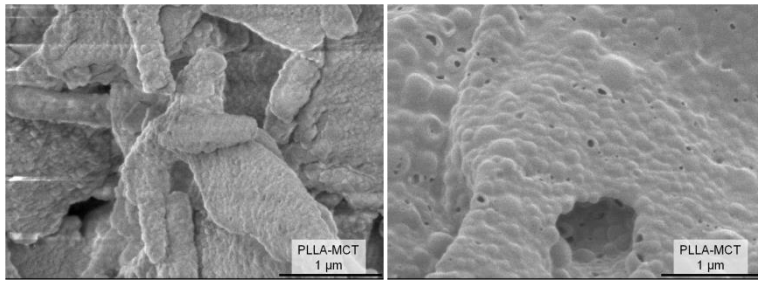


Figure 81. SEM images of PLLA_MCT capsules based on SDS-solution (l.) and PVA-solution (r.).

Freeze-dried samples of the PLLA_MCT capsules were analyzed with an electron microscope to obtain a detailed view of the shape, surface and size (Figure 81). The smaller capsules made with SDS-solution seemed to agglomerate strongly and lose their spherical shape. The picture of the capsules made with PVA-solution was more difficult to interpret because the freeze-dried PVA cake was coating the capsules. A sponge like cake was formed by the PVA-capsule mixture. Nevertheless, capsules could be guessed to be inside the PVA cake as well as being separated from each other within the PVA. The PVA coating should improve the stability and long term storage properties of the freeze-dried samples. Based on water soluble PVA coating a re-dispersion in water was possible.

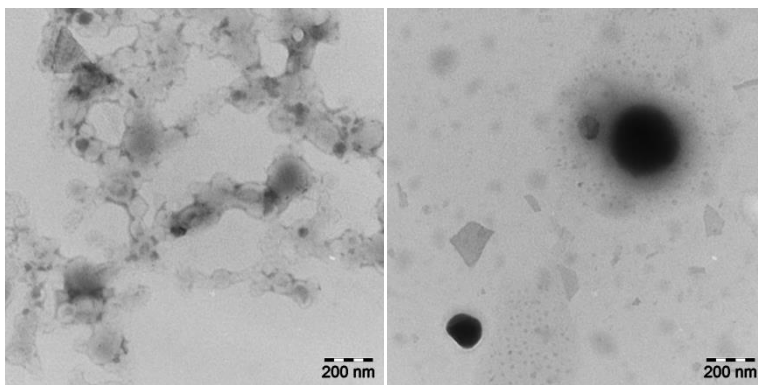


Figure 82. TEM images of PLLA_MCT capsules based on SDS-solution (l.) and PVA-solution (r.).

Diluted solutions of the finished nanocapsule suspension were measured in TEM (Figure 82). The pictures of the PLLA_MCT capsules solutions showed the formation of spherical capsules. The smaller capsules made with SDS-solution seem to agglomerate strongly and lose their perfect round shape. The picture of the capsules made with PVA-solution was clearly showing single formed, round shaped capsule. Also the crystals formed by PVA were visible.

4.0 Experimental Part

4.1 Chemicals and Materials

All chemicals were purchased from Sigma-Aldrich, except Ascorbic Acid (Merck), HDI (Merck), Urea (Merck), PEG-400 (Fluka), 6-Chloro-hexyne (Alfa Aesar), Hexadecane (Alfa Aesar), Limonene (Alfa Aesar), Methane sulfonyl chloride (Alfa Aesar), PVF powder (Alfa Aesar), Sn(oct)₂ (Alfa Aesar), Cu₂O (abcr), PVA (Kuraray Europe GmbH), Diethyl-2-ethylmalonate (J&K), Hydrogen peroxide (Gruessing), 5-Amino-fluorescein (TCI), Bisphenol E (TCI), TMSA (TCI), DBTDL (TCI), L-Lactide (TCI), Triethyl amine (TCI) and 2-amino-4-hydroxy-6-methylpyrimidine (TCI). The bivalent functionalized PIB was bought from Kaneka. The chemicals were used without further purification, if not mentioned otherwise.

L-lactide was dried over P₂O₅ in a desiccator. Caprolactone was dried over CaH₂ and freshly distilled before use. Sn(oct)₂ was vacuum distilled and dried at high vacuum. K₂CO₃ was dried in vacuum at 150 °C before use. THF was pre-dried over potassium hydroxide, while toluene was predried over calcium chloride. These solvents were heated under reflux over sodium/benzophenone until the blue color persists. DCM was predried over calcium chloride and dried finally by refluxing over calcium hydride. DMF, ACN, and DMSO were dried by refluxing over calcium hydride and freshly distilled prior use. All other solvents were distilled once before use. Polymers were dried in high vacuum above their melting point, when reacted with isocyanates.

MCT and the fluorogenic polymers (CN-PPV, PF8BT) were provided by the pharmaceutical department of the MLU (AG Dailey).

4.2 Instrumentation

DSC measurements of pure PCL and of the composites were done on a Netzsch DSC 204 F1. Samples pieces with a mass of 5 – 10 mg were placed into aluminum crucibles and were heated under nitrogen atmosphere with a heating rate of 10 K·min⁻¹. Evaluation of the measured data was done with Netzsch Proteus Analytic software.

TGA measurements were done on a Netzsch TG 209 F3. Samples pieces with a mass of 1 - 10 mg were placed into alumina crucibles and were heated under nitrogen atmosphere with a heating rate of 10 K·min⁻¹. The mass losses were evaluated with Netzsch Proteus Analytic software.

For *rheology measurements* the polymer samples were filtered through a Teflon GPC-filter (0.2 μm) and dried in vacuum at 60 - 80 °C for three days. The rheology experiments were executed on an Anton Paar MCR-101 DSO rheometer using parallel plate-plate geometry with a diameter of 8 mm. The temperature was controlled with a thermoelectric cooler/heater in a chamber filled with dry air. For each measured

temperature the samples were preheated for 30 minutes reaching their equilibrium state. For 3D printing the mandatory temperature-dependent measurements of the viscosity *versus* shear rate ($0.1 - 100 \text{ s}^{-1}$) were performed. If not mentioned otherwise temperature-dependent frequency measurements (FS) were done within the linear viscoelastic regime (LVE). Data were evaluated by using the RheoPlus / 32 software (V 3.40) and OriginPro8G.

For 3D printing different geometrical shapes were programmed with the help of the CAD program *BioCAD*TM. Each individual polymer strand was drawn in the CAD program and stacked up to six layers. For the attached 0.20 mm printing needle the strand thickness was set to 0.18 mm (90 % of the needle diameter due to its movement with a velocity of 10 mm/s during printing). The CAD file was automatically transformed to an ISO file for communication with the 3D printer. The printer *regenHU 3D Discovery*, equipped with a heatable polymer extrusion printing head with a 0.20 or 0.33 mm inner diameter needle, was used for printing of supramolecular polymers. For 3D printing the polymer samples were filtered through a glass fiber GPC-filter ($1.2 \mu\text{m}$) and dried in vacuum at $60 \text{ }^\circ\text{C}$ for three days. Each polymer was filled into the heatable tank of the printing head. The temperature of the printing needle was adjusted according to the printability window determined by the viscosity versus shear rate measurements. The temperature of the tank of the printing head was set $10 \text{ }^\circ\text{C}$ higher than the temperature of the printing needle. The extrusion printing head works with an air pressure of 0.2 MPa and the molten polymers flow from the tank to the extrusion screw. The polymer layers were printed directly on a standard glass or teflon slide. The composites were printed on a standard glass slide equipped with masking tape for mechanical adhesion (Figure 83). The drop-on-demand liquid printing head was set to one drop per grid hole at room temperature. The 3 mL cartridge was filled with oils and pressed with air of 0.020 MPa to move the liquid through the inkjet nozzle.

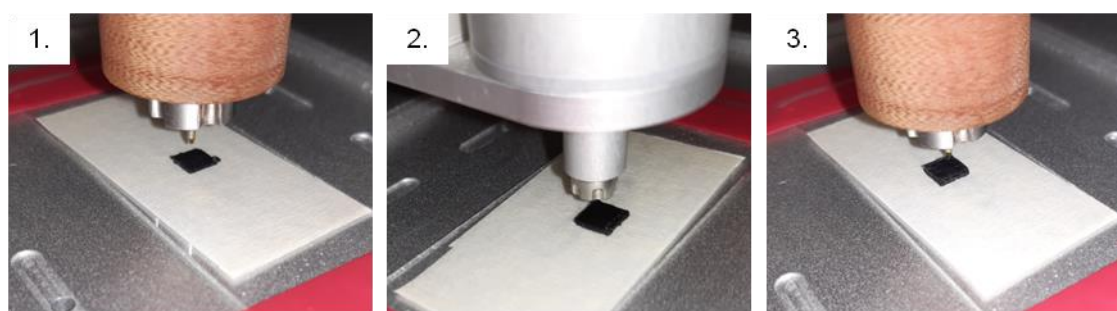


Figure 83: The different printing heads for the printer *regenHU 3D Discovery*. 1. The polymer extruder deposited the two base layers of composite 10, 2. inkjet drop-on-demand head filled the grid gaps with trivalent alkyne, 3. the filled grid was closed with two layers of composite 10.

Contact angle measurements were performed on an Optical Contact Angle Measuring System OCA 20. Three drops of each liquid were placed onto the surface of the printed PCL plates (1 drop $5 \mu\text{L}$). The contact angle was determined on both sides of the drop using the OCA 20 instrument at a temperature of $20 \text{ }^\circ\text{C}$.

NMR-spectra were measured on a Varian Gemini 400 spectrometer. For ^1H -NMR spectra 400 MHz at 27 °C were used and for ^{13}C -NMR spectra 100 MHz at 27 °C were used. As solvents CDCl_3 and DMSO were used. For interpretation of the NMR spectra MestReNova software (version 9.0.1-13254) was utilized and chemical shifts were given in ppm and coupling constants in Hz.

ATR-FTIR-spectra were recorded on a Bruker Tensor VERTEX 70 spectrometer equipped with a Golden Gate Diamond ATR top-plate. Samples were measured with 32 background scans and 32 sample scans. For analysing of data Opus 6.5 was utilized. Temperature dependent AT-IR measurements were performed between 30 to 120 °C in 10 K steps. The samples were allowed to equilibrate at each temperature for 10 minutes.

Gel permeation chromatography (GPC) investigations were performed at 40 °C on a Viscotek GPCmax VE 2002 from Viscotek™ applying a H_{HR}H Guard-17369 and a GMH_{HR}-N-18055 column. As solvent THF was used and the sample concentration was adjusted to 3 mg·mL⁻¹ while applying a flow rate of 1 mL·min⁻¹. For determination of the molecular weights the refractive index of the investigated sample was detected with a VE 3580 RI detector of Viscotek™ and PIB-standards (320 g·mol⁻¹ to 578,000 g·mol⁻¹) were used as reference from Viscotek™.

Matrix-assisted laser desorption / ionization time-of-flight mass spectrometry (MALDI-ToF-MS) measurements of polymers with similar molecular weight were done on a Bruker Autoflex III system in linear mode. Data evaluation was performed with flexAnalysis software (version 3.0). Formation of ions was obtained by laser desorption (smart beam laser at 355, 532, 808, and 1064 ± 6.5 nm; 3 ns pulse width; up to 2500 Hz repetition rate). Ions were accelerated by a voltage of 20 kV and detected as positive ions. *Trans*-2-[3-(4-*tert*-butylphenyl)-2-methyl-2-propenylidene]malononitrile (DCTB, 20 mg·mL⁻¹ THF) was used as matrix and lithium trifluoroacetate (LiTFA, 20 mg·mL⁻¹ THF) or silver trifluoroacetate (AgTFA, 20 mg·mL⁻¹ THF) were used as salts for ionizing supramolecular star polymers functionalized with hydrogen-bonding moieties (20 mg·mL⁻¹ THF) while applying a volume ratio of 25:5:1 or 100:10:1. Baseline subtraction and smoothing of all recorded MALDI-ToF-MS spectra was done by applying a three point Savitzky–Golay algorithm.

Electrospray Ionization – Time of Flight Mass Spectrometry (ESI-ToF-MS) was performed on a Bruker Daltonics microTOF *via* direct injection with a flow rate of 180 µL/h using the positive mode / negative mode. Solutions were prepared by dissolving the sample in THF or MeOH and concentrations of 0.1 mg/mL were adjusted. For neutral compounds the salt NaI was added.

Small-angle X-ray scattering (SAXS) experiments were accomplished at room temperature using a Retro-F laboratory setup (SAXSLAB, Massachusetts) in transmission. The instrument is equipped with an microfocus X-ray source (AXO Dresden GmbH, Germany) with an ASTIX multilayer X-ray optic (AXO Dresden GmbH,

Germany) as monochromator for Cu K α radiation ($\lambda = 0.154$ nm). A PILATUS3 R 300K detector (Dectris Ltd., Switzerland) with a sample-to-detector distance of 1035.5707 mm for SAXS measurements, respectively, was used to record the two-dimensional scattering patterns.

XRD measurement were performed, using a Bruker AXS D8 advanced X-ray diffractometer with CuK α ($\lambda = 0.15406$ nm) radiation in the 2θ range between 5–80° with a scan rate of 2°/min.

UV/Vis spectra were measured on LAMBDA 365 UV/Vis Spectrophotometer using tungsten-halogen and deuterium lamps. The sample solutions were prepared in quartz cuvettes with different solvents (CHCl₃, THF, MeOH, H₂O).

Fluorescence investigations in solution and solid state were done using in a Cary Eclipse Fluorescence Spectrophotometer. The solution measurements were performed in quartz cuvettes in different solvents (EtOH, THF, MeOH) depending on the dye. For the solid state measurements the sample was fixed between two glass slides and the reflected fluorescence of a small area (10 mm x 0.2 mm) was detected. For each sample the measurements were repeated 2 – 3 times.

DLS analysis was done in PMMA cuvettes using a Viscotek 802 DLS instrument. After solvent evaporation encapsulation, the remaining capsule dispersion was filtrated and 10 μ L of the dispersion was diluted to 3 mL with water. Each sample was measured 10 times for 10 seconds and a hydrodynamic radius distribution was calculated.

For the *synthesis of TRGO* a glass tube oven from Nabertherm, Mod. RSR-B120 / 750 / 11 was used with a nitrogen atmosphere at 700 °C.

Scanning electron microscope (SEM) images were recorded on a scanning electron microscope Phenom ProX with a zoom up to 50.000x, voltage of 5 – 15 kV and a BSE-Detector with EDX (Energy-dispersive X-ray spectroscopy).

For *transmission electron microscopy (TEM)* the samples (TRGO) were dispersed in isopropanol, using a sonication bath and spread onto a Cu-grid coated with a Carbon-film. The solvent evaporated over a time period of two hours. The dried specimens were examined with an EM 900 transmission electron microscope (Carl Zeiss Microscopy GmbH, Oberkochen, Germany). Micrographs were taken with a SSCCD SM-1k-120 camera (TRS, Moorenweis, Germany).

Ultrasonication experiments for nanocapsules synthesis used the Sonics VCX 500 ultrasonic processor at a frequency of 20 kHz equipped with a long full wave solid probe (254 mm) out of titanium alloy (Ti-Al-4V) with a diameter of 13 mm. The emulsion was sonicated in an ice bath for two minutes (30 s pulse, 15 s pause) with amplitude of 60 % - 90 %.

Freeze-drying of samples took place with the Telstar LyoQuest -85 Laboratory Freeze-dryer. The samples were dispersed or dissolved in a low amount of water (5 – 10 mL) and cooled down very fast in liquid nitrogen. The frozen samples were attached to a vacuum of 0.2 mbar and a condenser temperature of ~ -80 °C. After 24 hours the samples were removed from the freeze-dryer.

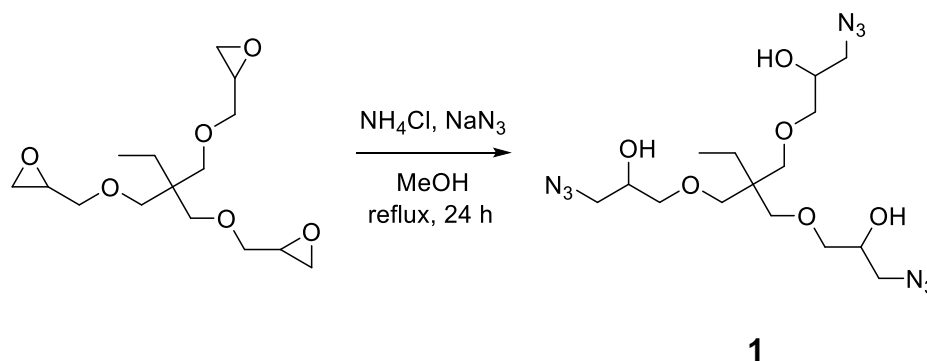
The *compression cycles* were conducted on the automatic hydraulic Atlas Power Presses T15 from Specac together with an Atlas 13 mm evacuable pellet die applying 10 tons' pressure.

TLC was done on Silica Gel 60 F254 aluminum plates.

4.3 Syntheses

4.3.1 Monomers for “Click”-reaction resins

4.3.1.1 Synthesis of 1,1,1-Trimethylolpropane tri(3-azido-2-hydroxypropyl)ether (**1**)

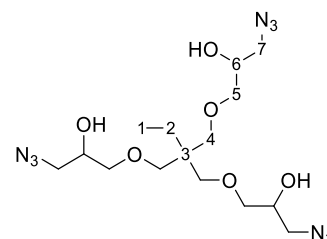


1,1,1-Trimethylolpropane triglycidyl ether (5 g, 0.0165 mol), NH_4Cl (4.41 g, 0.0825 mol) and NaN_3 (5.36 g, 0.0825 mol) were dissolved in methanol (75 mL). The reaction solution was refluxed for 24 hours. After cooling down to room temperature the solvent was removed under reduced pressure. The inorganic salts were extracted with chloroform (3x30 mL). The collected organic solvent was washed with water (3x50 mL) and brine (3x50 mL). After drying over MgSO_4 the solvent was evaporated in vacuum.²⁶⁰

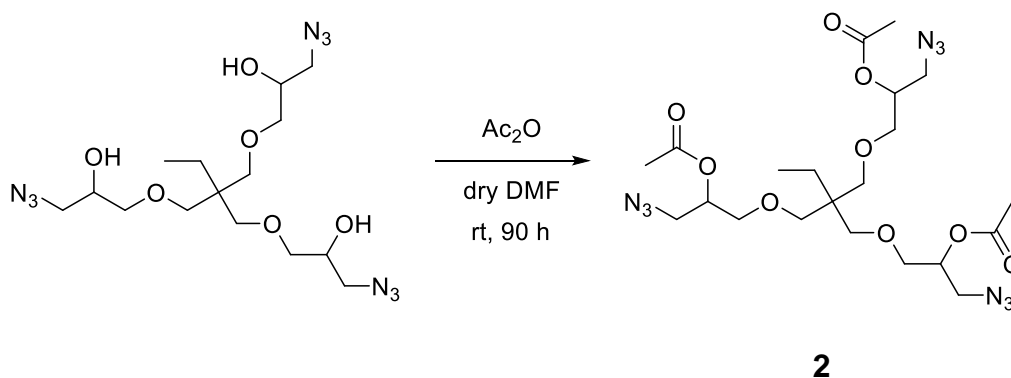
Product: yellow oil

Yield: 4.74 g (67 %)

$^1\text{H-NMR}$ (400 MHz, CDCl_3): 3.90 (3H, dd, $J = 9.97, 5.27\text{Hz}$, C_6), 3.41 (18H, m, $\text{C}_{4,5,7}$), 2.78 (3H, s, OH), 1.37 (2H, m, C_2), 0.81 (3H, t, $J = 7.57\text{Hz}$, C_1); $^{13}\text{C-NMR}$ (100 MHz, CDCl_3): 72.6 (C_4), 72.3 (C_5), 69.5 (C_6), 53.4 (C_7), 43.3 (C_3), 23.3 (C_2), 7.6 (C_1);



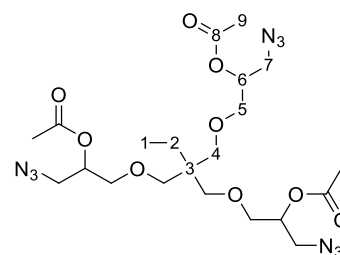
4.3.1.2 Acetylation of 1,1,1-Trimethylolpropane tri(3-Azido-2-hydroxypropanyl)ether (2)



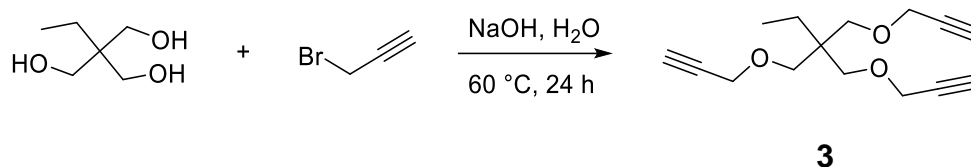
Over CaH₂ distilled DMF (30 mL) was purged with nitrogen. In a flask compound **1** (4.32 g, 10 mmol) and 4-DMAP (0.244 g, 2 mmol) were placed. The reaction was performed under nitrogen atmosphere and dry DMF was added with a syringe. After complete dissolution acetic anhydride (6.13 g, 60 mmol, 5.67 mL) was added drop wise. The solution was stirred at room temperature for four days. The finished reaction was diluted with an excess of water (100 mL) and was extracted with Et₂O (3x30 mL). The organic phase was washed with water (3x75 mL), brine (1x50 mL) and water (2x75 mL). After drying over MgSO₄ the solvent was evaporated under reduced pressure and azeotrope distillation with *n*-heptane (3x2 mL) was used to remove all DMF traces. The crude product was purified with a flash column in Et₂O and drying under high vacuum for two days.²⁷⁶

Product: slightly yellow oil **Yield:** 4.11 g (75 %)

¹H-NMR (400 MHz, CDCl₃): 5.06 (3H, m, C₆), 3.46-3.54 (12H, m, C_{4,5}), 3.26 (6H, s, C₇), 2.08 (9H, s, C₉), 1.35 (2H, d, J = 7.58Hz, C₂), 0.81 (3H, d, J = 7.50Hz, C₁); ¹³C-NMR (100 MHz, CDCl₃): 170.1 (C₈), 71.6 (C₄), 71.1 (C₅), 69.5 (C₆), 51.0 (C₇), 43.4 (C₃), 22.9 (C₂), 20.9 (C₉), 7.6 (C₁);



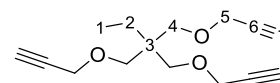
4.3.1.3 Synthesis of 1,1,1-Trimethylolpropane tripropargylether (3)



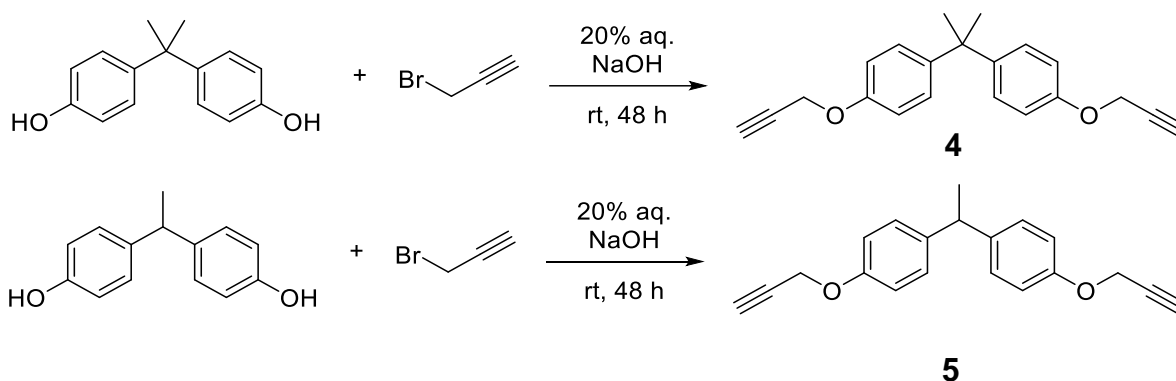
A 2-neck flask equipped with a gas tap and a septum was flushed three times with nitrogen. In a counter flow of nitrogen 1,1,1-trimethylol propane (6.71 g, 0.050 mol), NaOH (12 g, 0.30 mol) and TBAB (0.80 g, 0.0025 mol) were placed into the flask. Then water (1.5 mL) and subsequently propargyl bromide (45.0 g, 0.30 mol, 33 mL, 80 wt% in toluene) was added drop wise over a period of ten minutes. The reaction mixture was slowly heated to 60 °C and stirred for 24 hours. The reaction progress was checked with TLC ($R_f = 0.9$ and 1.0 in Et_2O). After cooling down to room temperature the mixture was extracted with Et_2O (3x50 mL). The organic phase was washed with water (3x200 mL) and then dried with Na_2SO_4 . The solvent was evaporated under reduced pressure and the crude product was purified with column chromatography in chloroform ($R_f = 0.4$).²⁵⁹

Product: slightly yellow liquid **Yield:** 5.11 g (40 %)

$^1\text{H-NMR}$ (400 MHz, CDCl_3): 4.08 (6H, d, $J = 2.4\text{Hz}$, C_5), 3.36 (6H, s, C_4), 2.39 (3H, t, $J = 2.4\text{Hz}$, C_7), 1.39 (2H, q, $J = 7.6$, C_2), 0.84 (3H, t, $J = 7.6\text{Hz}$, C_1); $^{13}\text{C-NMR}$ (100 MHz, CDCl_3): 80.2 (C_6), 74.2 (C_7), 70.4 (C_4), 58.7 (C_5), 42.8 (C_3), 22.8 (C_2), 7.6 (C_1);



4.3.1.4 Synthesis of Bisphenol A/E propargyl ether (4/5)

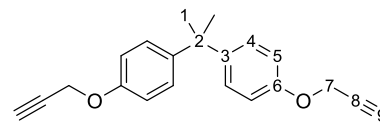


A 20%-solution of NaOH (2.8 g, 0.07 mol) and water (14 mL) was prepared. Bisphenol A/E (5 g, 0.023 mol), TBAB (0.39 g, 1.2 mmol) and the NaOH-solution were placed in a flask and dissolved during ten minutes. The aqueous solution was purged 30 minutes with nitrogen and subsequently propargyl bromide (8.33 g, 0.07 mol, 7.55 mL, 80 wt% in toluene) was slowly added drop wise. The reaction mixture was stirred for 48 hours at room temperature. The solution was diluted with Et_2O (100 mL) and washed with water (5x100 mL). The organic layer was dried with MgSO_4 and was removed under reduced pressure.²⁹¹

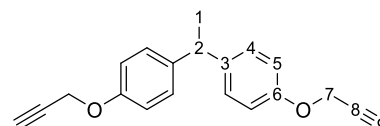
Product: slightly yellow powder (BAPE), yellow oil (BEPE)

Yield: 6.09 g (91 %), 6.23 g (96 %)

$^1\text{H-NMR}$ (400 MHz, CDCl_3): 7.21-7.08 (4H, m, C₄), 6.97-6.79 (4H, m, C₅), 4.67 (4H, d, J = 2.4Hz, C₇), 2.52 (2H, t, J = 2.4Hz, C₉), 1.65 (6H, s, C₁); $^{13}\text{C-NMR}$ (100 MHz, CDCl_3): 155.5 (C₆), 143.9 (C₃), 127.7 (C₅), 114.2 (C₄), 78.8 (C₈), 75.3 (C₉), 55.8 (C₇), 41.8 (C₂), 31.0 (C₁);

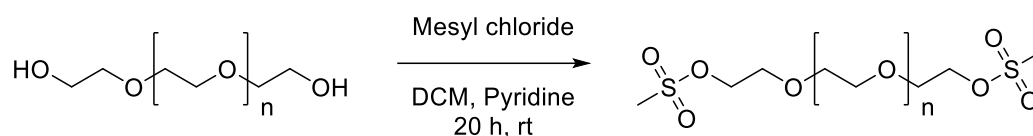


$^1\text{H-NMR}$ (400 MHz, CDCl_3): 7.22-7.06 (4H, m, C₄), 7.00-6.84 (4H, m, C₅), 4.67 (4H, d, J = 2.4Hz, C₇), 4.09 (1H, q, J = 7.2Hz, C₂), 2.52 (2H, t, J = 2.4Hz, C₉), 1.61 (3H, d, J = 7.2Hz, C₁); $^{13}\text{C-NMR}$ (100 MHz, CDCl_3): 155.8 (C₆), 139.7 (C₃), 128.4 (C₅), 114.7 (C₄), 78.8 (C₈), 75.3 (C₉), 55.8 (C₇), 43.1 (C₂), 22.2 (C₁);



4.3.2 Syntheses of supramolecular polymers

4.3.2.1 Synthesis of telechelic bimesylated PEG (400, 1500, 8000) (6)



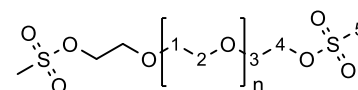
6

A methanesulfonyl chloride (968 μL , 12.5 mmol) solution in DCM (40 mL) was added drop-wise to polyethylene glycol M_n 400 (1 g, 2.5 mmol) in pyridine (3 mL) at 0 °C. The reaction mixture was allowed to warm up to room temperature and stirred for 24 hours. After removing the DCM under reduced pressure the residue was reacted with a saturated solution of sodium hydrogen carbonate (250 mL) and extracted with DCM (5x50 mL). After drying the organic layer over Na_2SO_4 the solvent was evaporated.³⁰⁹

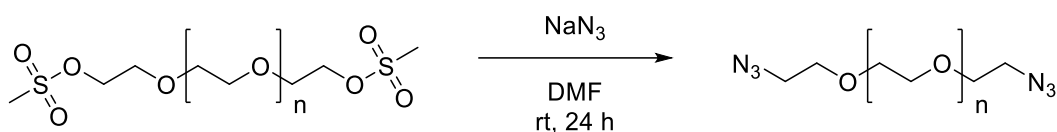
Product: yellow liquid

Yield: 0.95 g (95 %)

$^1\text{H-NMR}$ (400 MHz, CDCl_3): 4.27 (4H, m, C₄), 3.66 (4H, m, C₃), 3.54 (28H, m, C₁₊₂), 2.98 (6H, s, C₅);



4.3.2.2 Synthesis of telechelic bisazido PEG (400, 1500, 8000) (**7**)

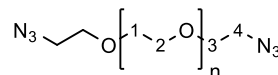


7

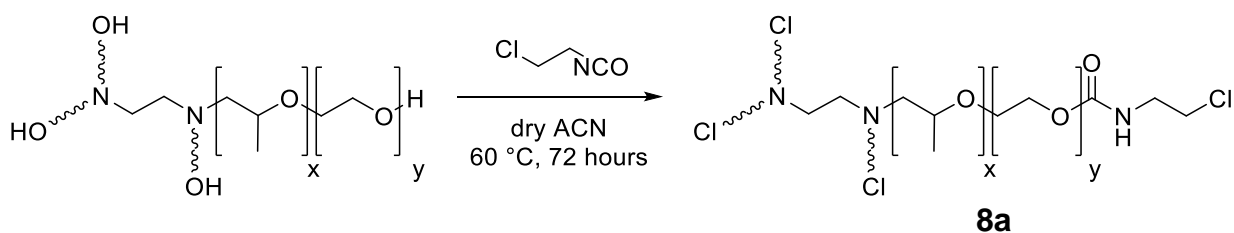
The obtained bis-sulfonated PEG M_n 400 (1 g, 2.5 mmol) was dissolved in DMF (7 ml) and sodium azide (813 mg, 12.5 mmol) was added to the solution. The reaction mixture was stirred for 24 hours at room temperature and was then concentrated by rotary evaporator. The product was extracted with DCM (3x50 mL) and dried in vacuum.³⁰⁹

Product: yellow polymer **Yield:** 0.95 g (99 %)

$^1\text{H-NMR}$ (400 MHz, CDCl_3): 3.61 (4H, m, C₃), 3.59 (28H, m, C₁₊₂), 3.32 (4H, m, C₄);



4.3.2.3 Synthesis of tetravalent telechelic azido Tetronic 3600 (**8a-b**)

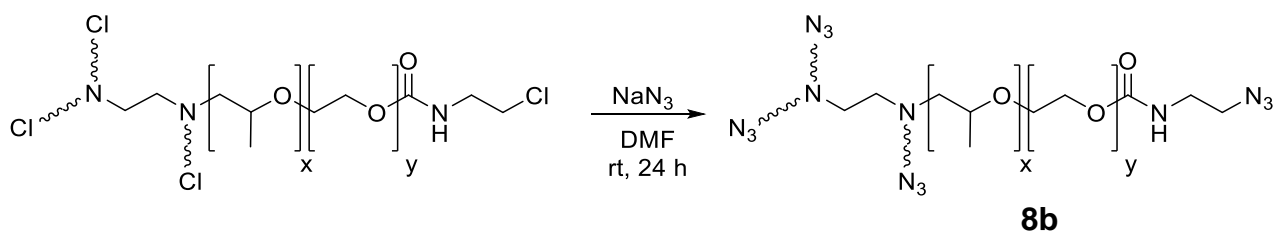


8a

Tetronic 3600-OH (5 g, 1.39 mmol) was dried in high vacuum for 24 hours. The reaction took place under dry nitrogen atmosphere. The polymer was dissolved in dry acetonitrile (50 mL) and 2-chloroethyl isocyanate (912 μL , 9 mmol) was added as well as a catalytic amount of DBTDL. The reaction was stirred at 60 °C for 72 hours. The solvent was removed under reduced pressure and the final polymer Tetronic 3600-Cl was dried in high vacuum at 60 °C. No further purification was realized.

Product: yellow polymer **Yield:** 4.1 g (80 %)

$^1\text{H-NMR}$ (400 MHz, DMSO): 7.46 + 7.31 (4H, s), 4.37 + 3.86 (16H, t, $J = 6.0\text{Hz}$), 3.49 (197H, m), 1.03 (120H, d, $J = 5.9\text{Hz}$);



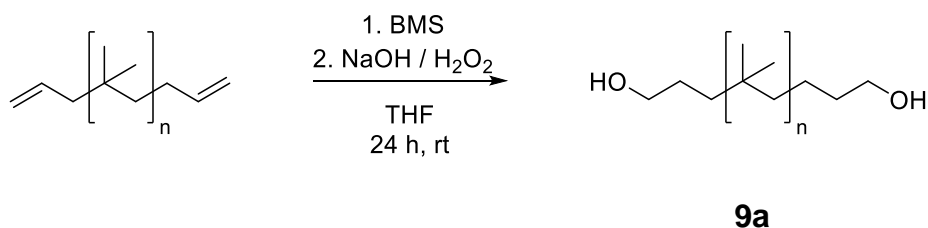
The followed reaction to Tetronic 3600-N₃ was performed like described for telechelic biazido PEG with accordingly more sodium azide. No further purification was performed.

Product: yellow polymer **Yield:** 4.0 g (97 %)

¹H-NMR (400 MHz, DMSO): 7.42 + 7.28 (4H, s), 4.37 + 3.86 (16H, t, J = 6.0Hz), 3.49 (197H, m), 1.03 (120H, d, J = 5.9Hz);

FT-IR: $\nu(\text{C-H}) = 2869 \text{ cm}^{-1}$, $\nu(\text{N}_3) = 2100 \text{ cm}^{-1}$, $\nu(\text{C=O}) = 1720 \text{ cm}^{-1}$, $\nu(\text{C-O}) = 1251 \text{ cm}^{-1}$, $\nu(\text{C-C-O}) = 1095 \text{ cm}^{-1}$;

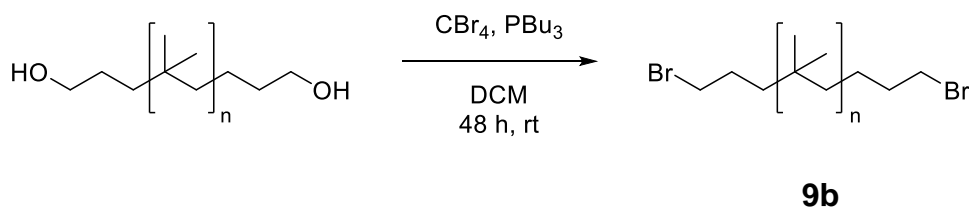
4.3.2.4 Synthesis of bivalent telechelic azido PIB (**9a-c**)



Bivalent allyl-telechelic PIB 8000 (10 g, 1.25 mmol) was dissolved in dry THF (50 mL) and after complete dissolution borane dimethyl sulfide (105 μL , 1.1 mmol) was added dropwise. After five minutes a gel was formed and was kept at room temperature for 20 hours. Afterwards aqueous NaOH (120 mg, 3 mmol) was added, followed by H₂O₂ (1.5 mL, 35 %). The reaction mixture was kept stirring for 24 hours at room temperature. The solvent was removed under vacuum and the polymer was extracted with *n*-hexane (100 mL). The organic phase was washed with water (100 mL) and brine (100 mL), dried over Na₂SO₄, filtered and the solvent was removed under vacuum.

Product: colorless polymer **Yield:** 8.44 g (84 %)

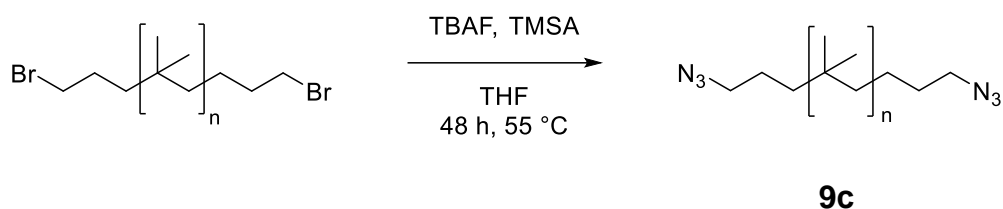
¹H-NMR (400 MHz, CDCl₃): 3.61 (4H, t, J = 5.7Hz), 1.42 (504H, m), 1.11 (1525H, m);



Bivalent hydroxy-telechelic PIB 8000 (8.44 g, 1.06 mmol), CBr_4 (7.7 g, 23.21 mmol) and Tri-*n*-butylphosphin (5.27 mL, 21.1 mmol) were dissolved in dry DCM (200 mL) and stirred under nitrogen atmosphere for 48 hours at room temperature. The reaction progress was checked with TLC ($R_f = 1$ in hexane). The solvent was removed in vacuum and the polymer was extracted with *n*-hexane (3x30 mL). The solid residues and impurities were removed with centrifugation and the concentrated polymer solution was purified by column chromatography in hexane / ethyl acetate (40 / 1, $R_f = 0.9$). After removing the solvent the polymer was dried in vacuum.^{146, 310}

Product: colorless polymer **Yield:** 6.9 g (81 %)

$^1\text{H-NMR}$ (400 MHz, CDCl_3): 3.37 (4H, t, $J = 6.9\text{Hz}$), 1.42 (533H, m), 1.11 (1589H, m);



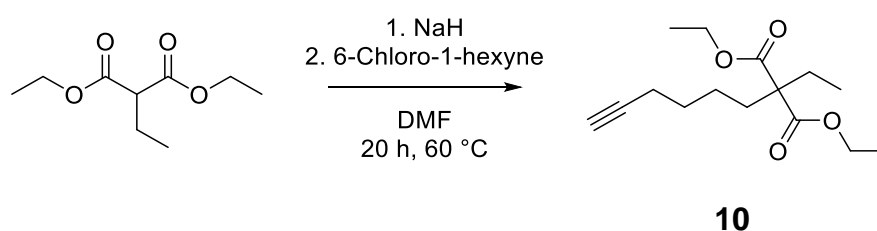
Bivalent bromo-telechelic PIB 8000 (6.9 g, 0.86 mmol) was dissolved in dry THF (70 mL). After complete dissolution TBAF (13.8 mL, 13.8 mmol, 1 M in THF) and TMSA (2.8 mL, 13.8 mmol) were added and the reaction was stirred for 24 hours at 55 °C. The solvent was removed under vacuum and the crude polymer was dissolved in *n*-hexane and purified with centrifugation and column chromatography in *n*-hexane ($R_f = 1$). The solvent was removed under vacuum.^{147, 311}

Product: colorless polymer **Yield:** 5.8 g (85 %)

$^1\text{H-NMR}$ (400 MHz, CDCl_3): 3.23 (4H, t, $J = 7.0\text{Hz}$), 1.42 (517H, m), 1.11 (1553H, m);

FT-IR: $\nu(\text{-CH}_3) = 2950 \text{ cm}^{-1}$, $\nu(\text{C-H}) = 2897 \text{ cm}^{-1}$, $\nu(\text{N}_3) = 2111 \text{ cm}^{-1}$;

4.3.2.5 Synthesis of diethyl 2-hexynyl-2-ethylmalonate (**10**)

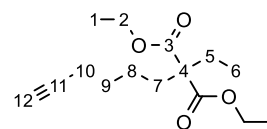


Sodium hydride in mineral oil (0.41 g, 10 mmol) was suspended in dry DMF (4 mL), while cooled in an ice bath. Diethyl 2-ethylmalonate (1.80 g, 9.6 mmol) was added slowly drop wise at 0°C. The mixture was stirred for 20 minutes at 0°C till a clear yellow solution and no gas production was visual. Then, 6-chloro-1-hexyne (1.12 g, 9.6 mmol)

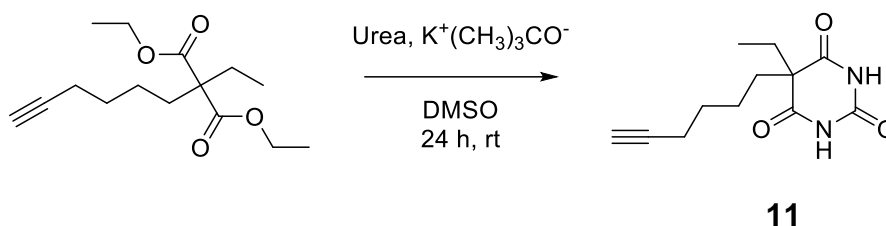
was added drop wise. The reaction was stirred at 60 °C for 20 hours. Then this solution was cooled down to room temperature and was concentrated. The salts were extracted with DCM (2x10 mL) and the solvents were removed under reduced pressure. Final purification was done with flash column chromatography in n-hexane ($R_f = 0$) and then in CHCl_3 ($R_f = 0.6$). The colorless liquid still contained a small amount of non-reacted diethyl 2-ethylmalonate.

Product: colorless liquid **Yield:** 2.1 g (80 %)

$^1\text{H-NMR}$ (400 MHz, CDCl_3): 4.16 (4H, q, $J = 7.1\text{Hz}$, C_2), 2.18 (2H, td, $J = 7.1, 2.6\text{Hz}$, C_{10}), 1.90 (5H, m, $\text{C}_{5,7,12}$), 1.52 (2H, m, C_9), 1.28 (2H, m, C_8), 1.24 (6H, t, $J = 7.1\text{Hz}$, C_1), 0.80 (3H, t, $J = 7.6\text{Hz}$, C_6); $^{13}\text{C-NMR}$ (100 MHz, CDCl_3): 171.7 (C_3), 84.1 (C_{11}), 68.4 (C_4), 61.0 (C_5), 57.9 (C_7), 31.0 (C_9), 28.6 (C_8), 25.2 (C), 22.9 (C_6), 18.1 (C_{6E}), 14.1 (C_1), 8.4 (C_{1E});



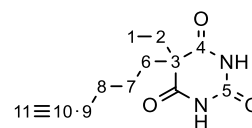
4.3.2.6 Synthesis of 2-hexynyl-2-ethyl barbiturate (**11**)



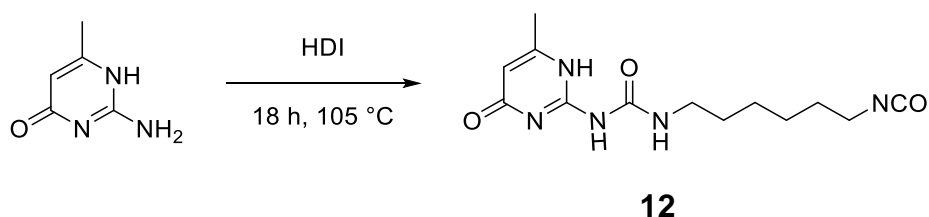
Urea (11.5 g, 192 mmol) and potassium *tert*-butoxide (1.08 g, 9.6 mmol) were dissolved in dry DMSO (30 mL). While cooling in an ice bath the diethyl 2-hexynyl-2-ethylmalonate (1.3 g, 4.8 mmol) was added dropwise. The mixture was stirred for 24 hours at room temperature. Then, water (120 mL) was added and the pH-value was adjusted to 10, if required with NaOH solution (1 M). The aqueous layer was washed with Et_2O (2x60 mL). The water phase was acidified to pH = 2 with HCl solution (1 M). The barbiturate was extracted with Et_2O (2x60 mL). The combined organic phases were washed with water (1x60 mL). The solvents were removed under reduced pressure and recrystallization from hot toluene was performed over night in the fridge.

Product: colorless crystals **Yield:** 794 mg (70 %)

$^1\text{H-NMR}$ (400 MHz, DMSO): 11.51 (2 H, s, NH), 2.69 (1 H, t, $J = 2.6\text{ Hz}$, C_{11}), 2.09 (2 H, td, $J = 6.9, 2.6\text{ Hz}$, C_9), 1.79 (4 H, m, $\text{C}_{2,6}$), 1.34 (2 H, m, C_8), 1.16 (2 H, m, C_7), 0.72 (3 H, t, $J = 7.4\text{ Hz}$, C_1); $^{13}\text{C-NMR}$: 173.5 (C_4), 150.3 (C_5), 84.6 (C_{10}), 71.8 (C_{11}), 56.1 (C_3), 37.9 (C_2), 32.0 (C_6), 28.3 (C_8), 24.1 (C_7), 17.9 (C_9), 9.5 (C_1);



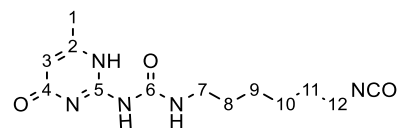
4.3.2.7 Synthesis of UPy isocyanate (**12**)



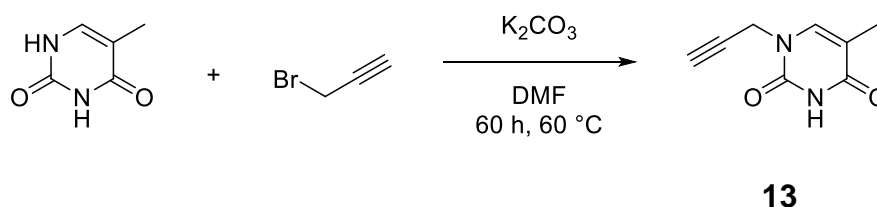
6-Methylisocytosine (2 g, 16 mmol) and hexamethylene diisocyanate (20 mL) were mixed in a flask under nitrogen atmosphere. The reaction was stirred at 105 °C for 18 hours. After cooling down to room temperature, the white powder was washed with *n*-pentane (5x100 mL) and dried in vacuum.¹⁴¹

Product: colorless crystals **Yield:** 4.2 g (90 %)

¹H-NMR (400 MHz, CDCl₃): 13.11 (1H, s, NH), 11.86 (1 H, s, NH), 10.18 (1 H, s, NH), 5.81 (1 H, s, C₃), 3.28 (4 H, m, C_{7,12}), 2.23 (3 H, s, C₁), 1.62 (4 H, m, C_{8,11}), 1.39 (4 H, m, C_{9,10}); ¹³C-NMR (100 MHz, CDCl₃): 173.0 (C₅), 156.6 (C₆), 154.8 (C₁₂), 148.2 (C₄), 121.9 (C_{NCO}), 106.7 (C₃), 42.9 (C₂), 39.8 (C₁), 31.2 (C₇), 29.3 (C₁₂), 26.2 (C₁₁), 26.1 (C₈), 18.9 (C₉);



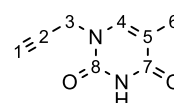
4.3.2.8 Synthesis of alkyne thymine (**13**)



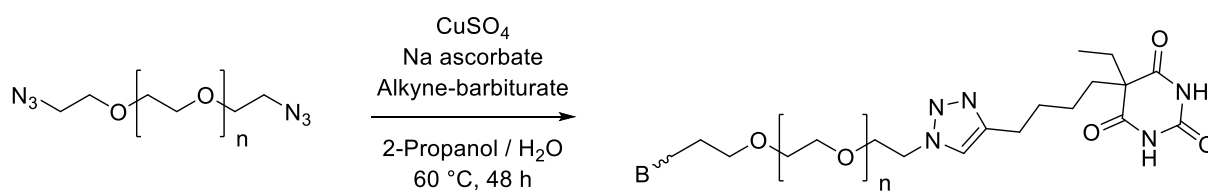
K₂CO₃ (5.53 g, 40 mmol) was dried over night before use. Thymine (5 g, 40 mmol) and dry K₂CO₃ were placed in a flask and were flushed with N₂. Dry DMF (60 mL) was added and the mixture was stirred for 5 minutes. Propargyl bromide (5.23 g, 4.9 mL, 44 mmol) was added drop wise to the solution. The reaction was run at 60 °C for 60 hours. Afterwards, the solvent was removed in vacuum. The product was extracted with ethyl acetate (2x50 mL) and concentrated under vacuum. Final purification was done by recrystallization in hot toluene (200 mL).

Product: slight yellow crystals **Yield:** 3.2 g (50 %)

¹H-NMR (400 MHz, DMSO): 11.34 (1 H, s, NH), 7.56 (1 H, d, J = 1.2 Hz, C₄), 4.47 (2 H, d, J = 2.5 Hz, C₃), 3.38 (1 H, t, J = 2.5 Hz, C₁), 1.77 (3 H, d, J = 1.2 Hz, C₆); ¹³C-NMR (100 MHz, DMSO): 164.6 (C₇), 150.8 (C₈), 140.6 (C₄), 109.8 (C₅), 79.1 (C₂), 76.1 (C₁), 36.8 (C₃), 12.4 (C₆);



4.3.2.9 Synthesis of bivalent PEG-barbiturate via click reaction (**14**)

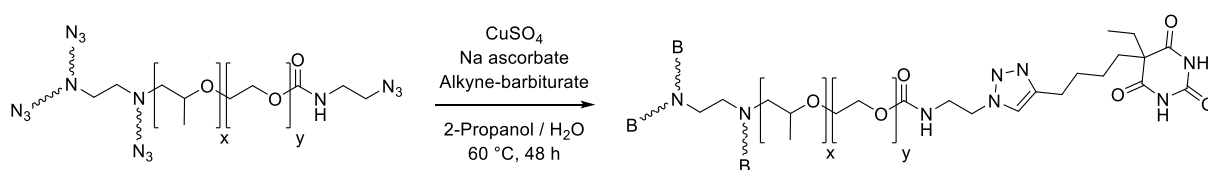


14

Barbiturate **14** (750 mg, 3.17 mmol) and bivalent azido PEG 400 (422 mg, 1.06 mmol) were dissolved in 2-propanol and placed under a nitrogen atmosphere. The $\text{CuSO}_4 \cdot 5 \cdot \text{H}_2\text{O}$ (40 mg, 0.16 mmol) was dissolved in 10 mL water, added to the reaction and degassed with nitrogen. Finally sodium ascorbate (64 mg, 0.32 mmol) was added in counter flow of nitrogen. The reaction mixture was stirred for 48 hours at 60 °C. Afterwards, the solvents were removed and the crude product was extracted with DCM (50 mL) and centrifuged. The solution was concentrated and purified with column chromatography in Et_2O ($R_f = 0$) and $\text{Et}_2\text{O} / \text{MeOH}$ (9 / 1, $R_f = 1$). The polymer solution was filtrated through a glass fiber GPC filter (1.2 μm). The solvents were removed in vacuum and the polymer was dried for 72 hours in high vacuum at 60 °C.²⁸⁶

Yield: 832 mg (90 %), $^1\text{H-NMR}$ (DMSO): 11.50 (4 H, s), 7.75 (2 H, s), 4.44 (4 H, t, $J = 5.3$ Hz), 3.77 (4 H, t, $J = 5.3$ Hz), 3.49 (28 H, m), 2.54 (4 H, t, $J = 7.6$ Hz), 1.8 (8 H, m), 1.51 (4 H, m), 1.13 (4 H, m), 0.74 (6 H, t, $J = 7.4$ Hz), ESI-MS: $[\text{M} - \text{H}]^-$ 891.45 m/z, simulated: 891.46 m/z.

4.3.2.10 Synthesis of tetravalent Tetronic-barbiturate via click reaction (**15**)

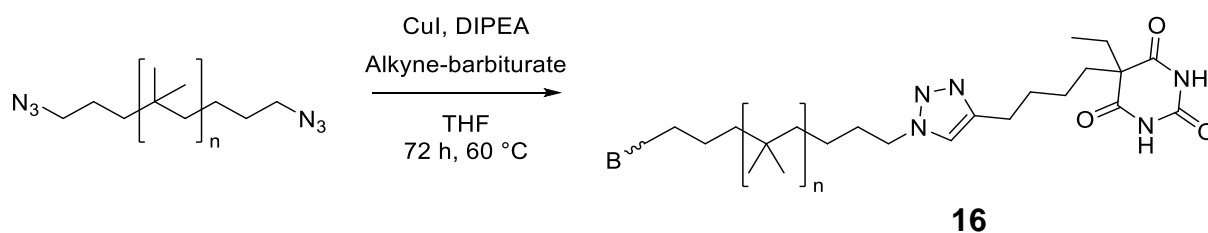


15

The click reaction was conducted in the same way described for the PEG polymers, except more barbiturate **14** was added and column chromatography in Et_2O ($R_f = 0$) and THF ($R_f = 1$) was conducted. The final polymer was precipitated twice in cold Et_2O and was dried for 72 hours in high vacuum at 60 °C.²⁸⁶

Yield: 3 g (66 %), $^1\text{H-NMR}$ (DMSO): 11.50 (8 H, s), 7.74 + 7.71 (4 H, s), 7.36 + 7.22 (4 H, s), 4.33 + 4.03 (16 H, t, $J = 6.0$ Hz), 3.49 (197 H, m), 2.54 (8 H, t, $J = 7.6$ Hz), 1.81 (16 H, m), 1.51 (8 H, m), 1.12 (8 H, m), 1.03 (120 H, d, $J = 5.9$ Hz), 0.74 (12 H, t, $J = 7.4$ Hz).

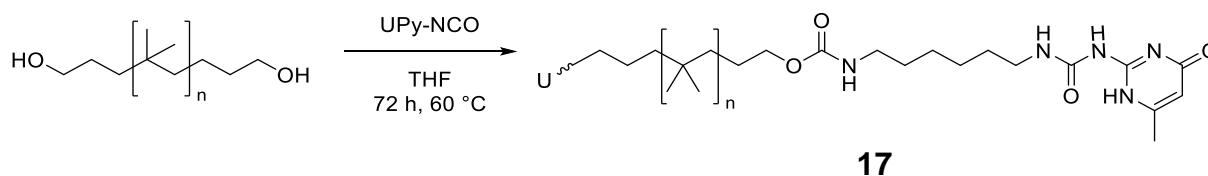
4.3.2.11 Synthesis of bivalent PIB-8000-barbiturate via click reaction (**16**)



The reaction was conducted according to literature³¹² with slight modifications. DIPEA was used in 6-fold excess. After completion of the reaction, checked with TLC (*n*-hexane), the solvent was removed in vacuum and the crude polymer was dissolved in *n*-hexane. The non-soluble impurities were removed with centrifugation and a yellow colored polymer was obtained after drying in high vacuum for 72 hours at 60 °C.³¹²

Yield: 5.5 g (90 %), ¹H-NMR (CDCl₃): 8.01 (s, 4H), 7.25 (s, 1H), 4.35 (t, *J* = 7.0 Hz, 4H), 2.16 (td, *J* = 7.0, 2.6 Hz, 2H), 2.01 (m, 7H), 1.85 (m, 10H), 1.41 (m, 511H), 1.11 (m, 1532H), 0.78 (s, 10H).

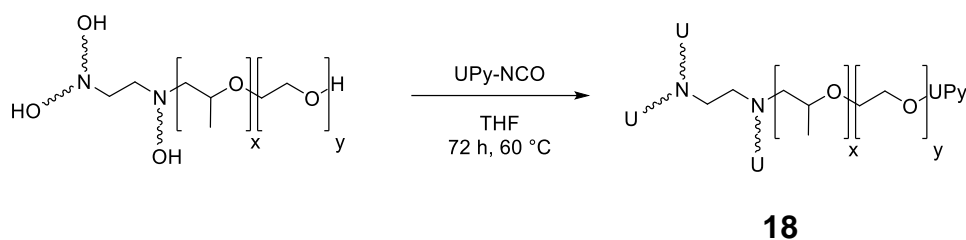
4.3.2.12 Synthesis of bivalent PIB-8000-UPy (**17**)



The synthesis was performed as described in literature with THF instead of CHCl₃ and was observed with TLC (CHCl₃). After the reaction, the solvent was removed in vacuum and the polymer was redissolved in *n*-hexane over night. The solid impurities were removed via centrifugation. The solvent was removed under reduced pressure and a colorless polymer was dried in high vacuum for 72 hours at 60 °C.²⁸

Yield: 5.1 g (73 %), ¹H-NMR (CDCl₃): 13.13 (m, 2H), 11.86 (s, 2H), 10.13 (s, 2H), 5.85 (m, 2H), 4.82 (t, *J* = 5.8 Hz, 1H), 3.97 (m, 9H), 3.20 (m, 7H), 2.22 (s, 4H), 1.42 (m, 462H), 1.11 (m, 1315H).

4.3.2.13 Synthesis of tetravalent Tetronic-UPy (**18**)

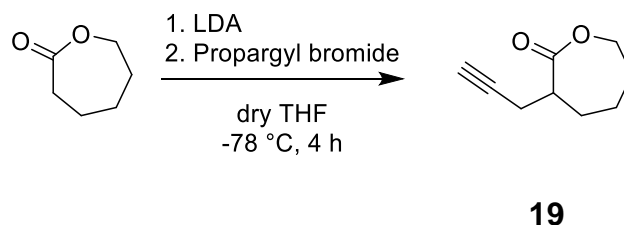


This reaction was conducted in the same way as the PIB polymer with accordingly more isocyanate and centrifugation in THF. The final polymer was precipitated twice in cold Et₂O and was dried in high vacuum for 72 hours at 60 °C. A residue of UPy isocyanate was still part of the final polymer because of slight solubility in all solvents suitable for Tetronic and same behavior during column chromatography in THF ($R_f = 0.9$ for both).²⁸

Yield: 3 g (60 %), ¹H-NMR (CDCl₃): 13.13 (m, 4H), 11.86 (s, 4H), 10.13 (s, 4H), 5.85 (m, 4H), 4.91 (m, 4H), 4.15 (m, 8H), 3.49 (114 H, m), 2.22 (s, 12H), 1.59 (m, 8H), 1.49 (m, 8H), 1.36 (m, 18 H), 1.22 (t, $J = 7.0$ Hz, 10H), 1.03 (73 H, d, $J = 5.9$ Hz).

4.3.3 Syntheses of other “Click”-reaction compounds

4.3.3.1 Synthesis of α -propargyl- ϵ -caprolactone (**19**)

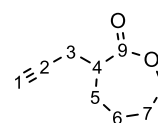


ϵ -Caprolactone was freshly distilled over CaH₂. A 2-molar solution of LDA (4.4 mL, 8.80 mmol) was dissolved in dry THF (30 mL) and ϵ -caprolactone (1 g, 8.65 mmol) was added at -78 °C. After stirring for one hour at -78 °C, propargyl bromide (1.2 mL, 10.56 mmol) was added to the reaction solution and stirred for three hours at -30 °C. The reaction mixture was quenched with saturated ammonium chloride solution (100 mL). The organic phase was extracted with Et₂O (3x 30 mL) and combined for washing with brine (3x 30 mL). Finally the organic layer is dried over Na₂SO₄ and the solvent was evaporated in vacuum. Column chromatography was performed in CHCl₃ ($R_f = 0.5$).²⁹⁰

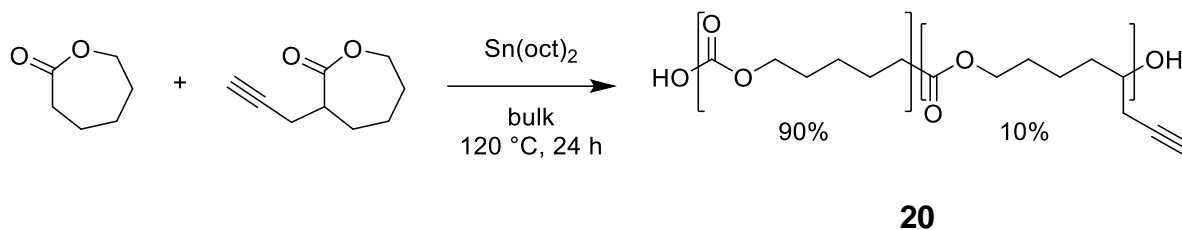
Product: slight yellow liquid

Yield: 200 mg (20 %)

¹H-NMR (400 MHz, CDCl₃): 4.29 (m, 2H, C₈), 2.78 (m, 1H, C₄), 2.63 (m, 1H, C₃), 2.36 (m, 1H, C₃), 2.12 (m, 2H, C₇), 1.99 (t-d, 1H, C₁), 1.69 (m, 1H, C₆), 1.46 (m, 2H, C₅). ¹³C-NMR (100 MHz, CDCl₃) 176.1 (C₉), 82.1 (C₂), 69.6 (C₈), 68.7 (C₁), 42.5 (C₄), 28.8, 28.7, 28.3, 21.9 (C₃).



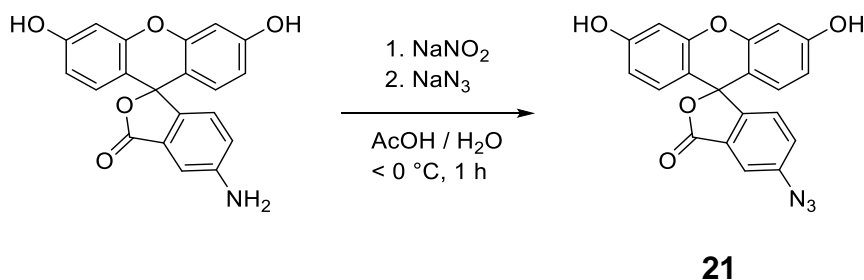
4.3.3.2 Synthesis of poly(ϵ -caprolactone)-co-(α -propargyl- ϵ -caprolactone) (**20**)



Over CaH_2 distilled ϵ -caprolactone (900 mg, 7.9 mmol) and dry α -propargyl- ϵ -caprolactone (100 mg, 0.7 mmol) were placed in a silanized schlenk-tube. In a counter flow of nitrogen catalytic amounts of $\text{Sn}(\text{Oct})_2$ were added. The bulk polymerization proceeded at 120 °C for 24 hours. The polymer was precipitated twice in cold Et_2O (2x200 mL). After drying in vacuum, a white powder (900 mg, 90 %) was obtained.²⁹⁰

$^1\text{H-NMR}$ (400 MHz, CDCl_3): 4.05 (t, $J = 6.7$ Hz, 210H), 3.63 (t, $J = 6.5$ Hz, 2H), 2.29 (t, $J = 7.5$ Hz, 210H), 1.98 (t, $J = 2.6$ Hz, 8H), 1.69 – 1.56 (m, 420H), 1.43 – 1.32 (m, 210H).

4.3.3.3 Synthesis of 5-Azido-fluorescein (**21**)



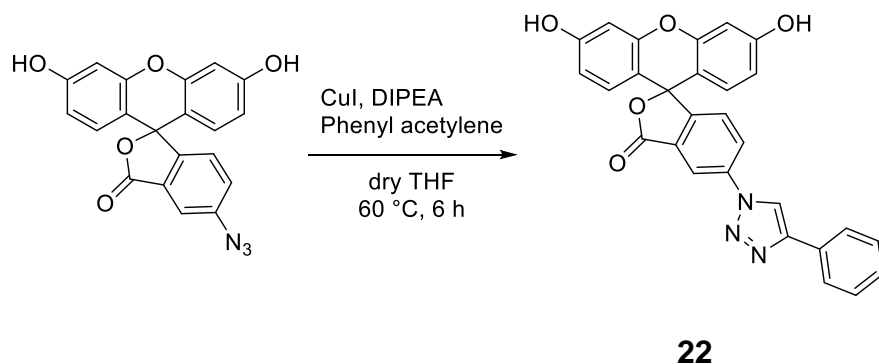
5-Amino-fluorescein (100.0 mg, 0.29 mmol) was dissolved in a water-acetic acid solution (10.0 mL, ratio 1 / 2). Ice water (5.0 mL) was added and the reaction mixture was cooled down with an ice bath. The temperature of the reaction mixture was kept below 0 °C during the whole synthesis. NaNO_2 (41.4 mg, 0.60 mmol) was dissolved in water (0.25 mL) and was added drop wise to the solution. After stirring for 15 minutes, NaN_3 (58.5 mg, 0.90 mmol) was dissolved in water (0.25 mL) and was added dropwise to the solution. After 20 minutes a yellow precipitate was formed. The reaction mixture was centrifuged and the precipitate was collected and was washed with HCl (1 M, 2x 50 mL) and water (3x 50 mL). The crude product was dried in a desiccator over night. Final purification was done by flash column chromatography in acetone ($R_f = 0.9$). A yellow powder was obtained (76.0 mg, 0.20 mmol, 70 %).³¹³

$R_f = 0.4$ (10:1 $\text{CHCl}_3/\text{MeOH}$); $R_f = 0.9$ in acetone

$^1\text{H-NMR}$ (400 MHz, $d_6\text{-DMSO}$): δ 6.51-6.63 (m, 4H), 6.67 (d, 2H, $J = 2.3$ Hz), 7.30 (d, 1H, $J = 8.2$ Hz), 7.51 (dd, 1H, $J = 8.2$ Hz, $J = 2.3$ Hz), 7.64 (d, 1H, $J = 2.2$ Hz), 10.13 (s, 2H); $^{13}\text{C-NMR}$ (100 MHz, $d_6\text{-DMSO}$): δ 83.3, 102.2, 109.3, 112.6, 114.4, 125.6, 126.8, 128.0, 129.0, 141.7, 148.7, 151.9, 159.5, 167.8; HRMS (ESI): Calculated for $[\text{C}_{20}\text{H}_{10}\text{O}_5\text{N}_3]^-$ [M-H] $^-$

372.07, found 372.06; FT-IR: ν 3429 cm^{-1} (-OH), 2120 cm^{-1} (-N₃), 1729 cm^{-1} (C=O), 1633 cm^{-1} (C=C).

4.3.3.4 "Click"-reaction of 5-azido-fluorescein (**22**)



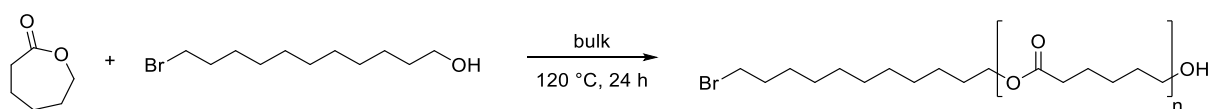
The reaction was performed under a dry atmosphere of nitrogen. 5-Azido-fluorescein (50.0 mg, 0.13 mmol) and catalytic amounts of CuI were dissolved in dry DMF (2 mL) and were purged with nitrogen for 30 minutes. DIPEA (39.0 mg, 0.30 mmol, 51 μL) and phenyl acetylene (15.3 mg, 0.15 mmol, 17 μL) were added in a counter flow of nitrogen. The reaction mixture was stirred at 60 °C for six hours. The progress of the reaction was followed by FT-IR spectroscopy. After completion of the reaction, the solvent was removed under vacuum. Final purification was done by flash column chromatography in acetone ($R_f = 0.9$). An orange powder was obtained (60.0 mg, 0.13 mmol, 97 %).

$R_f = 0.05$ (10:1 $\text{CHCl}_3/\text{MeOH}$); $R_f = 0.9$ in acetone

¹H-NMR (400 MHz, d_6 -DMSO): δ 6.58 (d, 1H, $J = 9.6$ Hz), 6.71 (d, 2H, $J = 6.6$ Hz), 7.40 (dd, 1H, $J = 17.3$ Hz, 9.9 Hz), 7.48-7.63 (m, 2H), 7.98 (d, 1H, $J = 7.1$ Hz), 8.43 (d, 1H, $J = 8.3$ Hz), 8.54 (s, 1H), 9.59 (s, 1H), 10.16 (s, 2H); ¹³C-NMR (100 MHz, d_6 -DMSO): δ 102.8, 109.5, 113.2, 115.8, 120.5, 125.8, 126.4, 127.5, 128.4, 128.9, 129.5, 129.7, 138.1, 148.1, 152.4, 160.7, 168.1; FT-IR: ν 3080 cm^{-1} (-OH), 1748 cm^{-1} (C=O), 1589 cm^{-1} (C=C).

4.3.4 Syntheses of the mechanophores

4.3.4.1 Synthesis of bromo-poly(ϵ -caprolactone) (**23**)

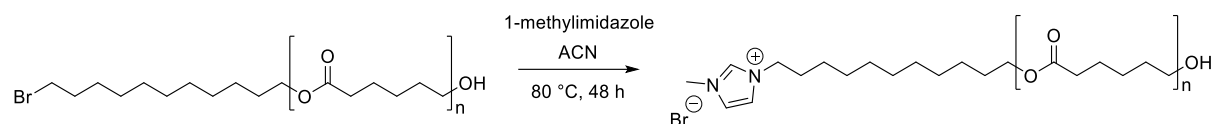


Over CaH_2 distilled ϵ -caprolactone (2.16 g, 2 mL, 18.92 mmol) was placed in a silanized Schlenk-tube. In a counter flow of nitrogen the 1-bromo-undecanol (111 mg, 14.83 mmol) and catalytic amounts of $\text{Sn}(\text{Oct})_2$ were added. The bulk polymerization

proceeded at 120 °C for 24 hours. The polymer was precipitated twice in cold Et₂O (2x200 mL). After drying in vacuum, a white powder (1.8 g, 90 %) was obtained.

¹H NMR (400 MHz, d₁-CDCl₃): δ 4.05 (t, J = 6.7 Hz, 33H), 3.63 (t, J = 6.5 Hz, 2H), 3.39 (t, J = 6.9 Hz, 2H), 2.29 (t, J = 7.5 Hz, 33H), 1.69 – 1.58 (m, 66H), 1.43 – 1.33 (m, 33H).

4.3.4.2 Synthesis of 1-methylimidazole-poly(ϵ -caprolactone) (**24**)

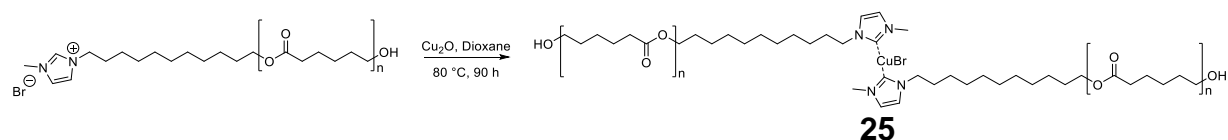


24

Bromo-PCL (1 g, 0.2 mmol) and 1-methylimidazole (33 mg, 32 μ L, 0.4 mmol) were dissolved in refluxing ACN (20 mL). The reaction mixture was stirred at 80 °C for 48 hours. The solvent was removed under reduced pressure and the polymer was precipitated twice in cold Et₂O (2x100 mL). After drying in vacuum, a white powder (1 g, 99 %) was obtained.

¹H NMR (400 MHz, d₁-CDCl₃): δ 10.64 (s, 1H), 7.27 (t, J = 1.8 Hz, 1H), 7.22 (t, J = 1.7 Hz, 1H), 4.30 (t, J = 7.2 Hz, 2H), 4.11 (s, 3H), 4.05 (t, J = 6.7 Hz, 37H), 3.63 (t, J = 6.5 Hz, 2H), 2.29 (t, J = 7.5 Hz, 37H), 1.69 – 1.58 (m, 74H), 1.43 – 1.33 (m, 37H).

4.3.4.3 Synthesis of PCL-mechanophore (**25**)

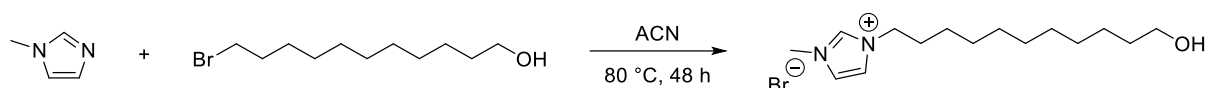


25

1-Methylimidazole-PCL (500 mg, 0.1 mmol) and Cu₂O (72 mg, 0.5 mmol) were mixed into dry 1,4-dioxane (10 mL) and molecular sieve 3A was added. The reaction mixture was stirred at 80 °C for 90 hours. After filtration, the solvent was removed under reduced pressure and the polymer was precipitated twice in cold Et₂O. Final purification was performed by flash column in CHCl₃ / MeOH (95 : 5). No further purification of the PCL mixture was possible without decomposition of the PCL-mechanophore. After drying in vacuum a white polymer (400 mg, 80 %) was obtained.¹⁹²

¹H NMR (400 MHz, d₁-CDCl₃): δ 6.16 (dd, J = 8.5, 2.9 Hz, 1H), 4.06 (t, J = 6.7 Hz, 37H), 3.64 (t, J = 6.5 Hz, 2H), 3.60 – 3.55 (m, 1H), 3.24 (s, 2H), 2.30 (t, J = 7.5 Hz, 37H), 1.69 – 1.58 (m, 74H), 1.43 – 1.33 (m, 37H).

4.3.4.4 Synthesis of 1-methylimidazole-undecanol (C11) (26)

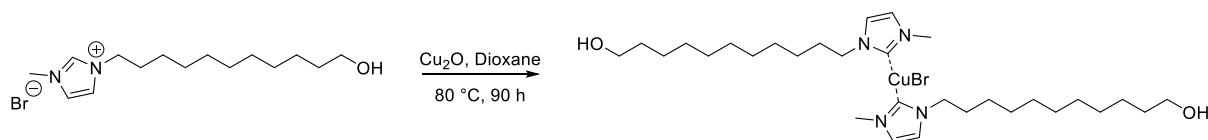


26

11-Bromo-1-undecanol (3 g, 12 mmol) and 1-methylimidazole (900 mg, 877 μ L, 11 mmol) were dissolved in refluxing ACN (8 mL). The reaction mixture was stirred at 80 °C for 48 hours. During cooling down to room temperature, a white precipitate was formed, which was subsequently washed with Et₂O (10x20 mL). After drying in vacuum, a white powder with a yield of 97 % (3.8 g) was obtained.¹⁹²

¹H-NMR (400 MHz, d₆-DMSO): δ 9.18 (s, 1H), 7.79 (t, J = 1.8 Hz, 1H), 7.72 (t, J = 1.7 Hz, 1H), 4.31 (s, 1H), 4.16 (t, J = 7.2 Hz, 2H), 3.85 (s, 3H), 3.36 (d, J = 3.0 Hz, 2H), 1.86 – 1.68 (m, 2H), 1.38 (dd, J = 13.2, 6.6 Hz, 2H), 1.24 (s, 14H); ¹³C-NMR (100 MHz, d₆-DMSO): δ 136.9, 124.0, 122.7, 61.1, 49.2, 33.0, 29.8, 29.5, 29.4, 29.3, 29.2, 28.8, 25.9, 25.0; HRMS (ESI): Calculated for [C₁₅H₂₉ON₂]⁺ [M]⁺ 253.26, found 253.23.

4.3.4.5 Synthesis of C11-mechanophore (27)

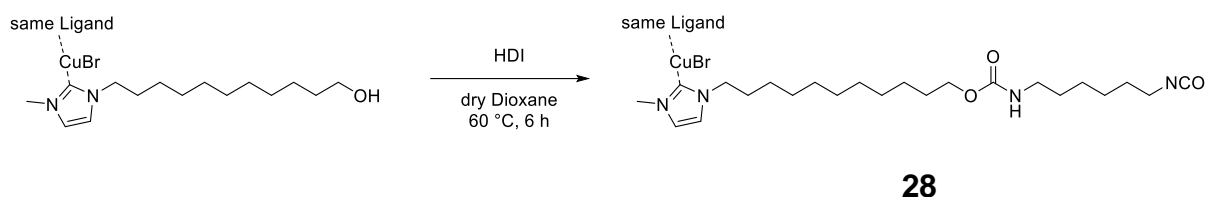


27

1-Methylimidazole-undecanol (183 mg, 0.55 mmol) and Cu₂O (394 mg, 2.75 mmol) were dissolved in dry 1,4-dioxane (10 mL) and molecular sieve 3A was added. The reaction mixture was stirred at 100 °C for 48 hours. After filtration, the solvent was removed under reduced pressure and the crude product was dissolved in Et₂O to precipitate side products. After removing the solvent under reduced pressure, final purification was performed by column chromatography in CHCl₃ / MeOH (gradient: 40:1 to 20:1) to obtain the C11-mechanophore (143 mg, 40 %).¹⁹²

¹H-NMR (400 MHz, CDCl₃): δ 6.15 (dd, J = 7.3, 2.9 Hz, 4H), 3.62 (t, J = 6.6 Hz, 4H), 3.60 – 3.54 (m, 4H), 3.24 (s, 6H), 1.68 – 1.50 (m, 10H), 1.37 – 1.22 (m, 28H); ¹³C-NMR (100 MHz, CDCl₃): δ 153.2, 111.1, 110.0, 62.9, 43.6, 33.0, 29.5, 29.4, 29.4, 29.3, 29.3, 26.5, 25.7.

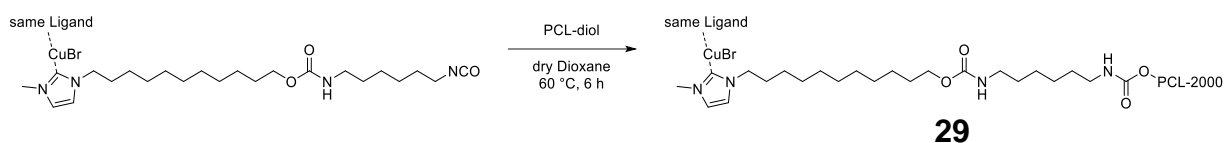
4.3.4.6 Synthesis of NCO-mechanophore (28)



C11-Mechanophore (112 mg, 0.17 mmol) and HDI (1 mL, 5.9 mmol) were dissolved in dry 1,4-dioxane (10 mL). The reaction mixture was stirred at 60 °C for six hours. After cooling down in the fridge, the white powder was washed with petrol ether (3x50 mL) and dried in vacuum.¹⁹²

¹H NMR (400 MHz, CDCl₃): δ 6.15 (dd, J = 7.2, 2.9 Hz, 4H), 3.63 (t, J = 6.6 Hz, 2H), 3.60 – 3.54 (m, 4H), 3.31 (t, J = 6.6 Hz, 2H), 3.29 (t, J = 6.7 Hz, 2H), 3.24 (s, 6H), 1.68 – 1.50 (m, 20H), 1.37 – 1.22 (m, 40H).

4.3.4.7 Synthesis of PCL-urethane-mechanophore (29)

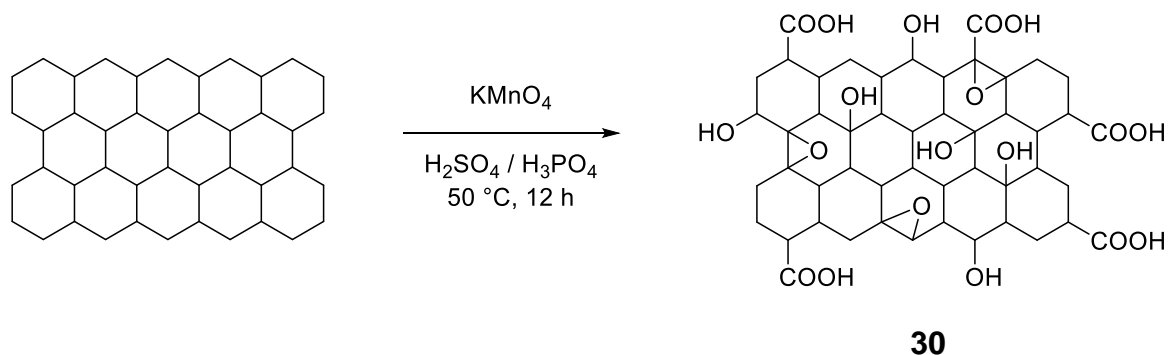


NCO-Mechanophore (0.15 mmol) and PCL-2000-diol (3 g, 1.5 mmol) were dissolved in dry 1,4-dioxane (10 mL). The reaction mixture was stirred at 60 °C for six hours. After filtration, the solvent was removed under reduced pressure and the polymer was precipitated twice in cold Et₂O.¹⁹²

¹H NMR (400 MHz, d₁-CDCl₃): δ 6.16 (dd, J = 8.5, 2.9 Hz, <1H), 4.06 (t, J = 6.7 Hz, 35H), 2.30 (t, J = 7.5 Hz, 35H), 1.69 – 1.58 (m, 70H), 1.43 – 1.33 (m, 35H).

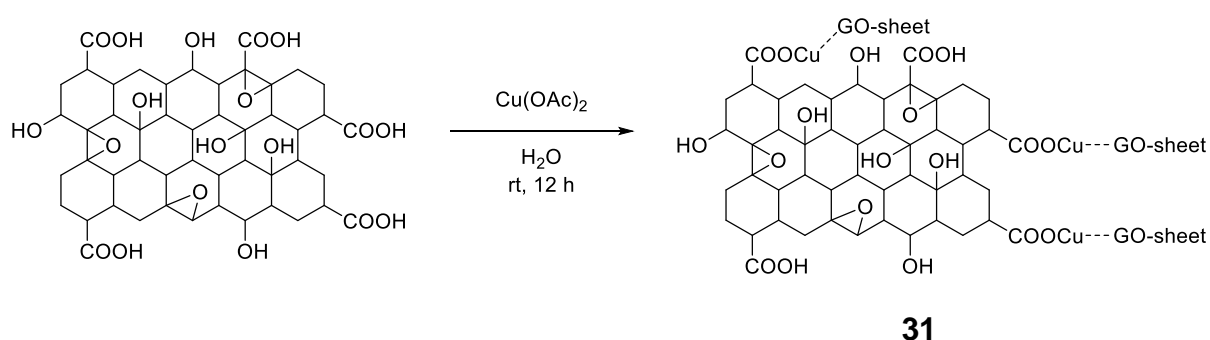
4.3.5 Syntheses of carbon materials

4.3.5.1 Synthesis graphene oxide (GO) (30)



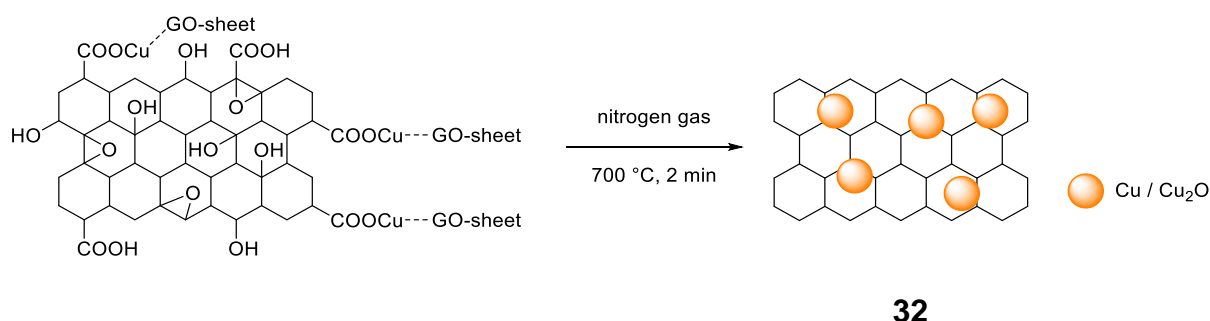
To a solution of concentrated $\text{H}_2\text{SO}_4 / \text{H}_3\text{PO}_4$ (360 mL / 40 mL) Graphite (3 g, 20 μm flakes) was added and the reaction mixture was cooled in an ice bath. The large amount of KMnO_4 (18 g) was slowly added to ensure that the temperature didn't exceed 50 °C. The reaction mixture was heated to 50 °C for 12 hours. After cooling down to room temperature the mixture was poured into a large amount of ice water (400 mL) containing H_2O_2 (5 mL, 35 wt%). The formed precipitate was washed with water (1x200 mL), HCL (2x200 mL, 1 M) and several times with water (5x 200 mL). The cleaned graphene oxide was freeze-dried for 48 hours and yielded 5 g. **FWHM:** 11.12° - 10.01° = **1.11°**.²⁹²

4.3.5.2 Synthesis of graphene oxide + Cu^{2+} (GO-Cu^{2+}) (31)



Graphene oxide (1 g) was dispersed in water (300 mL) by ultrasonication (30% amplitude, 30 min). Subsequently, copper(II)-acetate-hydrate (336 mg, 1.65 mmol) was added, sonicated again for five minutes and stirred at room temperature overnight. After several washing steps with water (5x200 mL) the graphene oxide containing Cu^{2+} ions was freeze-dried and yielded in 1 g GO-Cu^{2+} . **FWHM:** 11.96° - 10.59° = **1.37°**.²⁷⁶

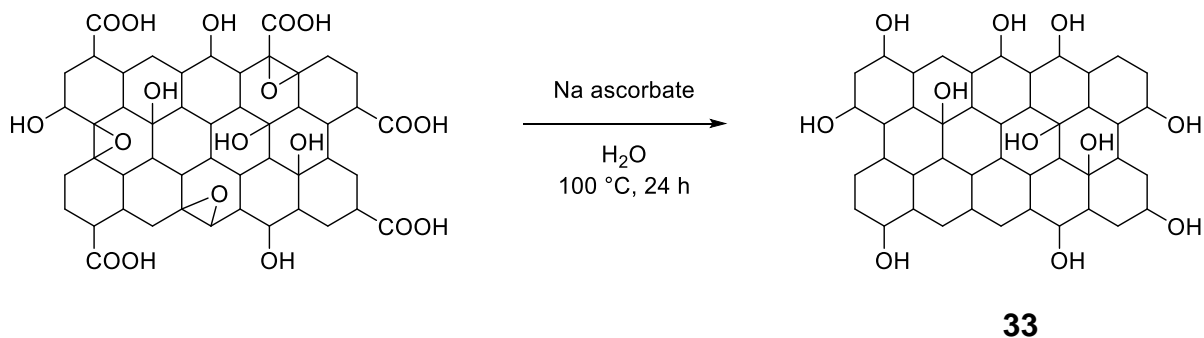
4.3.5.3 Synthesis of thermally reduced graphene oxide - $\text{Cu}/\text{Cu}_2\text{O}$ nanoparticles (TRGO) (32)



GO-Cu^{2+} (1 g) was placed into the quartz flask of an oven and flushed with nitrogen for 60 minutes. The oven was then heated to 700 °C with a heating rate of 10 °C/min and kept at 700 °C for two minutes. Afterwards the oven was cooled down to room

temperature under nitrogen atmosphere. The cooled down TRGO flakes were collected with a yield of 50 wt% (500 mg). **FWHM**: $26.65^\circ - 24.76^\circ = 1.89^\circ$.²⁷⁶

4.3.5.4 Synthesis of chemically reduced graphene oxide (CRGO) (33)



GO (1 g) was placed into a flask with water (50 mL) and flushed with nitrogen for 30 minutes. Sodium ascorbate (1 g) was added in a counter flow of nitrogen. The reaction mixture was refluxed for 24 hours. After cooled down to room temperature, the black flakes were filtered off and washed several times with water (5x100 mL) and acetone (5x100 mL). After drying in vacuum black flakes with a yield of 550 mg (55 wt%) were obtained. **FWHM**: $28.18^\circ - 22.12^\circ = 6.06^\circ$

4.3.5.5 Synthesis of nanocapsules

Polymer PVF (100 mg) and trivalent azide (100 mg) were dissolved in DCM (2 mL) and emulsified into SDS-solution (10 mL, $1 \text{ mg}\cdot\text{mL}^{-1}$) at 1100 rpm. The emulsion was sonicated in an ice bath for two minutes (30 s pulse, 15 s pause). In the end the solvent was evaporated at room temperature over night while stirring with 500 rpm. After removing micrometer sized impurities by filtration the capsule dispersion was freeze-dried for 24 hours. With slight modifications to the organic phase, 3-azido-hydroxycoumarin was co-encapsulated within PVF-azide capsules. Therefore, DCM (2 mL) was mixed with MeOH (200 μL), 3-azido-hydroxycoumarin (3 mg), trivalent azide (100 mg) and PVF (100 mg) to obtain a homogeneous organic phase. The nanocapsules showed a hydrodynamic diameter of $208 \pm 30 \text{ nm}$. The SEM image of freeze-dried azide capsules also confirmed capsules in the size of around 200 nm. The ratio of azide to PVF was analyzed with NMR, using toluene (8.7 mg, 10 μL) as a standard and calculated to 45 wt% azide and 55 wt% PVF. All other encapsulations with PLLA and PCL used the same method with modified system parameters (Chapter 3.5.3).²⁰⁷

5.0 Summary

A novel 3D-printing process, where a multiple-dispensing system allowed printing of liquid capsules into a solid, thermoplastic matrix, was developed. The approach allows to generate functional composite materials based on a biodegradable polymer (PCL) filled with nanocapsules and micro-scaled, 3D-printed, liquid-filled capsules. Grids, generated during printing, were filled with different hydrophobic liquids, starting with simple farnesol and limonene, continuing with trivalent alkynes, useful for a subsequent capsule based, self-healing material. Voids with sizes between 100 micron and 800 microns can be reliably printed (Figure 84). It was demonstrated that two reactive components can be efficiently separated *via* 3D-printed capsules and nanocapsules being directly embedded into the PCL-polymer before printing. Thermal control of the printing process allowed retaining sufficient reactivity for a subsequent “click”-reaction, underscoring the possibility to embed two separate, highly reactive components into one and the same thermoplastic material. This approach was used for a proof-of-concept self-healing material based on capsules and a triggered “click”-reaction, visualized by a fluorogenic dye.

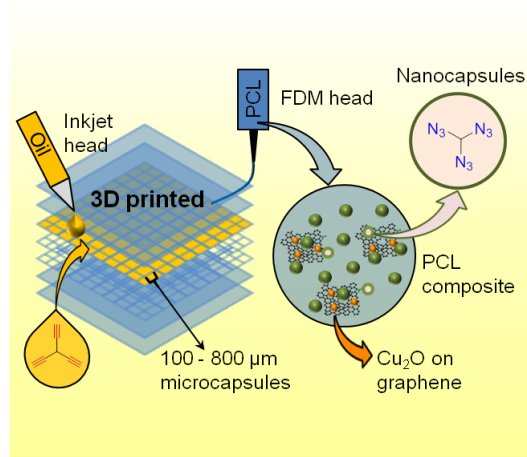


Figure 84: 3D-printing of core-shell capsule composites.

In the second part, the 3D-printing of copper(I)-bis(NHC)-mechanophores was investigated using a multicomponent-printing-system, generating polymer-composites with stress-detecting properties. As demonstrated here the printing-results and final activities of the three different mechanophores strongly depended on the chain length used under the 3D-printing conditions. Short chain C11-mechanophores (**29**) can easily be mixed with the printable PCL polymer and subsequently be extruded retaining their mechanophoric activity. Higher molecular weight mechanophores (**27**, $M_{w, PCL-M} = 1800$ Da, and **31**, $M_{w, Urethane-M} = 2000$ Da) lost their mechanophoric activity during printing, although both showed catalytic activity (1.0 – 1.7 %) when being solvent cast in molds. The fabrication of multilayer-polymers, where the stress-reporting tool is placed in a specific part of the specimen can be realized (Figure 85).

3D-printing: Mechanophore composite

Stress sensing by mechanoactive
"Click"-reaction

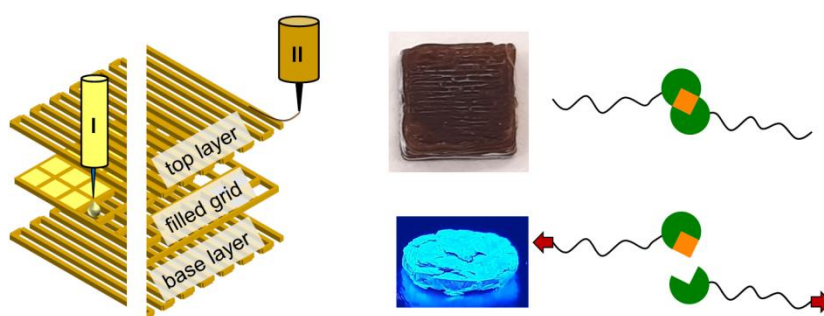


Figure 85: 3D-printing of labile copper(I)-(NHC)-mechanophores.

The last big topic of the thesis was about printing of amorphous polymers with low glass transition temperatures, achieved by attaching hydrogen-bonding groups to the end of the polymer chain. Self-supporting, supramolecular PIB-based polymers were successfully printed and compared to more polar based PEG supramolecular polymers, which did not show a phase separation between polymer chain and the barbiturate moieties. The polar PEGs did not show a good printing behavior or no shape stability compared to the supramolecular PIBs, clearly due to the missing supramolecular cluster (network) formation, and their hygroscopic nature. The supramolecular PIB polymers with linear and star architecture showed a rubber like behavior and were able to form self-supported 3D-printed objects at room temperature (Figure 86), reaching printing resolutions and polymer strand diameters down to 200 - 300 μm . The phase segregated structure (micellar aggregates) enabled the tune-ability for the printability. The blends and composites allowed addressing a proper printability window and self-supporting strength.

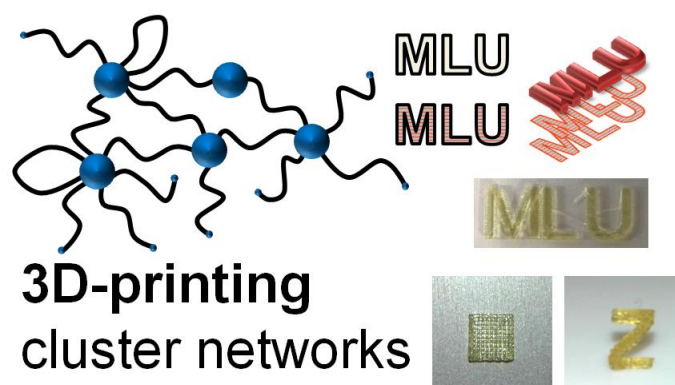


Figure 86: 3D-printing of supramolecular polymers and their composites.

6.0 Appendix

6.1 Chemical reaction between trivalent azide and trivalent alkyne.

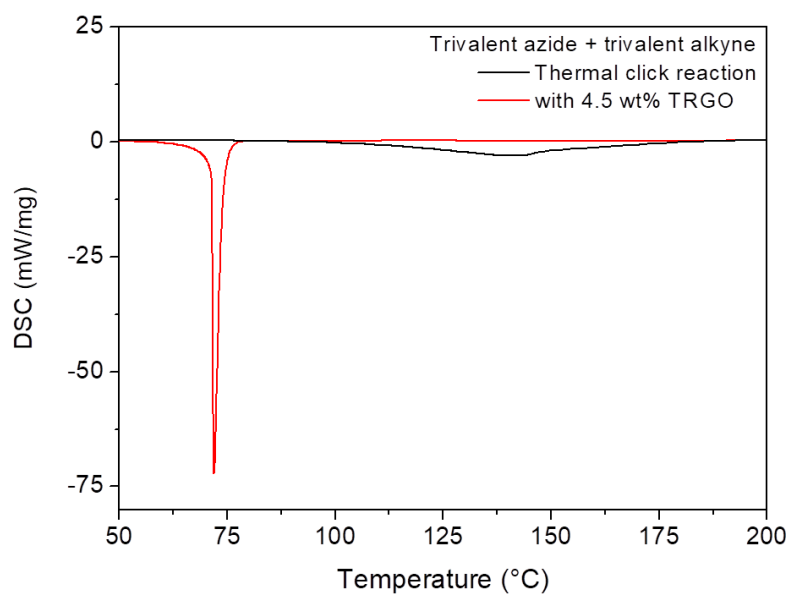


Figure S 1. Thermal and TRGO-catalyzed "click"-reaction of trivalent azide with trivalent alkyne.

6.2 Chemical reaction between alkyne_PCL with trivalent azide.

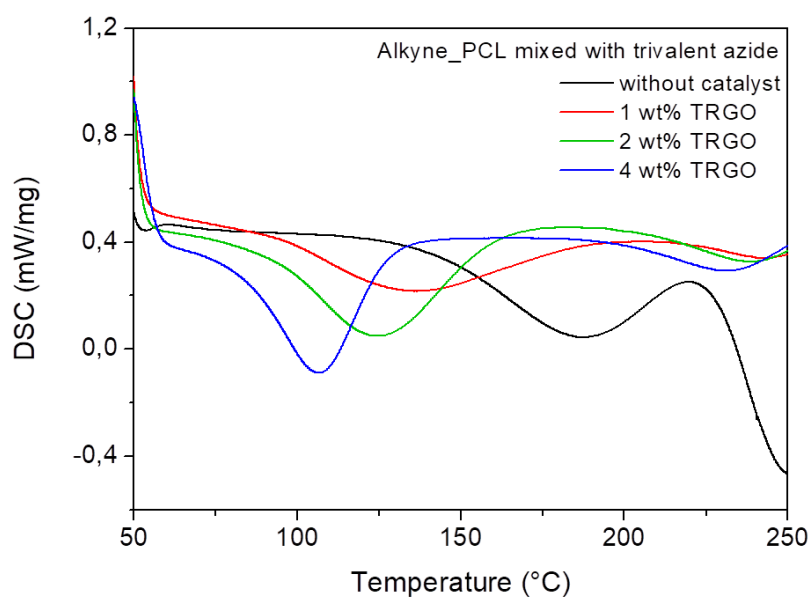


Figure S 2. Thermal and TRGO-catalyst "click"-reaction of trivalent azide and alkyne-PCL.

6.3 Chemical reaction between BEPE and trivalent azide.

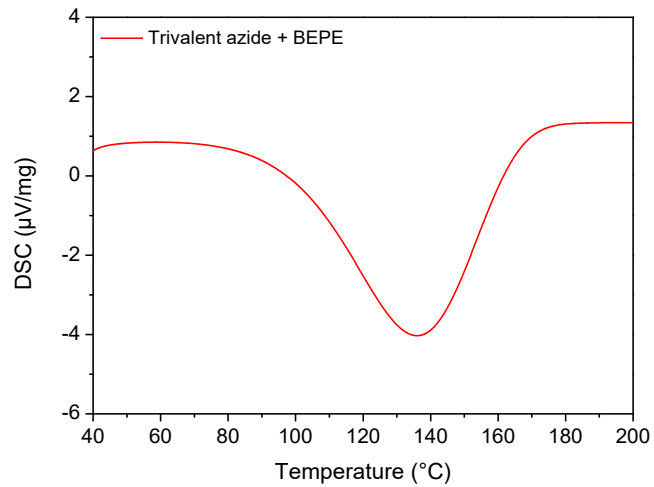


Figure S 3: Thermal "click"-reaction of trivalent azide with BEPE.

6.4 Nanocapsules of trivalent azide in PVF polymer shells.

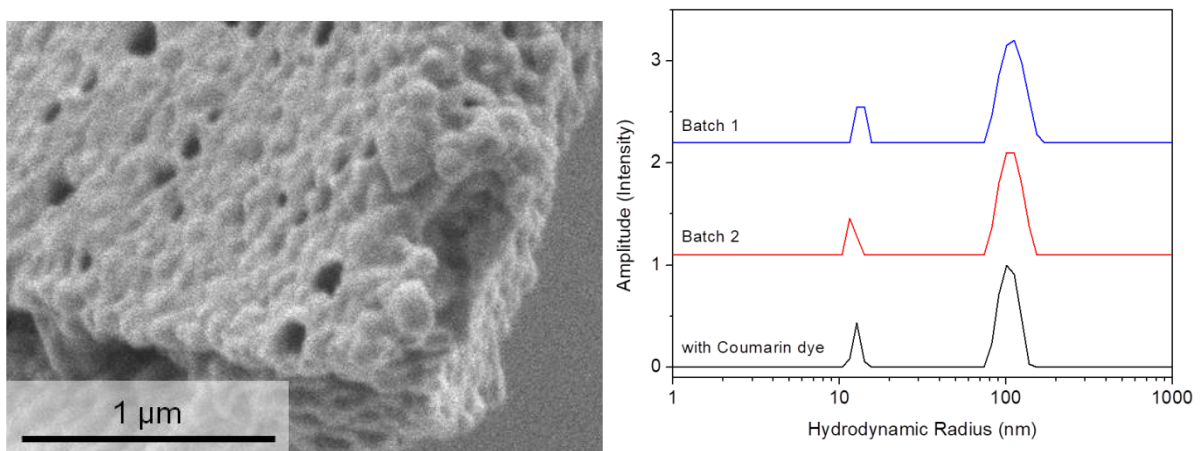


Figure S 4: SEM image of freeze-dried PVF-azide capsules with a diameter around 200 nm as well as dynamic light scattering measurements of the hydrodynamic radius of 100 nm in aqueous SDS-solution. The small peaks refer to single chain nanoparticles and SDS micelles.

6.5 PCL analysis *via* GPC and DSC before and after 3D-printing.

Table S 1: Polycaprolactone analysis before and after printing with GPC and DSC methods.

Polymer	M_n [Da]	M_w [Da]	PDI	ϑ_{Peak} [°C]	ΔH_m [J·g ⁻¹]
PCL, before	47000	80000	1.7	61.9	90.7
Limonene	34000	55000	2.0	62.2	96.5
Linalool	33000	54000	2.0	60.4	92.2
Farnesol	34000	56000	2.0	60.2	90.3
TA	32000	52000	2.0	60.1	82.0

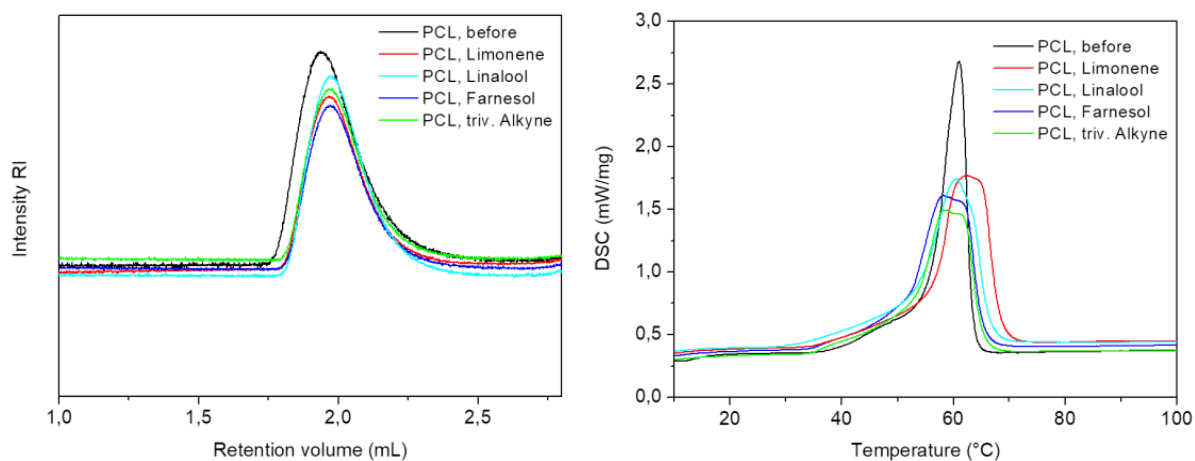


Figure S 5: GPC measurement of PCL before printing and the printed capsule systems (l.) and DSC measurement of the same polymers (r.).

6.6 DSC analysis of PCL composites before and after 3D-printing.

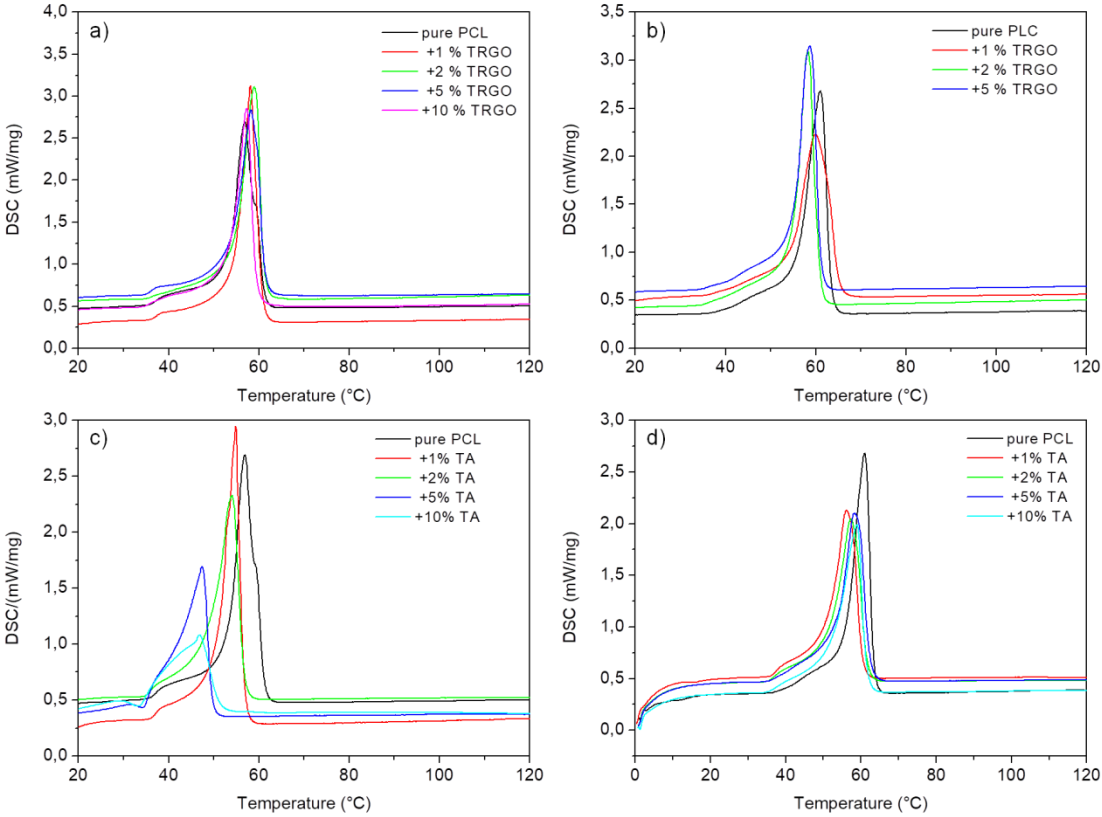


Figure S 6: DSC measurements of PCL and its composites of TRGO (1 – 10 wt%) and trivalent alkyne (TA, 1 – 10 wt%) under nitrogen atmosphere with a heating rate of 10 °C·min⁻¹. Freshly mixed and dried composites of PCL and TRGO (a) as well as after 3D-printing (b) were analyzed for their thermal properties. The PCL composites with the liquid TA were measured before (c) and after 3D-printing (d).

6.7 Calibration of 3-Azido-7-hydroxycoumarin in THF.

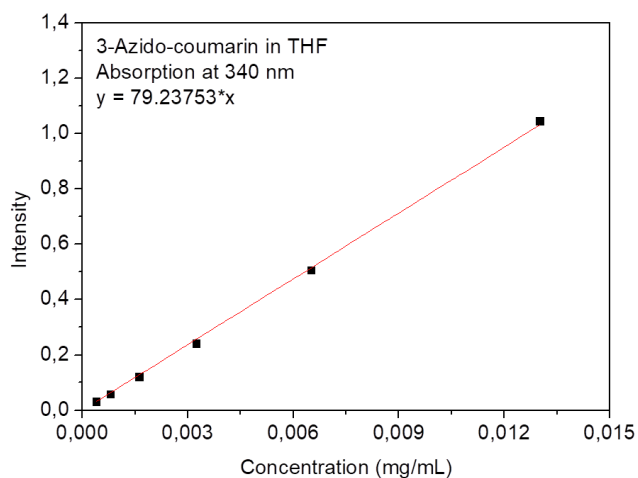


Figure S 7: Calibration curve for 3-Azido-hydroxycoumarin in THF.

With the calibration curve, the content of 3-azido-coumarin for freeze-dried core-shell nanocapsules containing PVF, trivalent azide and the just mentioned dye could be measured and calculated. Therefore, capsules samples (~0.5 mg) were dissolved in THF (3 mL) and the absorption intensity at 340 nm was detected and the data was analyzed (Table S2).

Table S 2: Encapsulation of coumarin dye within PVF-azide capsules.

	Capsule [mg]	Coumarin [μ g]	wt%	Encapsulation [%]
Theoretical	200	3000	1.48	100
Sample 1	0.48	5.4	1.12	76
Sample 2	0.49	5.8	1.18	80
Average		5.6 ± 0.2	1.15 ± 0.03	78 ± 2

6.8 Analysis of carbon based materials.

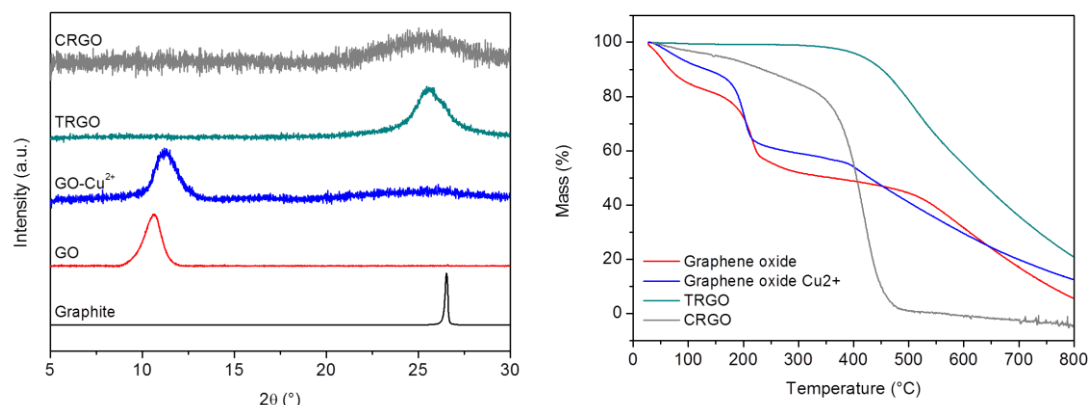


Figure S 8: Powder-XRD analysis for the different reaction steps for TRGO synthesis as well as CRGO (l.). The thermal gravimetric analysis of the intermediate and final products are shown, too (r.).

The different synthesized graphene modifications were analyzed *via* powder x-ray diffraction in a short 2θ range of 5° - 30° . The main reflexes of each compound were visible and indicated a successful conversion, starting from graphite over graphene oxide to the reduced graphene oxides.

Table S 3: Results of the XRD analysis.

Compound	Reflex (°)	FWHM (°)
Graphite	26.54	0.16
GO	10.65	1.11
GO-Cu ²⁺	11.18	1.37
TRGO	25.56	1.89
CRGO	25.42	6.06

Thermal gravimetric analysis was the next very useful tool to analyze the graphene modifications. The measuring conditions were nitrogen atmosphere ($20 \text{ mL}\cdot\text{min}^{-1}$), heating rate $10 \text{ }^\circ\text{C}\cdot\text{min}^{-1}$ and a temperature range of 40 - $800 \text{ }^\circ\text{C}$.

6.9 TEM analysis of TRGO based material.

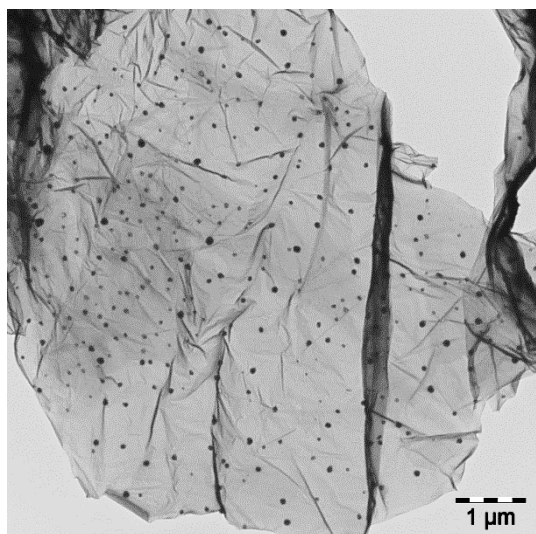


Figure S 9. TEM image of the final TRGO-catalyst containing Cu / Cu₂O nanoparticles.

6.10 TEM analysis of CRGO based material.

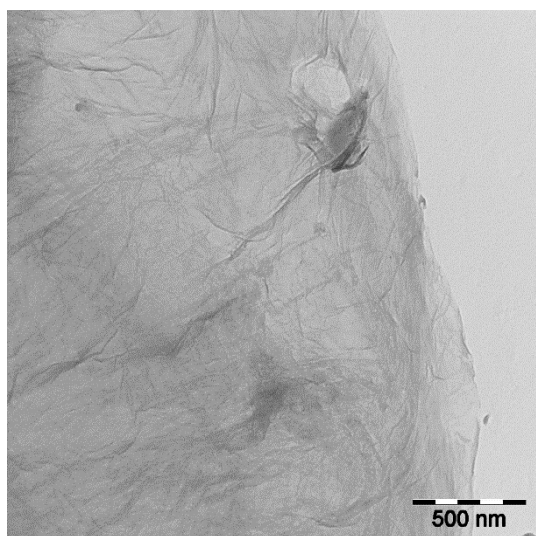


Figure S 10. TEM image of CRGO.

6.11 FAAS analysis of copper content.

Table S 4. Copper content was determined by FAAS measurement of a burned sample (800 °C, 1 hour, air) in nitric acid (2 M).

Sample	Weight	Concentration	FAAS		Cu on TRGO	
	(mg)	(mg·L ⁻¹)	(mg·L ⁻¹)	(wt%)	(mmol·L ⁻¹)	(mmol·mg ⁻¹)
TRGO	3.4	68	5.67	8.34	0.0892	0.0013

6.12 Rheology measurements for 3D-printing.

The following rheology measurements are based on the following temperature labeling, if not mentioned otherwise.

- ★ 50 °C ▲ 80 °C ◀ 110 °C
- 60 °C ▼ 90 °C ▶ 120 °C
- 70 °C ◆ 100 °C ● 130 °C

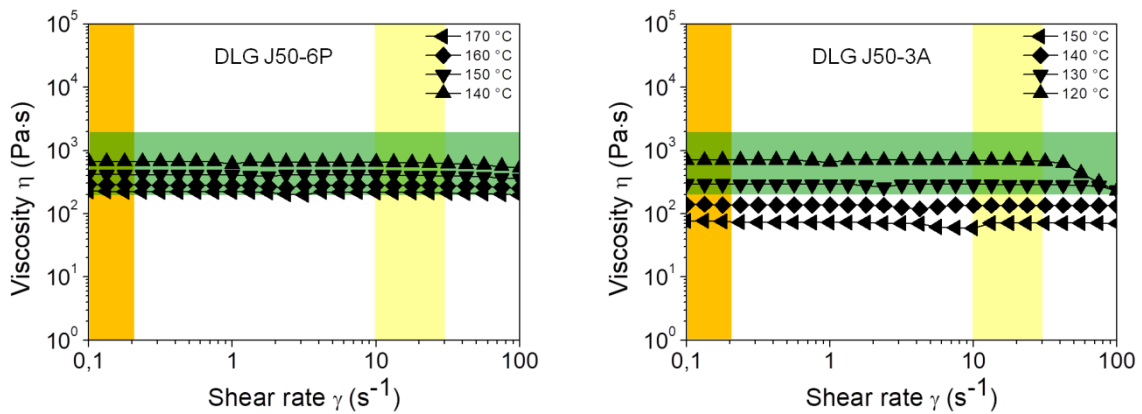


Figure S 11. Rheology measurements of viscosity-shear rate-temperature dependence for DLG J50-6P (32 kDa, l.) and DLG J50-3A (17 kDa, r.).

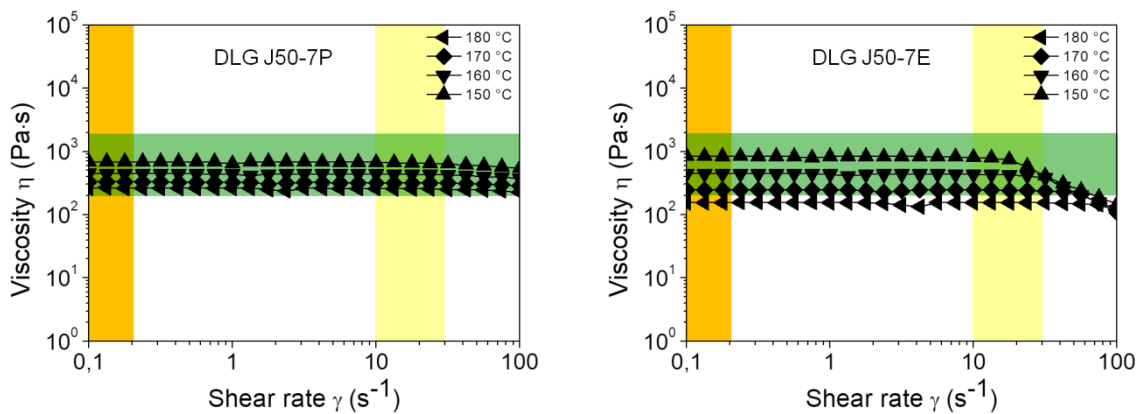


Figure S 12. Rheology measurements of viscosity-shear rate-temperature dependence for DLG J50-7P (46 kDa, l.) and DLG J50-7E (41 kDa, r.).

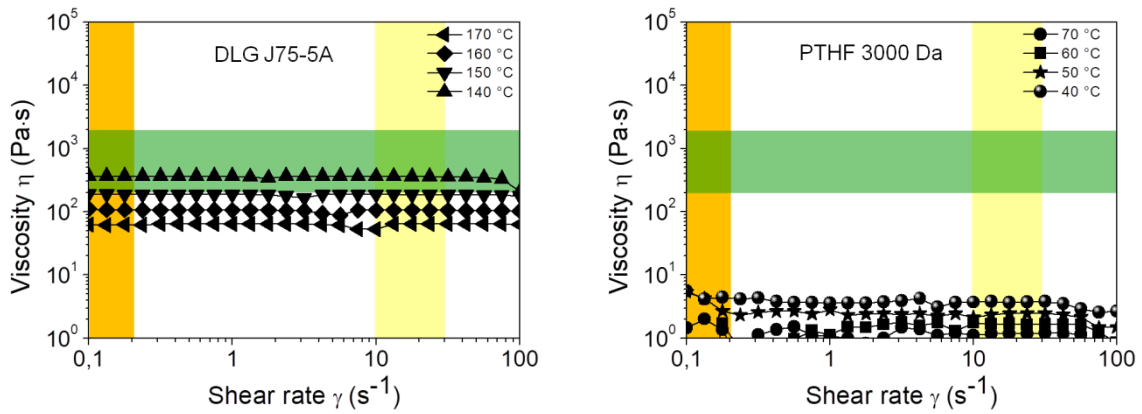


Figure S 13. Rheology measurements of viscosity-shear rate-temperature dependence for DLG J75-5A (27 kDa, l.) and PTHF (3000 Da, r.).

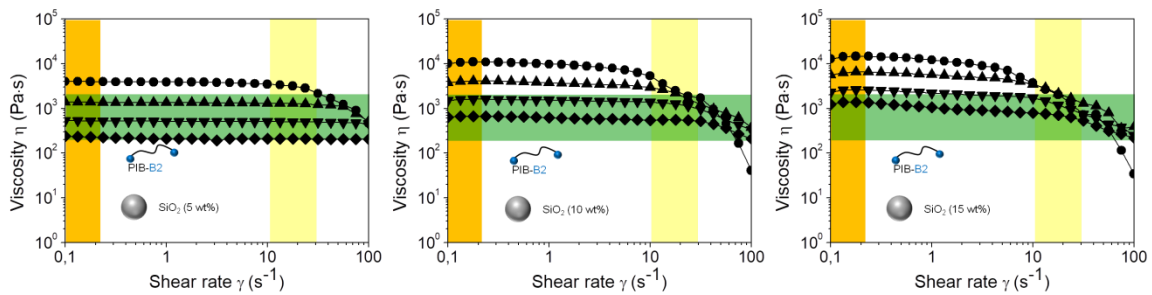


Figure S 14. Rheology measurements of viscosity-shear rate-temperature dependence for PIB-B2-SNP 5-15 in a temperature range of 70 – 100 °C.

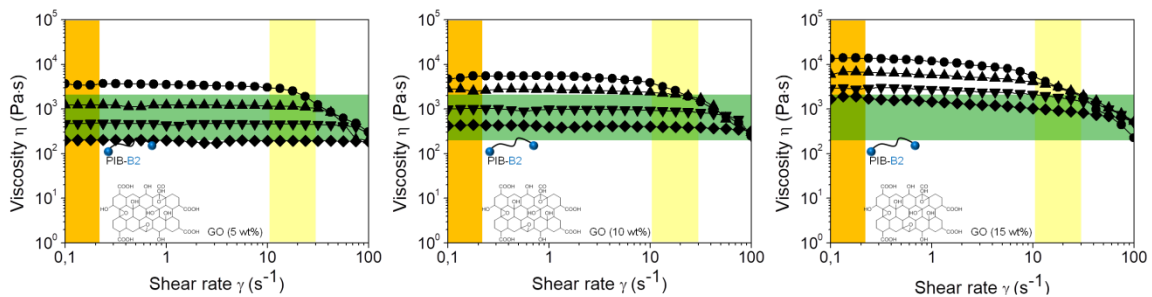


Figure S 15. Rheology measurements of viscosity-shear rate-temperature dependence for PIB-B2-GO 5-15 in a temperature range of 70 – 100 °C.

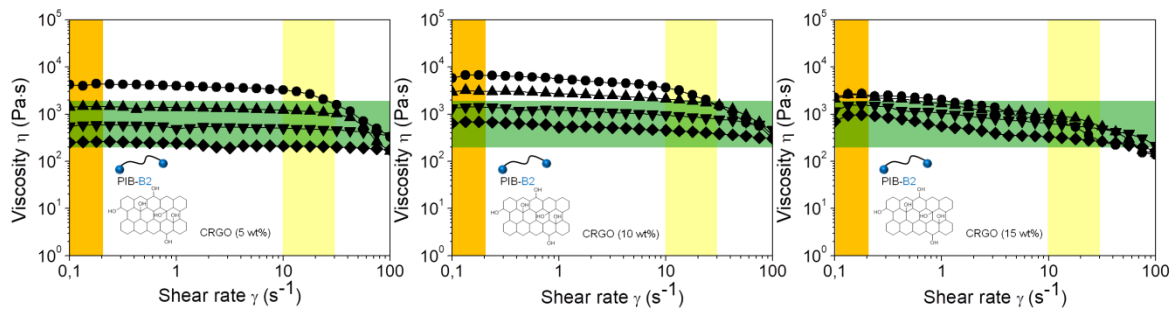


Figure S 16. Rheology measurements of viscosity-shear rate-temperature dependence for PIB-B2-CRGO 5-15 in a temperature range of 70 – 100 °C.

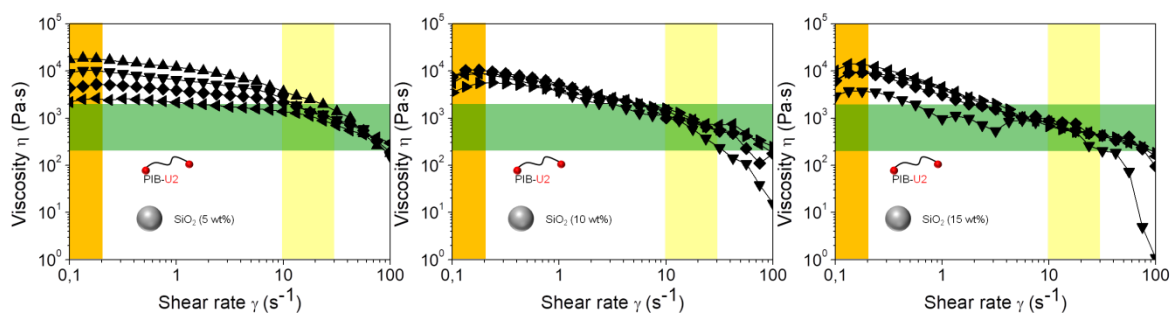


Figure S 17. Rheology measurements of viscosity-shear rate-temperature dependence for PIB-U2-SNP 5-15 in a temperature range of 80 – 110 °C.

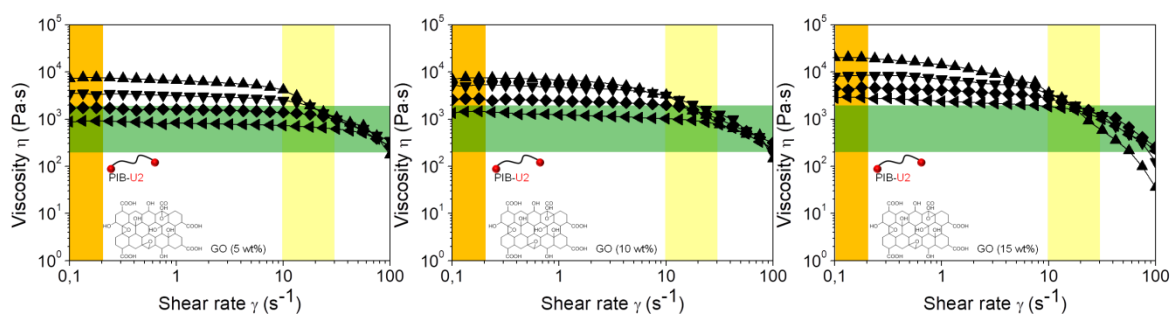


Figure S 18. Rheology measurements of viscosity-shear rate-temperature dependence for PIB-U2-GO 5-15 in a temperature range of 80 – 110 °C.

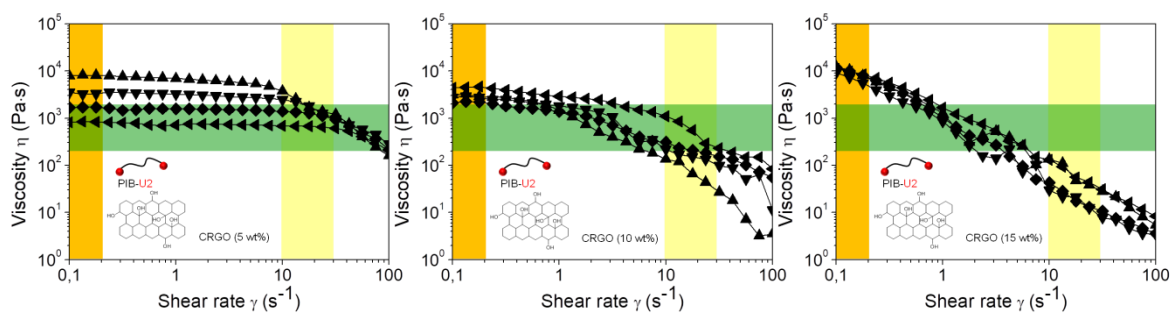


Figure S 19. Rheology measurements of viscosity-shear rate-temperature dependence for PIB-U2-CRGO 5-15 in a temperature range of 80 – 110 °C.

6.13 Frequency sweep measurements of supramolecular polymers and their composites.

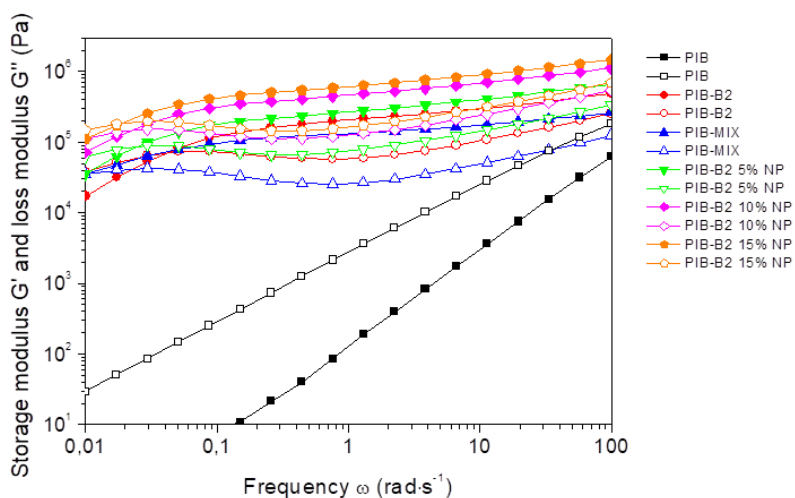


Figure S 20. Frequency sweep measurements of PIB, PIB-B2, PIB-B-blend, PIB-B2-SNP5, PIB-B2-SNP10, PIB-B2-SNP15: Storage modulus (filled ■) and loss modulus (empty □) versus frequency at room temperature (20 °C).

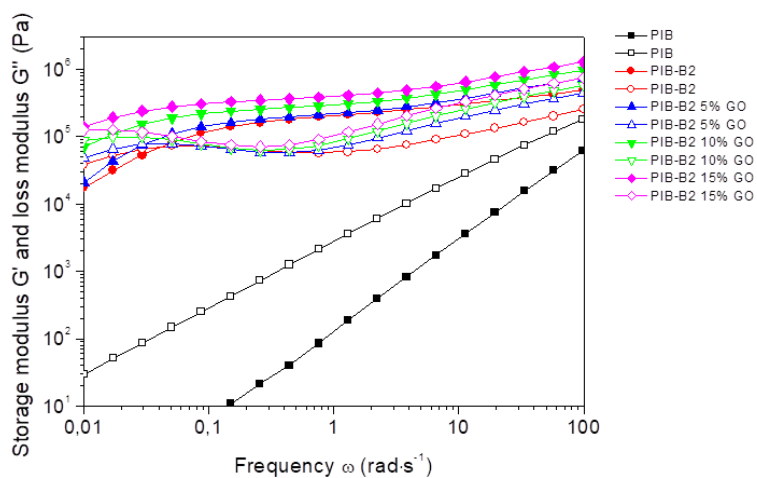


Figure S 21. Frequency sweep measurements of PIB, PIB-B2, PIB-B2-GO5, PIB-B2-GO10, PIB-B2-GO15: Storage modulus (filled ■) and loss modulus (empty □) versus frequency at room temperature (20 °C).

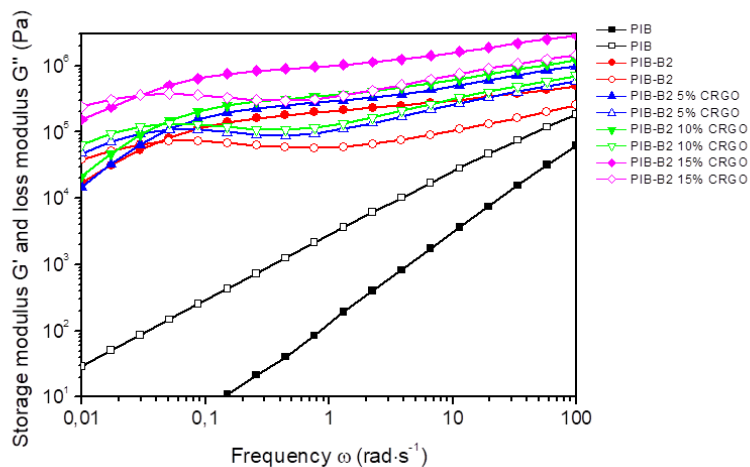


Figure S 22. Frequency sweep measurements of PIB, PIB-B2, PIB-B2-CRGO5, PIB-B2-CRGO10, PIB-B2-CRGO15: Storage modulus (filled ■) and loss modulus (empty □) versus frequency at room temperature (20 °C).

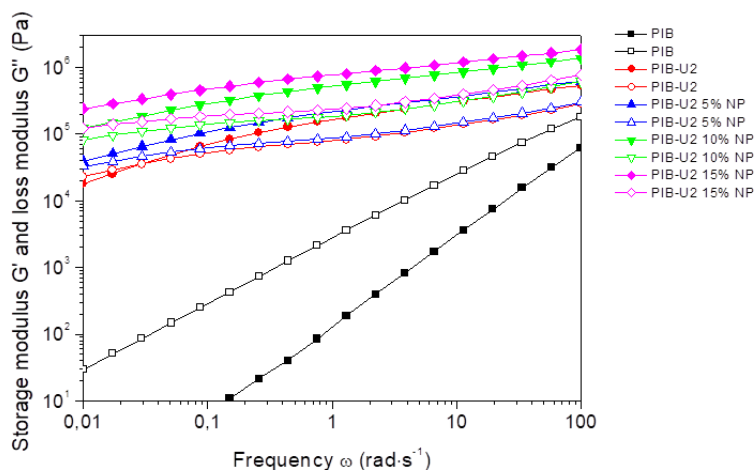


Figure S 23. Frequency sweep measurements of PIB, PIB-U2, PIB-U2-SNP5, PIB-U2-SNP10, PIB-U2-SNP15: Storage modulus (filled ■) and loss modulus (empty □) versus frequency at room temperature (20 °C).

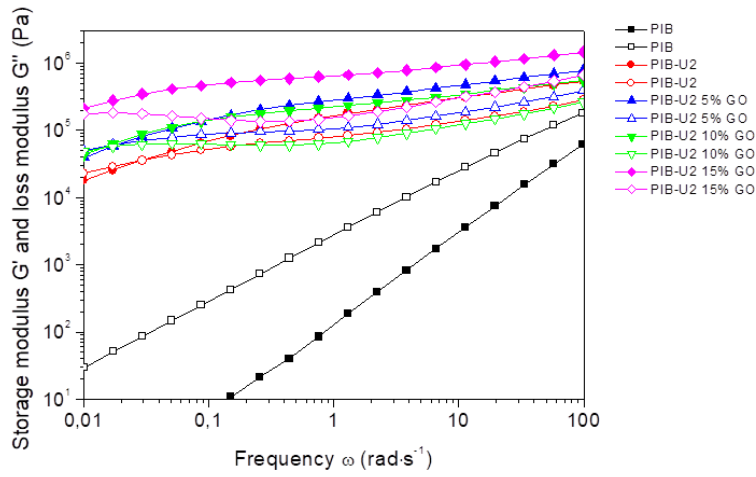


Figure S 24. Frequency sweep measurements of PIB, PIB-U2, PIB-U2-GO5, PIB-U2-GO10, PIB-U2-GO15: Storage modulus (filled ■) and loss modulus (empty □) versus frequency at room temperature (20 °C).

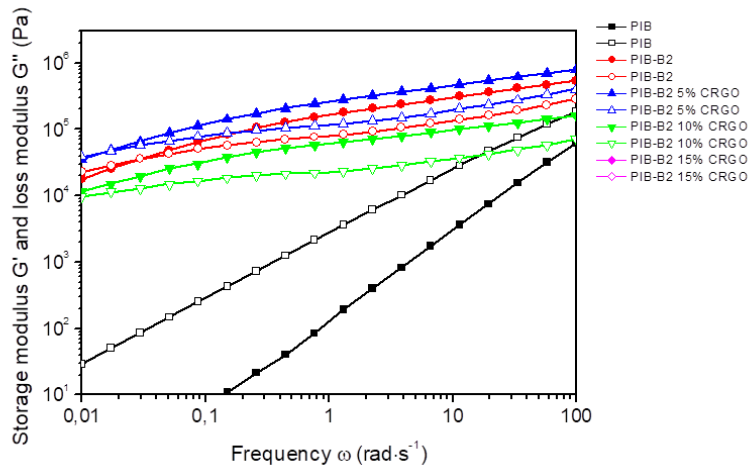


Figure S 25. Frequency sweep measurements of PIB, PIB-U2, PIB-U2-CRGO5, PIB-U2-CRGO10: Storage modulus (filled ■) and loss modulus (empty □) versus frequency at room temperature (20 °C).

6.14 Temperature-dependent FT-IR for supramolecular polymers.

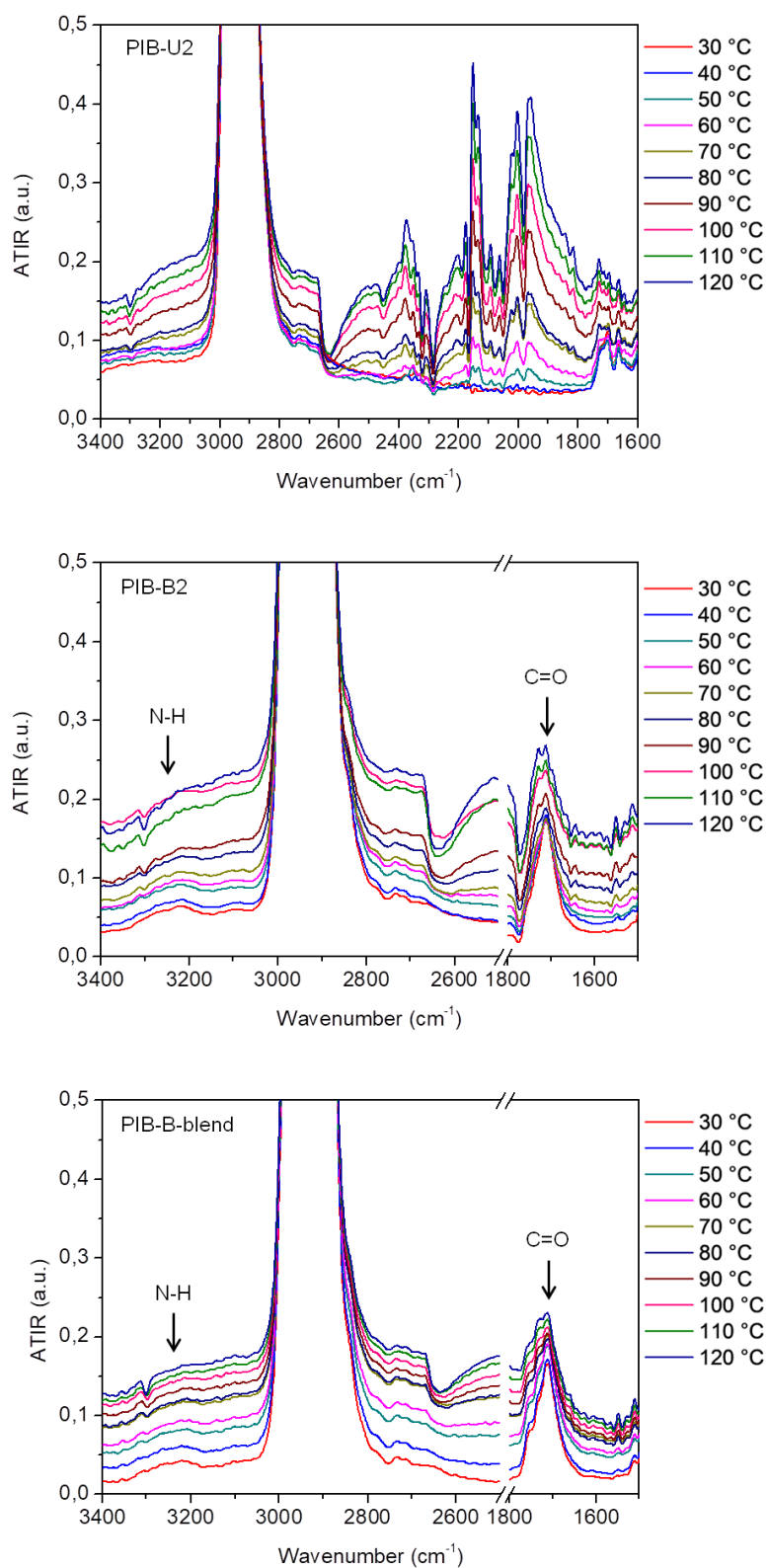


Figure S 26. Temperature dependent FT-IR measurements of PIB-U2, PIB-B2 and PIB-B-blend in a temperature range of 30 - 120 °C.

6.15 Rheology data for printable supramolecular polymers.

Storage modulus is the filled symbol. Loss modulus is the empty symbol.

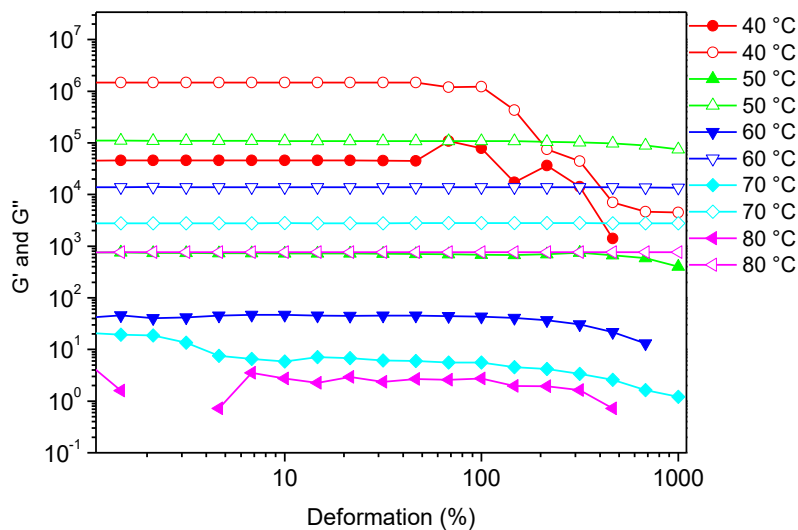


Figure S 27: Amplitude sweep for PEG-400-B2.

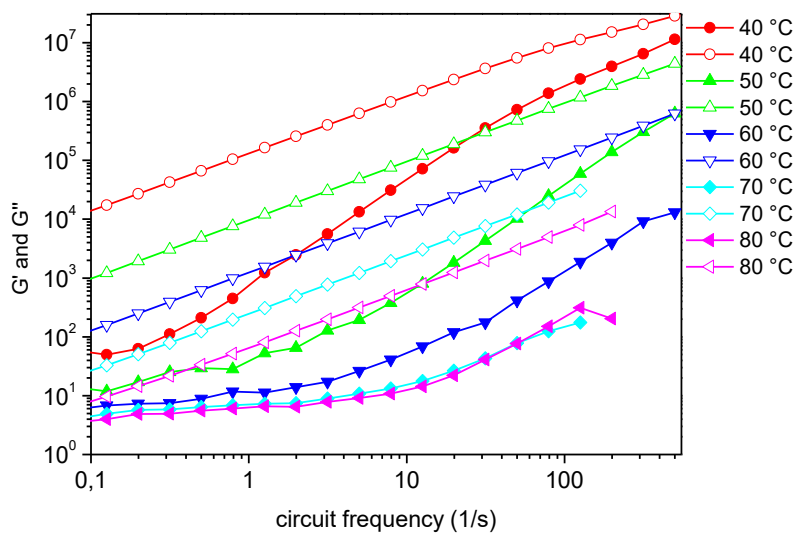


Figure S 28: Frequency sweep for PEG-400-B2.

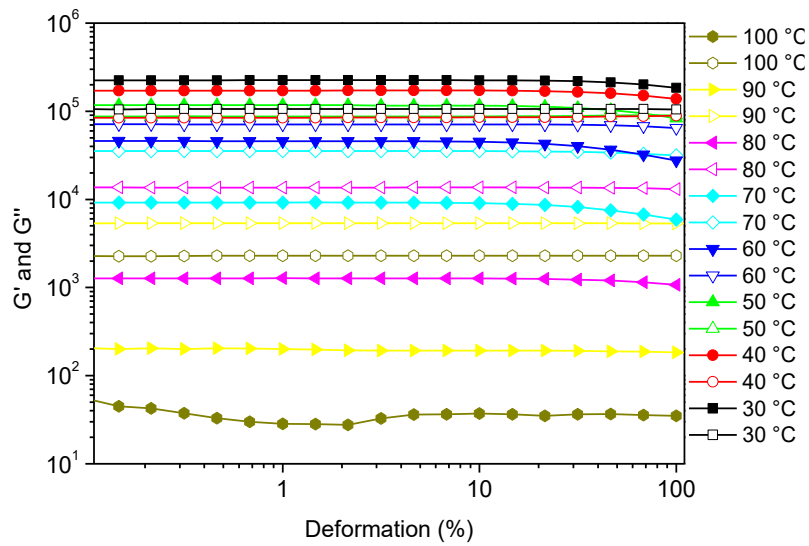


Figure S 29: Amplitude sweep for PIB-B2.

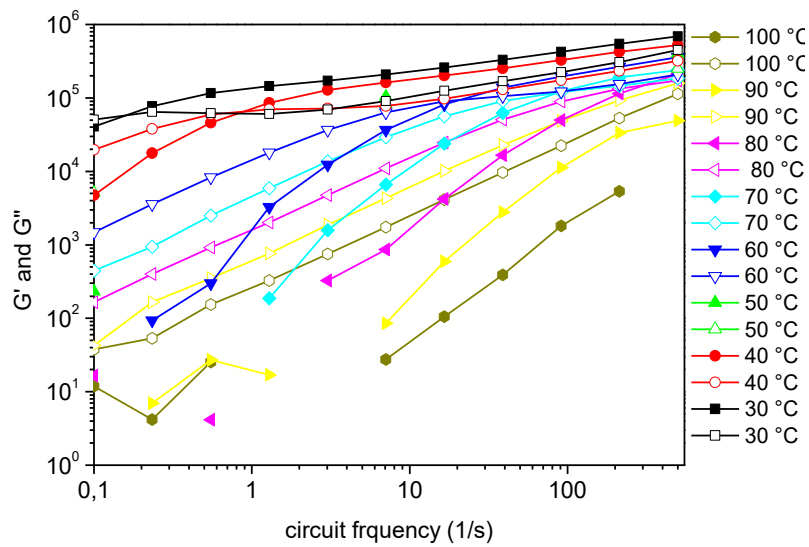


Figure S 30: Frequency sweep for PIB-B2.

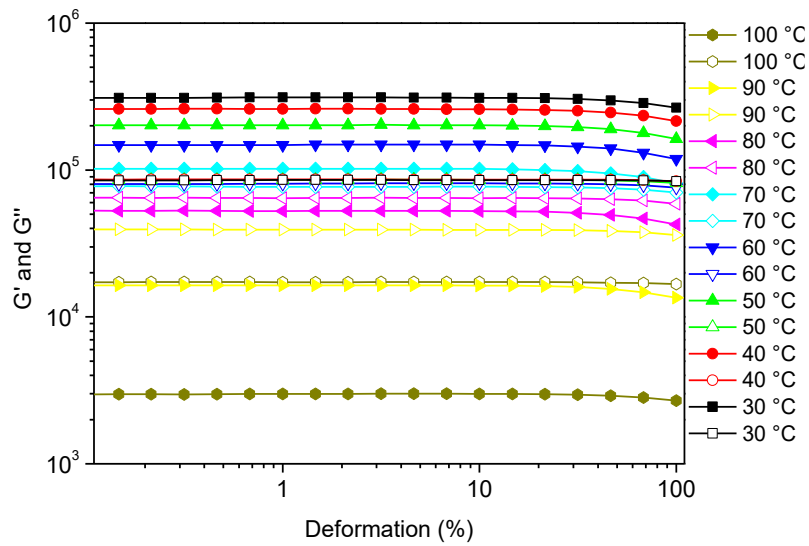


Figure S 31: Amplitude sweep for PIB-U2.

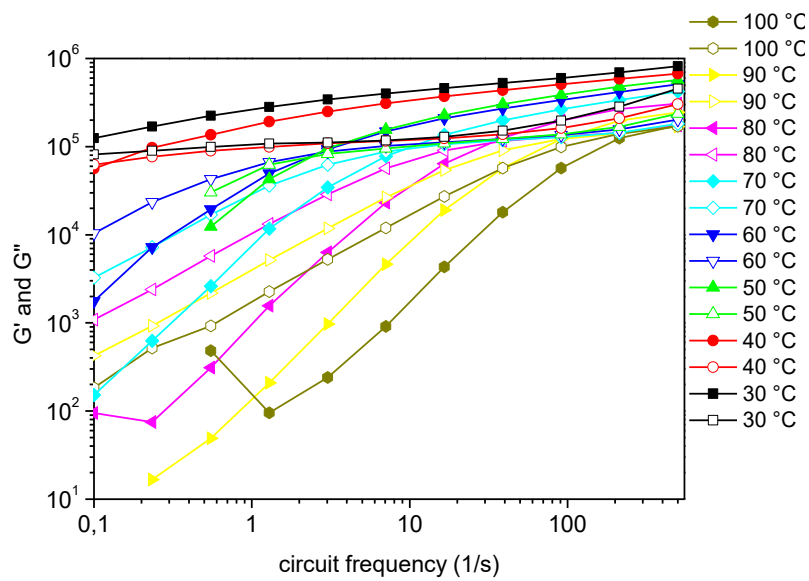


Figure S 32: Frequency sweep for PIB-U2.

6.16 Rheology analysis for mechanophore 3D-printing.

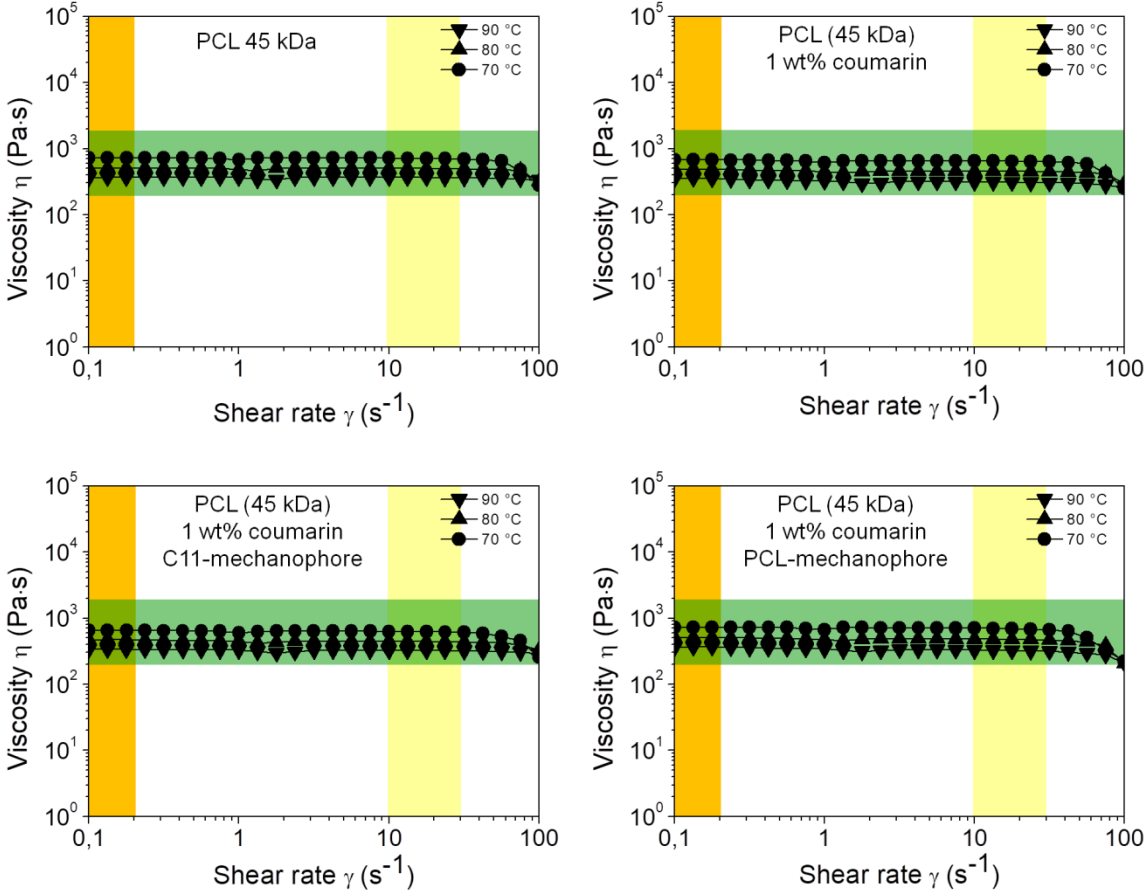


Figure S 33. Viscosity-temperature rheology measurements for polycaprolactone (PCL) with the molecular weight of $M_n = 45$ kDa and its composites with 1 wt% coumarin, as well as the composites based on C₁₁-mechanophore and PCL-mechanophore. The printing range of the 3D printer is marked in green and yellow to ensure printability with regenHU 3D Discovery printer ($\eta = 200 - 2000$ Pa·s, $\gamma = 10 - 30 s^{-1}$).

6.17 Control reaction between PCL and Cu₂O in 1,4-dioxane.

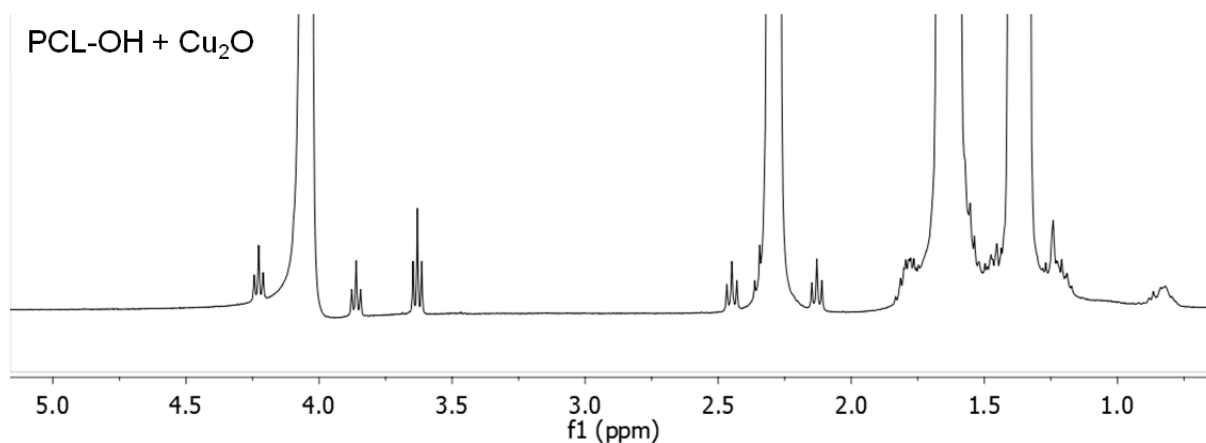


Figure S 34. ¹H-NMR of a control reaction between PCL-OH and Cu₂O showing no side reaction taking place on the polymer backbone within the reaction conditions.

PCL-OH (500 mg) and Cu₂O (100 mg) were mixed into dry 1,4-dioxane (20 mL). The reaction mixture was stirred at 80 °C for 48 hours. After filtration, the solvent was removed under reduced pressure and the polymer was precipitated twice in cold Et₂O. After drying in vacuum a white polymer (500 mg, 99 %) was obtained. When compared to the mechanophore synthesis (a), no reaction between PCL and Cu₂O occurred while using the same solvent and temperature conditions. The polymer chain was not decomposed by the used reaction conditions as checked by subsequent SEC. During the mechanophore synthesis several side reactions took place. Signals for other imidazole endgroups (*1-methylimidazole-poly(ε-caprolactone)*) were not present anymore. Elimination of the imidazole endgroup probably led to bromo- and allyl-functionalized PCL (3.4 ppm, 4.6 ppm).

6.18 Fluorescence calibration (solid state reflection mode).

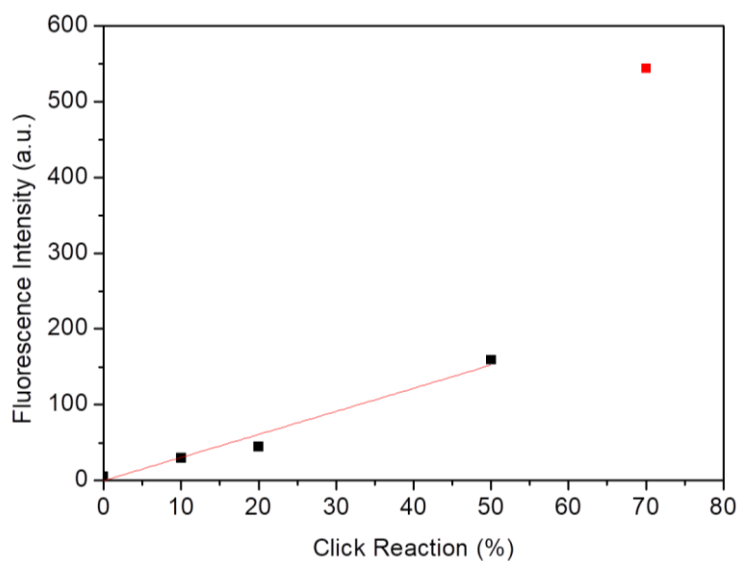


Figure S 35. Calibration curve for the conversion of the fluorogenic “click” reaction based on 3-azido-7-hydroxycoumarin and phenylacetylene.

The fluorescence measurements were calibrated by mixing 3-azido-7-hydroxycoumarin with its clicked dye. For lower conversion rates the fluorescence increase was linear. With linear fitting the calibration curve $y = 3.05 \cdot x$ could be obtained.

6.19 Absorption and fluorescence of 5-azido-fluorescein and the “clicked” product

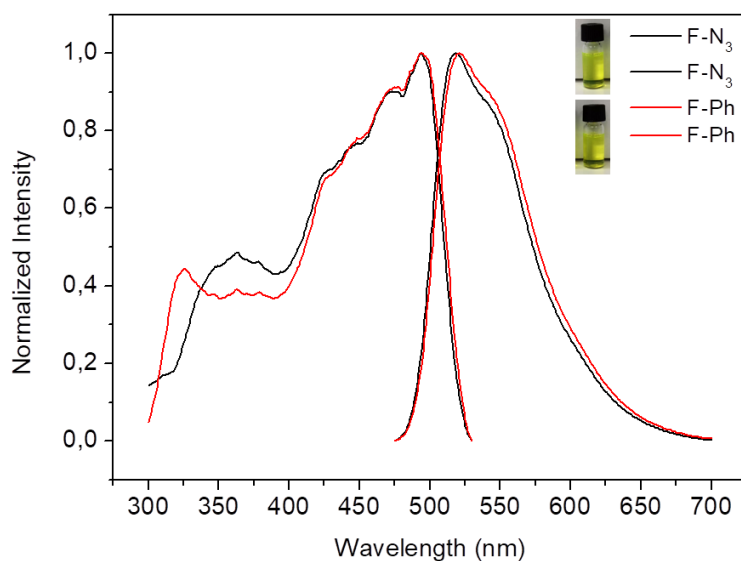


Figure S 36: Normalized absorption and fluorescence spectra of 5-azido-fluorescein (schwarz, F-N₃) and the dye after “click”-reaction with phenylacetylene (rot, F-Ph).

6.20 NMR spectra of the tetronic polymers.

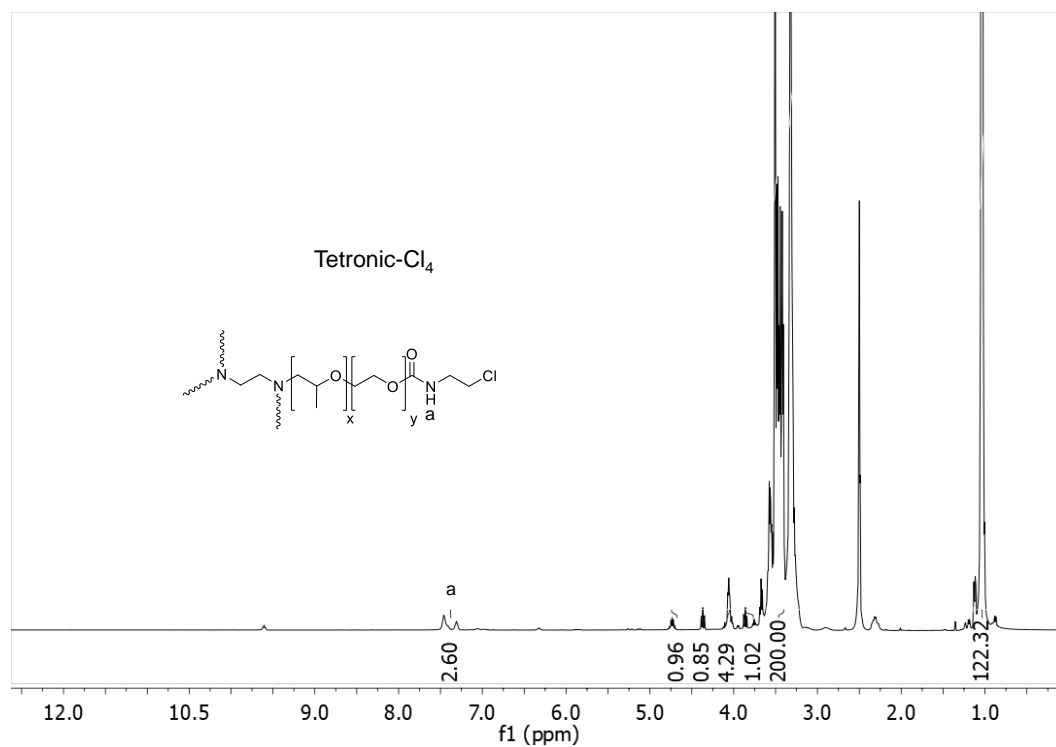


Figure S 37: ¹H-NMR of Tetronic-3600-Cl₄ in CDCl₃.

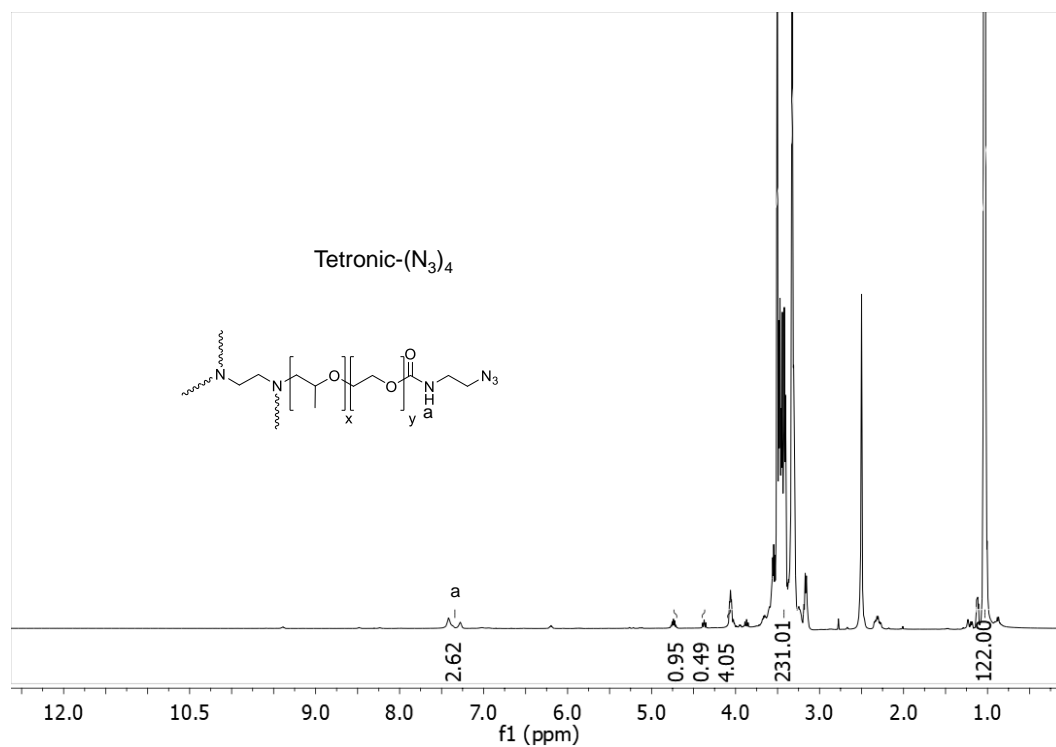


Figure S 38: ¹H-NMR of Tetronic-3600-(N₃)₄ in CDCl₃.

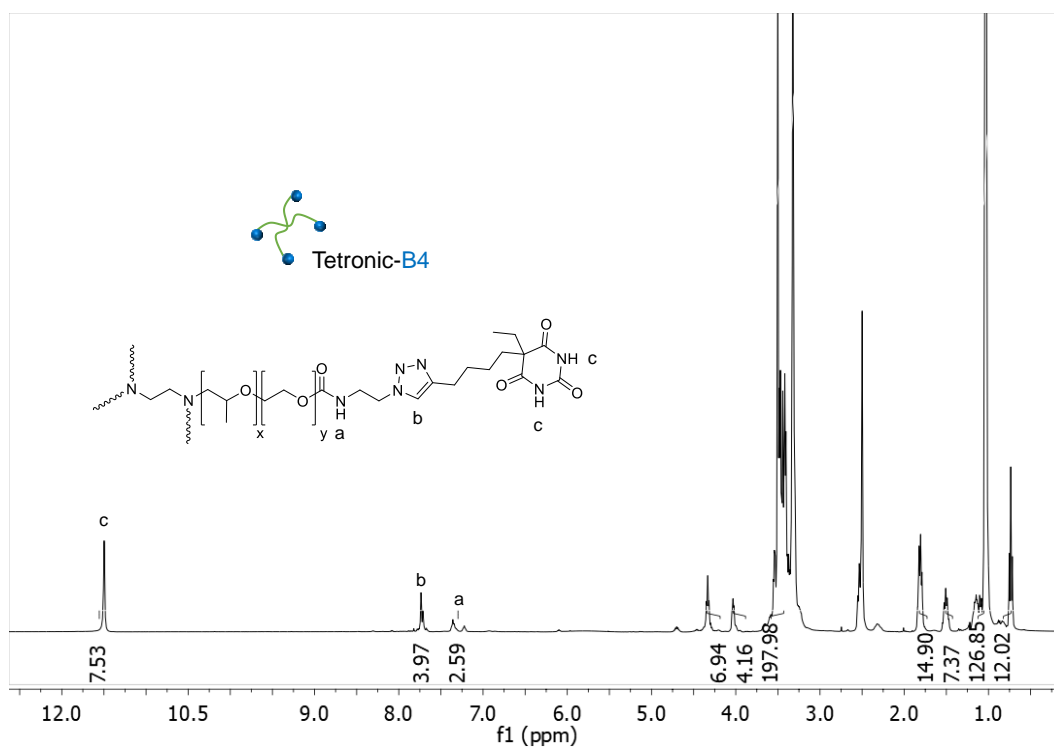


Figure S 39: $^1\text{H-NMR}$ of Tetronic-3600-B4 in CDCl_3 .

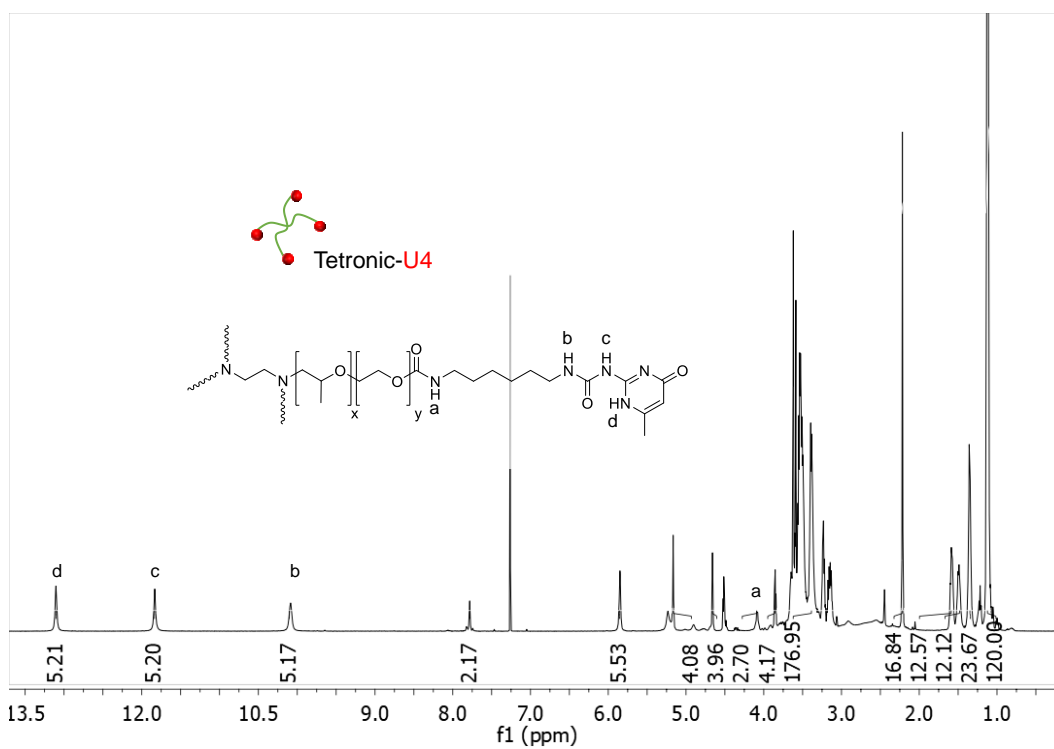


Figure S 40: $^1\text{H-NMR}$ of Tetronic-3600-U4 in CDCl_3 .

6.21 NMR spectra of the intermediates.

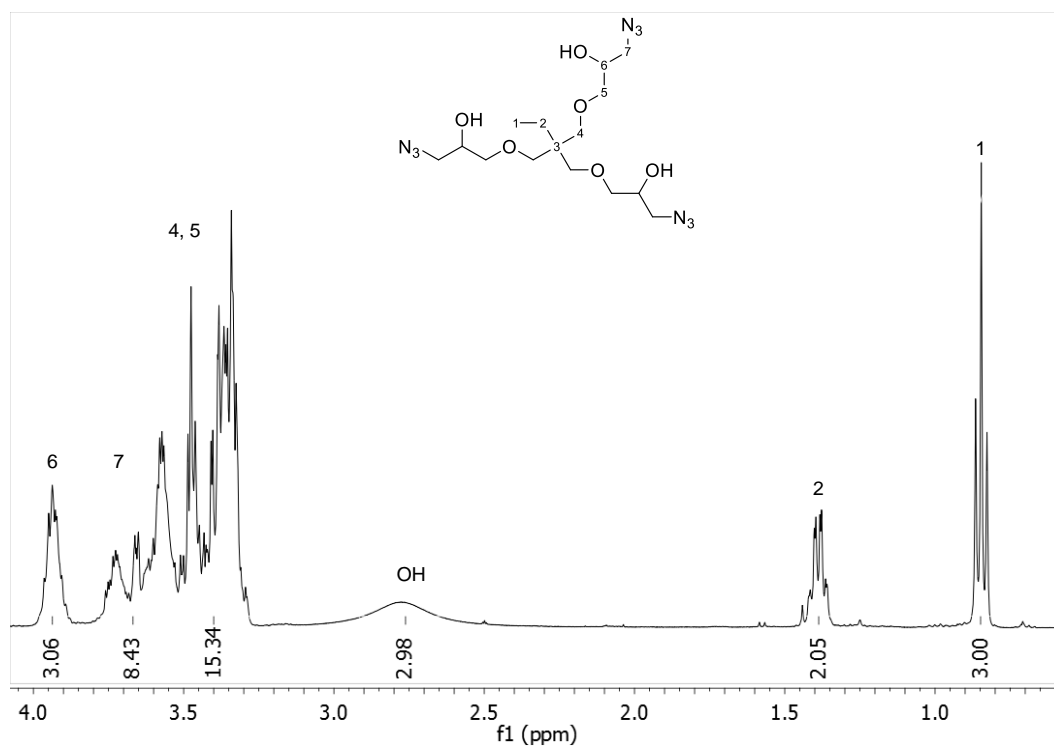


Figure S 41: $^1\text{H-NMR}$ of trivalent azide (-OH) in CDCl_3 .

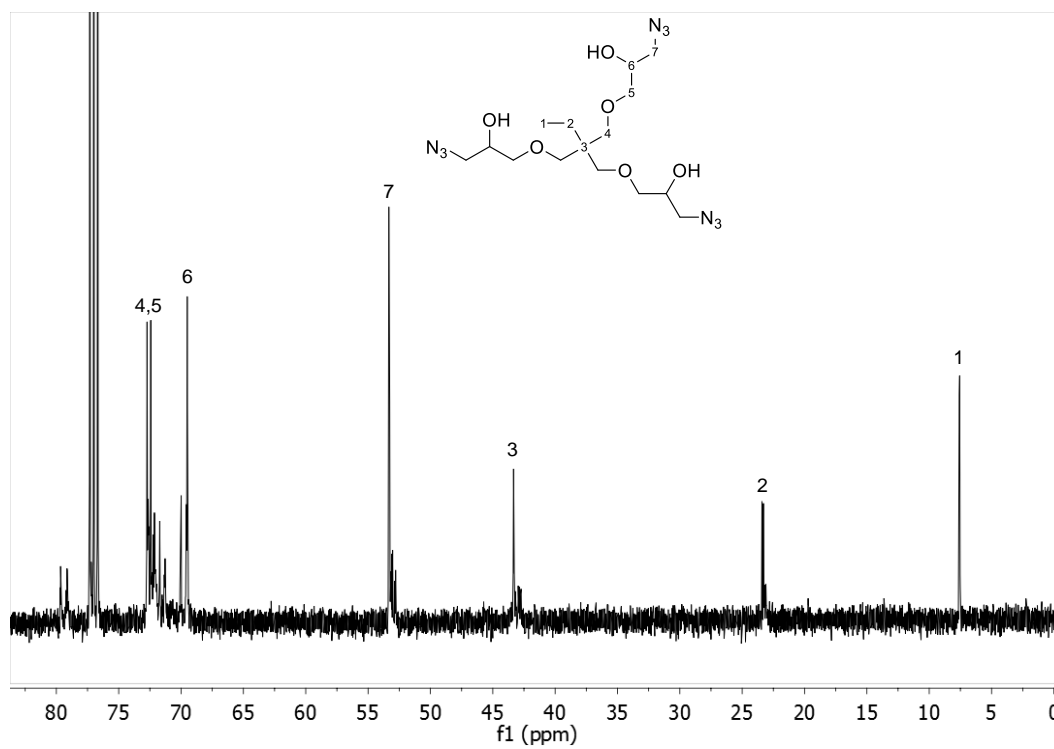


Figure S 42: $^{13}\text{C-NMR}$ of trivalent azide (-OH) in CDCl_3 .

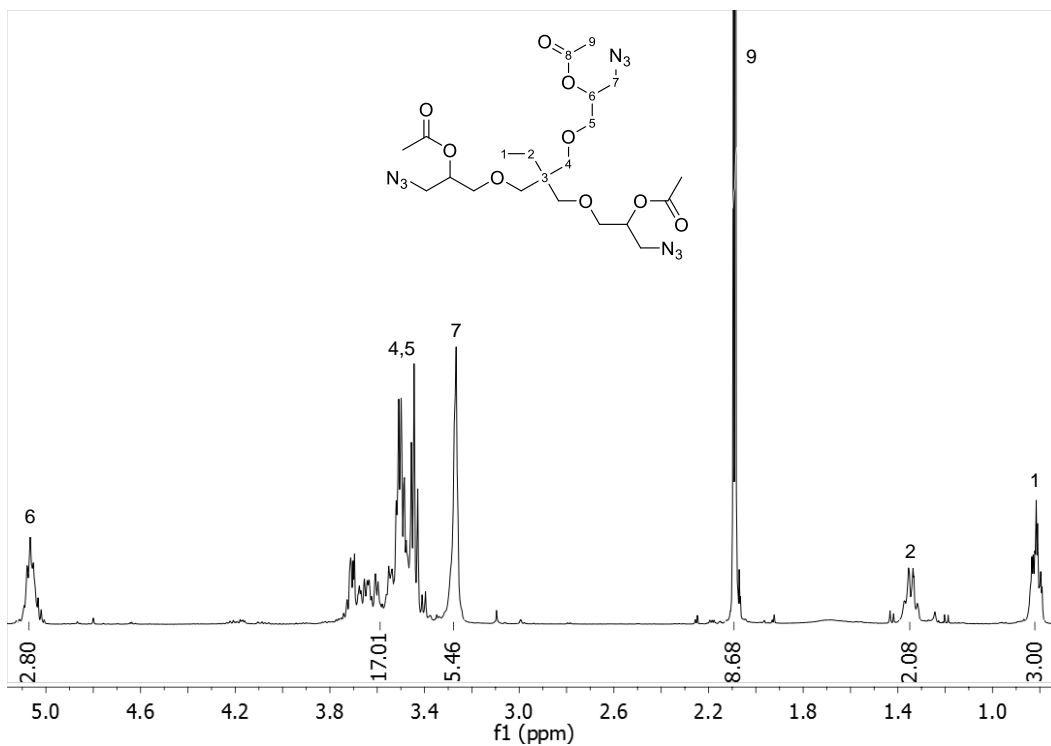


Figure S 43: $^1\text{H-NMR}$ of trivalent azide (-OAc) in CDCl_3 .

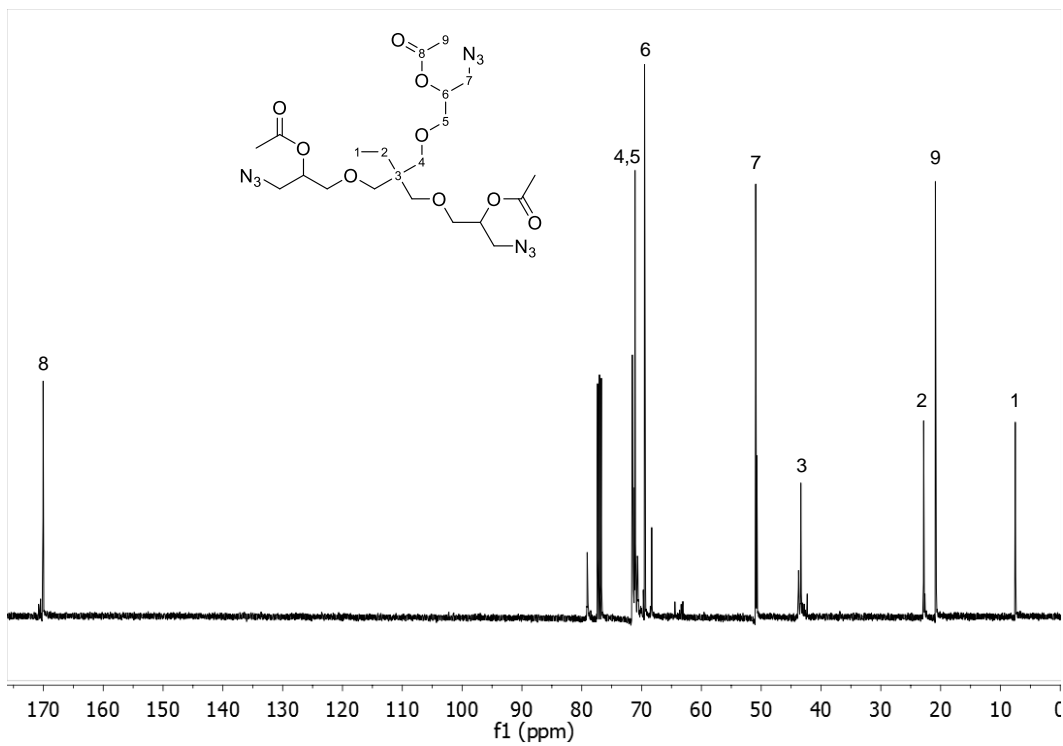


Figure S 44: $^{13}\text{C-NMR}$ of trivalent azide (-OAc) in CDCl_3 .

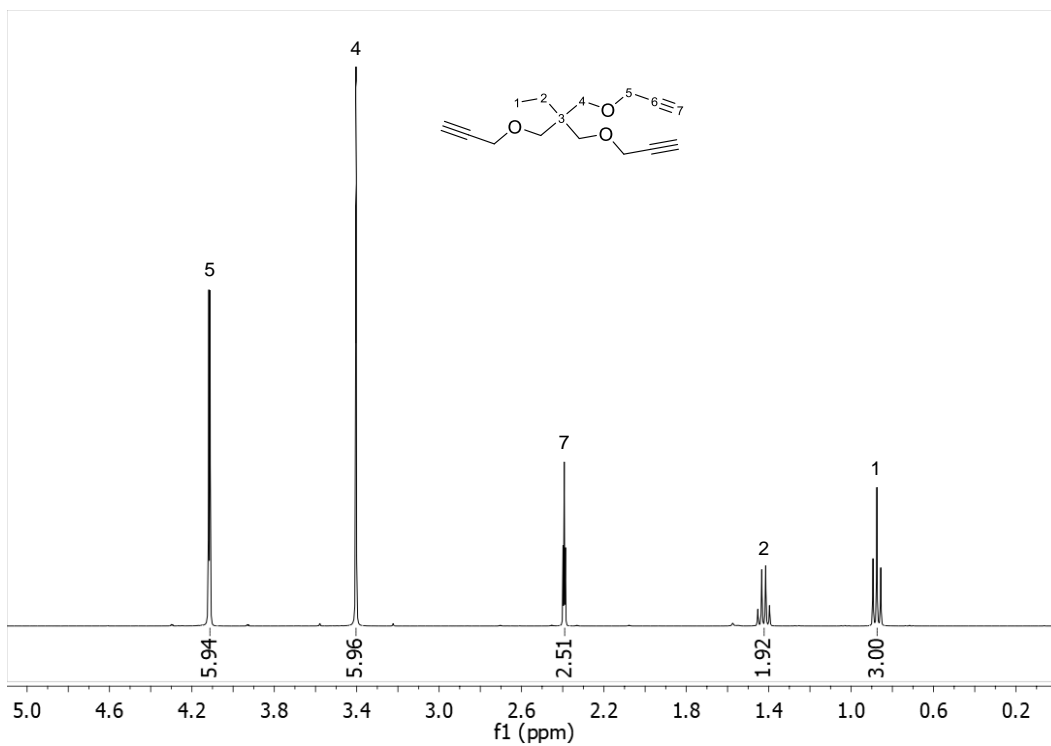


Figure S 45: $^1\text{H-NMR}$ of trivalent alkyne in CDCl_3 .

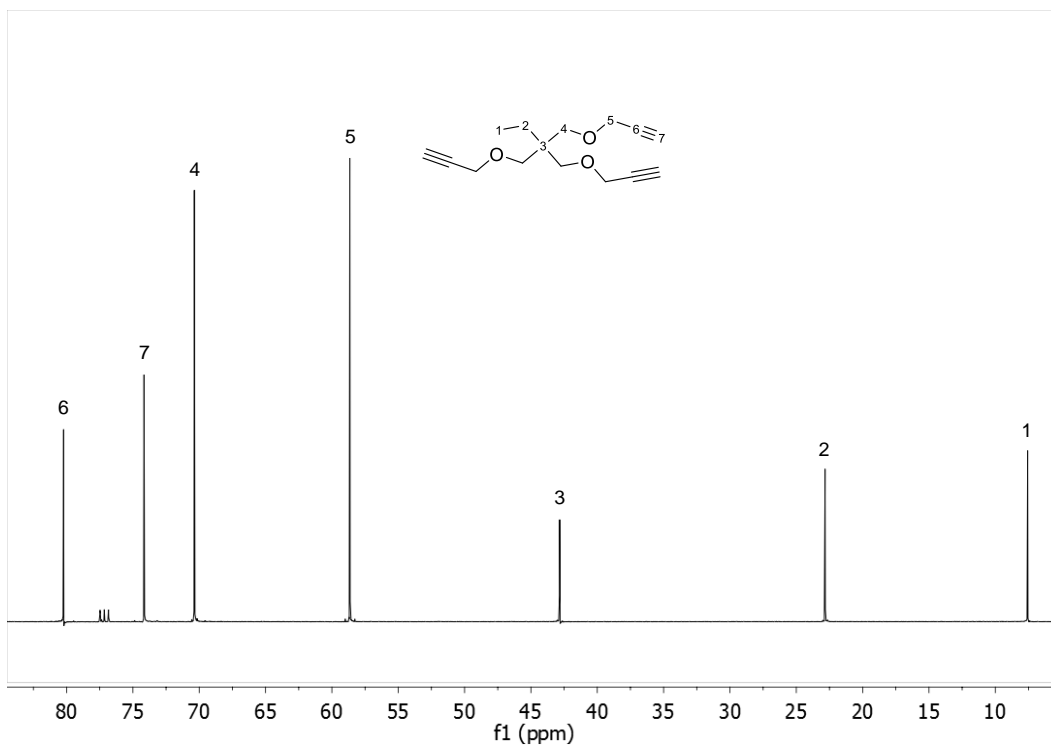


Figure S 46: $^{13}\text{C-NMR}$ of trivalent alkyne in CDCl_3 .

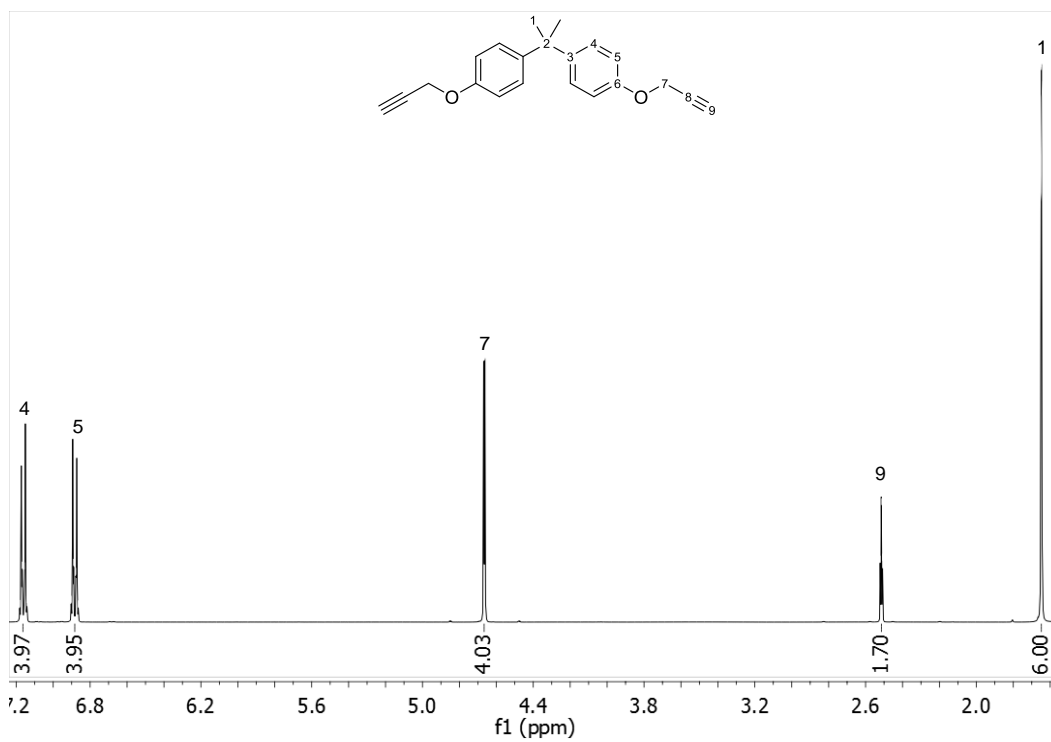


Figure S 47: ¹H-NMR of BAPE in CDCl₃.

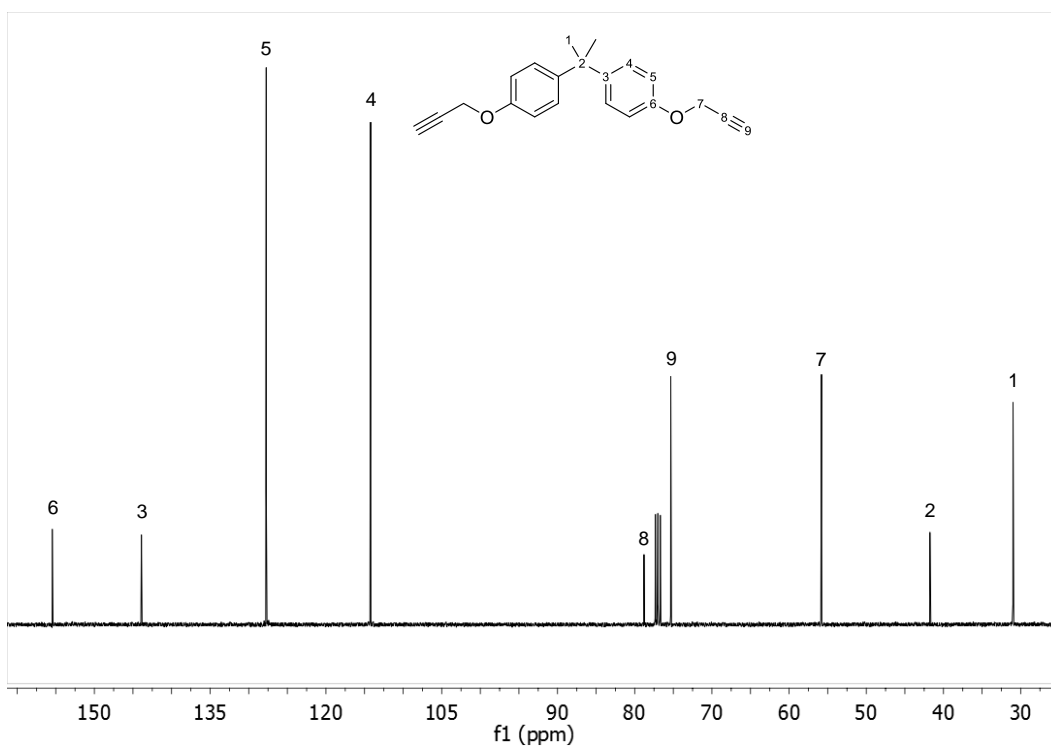


Figure S 48: ¹³C-NMR of BAPE in CDCl₃.

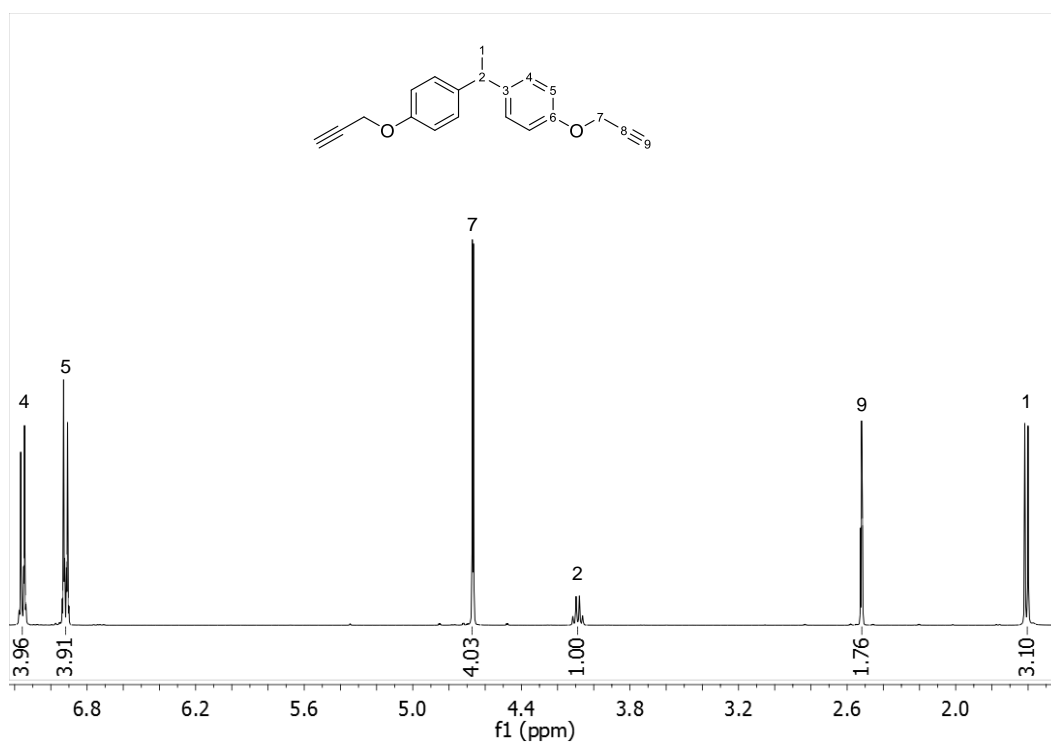


Figure S 49: $^1\text{H-NMR}$ of BEPE in CDCl_3 .

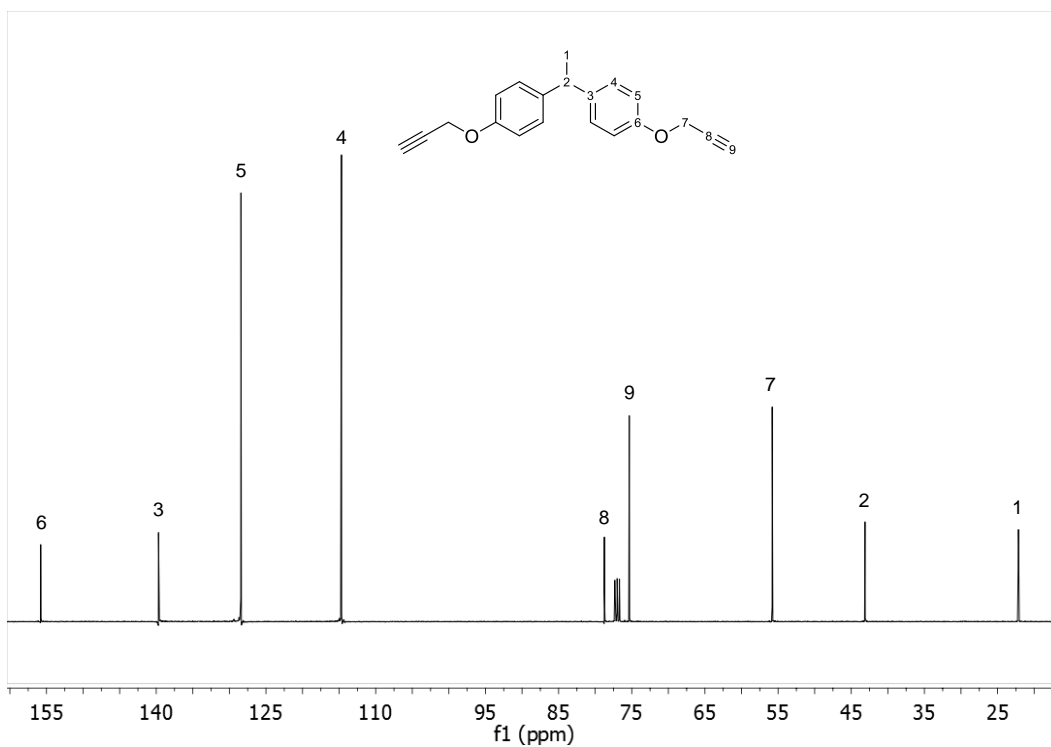


Figure S 50: $^{13}\text{C-NMR}$ of BEPE in CDCl_3 .

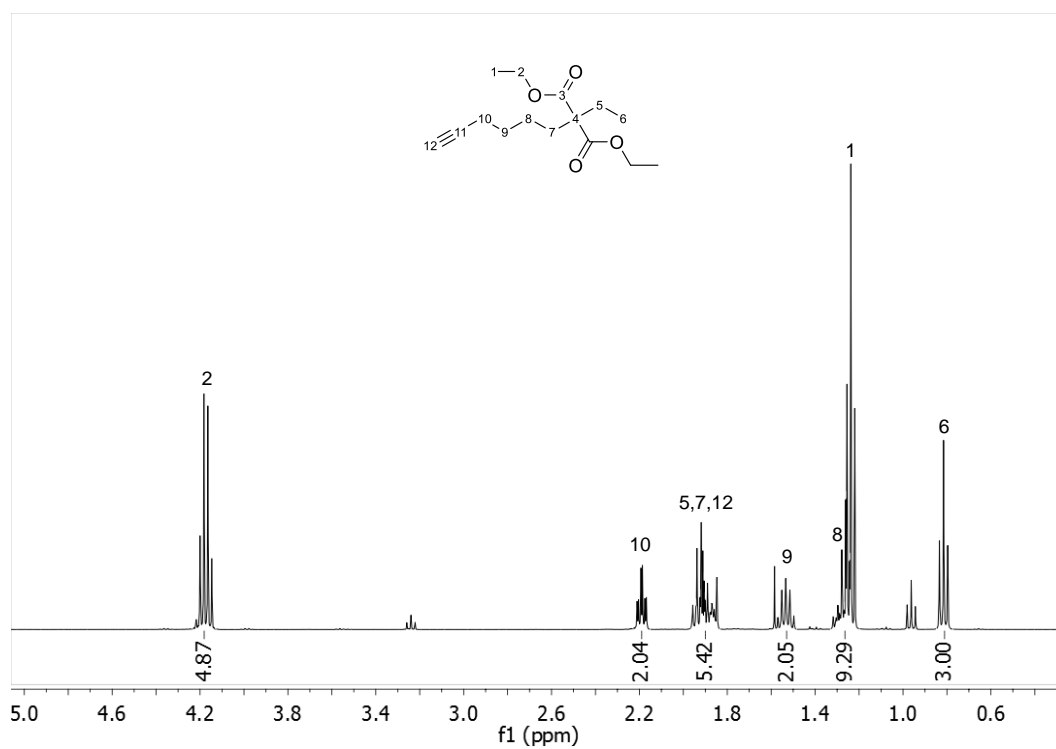


Figure S 51: ¹H-NMR of Diethyl 2-hexynyl-2-ethylmalonate in CDCl₃.

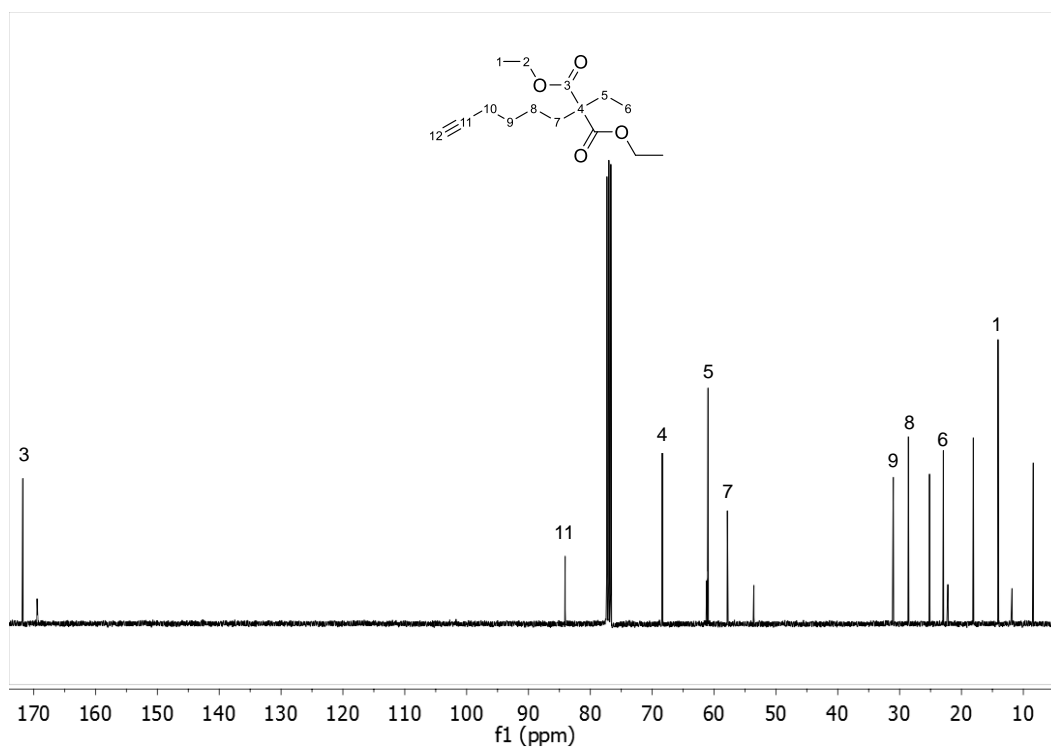


Figure S 52: ¹³C-NMR of Diethyl 2-hexynyl-2-ethylmalonate in CDCl₃.

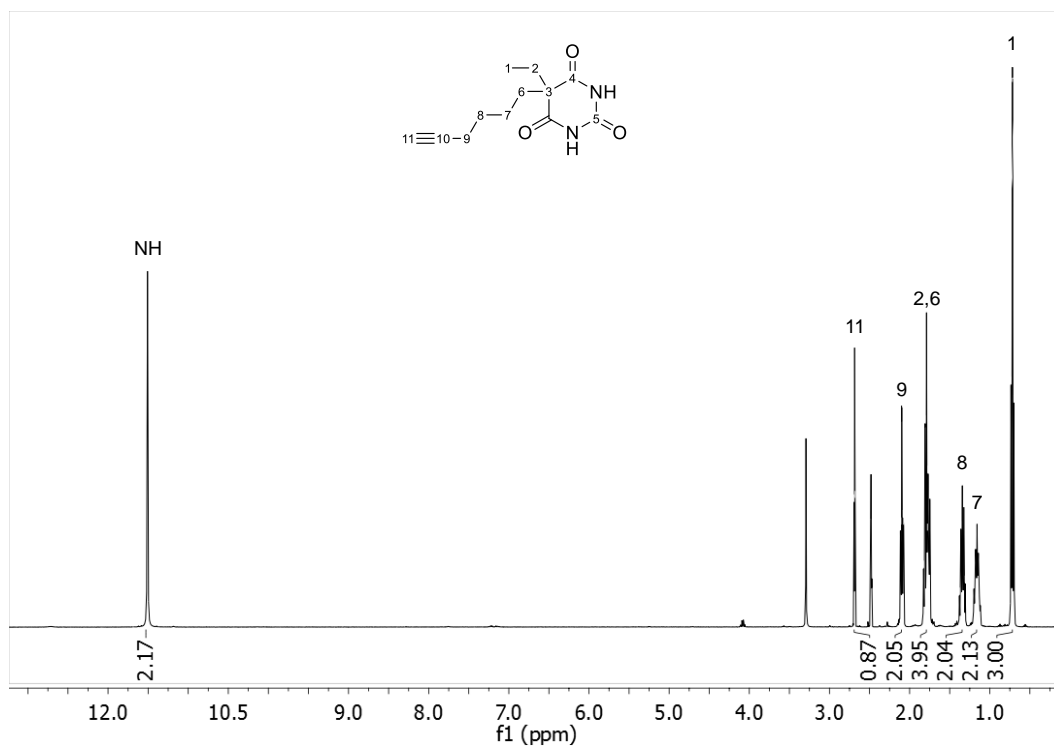


Figure S 53: $^1\text{H-NMR}$ of 2-hexynyl-2-ethyl barbiturate in DMSO.

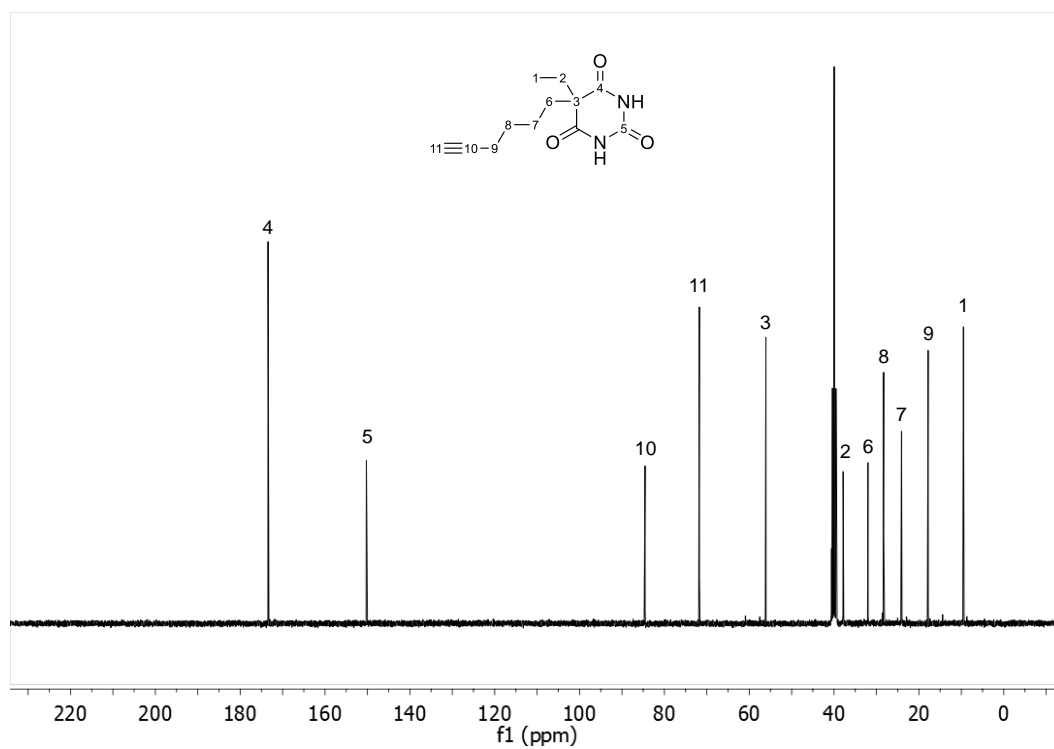


Figure S 54: $^{13}\text{C-NMR}$ of 2-hexynyl-2-ethyl barbiturate in DMSO.

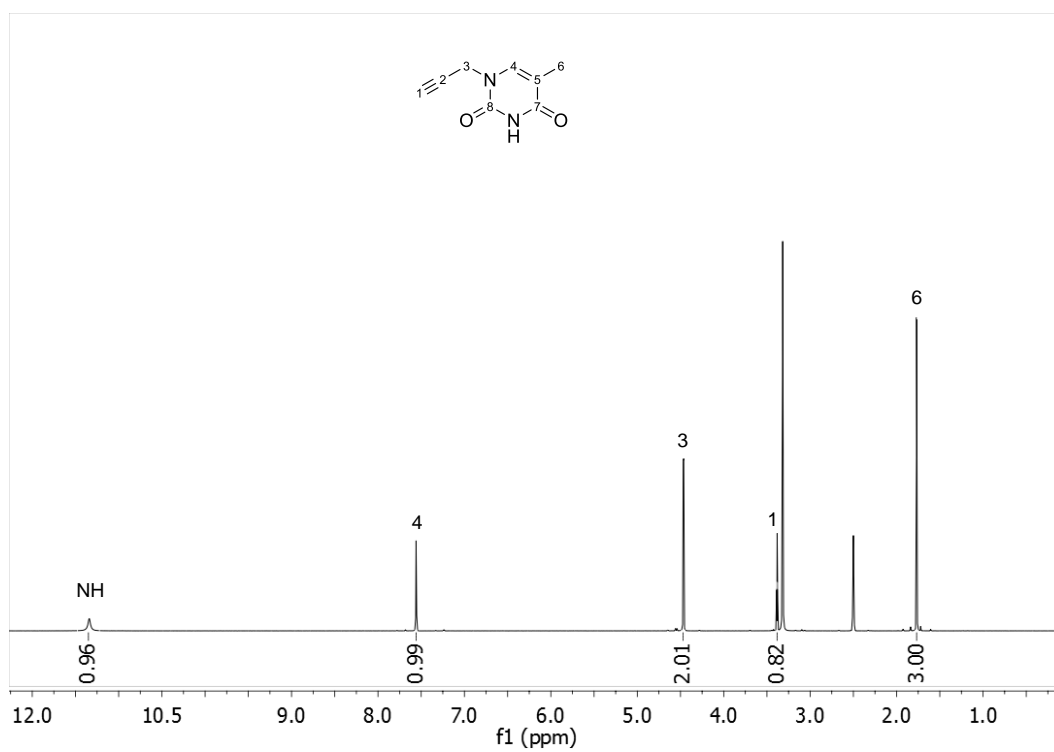


Figure S 55: $^1\text{H-NMR}$ of alkyne-thymine in DMSO.

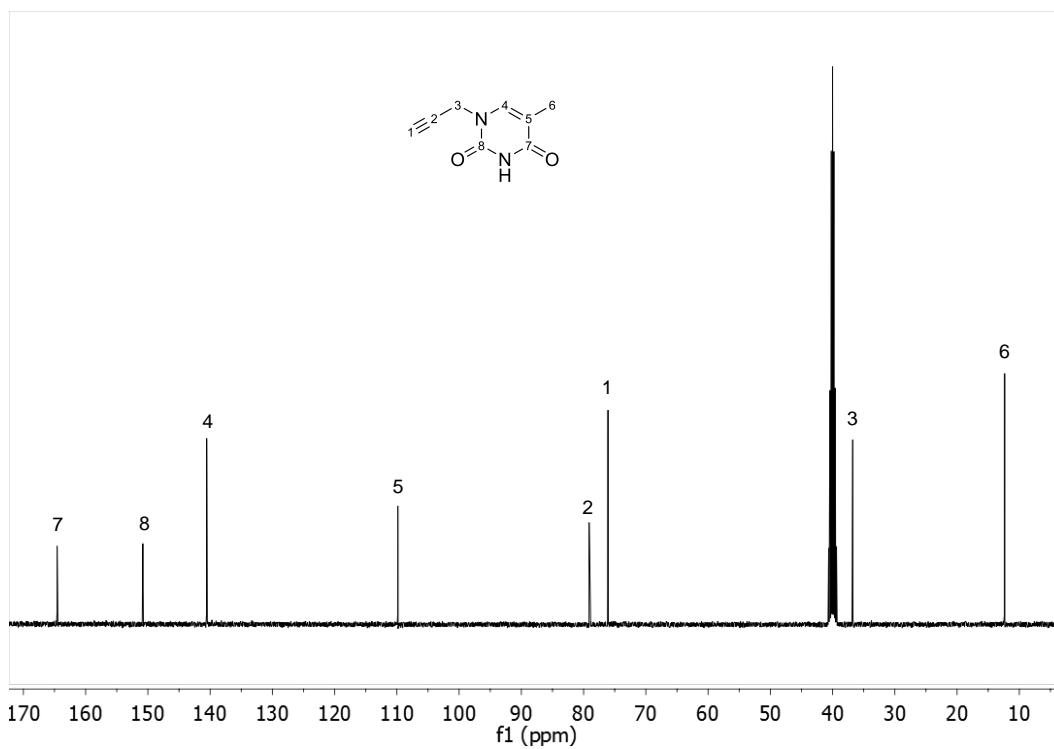


Figure S 56: $^{13}\text{C-NMR}$ of alkyne-thymine in DMSO.

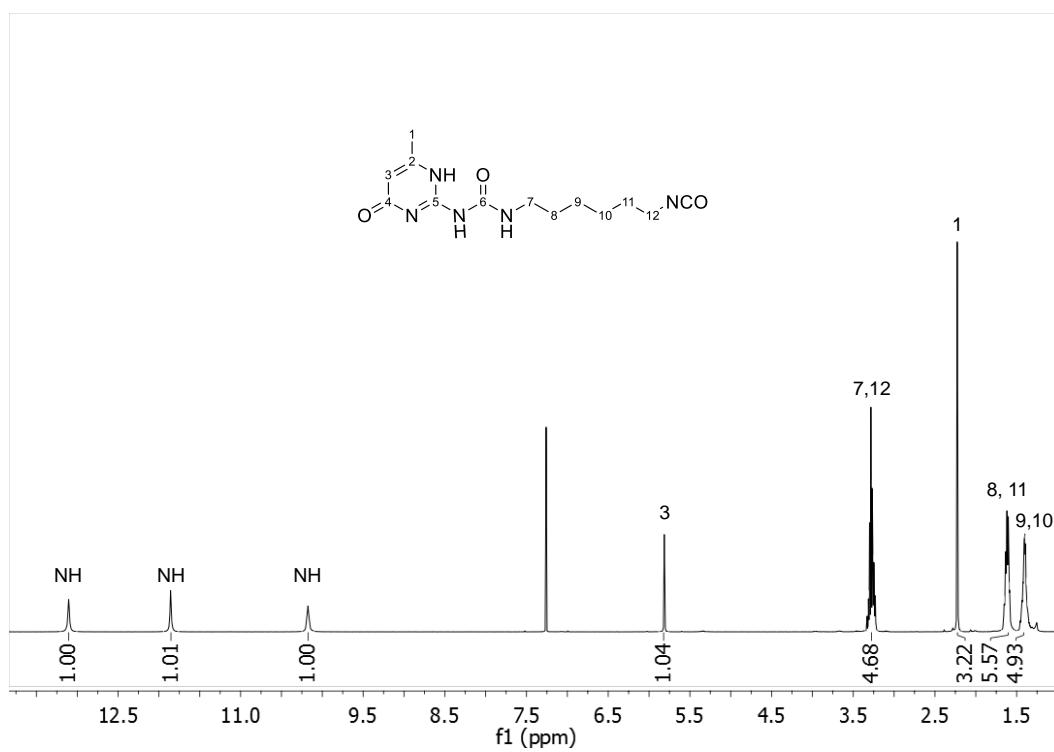


Figure S 57: $^1\text{H-NMR}$ of UPy-NCO in CDCl_3 .

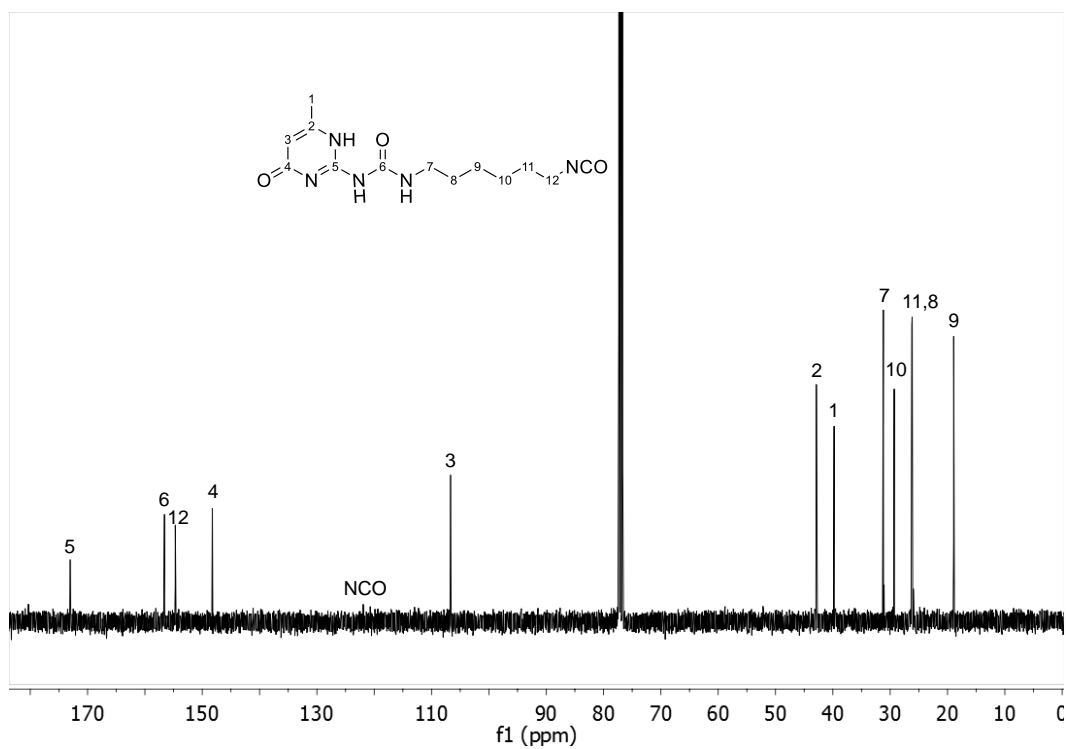


Figure S 58: $^{13}\text{C-NMR}$ of UPy-NCO in CDCl_3 .

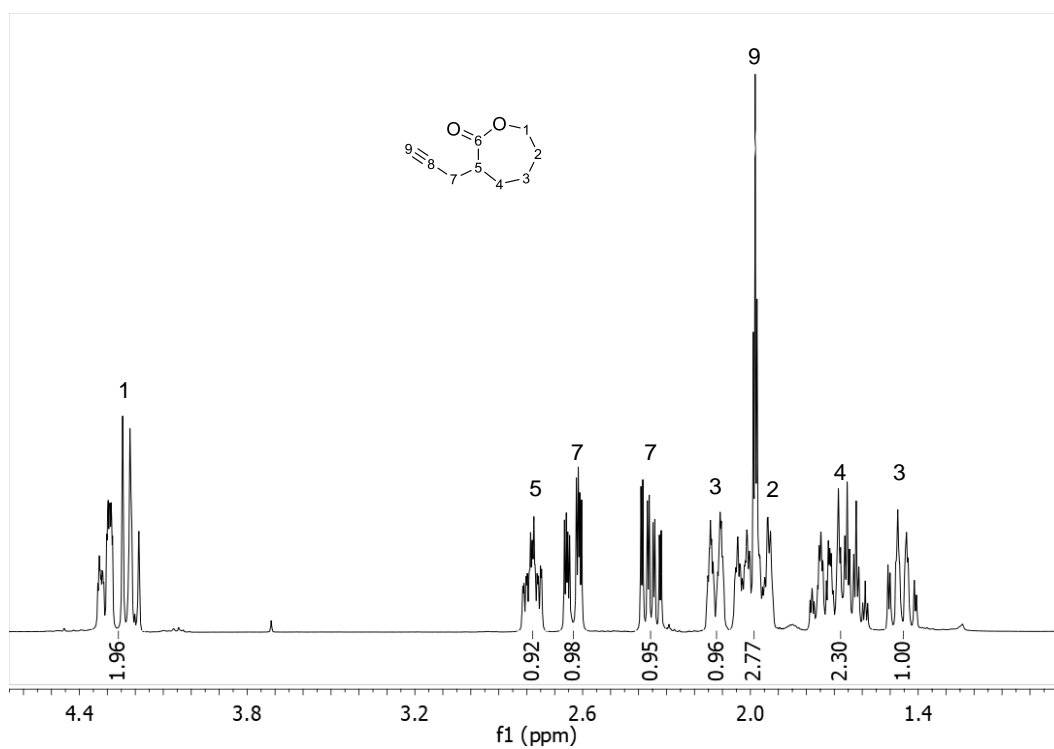


Figure S 59: $^1\text{H-NMR}$ of α -propargyl- ϵ -caprolactone in CDCl_3 .

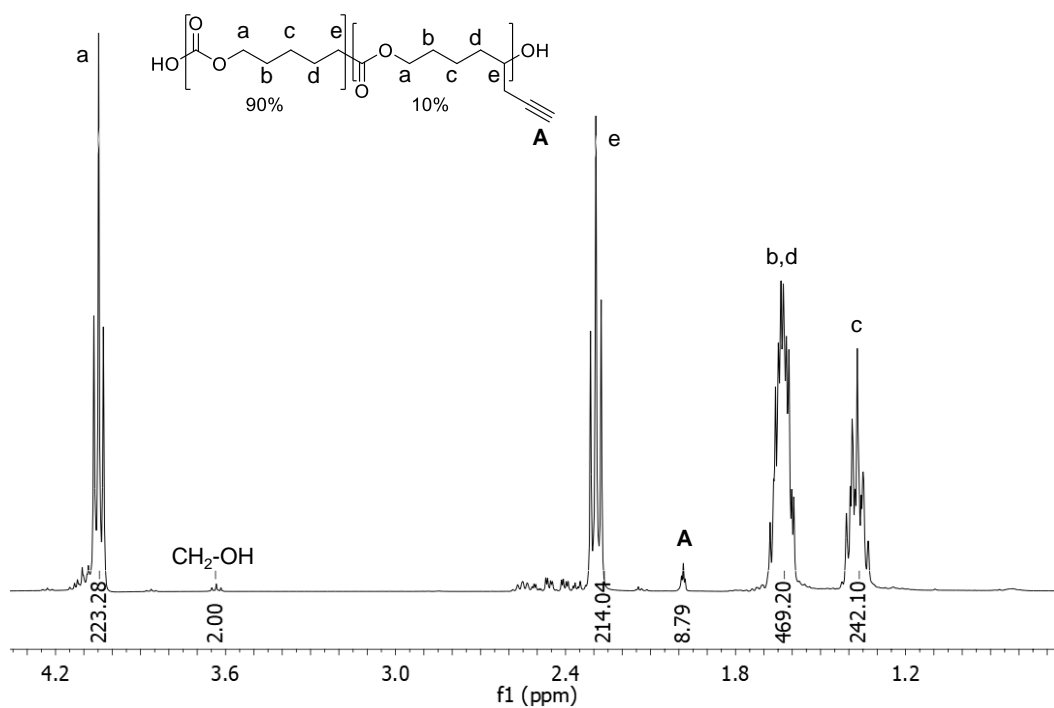


Figure S 60: $^1\text{H-NMR}$ of poly(ϵ -caprolactone)-co-(α -propargyl- ϵ -caprolactone) in CDCl_3 .

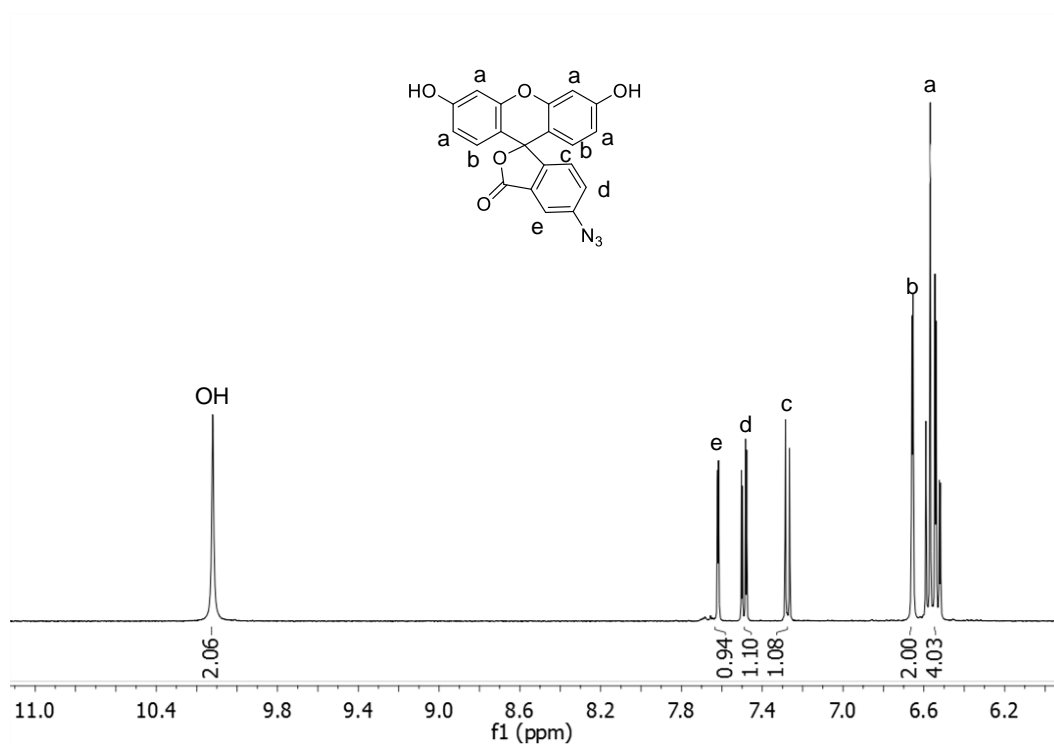


Figure S 61: $^1\text{H-NMR}$ of 5-azidofluorecein in DMSO.

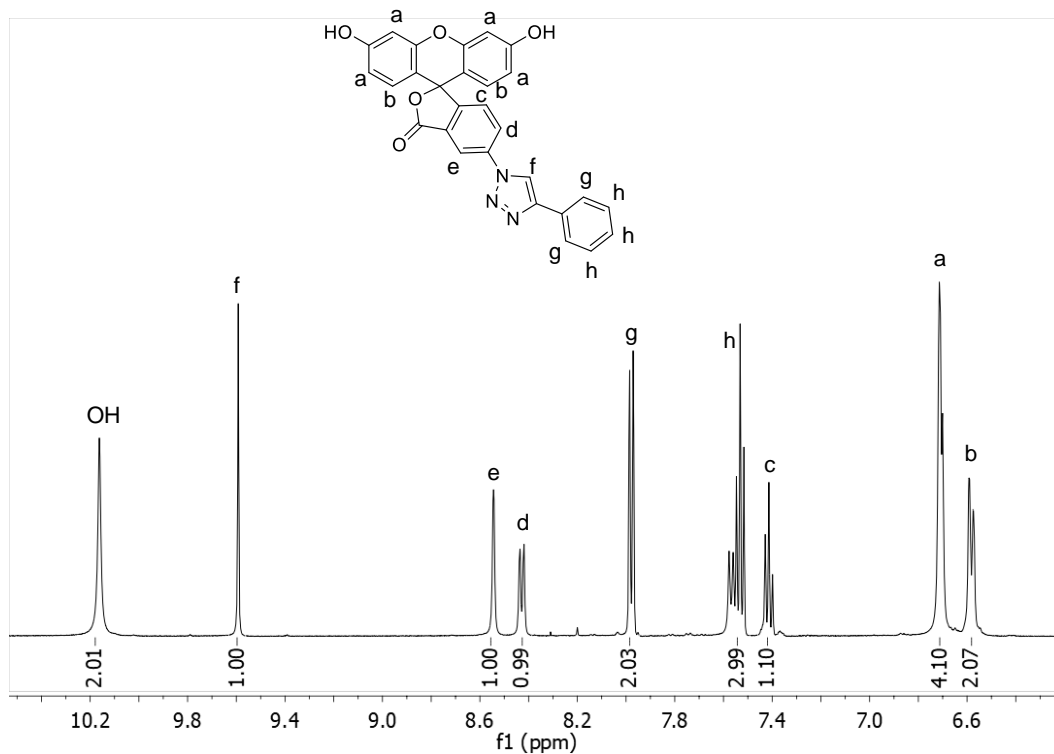


Figure S 62: $^1\text{H-NMR}$ of clicked 5-azidofluorecein in DMSO.

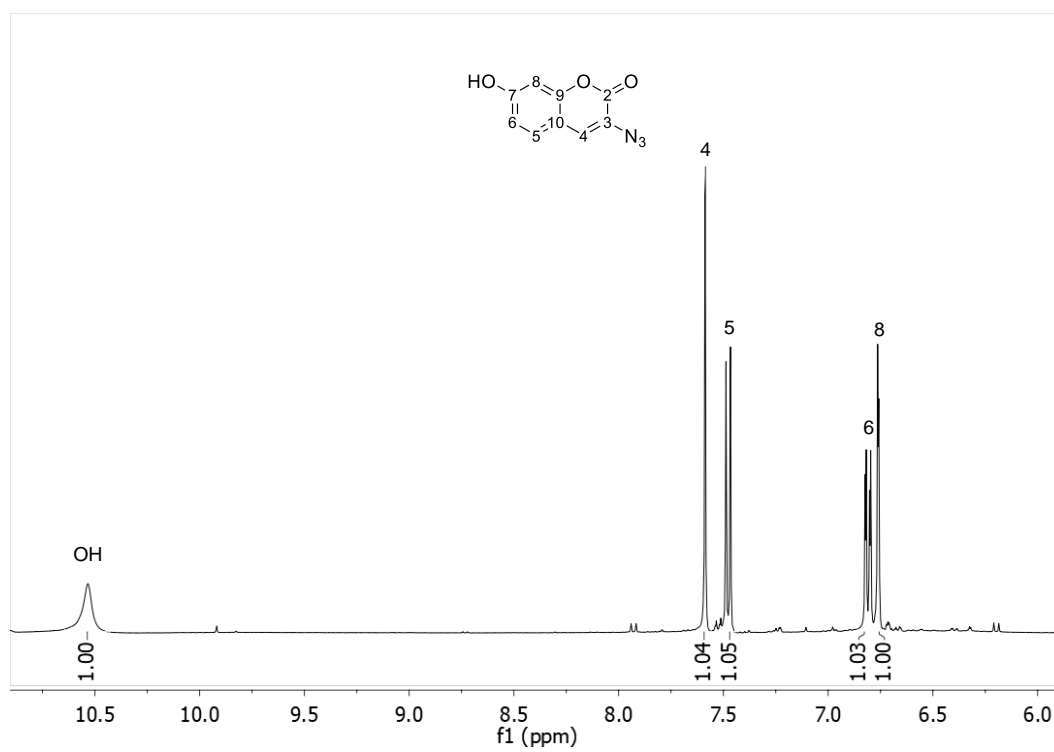


Figure S 63: ¹H-NMR of 3-azido-7-hydroxycoumarin in DMSO.

7.0 References

1. Huang, J., et al., A review of stereolithography: Processes and systems. *Processes* **2020**, *8* (9), 1138.
2. Peltola, S. M., et al., A review of rapid prototyping techniques for tissue engineering purposes. *Ann. Med.* **2008**, *40* (4), 268-280.
3. Bhavar, V., et al. In *A review on powder bed fusion technology of metal additive manufacturing*, 4th International conference and exhibition on Additive Manufacturing Technologies-AM, **2014**, 1-2.
4. Yang, H., et al., Performance evaluation of projet multi-material jetting 3D printer. *Virtual Phys. Prototyp.* **2017**, *12* (1), 95-103.
5. Ngo, T. D., et al., Additive manufacturing (3D printing): A review of materials, methods, applications and challenges. *Compos. B Eng.* **2018**, *143*, 172-196.
6. Crump, S., Fast precise, safe prototypes with FDM. In *ASME Annual Winter Conference*, Atlanta, **1991**, *50*, 53-60.
7. Boparai Kamaljit, S., et al., Development of rapid tooling using fused deposition modeling: a review. *Rapid Prototyp. J.* **2016**, *22* (2), 281-299.
8. Mohamed, O. A., et al., Optimization of fused deposition modeling process parameters: a review of current research and future prospects. *Adv. Manuf.* **2015**, *3* (1), 42-53.
9. Anitha, R., et al., Critical parameters influencing the quality of prototypes in fused deposition modelling. *J. Mater. Process. Technol.* **2001**, *118* (1-3), 385-388.
10. Nancharaiah, T., et al., An experimental investigation on surface quality and dimensional accuracy of FDM components. *Int. J. Emerg. Technol.* **2010**, *1* (2), 106-111.
11. Thrimurthulu, K., et al., Optimum part deposition orientation in fused deposition modeling. *Int. J. Mach. Tools Manuf.* **2004**, *44* (6), 585-594.
12. Wang, C. C., et al., Optimizing the rapid prototyping process by integrating the Taguchi method with the Gray relational analysis. *Rapid prototyp. J.* **2007**, *13* (5), 304-315.
13. Wang, P., et al., Effects of printing parameters of fused deposition modeling on mechanical properties, surface quality, and microstructure of PEEK. *J. Mater. Process. Technol.* **2019**, *271*, 62-74.
14. Drummer, D., et al., Suitability of PLA/TCP for fused deposition modeling. *Rapid Prototyp. J.* **2012**, *18* (6), 500-507.
15. Zhang, B., et al., 3D printing of high-resolution PLA-based structures by hybrid electrohydrodynamic and fused deposition modeling techniques. *J. Micromech. Microeng.* **2016**, *26* (2), 025015.
16. Dávila, J., et al., Fabrication of PCL/ β -TCP scaffolds by 3D mini-screw extrusion printing. *J. Appl. Polym. Sci.* **2016**, *133* (15).
17. Hoque, M. E., et al., Fabrication and characterization of hybrid PCL/PEG 3D scaffolds for potential tissue engineering applications. *Mater. Lett.* **2014**, *131*, 255-258.
18. Billiet, T., et al., A review of trends and limitations in hydrogel-rapid prototyping for tissue engineering. *Biomaterials* **2012**, *33* (26), 6020-6041.
19. Yeong, W.-Y., et al., Rapid prototyping in tissue engineering: challenges and potential. *Trends Biotechnol.* **2004**, *22* (12), 643-652.
20. Bochmann, E. S., et al., Predicting melt rheology for hot-melt extrusion by means of a simple Tg-measurement. *Eur. J. Pharm. Biopharm.* **2017**, *119*, 47-55.
21. Yang, F., et al., Rheology Guided Rational Selection of Processing Temperature To Prepare Copovidone–Nifedipine Amorphous Solid Dispersions via Hot Melt Extrusion (HME). *Mol. Pharm.* **2016**, *13* (10), 3494-3505.
22. Aho, J., et al., Rheology as a tool for evaluation of melt processability of innovative dosage forms. *Int. J. Pharm.* **2015**, *494* (2), 623-642.

23. Wang, S.-Q., et al., New Experiments for Improved Theoretical Description of Nonlinear Rheology of Entangled Polymers. *Macromolecules* **2013**, *46* (8), 3147-3159.
24. Vlachopoulos, J.; Strutt, D. In *The role of rheology in polymer extrusion*, New Technology for Extrusion Conference. Milan, Italy. Nov, **2003**, 20-21.
25. Larson, R. G.; Desai, P. S., Modeling the Rheology of Polymer Melts and Solutions. *Annu. Rev. Fluid Mech.* **2015**, *47* (1), 47-65.
26. Herbst, F., et al., Aggregation and Chain Dynamics in Supramolecular Polymers by Dynamic Rheology: Cluster Formation and Self-Aggregation. *Macromolecules* **2010**, *43* (23), 10006-10016.
27. Seiffert, S.; Sprakel, J., Physical chemistry of supramolecular polymer networks. *Chem. Soc. Rev.* **2012**, *41* (2), 909-930.
28. Folmer, B. J., et al., Supramolecular polymer materials: chain extension of telechelic polymers using a reactive hydrogen-bonding synthon. *Adv. Mater.* **2000**, *12* (12), 874-878.
29. Patel, P. N., et al., Rheological and recovery properties of poly(ethylene glycol) diacrylate hydrogels and human adipose tissue. *J. Biomed. Mater. Res. A* **2005**, *73A* (3), 313-319.
30. Chen, M. H., et al., Methods To Assess Shear-Thinning Hydrogels for Application As Injectable Biomaterials. *ACS Biomater. Sci. Eng.* **2017**, *3* (12), 3146-3160.
31. Shao, Y., et al., Use of Microfibrillated Cellulose/Lignosulfonate Blends as Carbon Precursors: Impact of Hydrogel Rheology on 3D Printing. *Ind. Eng. Chem. Res.* **2015**, *54* (43), 10575-10582.
32. Dobrescu, V. E.; Radovici, C., Temperature dependence of melt viscosity of polymers. *Polym. Bull.* **1983**, *10* (3), 134-140.
33. Wang, J.-s.; Porter, R. S., On the viscosity-temperature behavior of polymer melts. *Rheol. Acta* **1995**, *34* (5), 496-503.
34. Mackay, M. E., The importance of rheological behavior in the additive manufacturing technique material extrusion. *J. Rheol.* **2018**, *62* (6), 1549-1561.
35. Liang, J.-Z., Characteristics of melt shear viscosity during extrusion of polymers. *Polym. Test.* **2002**, *21* (3), 307-311.
36. Ramanath, H., et al., Melt flow behaviour of poly- ϵ -caprolactone in fused deposition modelling. *J. Mater. Sci. Mater. Med.* **2008**, *19* (7), 2541-2550.
37. Sender, C., et al., Dynamic mechanical properties of a biomimetic hydroxyapatite/polyamide 6, 9 nanocomposite. *J. Biomed. Mater. Res.* **2007**, *83B* (2), 628-635.
38. Athreya, S. R., et al., Mechanical and microstructural properties of Nylon-12/carbon black composites: Selective laser sintering versus melt compounding and injection molding. *Compos. Sci. Technol.* **2011**, *71* (4), 506-510.
39. Fornes, T.; Paul, D., Modeling properties of nylon 6/clay nanocomposites using composite theories. *Polymer* **2003**, *44* (17), 4993-5013.
40. Zhang, X., et al., Thermal and crystallization studies of nano-hydroxyapatite reinforced polyamide 66 biocomposites. *Polymer degradation and stability* **2006**, *91* (5), 1202-1207.
41. Zhu, D., et al., Thermal and mechanical properties of polyamide 12/graphene nanoplatelets nanocomposites and parts fabricated by fused deposition modeling. *J. Appl. Polym. Sci.* **2017**, *134* (39), 45332.
42. Yang, C., et al., Influence of thermal processing conditions in 3D printing on the crystallinity and mechanical properties of PEEK material. *J. Mater. Process. Technol.* **2017**, *248*, 1-7.
43. Carneiro, O. S., et al., Fused deposition modeling with polypropylene. *Mater. Des.* **2015**, *83*, 768-776.
44. Tekinalp, H. L., et al., Highly oriented carbon fiber-polymer composites via additive manufacturing. *Compos. Sci. Technol.* **2014**, *105*, 144-150.
45. Weng, Z., et al., Mechanical and thermal properties of ABS/montmorillonite nanocomposites for fused deposition modeling 3D printing. *Mater. Des.* **2016**, *102*, 276-283.
46. Ning, F., et al., Additive manufacturing of carbon fiber reinforced thermoplastic composites using fused deposition modeling. *Compos. B Eng.* **2015**, *80*, 369-378.

47. Dul, S., et al., Fused deposition modelling with ABS–graphene nanocomposites. *Compos. Part A Appl. Sci. Manuf.* **2016**, *85*, 181-191.
48. Gkartzou, E., et al., Production and 3D printing processing of bio-based thermoplastic filament. *Manuf. Rev.* **2017**, *4*, 1.
49. Kalita, S. J., et al., Development of controlled porosity polymer-ceramic composite scaffolds via fused deposition modeling. *Mater. Sci. Eng. C* **2003**, *23* (5), 611-620.
50. Abdul Haq, R. H., et al. In *Improvement of mechanical properties of polycaprolactone (PCL) by addition of nano-montmorillonite (MMT) and hydroxyapatite (HA)*, Appl. Mech. Mater. **2013**, 815-819.
51. Rahim, T., et al., The improvement of mechanical and thermal properties of polyamide 12 3D printed parts by fused deposition modelling. *Express Polym. Lett.* **2017**, *11* (12), 963-982.
52. Rahim, T. N. A. T., et al., Recent developments in fused deposition modeling-based 3D printing of polymers and their composites. *Polym. Rev. (Philadelphia, PA, U. S.)* **2019**, *59* (4), 589-624.
53. Voet, V. S., et al., Biobased acrylate photocurable resin formulation for stereolithography 3D printing. *ACS Omega* **2018**, *3* (2), 1403-1408.
54. Hague, R., et al., Materials analysis of stereolithography resins for use in rapid manufacturing. *J. Mater. Sci.* **2004**, *39* (7), 2457-2464.
55. Esposito Corcione, C., et al., Photopolymerization kinetics of an epoxy-based resin for stereolithography. *J. Appl. Polym. Sci.* **2004**, *92* (6), 3484-3491.
56. Wang, W., et al., Computer-stereolithography-based laser rapid prototyping & manufacturing system. *IFAC Proc.* **1999**, *32* (2), 61-66.
57. Luo, X., et al. In *Galvanometer scanning technology for laser additive manufacturing*, Laser 3D Manufacturing IV, International Society for Optics and Photonics: **2017**, 1009512.
58. Bertsch, A., et al., Microstereolithography using a liquid crystal display as dynamic mask-generator. *Microsyst. Technol.* **1997**, *3* (2), 42-47.
59. Nakamoto, T.; Yamaguchi, K. In *Consideration on the producing of high aspect ratio micro parts using UV sensitive photopolymer*, MHS'96 Proceedings of the Seventh International Symposium on Micro Machine and Human Science, **1996**, 53-58.
60. Loubère, V., et al. In *Microstereolithography using a mask-generator display*, Proc. of the 4th Japan-France Congress and 2nd Asia-Europe Congress on Mechatronics, **1998**, 160-163.
61. Tumbleston, J. R., et al., Continuous liquid interface production of 3D objects. *Science* **2015**, *347* (6228), 1349-1352.
62. Januszewicz, R., et al., Layerless fabrication with continuous liquid interface production. *Proc. Natl. Acad. Sci.* **2016**, *113* (42), 11703-11708.
63. Shusteff, M., et al. In *Additive fabrication of 3d structures by holographic lithography*, 27th Annual Solid Freeform Fabrication Symposium (SFF), Austin, TX, **2016**, 8-10.
64. Shusteff, M., et al., One-step volumetric additive manufacturing of complex polymer structures. *Sci. Adv.* **2017**, *3* (12), eaao5496.
65. Kruth, J.-P., et al., Lasers and materials in selective laser sintering. *Assem. Autom.* **2003**, *23* (4), 357-371.
66. Schmid, M., et al. In *Polymer powders for selective laser sintering (SLS)*, AIP Conference proceedings, AIP Publishing LLC: **2015**, 160009.
67. Franco, A., et al., Experimental analysis of selective laser sintering of polyamide powders: an energy perspective. *J. Clean. Prod.* **2010**, *18* (16-17), 1722-1730.
68. Tan, K., et al., Selective laser sintering of biocompatible polymers for applications in tissue engineering. *Biomed. Mater. Eng.* **2005**, *15* (1, 2), 113-124.
69. Williams, J. M., et al., Bone tissue engineering using polycaprolactone scaffolds fabricated via selective laser sintering. *Biomaterials* **2005**, *26* (23), 4817-4827.
70. Alhnan, M. A., et al., Emergence of 3D printed dosage forms: opportunities and challenges. *Pharm. Res.* **2016**, *33* (8), 1817-1832.
71. Yu, D. G., et al., Three-dimensional printing in pharmaceuticals: promises and problems. *J. Pharm. Sci.* **2008**, *97* (9), 3666-3690.

72. Ziaee, M.; Crane, N. B., Binder jetting: A review of process, materials, and methods. *Addit. Manuf.* **2019**, *28*, 781-801.
73. Dini, F., et al., A review of binder jet process parameters; powder, binder, printing and sintering condition. *Met. Powder Rep.* **2020**, *75* (2), 95-100.
74. Gibson, I., et al., Material jetting. In *Addit. Manuf. Technol.*, Springer: **2015**, 175-203.
75. Rahman, Z., et al., Chapter 46 - Printing of personalized medication using binder jetting 3D printer. In *Precision Medicine for Investigators, Practitioners and Providers*, Faintuch, J.; Faintuch, S., Eds. Academic Press: **2020**, 473-481.
76. Patirupanusara, P., et al., Effect of binder content on the material properties of polymethyl methacrylate fabricated by three dimensional printing technique. *J. Mater. Process. Technol.* **2008**, *207* (1), 40-45.
77. Meisel, N. A., et al., Impact of material concentration and distribution on composite parts manufactured via multi-material jetting. *Rapid Prototyp. J.* **2018**, *24* (5), 872-879.
78. Kokkinis, D., et al., Multimaterial magnetically assisted 3D printing of composite materials. *Nat. Commun.* **2015**, *6*, 8643.
79. Berman, B., 3-D printing: The new industrial revolution. *Bus. Horiz.* **2012**, *55* (2), 155-162.
80. Ventola, C. L., Medical applications for 3D printing: current and projected uses. *Pharm. Ther.* **2014**, *39* (10), 704.
81. Sears, N. A., et al., A review of three-dimensional printing in tissue engineering. *Tissue Eng. Part B Rev.* **2016**, *22* (4), 298-310.
82. Yan, Q., et al., A review of 3D printing technology for medical applications. *Engineering* **2018**, *4* (5), 729-742.
83. Tack, P., et al., 3D-printing techniques in a medical setting: a systematic literature review. *Biomed. Eng. Online* **2016**, *15* (1), 115.
84. Okwuosa, T. C., et al., A Lower Temperature FDM 3D Printing for the Manufacture of Patient-Specific Immediate Release Tablets. *Pharm. Res.* **2016**, *33* (11), 2704-2712.
85. Prasad, L. K.; Smyth, H., 3D Printing technologies for drug delivery: a review. *Drug Dev. Ind. Pharm.* **2016**, *42* (7), 1019-1031.
86. Goyanes, A., et al., 3D printing of modified-release aminosaliclylate (4-ASA and 5-ASA) tablets. *Eur. J. Pharm. Biopharm.* **2015**, *89*, 157-162.
87. Melocchi, A., et al., 3D printing by fused deposition modeling (FDM) of a swellable/erodible capsular device for oral pulsatile release of drugs. *J. Drug Deliv. Sci. Technol.* **2015**, *30*, 360-367.
88. Okwuosa, T. C., et al., Fabricating a Shell-Core Delayed Release Tablet Using Dual FDM 3D Printing for Patient-Centred Therapy. *Pharm. Res.* **2017**, *34* (2), 427-437.
89. Melocchi, A., et al., Hot-melt extruded filaments based on pharmaceutical grade polymers for 3D printing by fused deposition modeling. *Int. J. Pharm.* **2016**, *509* (1), 255-263.
90. Maroni, A., et al., 3D printed multi-compartment capsular devices for two-pulse oral drug delivery. *J. Control. Release* **2017**, *268*, 10-18.
91. Gazzaniga, A., et al., A Novel Injection-Molded Capsular Device for Oral Pulsatile Delivery Based on Swellable/Erodible Polymers. *Pharm. Sci. Tech.* **2011**, *12* (1), 295-303.
92. Charoenying, T., et al., Fabrication of floating capsule-in- 3D-printed devices as gastro-retentive delivery systems of amoxicillin. *J. Drug Deliv. Sci. Technol.* **2020**, *55*, 101393.
93. Melocchi, A., et al., Industrial Development of a 3D-Printed Nutraceutical Delivery Platform in the Form of a Multicompartment HPC Capsule. *Pharm. Sci. Tech.* **2018**, *19* (8), 3343-3354.
94. Melocchi, A., et al., Retentive device for intravesical drug delivery based on water-induced shape memory response of poly(vinyl alcohol): design concept and 4D printing feasibility. *Int. J. Pharm.* **2019**, *559*, 299-311.
95. Huanbutta, K.; Sangnim, T., Design and development of zero-order drug release gastroretentive floating tablets fabricated by 3D printing technology. *J. Drug Deliv. Sci. Technol.* **2019**, *52*, 831-837.

96. Shin, S., et al., Development of a gastroretentive delivery system for acyclovir by 3D printing technology and its in vivo pharmacokinetic evaluation in Beagle dogs. *Plos One* **2019**, *14* (5), e0216875.
97. Fu, J., et al., Combination of 3D printing technologies and compressed tablets for preparation of riboflavin floating tablet-in-device (TiD) systems. *Int. J. Pharm.* **2018**, *549* (1), 370-379.
98. Genina, N., et al., Anti-tuberculosis drug combination for controlled oral delivery using 3D printed compartmental dosage forms: From drug product design to in vivo testing. *J. Control. Release* **2017**, *268*, 40-48.
99. Matijašić, G., et al., Design and 3D printing of multi-compartmental PVA capsules for drug delivery. *J. Drug Deliv. Sci. Technol.* **2019**, *52*, 677-686.
100. Kempin, W., et al., Development of a dual extrusion printing technique for an acid- and thermo-labile drug. *Eur. J. Pharm. Sci.* **2018**, *123*, 191-198.
101. Smith, D., et al., 3D printed capsules for quantitative regional absorption studies in the GI tract. *Int. J. Pharm.* **2018**, *550* (1), 418-428.
102. Smith, D. M., et al., Pharmaceutical 3D printing: Design and qualification of a single step print and fill capsule. *Int. J. Pharm.* **2018**, *544* (1), 21-30.
103. Okwuosa, T. C., et al., On demand manufacturing of patient-specific liquid capsules via co-ordinated 3D printing and liquid dispensing. *Eur. J. Pharm. Sci.* **2018**, *118*, 134-143.
104. Gioumouxouzis, C. I., et al., Controlled Release of 5-Fluorouracil from Alginate Beads Encapsulated in 3D Printed pH-Responsive Solid Dosage Forms. *Pharm. Sci. Tech.* **2018**, *19* (8), 3362-3375.
105. Goyanes, A., et al., Fabrication of controlled-release budesonide tablets via desktop (FDM) 3D printing. *Int. J. Pharm.* **2015**, *496* (2), 414-420.
106. Goyanes, A., et al., Effect of geometry on drug release from 3D printed tablets. *Int. J. Pharm.* **2015**, *494* (2), 657-663.
107. Goyanes, A., et al., 3D Printing of Medicines: Engineering Novel Oral Devices with Unique Design and Drug Release Characteristics. *Mol. Pharm.* **2015**, *12* (11), 4077-4084.
108. Goyanes, A., et al., 3D scanning and 3D printing as innovative technologies for fabricating personalized topical drug delivery systems. *J. Control. Release* **2016**, *234*, 41-48.
109. Linares, V., et al., Printfills: 3D printed systems combining fused deposition modeling and injection volume filling. Application to colon-specific drug delivery. *Eur. J. Pharm. Biopharm.* **2019**, *134*, 138-143.
110. Gioumouxouzis, C. I., et al., Recent advances in pharmaceutical dosage forms and devices using additive manufacturing technologies. *Drug Discovery Today* **2019**, *24* (2), 636-643.
111. Gupta, M. K., et al., 3D Printed Programmable Release Capsules. *Nano Lett.* **2015**, *15* (8), 5321-5329.
112. Beck, R. C. R., et al., 3D printed tablets loaded with polymeric nanocapsules: An innovative approach to produce customized drug delivery systems. *Int. J. Pharm.* **2017**, *528* (1), 268-279.
113. Davoudinejad, A., et al., Fabrication of micro-structured surfaces by additive manufacturing, with simulation of dynamic contact angle. *Mater. Des.* **2019**, *176*, 107839.
114. Sanders, P., et al., Stereolithographic 3D printing of extrinsically self-healing composites. *Sci. Rep.* **2019**, *9* (1), 388.
115. Moore, J. S., Supramolecular polymers. *Curr. Opin. Colloid Interface Sci.* **1999**, *4* (2), 108-116.
116. Brunsveld, L., et al., Supramolecular Polymers. *Chem. Rev.* **2001**, *101* (12), 4071-4098.
117. Herbst, F., et al., Dynamic supramolecular poly(isobutylene)s for self-healing materials. *Polym. Chem.* **2012**, *3* (11), 3084-3092.
118. Herbst, F., et al., Self-Healing Polymers via Supramolecular Forces. *Macromol. Rapid Commun.* **2013**, *34* (3), 203-220.
119. de Greef, T. F. A.; Meijer, E. W., Supramolecular polymers. *Nature* **2008**, *453* (7192), 171-173.
120. Seiffert, S., et al., *Supramolecular polymer networks and gels*. Springer: **2015**, Vol. 268.
121. Appel, E. A., et al., Supramolecular polymeric hydrogels. *Chem. Soc. Rev.* **2012**, *41* (18), 6195-6214.

122. Li, S.-L., et al., Advanced supramolecular polymers constructed by orthogonal self-assembly. *Chem. Soc. Rev.* **2012**, *41* (18), 5950-5968.
123. Chen, S.; Binder, W. H., Dynamic Ordering and Phase Segregation in Hydrogen-Bonded Polymers. *Acc. Chem. Res.* **2016**, *49* (7), 1409-1420.
124. Chen, S., et al., Engineering the morphology of hydrogen-bonded comb-shaped supramolecular polymers: from solution self-assembly to confined assembly. *Polym. Chem.* **2020**, *11* (24), 4022-4028.
125. Pedde, R. D., et al., Emerging Biofabrication Strategies for Engineering Complex Tissue Constructs. *Adv. Mater.* **2017**, *29* (19), 1606061.
126. Bajaj, P., et al., 3D Biofabrication Strategies for Tissue Engineering and Regenerative Medicine. *Annu. Rev. Biomed. Eng.* **2014**, *16* (1), 247-276.
127. Melchels, F. P., et al., A review on stereolithography and its applications in biomedical engineering. *Biomaterials* **2010**, *31* (24), 6121-6130.
128. Pekkanen, A. M., et al., 3D Printing Polymers with Supramolecular Functionality for Biological Applications. *Biomacromolecules* **2017**, *18* (9), 2669-2687.
129. Thompson, C. B.; Korley, L. T. J., Harnessing Supramolecular and Peptidic Self-Assembly for the Construction of Reinforced Polymeric Tissue Scaffolds. *Bioconjug. Chem.* **2017**, *28* (5), 1325-1339.
130. De Santis, E.; Ryadnov, M. G., Peptide self-assembly for nanomaterials: the old new kid on the block. *Chem. Soc. Rev.* **2015**, *44* (22), 8288-8300.
131. Prins, L. J., et al., Noncovalent Synthesis Using Hydrogen Bonding. *Angew. Chem. Int. Ed.* **2001**, *40* (13), 2382-2426.
132. Murray, T. J.; Zimmerman, S. C., New triply hydrogen bonded complexes with highly variable stabilities. *J. Am. Chem. Soc.* **1992**, *114* (10), 4010-4011.
133. Jorgensen, W. L.; Pranata, J., Importance of secondary interactions in triply hydrogen bonded complexes: guanine-cytosine vs uracil-2, 6-diaminopyridine. *J. Am. Chem. Soc.* **1990**, *112* (5), 2008-2010.
134. Pranata, J., et al., OPLS potential functions for nucleotide bases. Relative association constants of hydrogen-bonded base pairs in chloroform. *J. Am. Chem. Soc.* **1991**, *113* (8), 2810-2819.
135. Wilson, A. J., Non-covalent polymer assembly using arrays of hydrogen-bonds. *Soft Matter* **2007**, *3* (4), 409-425.
136. Weck, M., Side-chain functionalized supramolecular polymers. *Polym. Int.* **2007**, *56* (4), 453-460.
137. Herbst, F.; Binder, W. H., Comparing solution and melt-state association of hydrogen bonds in supramolecular polymers. *Polym. Chem.* **2013**, *4* (12), 3602-3609.
138. Yan, T., et al., Nanostructure and rheology of hydrogen-bonding telechelic polymers in the melt: From micellar liquids and solids to supramolecular gels. *Macromolecules* **2014**, *47* (6), 2122-2130.
139. Nair, K. P., et al., Modulating mechanical properties of self-assembled polymer networks by multi-functional complementary hydrogen bonding. *Soft Matter* **2011**, *7* (2), 553-559.
140. Chen, X., et al., Quadruple Hydrogen Bonding Supramolecular Elastomers for Melt Extrusion Additive Manufacturing. *ACS Appl. Mater. Interfaces* **2020**, *12* (28), 32006-32016.
141. Bobade, S., et al., Synthesis and Characterization of Ureidopyrimidone Telechelics by CuAAC "Click" Reaction: Effect of T_g and Polarity. *Macromolecules* **2014**, *47* (15), 5040-5050.
142. Sen, M. Y., et al., Precision synthesis and characterization of thymine-functionalized polyisobutylene. *J. Polym. Sci. Part A Polym. Chem.* **2010**, *48* (16), 3501-3506.
143. Döhler, D., et al., A dual crosslinked self-healing system: Supramolecular and covalent network formation of four-arm star polymers. *Polymer* **2015**, *69*, 264-273.
144. Yan, T., et al., What controls the structure and the linear and nonlinear rheological properties of dense, dynamic supramolecular polymer networks? *Macromolecules* **2017**, *50* (7), 2973-2985.

145. Rupp, H., et al., 3D Printing of Supramolecular Polymers: Impact of Nanoparticles and Phase Separation on Printability. *Macromol. Rapid Commun.* **2019**, *40* (24), 1900467.
146. Binder, W. H., et al., Synthesis and analysis of telechelic polyisobutylenes for hydrogen-bonded supramolecular pseudo-block copolymers. *Macromolecules* **2004**, *37* (5), 1749-1759.
147. Binder, W. H., et al., Magnetic and Temperature-Sensitive Release Gels from Supramolecular Polymers. *Adv. Funct. Mat.* **2007**, *17* (8), 1317-1326.
148. Hirschberg, J. H. K. K., et al., Supramolecular Polymers from Linear Telechelic Siloxanes with Quadruple-Hydrogen-Bonded Units. *Macromolecules* **1999**, *32* (8), 2696-2705.
149. Graessley, W. W., The entanglement concept in polymer rheology. In *The entanglement concept in polymer rheology*, Springer: **1974**, 1-179.
150. Colby, R. H., et al., Chain entanglement in polymer melts and solutions. *Macromolecules* **1992**, *25* (2), 996-998.
151. Jangizehi, A., et al., Dominance of chain entanglement over transient sticking on chain dynamics in hydrogen-bonded supramolecular polymer networks in the melt. *Macromolecules* **2018**, *51* (8), 2859-2871.
152. Otazaghine, B., et al., Synthesis of Telechelic Oligomers via Atom Transfer Radical Polymerization, *Macromol. Chem. Phys.* **2004**, *205* (2), 154-164.
153. Lima, V., et al., Synthesis and characterization of telechelic polymethacrylates via RAFT polymerization. *J. Polym. Sci. Part A Polym. Chem.* **2005**, *43* (5), 959-973.
154. Morita, T., et al., A ring-opening metathesis polymerization (ROMP) approach to carboxyl- and amino-terminated telechelic poly (butadiene) s. *Macromolecules* **2000**, *33* (17), 6621-6623.
155. Tasdelen, M. A., et al., Telechelic polymers by living and controlled/living polymerization methods. *Prog. Polym. Sci.* **2011**, *36* (4), 455-567.
156. Song, Q., et al., Supramolecular polymers synthesized by thiol-ene click polymerization from supramonomers. *Polym. Chem.* **2015**, *6* (3), 369-372.
157. Hohl, D. K., et al., Toughening of Glassy Supramolecular Polymer Networks. *ACS Macro Let.* **2019**, *8* (11), 1484-1490.
158. Van Beek, D., et al., Unidirectional dimerization and stacking of ureidopyrimidinone end groups in polycaprolactone supramolecular polymers. *Macromolecules* **2007**, *40* (23), 8464-8475.
159. Hermida-Merino, D., et al., Electrospun supramolecular polymer fibres. *Eur. Polym. J.* **2012**, *48* (7), 1249-1255.
160. Dankers, P. Y., et al., Chemical and biological properties of supramolecular polymer systems based on oligocaprolactones. *Biomaterials* **2006**, *27* (32), 5490-5501.
161. Dankers, P. Y. W., et al., A modular and supramolecular approach to bioactive scaffolds for tissue engineering. *Nat. Mater.* **2005**, *4* (7), 568-574.
162. Hart, L. R., et al., 3D Printing of Biocompatible Supramolecular Polymers and their Composites. *ACS Appl. Mater. Interfaces* **2016**, *8* (5), 3115-3122.
163. Street, D. P., et al., Self-Complementary Multiple Hydrogen-Bonding Additives Enhance Thermomechanical Properties of 3D-Printed PMMA Structures. *Macromolecules* **2019**, *52* (15), 5574-5582.
164. Burattini, S., et al., A Supramolecular Polymer Based on Tweezer-Type π - π Stacking Interactions: Molecular Design for Healability and Enhanced Toughness. *Chem. Mater.* **2011**, *23* (1), 6-8.
165. Invernizzi, M., et al., 4D printed thermally activated self-healing and shape memory polycaprolactone-based polymers. *Eur. Polym. J.* **2018**, *101*, 169-176.
166. Invernizzi, M., et al., Processability of 4D printable modified polycaprolactone with self-healing abilities. *Mater. Today Proceed.* **2019**, *7*, 508-515.
167. Wilts, E. M., et al., Vat photopolymerization of charged monomers: 3D printing with supramolecular interactions. *Polym. Chem.* **2019**, *10* (12), 1442-1451.
168. Kautz, H., et al., Cooperative End-to-End and Lateral Hydrogen-Bonding Motifs in Supramolecular Thermoplastic Elastomers. *Macromolecules* **2006**, *39* (13), 4265-4267.

169. Schrettl, S., et al., Functional Polymers Through Mechanochemistry. *CHIMIA* **2019**, *73* (1), 7-11.
170. Omar, R. G., et al., Self-Reporting Fiber-Reinforced Composites That Mimic the Ability of Biological Materials to Sense and Report Damage. *Adv. Mater.* **2018**, *30* (19), 1705483.
171. Chen, Y., et al., Mechanically induced chemiluminescence from polymers incorporating a 1,2-dioxetane unit in the main chain. *Nature Chem.* **2012**, *4* (7), 559-562.
172. Chen, Y.; Sijbesma, R. P., Dioxetanes as Mechanoluminescent Probes in Thermoplastic Elastomers. *Macromolecules* **2014**, *47* (12), 3797-3805.
173. Clough, J. M.; Sijbesma, R. P., Dioxetane Scission Products Unchanged by Mechanical Force. *Chem. Phys. Chem.* **2014**, *15* (16), 3565-3571.
174. Diesendruck, C. E., et al., Proton-Coupled Mechanochemical Transduction: A Mechanogenerated Acid. *J. Am. Chem. Soc.* **2012**, *134* (30), 12446-12449.
175. Larsen, M. B.; Boydston, A. J., "Flex-Activated" Mechanophores: Using Polymer Mechanochemistry To Direct Bond Bending Activation. *J. Am. Chem. Soc.* **2013**, *135* (22), 8189-8192.
176. Larsen, M. B.; Boydston, A. J., Successive Mechanochemical Activation and Small Molecule Release in an Elastomeric Material. *J. Am. Chem. Soc.* **2014**, *136* (4), 1276-1279.
177. Gossweiler, G. R., et al., Mechanochemical Activation of Covalent Bonds in Polymers with Full and Repeatable Macroscopic Shape Recovery. *ACS Macro Let.* **2014**, *3* (3), 216-219.
178. Potisek, S. L., et al., Mechanophore-Linked Addition Polymers. *J. Am. Chem. Soc.* **2007**, *129* (45), 13808-13809.
179. Balkenende, D. W. R., et al., Mechanochemistry with Metallosupramolecular Polymers. *J. Am. Chem. Soc.* **2014**, *136* (29), 10493-10498.
180. Fitch, K. R.; Goodwin, A. P., Mechanochemical Reaction Cascade for Sensitive Detection of Covalent Bond Breakage in Hydrogels. *Chem. Mater.* **2014**, *26* (23), 6771-6776.
181. Sagara, Y., et al., Temperature-Dependent Mechanochromic Behavior of Mechanoresponsive Luminescent Compounds. *Chem. Mater.* **2017**, *29* (3), 1273-1278.
182. Sagara, Y., et al., Rotaxanes as Mechanochromic Fluorescent Force Transducers in Polymers. *J. Am. Chem. Soc.* **2018**, *140* (5), 1584-1587.
183. Watabe, T., et al., Mechanochromic dendrimers: the relationship between primary structure and mechanochromic properties in the bulk. *Chem. Commun.* **2019**, *55* (48), 6831-6834.
184. Sommer, M.; Komber, H., Spiropyran Main-Chain Conjugated Polymers. *Macromol. Rapid Commun.* **2013**, *34* (1), 57-62.
185. Metzler, L., et al., High molecular weight mechanochromic spiropyran main chain copolymers via reproducible microwave-assisted Suzuki polycondensation. *Polym. Chem.* **2015**, *6* (19), 3694-3707.
186. Raisch, M., et al., Highly Sensitive, Anisotropic, and Reversible Stress/Strain-Sensors from Mechanochromic Nanofiber Composites. *Adv. Mater.* **2018**, *30* (39), 1802813.
187. Piermattei, A., et al., Activating catalysts with mechanical force. *Nat. Chem.* **2009**, *1* (2), 133-137.
188. Jakobs, R. T. M.; Sijbesma, R. P., Mechanical Activation of a Latent Olefin Metathesis Catalyst and Persistence of its Active Species in ROMP. *Organometallics* **2012**, *31* (6), 2476-2481.
189. Jakobs, R. T. M., et al., Mechanocatalytic Polymerization and Cross-Linking in a Polymeric Matrix. *ACS Macro Let.* **2013**, *2* (7), 613-616.
190. Michael, P., et al., Synthesis and characterization of polymer linked copper(I) bis(N-heterocyclic carbene) mechanocatalysts. *J. Polym. Sci. Part A Polym. Chem.* **2017**, *55* (23), 3893-3907.
191. Funtan, S., et al., Synthesis and Mechanochemical Activity of Peptide-Based Cu(I) Bis(N-heterocyclic carbene) Complexes. *Biomimetics* **2019**, *4* (1), 24.
192. Biewend, M., et al., Detection of stress in polymers: mechanochemical activation of CuAAC click reactions in poly(urethane) networks. *Soft Matter* **2020**.
193. Michael, P., et al., Mechanochemical Activation of Fluorogenic CuAAC "Click" Reactions for Stress-Sensing Applications. *Macromol. Rapid Commun.* **2018**, *39* (22), 1800376.

194. Beiermann, B. A., et al., Role of Mechanophore Orientation in Mechanochemical Reactions. *ACS Macro Lett.* **2012**, *1* (1), 163-166.
195. Li, M., et al., Photo-inactive divinyl spiropyran mechanophore cross-linker for real-time stress sensing. *Polymer* **2016**, *99*, 521-528.
196. Kim, T. A., et al., Mechanical Reactivity of Two Different Spiropyran Mechanophores in Polydimethylsiloxane. *Macromolecules* **2018**, *51* (22), 9177-9183.
197. Li, M., et al., Let spiropyran help polymers feel force! *Prog. Polym. Sci.* **2018**, *79*, 26-39.
198. Celestine, A.-D. N., et al., Strain and stress mapping by mechanochemical activation of spiropyran in poly(methyl methacrylate). *Strain* **2019**, *55* (3), e12310.
199. Peterson Gregory, I., et al., Additive manufacturing of mechanochromic polycaprolactone on entry-level systems. *Rapid Prototyp. J.* **2015**, *21* (5), 520-527.
200. Peterson, G. I., et al., 3D-Printed Mechanochromic Materials. *ACS Appl. Mater. Interfaces* **2015**, *7* (1), 577-583.
201. Michael, P.; Binder, W. H., A Mechanochemically Triggered "Click" Catalyst. *Angew. Chem. Int. Ed.* **2015**, *54* (47), 13918-13922.
202. Binder, W. H., The "labile" chemical bond: A perspective on mechanochemistry in polymers. *Polymer* **2020**, *202*, 122639.
203. Brantley, J. N., et al., Polymer mechanochemistry: the design and study of mechanophores. *Polym. Int.* **2013**, *62* (1), 2-12.
204. Calvino, C., et al., Approaches to polymeric mechanochromic materials. *J. Polym. Sci. Part A Polym. Chem.* **2017**, *55* (4), 640-652.
205. Neumann, S., et al., The CuAAC: Principles, Homogeneous and Heterogeneous Catalysts, and Novel Developments and Applications. *Macromol. Rapid Commun.* **2020**, *41* (1), 1900359.
206. Cao, B., et al., Additive manufacturing with a flex activated mechanophore for nondestructive assessment of mechanochemical reactivity in complex object geometries. *Polymer* **2018**, *152*, 4-8.
207. Zhao, Y., et al., Encapsulation of Self-Healing Agents in Polymer Nanocapsules. *Small* **2012**, *8* (19), 2954-2958.
208. Gurny, R., et al., Development of Biodegradable and Injectable Latices for Controlled Release of Potent Drugs. *Drug Dev. Ind. Pharm.* **1981**, *7* (1), 1-25.
209. Julienne, M., et al. In *Characterisation of antibiotic loaded poly (dl-lactide-co-glycolide) nanoparticles produced by evaporation process*, Proc. Intern. Symp. Control. Rel. Bioact. Mater., **1989**, 77-78.
210. Coffin, M. D.; McGinity, J. W., Biodegradable Pseudolatexes: The Chemical Stability of Poly(D,L-Lactide) and Poly (ϵ -Caprolactone) Nanoparticles in Aqueous Media. *Pharm. Res.* **1992**, *9* (2), 200-205.
211. Watnasirichaikul, S., et al., Preparation of biodegradable insulin nanocapsules from biocompatible microemulsions. *Pharmaceutical research* **2000**, *17* (6), 684-689.
212. Gürsoy, A., et al., Evaluation of indomethacin nanocapsules for their physical stability and inhibitory activity on inflammation and platelet aggregation. *Int. J. Pharm.* **1989**, *52* (2), 101-108.
213. Hubert, B., et al., The preparation and acute antihypertensive effects of a nanocapsular form of darodipine, a dihydropyridine calcium entry blocker. *Pharm. Res.* **1991**, *8* (6), 734-738.
214. Kreuter, J., et al., The use of new polymethylmethacrylate adjuvants for split influenza vaccines. *Pathobiology* **1976**, *44* (1), 12-19.
215. Rolland, A., et al., Purification et propriétés physico-chimiques des suspensions de nanoparticules de polymere. *J. Pharm. Belg.* **1986**, *41*, 94-105.
216. Couvreur, P., et al., Tissue distribution of antitumor drugs associated with polyalkylcyanoacrylate nanoparticles. *J. Pharm. Sci.* **1980**, *69* (2), 199-202.
217. Mora-Huertas, C. E., et al., Polymer-based nanocapsules for drug delivery. *Int. J. Pharm.* **2010**, *385* (1), 113-142.
218. Erdoğar, N., et al., Nanocapsules for drug delivery: an updated review of the last decade. *Recent Pat. Drug Deliv. Formul.* **2018**, *12* (4), 252-266.

219. Couvreur, P., et al., Nanocapsule technology: a review. *Crit. Rev. Ther. Drug Carrier Syst.* **2002**, *19* (2).
220. Nagavarma, B., et al., Different techniques for preparation of polymeric nanoparticles-a review. *Asian J. Pharm. Clin. Res* **2012**, *5* (3), 16-23.
221. Verrecchia, T., et al., Adsorption/desorption of human serum albumin at the surface of poly (lactic acid) nanoparticles prepared by a solvent evaporation process. *J. Biomed. Mater. Res.* **1993**, *27* (8), 1019-1028.
222. Sanchez, A., et al., Development of biodegradable microspheres and nanospheres for the controlled release of cyclosporin A. *Int. J. Pharm.* **1993**, *99* (2-3), 263-273.
223. Verrecchia, T., et al., Non-stealth (poly (lactic acid/albumin)) and stealth (poly (lactic acid-polyethylene glycol)) nanoparticles as injectable drug carriers. *J. Control. Rel.* **1995**, *36* (1-2), 49-61.
224. Cheng, Y.-H., et al., A poly (D, L-lactide-co-glycolide) microsphere depot system for delivery of haloperidol. *J. Control. Rel.* **1998**, *55* (2-3), 203-212.
225. Suh, H., et al., Regulation of smooth muscle cell proliferation using paclitaxel-loaded poly(ethylene oxide)-poly(lactide/glycolide) nanospheres. *J. Biomed. Mater. Res.* **1998**, *42* (2), 331-338.
226. Tobio, M., et al., The role of PEG on the stability in digestive fluids and in vivo fate of PEG-PLA nanoparticles following oral administration. *Colloids Surf. B.* **2000**, *18* (3-4), 315-323.
227. Bhanvase, B.; Sonawane, S., Ultrasound assisted in situ emulsion polymerization for polymer nanocomposite: A review. *Chem. Eng. Process.* **2014**, *85*, 86-107.
228. Palaniappan, S.; John, A., Polyaniline materials by emulsion polymerization pathway. *Prog. Polym. Sci.* **2008**, *33* (7), 732-758.
229. Feuser, P. E., et al., Synthesis of ZnPc loaded poly(methyl methacrylate) nanoparticles via miniemulsion polymerization for photodynamic therapy in leukemic cells. *Mater. Sci. Eng.* **2016**, *60*, 458-466.
230. Allemann, E., et al., Drug-loaded nanoparticles: preparation methods and drug targeting issues. *Eur. J. Pharm. Biopharm.* **1993**, *39* (5), 173-191.
231. Sari, A., et al., Microencapsulated n-octacosane as phase change material for thermal energy storage. *Sol. Energy* **2009**, *83* (10), 1757-1763.
232. Alkan, C., et al., Preparation, characterization, and thermal properties of microencapsulated phase change material for thermal energy storage. *Sol. Energy Mater. Sol. Cells* **2009**, *93* (1), 143-147.
233. Sari, A., et al., Preparation, characterization and thermal properties of PMMA/n-heptadecane microcapsules as novel solid-liquid microPCM for thermal energy storage. *Appl. Energy* **2010**, *87* (5), 1529-1534.
234. Alay, S., et al., Synthesis and characterization of poly (methyl methacrylate)/n-hexadecane microcapsules using different cross-linkers and their application to some fabrics. *Thermochim. Acta* **2011**, *518* (1-2), 1-8.
235. Radwan, M.; Aboul-Enein, H., The effect of oral absorption enhancers on the in vivo performance of insulin-loaded poly (ethylcyanoacrylate) nanospheres in diabetic rats. *J. Microencapsul.* **2002**, *19* (2), 225-235.
236. Li, V. H., et al., Ocular drug delivery of progesterone using nanoparticles. *J. Microencapsul.* **1986**, *3* (3), 213-218.
237. Seijo, B., et al., Design of nanoparticles of less than 50 nm diameter: preparation, characterization and drug loading. *Int. J. Pharm.* **1990**, *62* (1), 1-7.
238. Maincent, P., et al., Disposition kinetics and oral bioavailability of vincamine-loaded polyalkyl cyanoacrylate nanoparticles. *J. Pharm. Sci.* **1986**, *75* (10), 955-958.
239. Krause, H. J., et al., Interfacial Polymerization, A Useful Method for the Preparation of Polymethylcyanoacrylate Nanoparticles. *Drug Dev. Ind. Pharm.* **1986**, *12* (4), 527-552.
240. Aprahamian, M., et al., Transmucosal passage of polyalkylcyanoacrylate nanocapsules as a new drug carrier in the small intestine. *Biol. Cell* **1987**, *61* (1-2), 69-76.

241. Lambert, G., et al., Polyisobutylcyanoacrylate nanocapsules containing an aqueous core as a novel colloidal carrier for the delivery of oligonucleotides. *Pharm. Res.* **2000**, *17* (6), 707-714.
242. Zhang, L., et al., Polypyrrole nanocapsules via interfacial polymerization. *Macromol. Res.* **2010**, *18* (7), 648-652.
243. Kobašlija, M.; McQuade, D. T., Polyurea Microcapsules from Oil-in-Oil Emulsions via Interfacial Polymerization. *Macromolecules* **2006**, *39* (19), 6371-6375.
244. Damgé, C., et al., New approach for oral administration of insulin with polyalkylcyanoacrylate nanocapsules as drug carrier. *Diabetes* **1988**, *37* (2), 246-251.
245. DAMGÉ, C., et al., Poly (alkyl cyanoacrylate) Nanocapsules as a Delivery System in the Rat for Octreotide, a Long-acting Somatostatin Analogue. *J. Pharm. Pharmacol.* **1997**, *49* (10), 949-954.
246. Fessi, H., et al., Nanocapsule formation by interfacial polymer deposition following solvent displacement. *Int. J. Pharm.* **1989**, *55* (1), R1-R4.
247. Yu, W., et al., A novel approach to the preparation of injectable emulsions by a spontaneous emulsification process. *Int. J. Pharm.* **1993**, *89* (2), 139-146.
248. Calvo, P., et al., Comparative in vitro evaluation of several colloidal systems, nanoparticles, nanocapsules, and nanoemulsions, as ocular drug carriers. *J. Pharm. Sci.* **1996**, *85* (5), 530-536.
249. Quintanar-Guerrero, D., et al., Preparation techniques and mechanisms of formation of biodegradable nanoparticles from preformed polymers. *Drug Dev. Ind. Pharm.* **1998**, *24* (12), 1113-1128.
250. Dimitrova, B., et al., Mass transport effects on the stability of emulsion: emulsion films with acetic acid and acetone diffusing across the interface. *J. Dispers. Sci. Technol.* **1988**, *9* (4), 321-341.
251. Salager, J.-L., et al. In *Dynamics of near-zero Energy Emulsification*, Proceedings of the 6th World Surfactant Congress CESIO, **2004**, 21-23.
252. Ammoury, N., et al., Jejunal absorption, pharmacological activity, and pharmacokinetic evaluation of indomethacin-loaded poly (D, L-lactide) and poly (isobutyl-cyanoacrylate) nanocapsules in rats. *Pharm. Res.* **1991**, *8* (1), 101-105.
253. Barichello, J. M., et al., Encapsulation of hydrophilic and lipophilic drugs in PLGA nanoparticles by the nanoprecipitation method. *Drug Dev. Ind. Pharm.* **1999**, *25* (4), 471-476.
254. Némati, F., et al., Reversion of multidrug resistance using nanoparticles in vitro: influence of the nature of the polymer. *Int. J. Pharm.* **1996**, *138* (2), 237-246.
255. Moinard-Chécot, D., et al., Mechanism of nanocapsules formation by the emulsion-diffusion process. *J. Colloid Interface Sci.* **2008**, *317* (2), 458-468.
256. Konan, Y. N., et al., Enhanced photodynamic activity of meso-tetra (4-hydroxyphenyl) porphyrin by incorporation into sub-200 nm nanoparticles. *Eur. J. Pharm. Sci.* **2003**, *18* (3-4), 241-249.
257. Perez, C., et al., Poly (lactic acid)-poly (ethylene glycol) nanoparticles as new carriers for the delivery of plasmid DNA. *J. Control. Rel.* **2001**, *75* (1-2), 211-224.
258. Esmaeili, F., et al., Preparation of PLGA nanoparticles using TPGS in the spontaneous emulsification solvent diffusion method. *J. Exp. Nanosci.* **2007**, *2* (3), 183-192.
259. Gorman, I. E., et al., Development of a triazole-cure resin system for composites: Evaluation of alkyne curatives. *Polymer* **2012**, *53* (13), 2548-2558.
260. Sheng, X., et al., Kinetics of bulk azide/alkyne "click" polymerization. *J. Polym. Sci. Part A Polym. Chem.* **2010**, *48* (18), 4093-4102.
261. Clará, R. A., et al., Density, Viscosity, and Refractive Index in the Range (283.15 to 353.15) K and Vapor Pressure of α -Pinene, d-Limonene, (\pm)-Linalool, and Citral Over the Pressure Range 1.0 kPa Atmospheric Pressure. *J. Chem. Eng. Data* **2009**, *54* (3), 1087-1090.
262. Gioumouxouzis, C. I., et al., 3D printed oral solid dosage forms containing hydrochlorothiazide for controlled drug delivery. *J. Drug Deliv. Sci. Technol.* **2017**, *40*, 164-171.

263. Gioumouxouzis, C. I., et al., A 3D printed bilayer oral solid dosage form combining metformin for prolonged and glimepiride for immediate drug delivery. *Eur. J. Pharm. Sci.* **2018**, *120*, 40-52.
264. Khaled, S. A., et al., 3D printing of five-in-one dose combination polypill with defined immediate and sustained release profiles. *J. Control. Rel.* **2015**, *217*, 308-314.
265. Markl, D., et al., Analysis of 3D Prints by X-ray Computed Microtomography and Terahertz Pulsed Imaging. *Pharm. Res.* **2017**, *34* (5), 1037-1052.
266. Nober, C., et al., Feasibility study into the potential use of fused-deposition modeling to manufacture 3D-printed enteric capsules in compounding pharmacies. *Int. J. Pharm.* **2019**, *569*, 118581.
267. Khaled, S. A., et al., 3D printing of tablets containing multiple drugs with defined release profiles. *Int. J. Pharm.* **2015**, *494* (2), 643-650.
268. Eleftheriadis, G. K., et al., FDM-printed pH-responsive capsules for the oral delivery of a model macromolecular dye. *Pharm. Dev. Technol.* **2020**, *25* (4), 517-523.
269. Chen, D., et al., Preparation and In vitro Evaluation of FDM 3D-Printed Ellipsoid-Shaped Gastric Floating Tablets with Low Infill Percentages. *Pharm. Sci. Tech.* **2019**, *21* (1), 6.
270. Ilkhanizadeh, S., et al., Inkjet printing of macromolecules on hydrogels to steer neural stem cell differentiation. *Biomaterials* **2007**, *28* (27), 3936-3943.
271. Ker, E. D. F., et al., Engineering spatial control of multiple differentiation fates within a stem cell population. *Biomaterials* **2011**, *32* (13), 3413-3422.
272. Ker, E. D. F., et al., Bioprinting of growth factors onto aligned sub-micron fibrous scaffolds for simultaneous control of cell differentiation and alignment. *Biomaterials* **2011**, *32* (32), 8097-8107.
273. Miller, E. D., et al., Spatially directed guidance of stem cell population migration by immobilized patterns of growth factors. *Biomaterials* **2011**, *32* (11), 2775-2785.
274. Rana, S., et al., "Click"-Triggered Self-Healing Graphene Nanocomposites. *Macromol. Rapid Commun.* **2016**, *37* (21), 1715-1722.
275. Shaygan Nia, A., et al., Click chemistry promoted by graphene supported copper nanomaterials. *Chem. Commun.* **2014**, *50* (97), 15374-15377.
276. Shaygan Nia, A., et al., Nanocomposites via a direct graphene-promoted "click"-reaction. *Polymer* **2015**, *79*, 21-28.
277. Kargarfard, N., et al., Improving Kinetics of "Click-Crosslinking" for Self-Healing Nanocomposites by Graphene-Supported Cu-Nanoparticles. *Polymers* **2018**, *10* (1), 17.
278. Brown, E. N., et al., In situ poly(urea-formaldehyde) microencapsulation of dicyclopentadiene. *J. Microencapsul.* **2003**, *20* (6), 719-730.
279. Arshady, R., Preparation of microspheres and microcapsules by interfacial polycondensation techniques. *J. Microencapsul.* **1989**, *6* (1), 13-28.
280. Zhang, H., et al., Silica encapsulation of n-octadecane via sol-gel process: A novel microencapsulated phase-change material with enhanced thermal conductivity and performance. *J. Colloid Interface Sci.* **2010**, *343* (1), 246-255.
281. Zhao, Y., et al., Facile Phase-Separation Approach to Encapsulate Functionalized Polymers in Core-Shell Nanoparticles. *Macromol. Chem. Phys.* **2014**, *215* (2), 198-204.
282. Averous, L., et al., Properties of thermoplastic blends: starch-polycaprolactone. *Polymer* **2000**, *41* (11), 4157-4167.
283. Schneider, C. A., et al., NIH Image to ImageJ: 25 years of image analysis. *Nat. Methods* **2012**, *9* (7), 671-675.
284. Schindelin, J., et al., The ImageJ ecosystem: An open platform for biomedical image analysis. *Mol. Reprod. Dev.* **2015**, *82* (7-8), 518-529.
285. Moss, S.; Zweifel, H., Degradation and stabilization of high density polyethylene during multiple extrusions. *Polym. Degrad. Stab.* **1989**, *25* (2), 217-245.
286. Hansen, T. V., et al., Just Click It: Undergraduate Procedures for the Copper(I)-Catalyzed Formation of 1,2,3-Triazoles from Azides and Terminal Acetylenes. *J. Chem. Educ.* **2005**, *82* (12), 1833.

287. Meldal, M.; Tornøe, C. W., Cu-Catalyzed Azide–Alkyne Cycloaddition. *Chem. Rev.* **2008**, *108* (8), 2952-3015.
288. Zhang, L., et al., Ruthenium-Catalyzed Cycloaddition of Alkynes and Organic Azides. *J. Am. Chem. Soc.* **2005**, *127* (46), 15998-15999.
289. Compton, B. G.; Lewis, J. A., 3D-Printing of Lightweight Cellular Composites. *Adv. Mater.* **2014**, *26* (34), 5930-5935.
290. Darcos, V., et al., Well-defined PCL-graft-PDMAEMA prepared by ring-opening polymerisation and click chemistry. *Polym. Chem.* **2010**, *1* (3), 280-282.
291. Dirlikov, S. K., Propargyl-terminated Resins—A Hydrophobic Substitute for Epoxy Resins. *High Perform. Polym.* **1990**, *2* (1), 67-77.
292. Marcano, D. C., et al., Improved Synthesis of Graphene Oxide. *ACS Nano* **2010**, *4* (8), 4806-4814.
293. Zhou, Z.; Fahrni, C. J., A Fluorogenic Probe for the Copper(I)-Catalyzed Azide–Alkyne Ligation Reaction: Modulation of the Fluorescence Emission via $3(n,\pi^*)-(\pi,\pi^*)$ Inversion. *J. Am. Chem. Soc.* **2004**, *126* (29), 8862-8863.
294. Le Droumaguet, C., et al., Fluorogenic click reaction. *Chem. Soc. Rev.* **2010**, *39* (4), 1233-1239.
295. Döhler, D., et al., Qualitative sensing of mechanical damage by a fluorogenic “click” reaction. *Chem. Commun.* **2016**, *52* (74), 11076-11079.
296. Rupp, H.; Binder, W. H., 3D Printing of Core–Shell Capsule Composites for Post-Reactive and Damage Sensing Applications. *Adv. Mat. Technol.* **2020**, 2000509.
297. Ng, W. L., et al., Polyelectrolyte gelatin-chitosan hydrogel optimized for 3D bioprinting in skin tissue engineering. *Int. J. Bioprint.* **2016**, *2* (1).
298. Li, C., et al., Rapid Formation of a Supramolecular Polypeptide–DNA Hydrogel for In Situ Three-Dimensional Multilayer Bioprinting. *Angew. Chem.* **2015**, *127* (13), 4029-4033.
299. Zhang, J., et al., Reduction of graphene oxide vial-ascorbic acid. *Chem. Commun.* **2010**, *46* (7), 1112-1114.
300. Bose, R. K., et al., Relationship between the network dynamics, supramolecular relaxation time and healing kinetics of cobalt poly(butyl acrylate) ionomers. *Polymer* **2015**, *69*, 228-232.
301. Lim, E., et al., Synthesis and Characterization of a New Light-Emitting Fluorene–Thieno[3,2-b]thiophene-Based Conjugated Copolymer. *Macromolecules* **2003**, *36* (12), 4288-4293.
302. Tillmann, H.; Hörhold, H. H., Synthesis, optical and redox properties of novel segmented cyano-PPV derivatives. *Synth. Met.* **1999**, *101* (1), 138-139.
303. Kowalski, S., et al., Synthesis of Poly(4,4-dialkyl-cyclopenta[2,1-b:3,4-b']dithiophene-alt-2,1,3-benzothiadiazole) (PCPDTBT) in a Direct Arylation Scheme. *ACS Macro Let.* **2012**, *1* (4), 465-468.
304. Facchetti, A., Polymer donor–polymer acceptor (all-polymer) solar cells. *Mater. Today* **2013**, *16* (4), 123-132.
305. Kirchherr, A.-K., et al., Stabilization of Indocyanine Green by Encapsulation within Micellar Systems. *Mol. Pharm.* **2009**, *6* (2), 480-491.
306. Kim, T. H., et al., Evaluation of Temperature-Sensitive, Indocyanine Green-Encapsulating Micelles for Noninvasive Near-Infrared Tumor Imaging. *Pharm. Res.* **2010**, *27* (9), 1900-1913.
307. Chávez, J. L., et al., Core–Shell Nanoparticles: Characterization and Study of Their Use for the Encapsulation of Hydrophobic Fluorescent Dyes. *Langmuir* **2008**, *24* (5), 2064-2071.
308. Zhou, L., et al., Semiconducting polymer nanoparticles for amplified photoacoustic imaging. *Wiley Interdiscip. Rev. Nanomed. Nanobiotechnol.* **2018**, *10* (5), e1510.
309. Gruskiene, R., et al., Grafting of poly(ethylene glycol) to chitosan at C(6) position of glucosamine units via “click chemistry” reactions. *Chemija* **2009**, *20* (4), 241-249.
310. Appel, R., Tertiary Phosphane/Tetrachloromethane, a Versatile Reagent for Chlorination, Dehydration, and P?N Linkage. *Angew. Chem. Int. Ed.* **1975**, *14* (12), 801-811.
311. Ito, M., et al., A Simple and Convenient Synthesis of Alkyl Azides under Mild Conditions. *Synthesis* **1995**, *1995* (04), 376-378.

312. Schulz, M., et al., Hybrid lipid/polymer giant unilamellar vesicles: effects of incorporated biocompatible PIB–PEO block copolymers on vesicle properties. *Soft Matter* **2011**, 7 (18), 8100-8110.
313. Shieh, P., et al., Fluorogenic Azidofluoresceins for Biological Imaging. *J. Am. Chem. Soc.* **2012**, 134 (42), 17428-17431.

8.0 Curriculum Vitae

Lebenslauf

Name: Harald Rupp
Anschrift: *****
Halle/Saale
Tel.: *****
E-Mail: *****
Geboren: 22.07.1990 in Homburg/Saar
Familienstand: ledig



Berufliche Laufbahn

- 04.05.2021 **Verteidigung der Dissertation**
summa cum laude
- 05.2020 – aktuell **Wissenschaftlicher Mitarbeiter für Lehre**
Martin-Luther-Universität Halle-Wittenberg
Master-Studiengang (Englisch): Polymer Materials Science (*Vorlesung, Seminar, Praktikum*), Organic chemistry, polymer synthesis, polymer analytics, polymer characterization
Betreuung von Bachelor- und Masterstudenten (Deutsch + Englisch)
Einarbeitung neuer Mitarbeiter
Forschung im Bereich 3D-Druck (FDM, Komposite)
- 10.12.2020 **Einreichen der Dissertation**
- 03.2016 – 11.2020 **Wissenschaftlicher Mitarbeiter (Promotion)**
Martin-Luther-Universität Halle-Wittenberg
in der makromolekularen Chemie bei Prof. Wolfgang H. Binder
Forschung im Bereich 3D-Druck (Kombination von FDM- und Inkjettechniken)
Synthese und Modifikation von Polymeren und reaktiven Kompositsystemen
Schreiben von wissenschaftlichen Publikationen
Teil des Leistungs- und Transferzentrum »Chemie- und Biosystemtechnik«
(www.chemie-bio-systemtechnik.de)
Betreuung von Bachelor- und Masterstudenten (Deutsch + Englisch)
Einarbeitung neuer Mitarbeiter

Bildungsweg

- 03.2016 – aktuell **Promotion in Chemie**
Martin-Luther-Universität Halle-Wittenberg
in der makromolekularen Chemie bei Prof. Dr. Wolfgang H. Binder
Thema: *Multicomponent 3D-printing for core-shell capsule composites and supramolecular polymers*

- 10.2013 – 11.2015 **Masterstudiengang Chemie**
Martin-Luther-Universität Halle-Wittenberg
 in der Festkörper-Chemie bei Prof. Dr. Stefan Ebbinghaus
 Abschluss: Master of Science, Note: 1,6
 Masterarbeit: *Synthese von Oxynitriden $AB(O,N)_3$ durch Ammonolyse von Oxideinkristallen*
- 10.2009 – 09.2013 **Bachelorstudiengang Chemie**
Martin-Luther-Universität Halle-Wittenberg
 in der makromolekularen Chemie bei Prof. Dr. Wolfgang H. Binder
 Abschluss: Bachelor of Science, Note: 2,2
 Bachelorarbeit: *Fluorogene Click-Reaktion an Polyisobutylene für selbstheilende Polymere*
- 09.2002 – 06.2009 **Wolkenberg-Gymnasium Michendorf**
 Abschluss: Abitur, Note: 2,4
 Leistungskurse: Chemie und Mathematik

Weitere Kenntnisse

- Sprachen:** Englisch – fließend (Unicert Stufe II)
 Japanisch – A1
 Französisch, Latein – Schulkenntnisse
- Preise:** Boosting the performance of long-chain polyamides – Evonik (via ekipa) –
 winning team ComPA12 (1st place)
 Schreiben eines Projektantrages
- Software:** MS Word, Powerpoint, Excel, LaTeX
 Grafische Datenauswertung mit Origin
 Analysesoftware: MestReNova, Diffrac.Suite Eva,
 Netzsch Proteus
- Sonstiges:** Führerscheinklasse B
 Steuerung und Auswertung von
 3D Drucker *regenHU 3DDiscovery*
 Rheometer *Anton Paar Physica MCR 201*
 Netzsch *DSC* und *TGA*
 Zonenschmelzofens *FZ-T-10000-H-VPO-PC*
 Gefriertrockner, UV-vis, Fluoreszenz, DLS,
 XRD, NMR, GPC, FT-IR, Kontaktwinkel, MALDI-MS, ESI-MS, SAXS,
 Ultraschall

Harald Rupp

Halle (Saale), 04.05.2021

Veröffentlichungen:

Marinow, Rupp, Binder "Materialien für die "Ewigkeit": selbstheilende Polymere – auch rezyklierbar!" *Chemie unserer Zeit*, ASAP, **2021**, ciuz.202100014R1.

Asche, Binder, Rupp „Gedruckt kombiniert!“ **2021**, VDI nachrichten, Seite 10, Jahrgang 75, Heft 12-13, <https://doi.org/10.51202/0042-1758-2021-12-13-10>.

Podcast: Druckwelle – ingenieur.de-Podcast zur Additiven Fertigung (Folge 15, 25.03.2021, Gedruckt kombiniert!)

Press release: Researchers develop new combined process for 3D printing. (Number 180/2020 from 16. December 2020)

Rupp and Binder "Multicomponent Stress-Sensing Composites Fabricated by 3D-Printing Methodologies." *Macromol. Rapid Commun.* **2020**, 2000450.

Rupp and Binder "3D Printing of Core-Shell Capsule Composites for Post-Reactive and Damage Sensing Applications." *Adv. Mater. Technol.* **2020**, 2000509.

Döhler, Kang, Cooper, Tok, Rupp, Binder and Bao "Tuning the Self-Healing Response of Poly(dimethylsiloxane)-Based Elastomers." *ACS Appl. Polym. Mater.* **2020**, 2 (9), 4127-4139.

Rupp, Döhler, Hilgeroth, Mahmood, Beiner and Binder "3D printing of supramolecular polymers: Impact of nanoparticles and phase separation on printability." *Macromol. Rapid Commun.* **2019**, 1900467.

Kargarfard, Diedrich, Rupp, Döhler and Binder "Improving Kinetics of "Click" Crosslinking" for Self-Healing Nanocomposites by Graphene-Supported Cu Nanoparticles." *Polymers* **2018**, 10 (1), 17.

Döhler, Rana, Rupp, Bergmann, Behzadi, Crespy and Binder "Qualitative sensing of mechanical damage by a fluorogenic "click" reaction." *Chem. Commun.* **2016**, 52 (74), 11076-11079.

9.0 Eigenständigkeitserklärung

Hiermit erkläre ich an Eides statt, dass ich die vorliegende Arbeit selbstständig und ohne fremde Hilfe verfasst habe. Andere als die angegebenen Quellen und Hilfsmittel wurden nicht benutzt und die den benutzten Werken wörtlich oder inhaltlich entnommenen Stellen wurden als solche kenntlich gemacht.

Außerdem erkläre ich, dass ich die vorliegende Dissertation an keiner anderen wissenschaftlichen Einrichtung zur Erlangung eines akademischen Grades eingereicht zu haben.

Halle (Saale), den

Harald Rupp